TECHNISCHE UNIVERSITÄT DRESDEN

Leibniz Institute for Solid State and Materials Research Dresden

Miniaturized Electron Optics based on Self-Assembled Micro Coils

Dissertation

zur Erlangung des akademischen Grades

Doctor rerum naturalium

(Dr. rer. nat.)

vorgelegt dem
Bereich Mathematik und Naturwissenschaften

der Technischen Universität Dresden

von

M. Sc. Felix Lucas Kern

geboren am 07.09.1991 in Gräfelfing

Eingereicht am 8. Februar 2022

Die Dissertation wurde in der Zeit von 05/2018 bis 02/2022 am Leibniz-Institut für Festkörper- und Werkstoffforschung Dresden angefertigt.

1. Gutachter: Prof. Dr. Bernd Büchner

2. Gutachter: Prof. Dr. Johan Verbeeck

Abstract

Beams of highly accelerated charged particles are essential for numerous indispensable devices used throughout natural sciences, industry and the healthcare sector, e.g., electron and ion microscopes, charged particle lithography machines and X-ray radiation sources. Magnetic charged particle optics that deflect, shape and focus high-energy charged particles are the backbone of all such devices, because of their superior optical power compared to electric field optics at large particle velocities. Conventional macroscopic magnetic optics, however, are large, costly and bulky, not high frequency capable and require active cooling for heat dissipation. They are therefore unsuitable for fast beam manipulation, multibeam instrumentation, and miniaturized applications, much desired for future advances in nanofabrication and analysis. The first on-chip micro-sized magnetic charged particle optics realized via a self-assembling micro-origami process were designed, fabricated and characterized within the frame of this work. The utilized micro-miniaturization approach overcomes all the aforementioned obstacles for conventional magnetic optics, while maintaining similar optical power. The exceptional properties of these optical elements are rendered possible by the unique features of strain-engineered micro-coils: small size, small inductance and small resistivity. Within the frame of this work, adaptive phase plates were fabricated, which generate electron vortex beams with an unprecedented orbital angular momentum of up to several 1000 ħ. Furthermore, fast electron beam deflectors for beam blanking, two-dimensional scanning and stroboscopic experiments were manufactured. They possess a deflection power in the mrad regime for 300 kV electrons and a high frequency passband up to 100 MHz. Additionally, miniaturized strong quadrupole lenses with focal lengths down to 46 mm for 300 kV electrons have been developed. These three types of electron optical elements are of great interest for a wide range of applications in nanofabrication and analysis, as they serve as integral components of future multibeam instruments, miniaturized devices, and stroboscopic measurement setups to be developed.

Kurzfassung

Zahlreiche Geräte, die in den Naturwissenschaften, in der Industrie und im Gesundheitswesen unverzichtbar sind, basieren auf Strahlen schneller geladener Teilchen. Dazu zählen unter anderem Elektronen- und Ionenmikroskope, entsprechende Lithographiestrahlanlagen und Röntgenstrahlungsquellen. Magnetische Optiken, die Strahlen geladener Teilchen ablenken, formen und fokussieren, sind das Rückgrat aller Geräte die mit hochenergetischen Teilchen arbeiten, da sie im Vergleich zu Optiken, die auf elektrischen Feldern basieren, bei hohen Teilchengeschwindigkeiten eine überlegene optische Leistung aufweisen. Konventionelle makroskopische magnetische Optiken sind jedoch groß, teuer und platzraubend, nicht hochfrequenzfähig und erfordern aktive (Wasser-)Kühlung zur Wärmeabfuhr. Sie sind daher für Mehrstrahlinstrumente, miniaturisierte Anwendungen und schnelle Strahlmanipulation ungeeignet, die für zukünftige Fortschritte in der Nanofabrikation und -analyse gebraucht werden. Im Rahmen dieser Arbeit wurden die ersten magnetischen selbst-assemblierenden Mikro-Origami-Elektronenoptiken entwickelt, hergestellt und charakterisiert. Mit dem verwendeten Miniaturisierungsansatz können, bei ähnlicher optischer Leistung, alle oben genannten Nachteile von konventionellen magnetischen Optiken überwunden werden. Die außergewöhnlichen Eigenschaften dieser optischen Elemente werden durch die einzigartigen Merkmale der Mikrospulen ermöglicht: geringe Größe, geringe Induktivität und geringer Widerstand. Im Rahmen dieser Arbeit wurden unter anderem adaptive Phasenplatten hergestellt, die Elektronenvortexstrahlen mit einem bislang unerreichten Bahndrehimpuls von bis zu mehreren 1000 $\hbar$ erzeugen. Des Weiteren wurden schnelle Elektronenstrahldeflektoren zur Strahlablenkung, zum zweidimensionalen Rastern und für stroboskopische Experimente gefertigt. Sie besitzen eine Ablenkleistung im mrad-Bereich für 300 kV Elektronen und einen Frequenzdurchgang bis zu 100 MHz. Darüber hinaus wurden miniaturisierte Quadrupollinsen mit Brennweiten kleiner als 46 mm für 300 kV Elektronen entwickelt. Diese drei Arten elektronenoptischer Elemente sind von großem Interesse für verschiedenste Anwendungen in der Nanofabrikation und -analyse, da sie unter anderem als integrale Bestandteile von zu entwickelnden Mehrstrahlinstrumenten, miniaturisierten Geräten und stroboskopischen Messaufbauten dienen können.

Contents

Abstract **I**

Notation **IV**

Remarks **VIII**

1 Introduction **1**

1.1 Charged Particle Optics 1

1.2 Miniaturized Charged Particle Optics 3

1.3 Phase Plates for Transmission Electron Microscopy 4

2 Charged Particle Optics **8**

2.1 Hamiltonian Formalism 8

2.2 Gaussian Matrix Optics 11

2.3 Transfer Matrices of Magnetic Elements 14

2.3.1 Single Quadrupole 14

2.3.2 Quadrupole Multiplets 19

2.3.2.1 Quadrupole Doublet 20

2.3.2.2 Quadrupole Triplet 26

2.3.2.3 Higher Order Quadrupole Multiplets 29

2.4 Scaling Laws for Charged Particle Optics 30

2.4.1 Thin Film 30

2.4.2 Electrostatic Scaling Laws 31

2.4.3 Magnetic Scaling Laws 35

3 Design and Fabrication of Miniaturized Electron Optics **42**

3.1 Basics of Polymer-Based Self-Assembly Technology 43

3.2 Basic Coil Design and Magnetic Field Simulations 44

3.3 CoFeSiB-Pyrex Core-Shell Micro Wires 46

3.4 Fabrication of Self-Assembled Micro Coil Devices 49

4 Optical Properties of Self-Assembled Miniaturized Electron Optics 52

4.1 Electron Vortex Phase Plate 57

4.1.1 Projected Magnetic Fields 58

4.1.2 Vortex Beam Characteristics 63

4.2 Miniaturized Deflector 66

4.3 Quadrupole Focusing Optic 75

4.4 High Frequency Characteristics of Self-Assembled Electron Optics 84

5 Summary and Outlook 93

5.1 Applications of Electron Vortex Beams with Large OAM 94

5.2 Optics of Large Optical Power for Pulsed Instruments 95

5.3 Stroboscopic TEM Measurements 96

5.4 Miniaturized Wigglers, Undulators and Free Electron Lasers 96

5.5 Towards Integrated Electron Optical Systems 97

List of Figures 100

List of Tables 102

List of Publications 103

References 104

Danksagung 125

Erklärung 127

Notation

AES	...	Auger Electron Spectroscopy
ALD	...	Atomic Layer Deposition
CCD	...	Charged Coupled Device
CESCOR	...	CEOS Scanning Corrector
CL	...	Cathodoluminescence spectroscopy
COM	...	Center of Mass
CPO	...	Charged Particle Optics
DC	...	Direct Current
DI water	...	DeIonized water
DPC	...	Differential Phase Contrast
EBSD	...	Electron Backscatter Diffraction
ED	...	Electron Diffraction
EDX	...	Energy-Dispersive X-ray spectroscopy
EEL(S)	...	Electron Energy Loss (Spectroscopy)
EMCD	...	Electron Magnetic Chiral Dichroism
EVB	...	Electron Vortex Beam
FEM	...	Finite Element Method
FIB	...	Focused Ion Beam
FOV	...	Field of View
HEOM	...	Hamiltonian Equations of Motion
HF	...	High Frequency
IAES	...	Ion induced Auger Electron Spectroscopy
ISS	...	Ion Scattering Spectroscopy
JVE	...	Jacobi Variational Equation
µCPO	...	miniaturized Charged Particle Optics
M	...	Metalloids
MFM	...	Magnetic Force Microscopy
MIP	...	Mean Inner (electrostatic) Potential
OAM	...	Orbital Angular Momentum
pH	...	pondus Hydrogenii
PPMS	...	Physical Properties Measurement System
ROI	...	Region of Interest
SA:V	...	Surface-Area-to-Volume ratio
SEM	...	Scanning Electron Microscopy / Microscope
SIMS	...	Secondary Ion Mass Spectrometry
SMA	...	Subminiature version A
SNR	...	Signal-to-Noise Ratio
SQUID	...	Superconducting Quantum Interference Device

(S)TEM	...	(Scanning) Transmission Electron Microscopy / Microscope
TM	...	Transition Metals
TOFMS	...	Time-of-Flight Mass Spectrometry
UED	...	Ultrafast Electron Diffraction
UEM	...	Ultrafast Electron Microscopy
UES	...	Ultrafast Electron Spectroscopy
VSM	...	Vibration Sample Magnetometry / Magnetometer

Institutes / Companies:

Accretech	...	Accretech (Europe) GmbH Landsberger Straße 396, 81241 München, Gemany
Ansys	...	Ansys Inc. Southpointe 2600 Ansys Drive Canonsburg, PA 15317, USA
Bruker	...	Bruker Corporation 40 Manning Road Billerica, MA 01821, USA
CEOS	...	Corrected Electron Optical Systems GmbH, Englerstrasse 28, 69126 Heidelberg, Germany
FEI	...	Field Electron and Ion Company now Thermofisher Scientific Materials & Structural Analysis Division 5350 NE Dawson Creek Drive Hillsboro, Oregon 97124, USA
Gatan	...	Gatan, Inc. 5794 W. Las Positas Blvd. Pleasanton, CA 94588, USA now AMETEK, Inc. 1100 Cassatt Road Berwyn, PA 19312, USA
Heidelberg Instruments	...	Heidelberg Instruments Mikrotechnik GmbH Mittelgewannweg 27, 69123 Heidelberg, Germany
ICMM	...	Instituto de Ciencia de Materiales de Madrid Sor Juan Inés de la Cruz 3, 28049 Madrid, Spain
IFF	...	Institut für Festkörperforschung, Helmholtzstraße 20, 01069 Dresden, Germany
IFW	...	Leibniz-Institut für Festkörper- und Werkstoffforschung, Helmholtzstraße 20, 01069 Dresden, Germany
IIN	...	Institut für Integrative Nanowissenschaften Helmholtzstraße 20, 01069 Dresden, Germany
Keithley	...	Tektronix, Inc. 14150 SW Karl Braun Drive Beaverton, OR 97077, USA
Keysight Technologies	...	Keysight Technologies Inc. 1400 Fountaingrove Parkway Santa Rosa, CA 95403-1738, USA

Micro Resist Technology	...	Micro Resist Technology GmbH Köpenicker Str. 325, 12555 Berlin, Germany
MicroChemicals	...	MicroChemicals GmbH Nicolaus-Otto-Straße 39, 89079 Ulm, Germany
Oxford Instruments Plasma Technology	...	Oxford Instruments plc N End, Yatton, Bristol BS49 4AP, United Kingdom
Protochips	...	Protochips Inc. 3800 Gateway Centre Blvd #306 Morrisville, NC 27560, USA
PVA Metrology & Plasma Solutions	...	PVA MPS GmbH Metrology & Plasma Solutions GmbH Im Westpark 10 - 12, 35435 Wettenberg, Germany
Quantum Design	...	Quantum Design Inc. 10307 Pacific Center Court San Diego, CA 92121, USA
Rhode Schwarz	...	Rhode Schwarz GmbH & Co. KG Mühldorfstraße 15, 81671 München, Germany
SPS-Europe	...	SPS-Europe B.V. Midden Engweg 41, 3882 TS Putten, Netherlands
Süss MicroTec	...	Süss MicroTec SE Schleissheimer Straße 90, 85748 Garching, Germany
Von Ardenne	...	Von Ardenne GmbH Am Hahnweg 8, 01328 Dresden, Germany
Zeiss	...	Carl Zeiss Microscopy Deutschland GmbH Carl-Zeiss-Strasse 22, 73447 Oberkochen, Germany

Chemicals:

BPDA	...	3,3',4,4'-benzophenonetetracarboxylic dianhydride
DADPS	...	3,3'- diaminodiphenyl sulfone
DEGMEE	...	diethylenglykol-monoethylether
DMA	...	N,N-dimethylacetamide
DMAEMA	...	dimethylaminoethyl methacrylate
EDTA	...	ethylenediaminetetraacetic acid
HEAA	...	N-2-hydroxyethyl acrylamide
MAPTMS	...	3-methacrylpropyltrimethoxysilane
NEP	...	N-ethyl-2-pyrrolidon
PEMA	...	polyethylene-alt-maleic anhydride

Remarks

This thesis was typesetted using TEX[1] and the macro package LATEX[2]. Charts as well as the data plots were created with LATEX's TIKZ and PGF package[3], respectively. The *Python* programming language[4] was employed of numerical investigations, *Ansys* Electronics[5] for the FEM analysis.

[1] D. E. Knuth, *The TeXbook*, Addison-Wesley, MA, USA (1986)
[2] L. Lamport, *Latex: a document preparation system*, Addison-Wesley, MA, USA (1986)
[3] T. Tantau, *Graph Drawing in TikZ*, Proceedings of the 20th International Conference on Graph Drawing, p. 517-528, (2013)
[4] Python Software Foundation. Python Language Reference, version 3.6.3. Available at http://www.python.org
[5] *Ansys* Electromagnetics, *Release 17.2*

1 Introduction

1.1 Charged Particle Optics

Beams of charged particles are essential for numerous indispensable devices used throughout natural sciences, industry and the healthcare sector. The fields of their application may be logically divided into characterization and manufacturing. Electron and ion beam techniques for characterization range from diffraction, through spectroscopy to microscopy. In manufacturing they are employed to break or create (chemical) bonds to manipulate objects enabling the fabrication of (micro) electronic systems for the use in many domains in industry and academia. A lot of groundbreaking insights in fundamental natural sciences were gained with the aid of charged particle techniques.

The deflection of cathode rays in an electrostatic field led to the discovery of the electron and their deflection in a magnetic field to the first determination of their charge-to-mass ratio [1]. The development of quantum theory was heavily influenced by experiments using electron beams, e.g. the Frank-Hertz experiment [2] or electron diffraction experiments that led to the discovery of the wave-particle duality of quantum objects [3, 4].

Many important findings in biological science were also predicated on beams of charged particles, for example the first-time imaging of viruses and hence the direct proof for their existence [5], and the discovery of ribosomes [6] as well as the determination of their structure [7, 8]. The generation of X-rays is also often realized by utilizing charged particle beams, e.g. by directing a focused electron beam on some material, in order to produce Bremsstrahlung or characteristic radiation, which is also how they were initially discovered [9]. Note, however, that the currently most brilliant X-ray sources are free electron lasers [10], which exploit the coherent Bremsstrahlung from an undulated electron beam.

Beams of charged particles are also vital for nuclear and particle physics, as they enable the generation of the highest man-made energy densities. Important milestones premised on beams of charged particles in these fields were the determination of the structure of atomic nuclei [11], the discovery of all quarks in the standard model of particle physics [12, 13, 14, 15, 16], of the W and Z bosons [17, 18] and finally also of the Higgs boson [19, 20].

Charged particle appliances are also of vital importance in state-of-the-art medical and research labs regardless of which kind of research, fundamental, applied or industrial. They may be classified into two logical categories depending on whether they are used to analyze properties of specimen in real or reciprocal (i.e. momentum) space or in time or frequency (i.e. energy) domain, although combinations are common. The first category contains microscopic techniques, like scanning electron microscopy (SEM), transmission electron microscopy (TEM), focused ion beam (FIB) microscopy or atom probe (microscopy). The second one comprises diffractive techniques, such as electron diffraction (ED) or electron backscatter diffraction (EBSD). Measurement schemes in the time domain are mostly referred to as time-resolved, dynamic or ultrafast. This field is dominated by photonic techniques, although ultrafast electron microscopy (UEM) [21, 22], diffraction (UED) [23, 24] and spectroscopy (UES) [25, 26] are actively explored. The last

category consists of spectroscopic techniques, e.g. electron energy loss spectroscopy (EELS), cathodoluminescence (CL) spectroscopy, energy dispersive X-ray spectroscopy (EDX), Auger electron spectroscopy (AES), ion scattering spectroscopy (ISS), ion induced Auger electron spectroscopy (IAES), secondary ion mass spectrometry (SIMS) and time-of-flight mass spectrometry (TOFMS).

Electron beams are also commonly used in industry, e.g. for welding, hardening, annealing, tempering, texturing, and polishing of surfaces, for curing inks, for metal powder production, for electron beam scrubbing and for food sterilization. Additionally, in micro-fabrication industry and research, electron and ion lithography devices are of fundamental importance, as they are used to produce masks for photo lithography machines. Besides that, electron and ion beam instruments are essential for quality control in this sector, as well as for sputtering and etching of materials and for vacuum generation by ion getter pumps. Furthermore, charged particle instrumentation is an integral element in every modern medical practice and hospital, not only for the generation of X-rays, but also for sterilization and cancer treatment in radiation therapy.

Charged particle optics (CPO), i.e., devices used to accelerate, direct or focus beams of charged particles, are mandatory for all the aforementioned applications of charged particle beams. The deflection of cathode rays in magnetic and electric fields was already outlined in 1858 [27] and 1890 [28], respectively, almost 40 and 10 years before Thomson's famous experiments, which are commonly considered as the discovery of the electron [1]. Shortly after the theoretical description of the wave properties of quantum objects by de Broglie in 1924 [29], the first focusing elements for electrons were proposed [30, 31]. Finally, the first magnetic [32] and electrostatic lenses [33] were built in 1937. Earliest ion beam accelerators were also constructed in that era, already reaching kinetic energies of several 10 kilovolts [34]. In 1936 Scherzer showed that aberrations of round static lenses without space charges in the path of the electron beam are inevitable [35], which limited the resolution of charged particle microscopes until the advent of aberration correctors (breaking the circular symmetry) in the late 1990s [36].

In spite of these tremendous developments and achievements there are several hurdles that still prevent CPO devices from a more wide spread use: Mostly the cost of the devices and the necessary surrounding infrastructure, as well as their size and weight. A very promising route to circumvent these obstacles is utilizing modern micro-fabrication techniques to produce miniaturized CPOs (μCPOs). The reduction in size and weight alone may widen the scope of their application, for example to build instruments where multiple characterization and manipulation methods are integrated in one device or for the retrofitting of conventional macroscopic devices with miniaturized CPOs. Additionally, miniaturization could enable the utilization of charged particle optical systems in remote locations where transport and maintenance is difficult, e.g. in space [37]. Systems of μCPOs do not only have advantages regarding their physical dimensions, the miniaturization also eases the requirements on the supporting equipment regarding vacuum system, water cooling or power supply.

1.2 Miniaturized Charged Particle Optics

There are several incitements for the ongoing miniaturization efforts in charged particle optics, most of which are driven by reduction of cost and necessary space, yet there are also various performance gains anticipated. Potential cost efficiency advantages are based on different effects: The vacuum requirements become more relaxed for smaller systems, because the ratio between system size and the mean free path lengths of the charged particles in a vacuum of particular pressure is reduced. Accordingly, miniaturization may also open up new pathways for environmental microscopy (e.g. *in vivo* analysis of biological specimen) and novel manufacturing techniques, where operation at higher pressure levels is beneficial. For CPO devices employing magnetic fields produced by electrical currents, the intrinsic increase in surface-area-to-volume ratio in miniaturized devices leads to better power dissipation, eventually rendering costly and failure-prone water cooling obsolete. Additionally, large, heavy and expensive vibration isolated fixation installations become much smaller, lighter and less expensive. Savings in the production process due to parallelization are anticipated for optical elements that can be fabricated with lithographic methods. The above mentioned benefits in performance through miniaturization may also be traded for lower costs at comparable performance, e.g. by decreasing the requirements for auxiliary components, e.g. costly power supplies that are very stable at large currents.

The frequency response of miniaturized elements is also expected to hugely benefit from miniaturization, as the corresponding inductance commonly scales with system size [38]. The increased frequency response enables novel time-resolved measurement schemes based on charged particles, without the need for expensive laser systems or high frequency cavities.

The miniaturization of the complete CPO system renders the fabrication of multibeam devices in a tightly packed multiple-column fashion possible, in contrast to multibeam devices with multiple sources sharing one column and the same optics (c.f. [39, 40, 41, 42]), or with a shared source and multiple columns and optics [43, 44, 45, 46, 47, 48, 49, 50, 51]. Multibeam devices are desired in lithography as well as in microscopy for quality control, as throughput, scaling linearly with the number of beams, could be increased by orders of magnitude. Increased throughput is also approached by conventional multibeam optics [52] with shared source and optics but with the disadvantage of large beam broadening due to space charge effects (Boersch effect [53]) and a much larger demand for low aberrations of the corresponding optics. Another factor that contributes to performance gains of miniaturized CPOs is the decreased impact of ambient magnetic stray fields on shorter beam paths, as compared to regular macroscopic apparatuses. Additionally, miniaturization leads to a reduction of the resolution limiting geometric, as well as chromatic aberrations, for many common lens designs [54, 55, 56, 57]. Optics with small chromatic aberrations are of particular interest, possibly being the key for the utilization of uncommon charged particle sources and accelerators with a comparably large energy spread [58, 59, 60].

These promising benefits led to several developments of miniaturized electron microscopes and electron lithography instruments. Most of which utilize electrostatic optics[6], limiting the acceleration voltages to few kilovolts, as electrostatic optics become increasingly ineffective for larger particle velocities. The attainable optical power of electrostatic optics is ultimately limited by the dielectric strength of the inter-

[6] one notable exception, employing a weak focusing axial magnetic field is given in [56]

mediate isolating material, which decreases linearly with system size (c.f. section 2.4.2 of this work). For electron lithography higher particle energies would be preferable, however, as the resolution limiting proximity effect [61] due to electron scattering in the photoresist decreases with acceleration voltage [62, 63]. Therefore, electron lithography with sub 10 nanometer resolution was realized by dedicated photoresists and relatively large acceleration voltages from 30 - 100 kilovolts [64, 65, 66, 67, 68, 69, 70]. Attainable depth of focus at similar lateral resolution also benefits from larger acceleration voltages. The main reasons why optics based on electromagnets for miniaturized charged particle systems have been mostly ignored so far[7] might be the difficulty of manufacturing miniaturized solenoids of good quality, the inaccessibility of microelectronic production technology for those, as well as the difficulty of micro manufacturing appropriate pole piece materials, as well as their integration. One especially elegant production scheme to surmount those challenges is the polymer-based self-assembly of micro coils with tapered soft magnetic micro wires as pole pieces, which will be introduced in chapter 3 of this thesis, before several such electron optical elements will be analyzed in greater detail in chapter 4.

1.3 Phase Plates for Transmission Electron Microscopy

Miniaturized charged particle optics, integrated into conventional macroscopic systems, recently found a lot of interest, harnessing the restricted space in macroscopic systems for modifications and additional installations. The available space in macroscopic CPO systems is mainly limited for two reasons: First, the vacuum volume needs to be small to reduce pumping times and the likelihood of leaks, and second the amplification of the flux density in magnetic CPOs, commonly achieved by the use of narrow pole pieces. The increasing availability of micro-fabrication equipment enabled the advent of miniaturized CPO elements and their wide spread utilization. Very prominent examples in that regard are the various types of phase plates for transmission electron microscopes used to shape the phase of the electron wave in manifold desired ways. The phase plates may be categorized into three main operation principles: electrostatic, magnetic and electromagnetic.

Electrostatic Phase Plates

The historically earliest type of phase plates were electrostatic Zernicke phase plates [73], with their development dating back to 1947 [74]. They were proposed for electron microscopes to overcome the poor phase contrast due to the quantum mechanical phase problem in electron optical images, where the recorded intensity is the amplitude of the wave function squared and the phase information is lost. Both the mean inner electrostatic potential (c.f. Eq. (2.104)) of a thin film, as well as the use of an electrostatic potential applied between two electrodes have been suggested to shift the phase of the electron wave. The first thin film phase plates were realized in 1949 [75] shortly after their proposal in 1947 [74]. Difficulties in manufacturing, however, restricted the progress in their development [76]. Charging due to ejection of secondary electrons, unwanted diffuse scattering and long-term stability issues due to contamination and

[7] although very promising results were obtained by surface machined electromagnets. The corresponding efforts, however, were more tailored towards very complicated miniaturized free electron lasers [71, 72].

radiation damage limit their application as a standard tool for phase contrast enhancement [77]. In so-called Volta phase plates [78], the additional potential from electron beam induced charging is exploited for the generation of the desired phase shift. This approach, however, also generates unwanted temporal variations of the resulting phase shifts [79]. Despite these challenges, thin film phase plates became a very valuable tool, especially for TEM analysis of biological specimen [79]. Once a thin film phase plate is manufactured, however, its phase shift can just be altered slightly by varying the intensity of the incident electrons and thus the charging of the film, or very drastically by changing the acceleration voltage. Electrostatic phase plates utilizing an external applied potential [80] are thus more flexible alternatives. Arrays of individually addressable electrode assemblies are promising candidates for adaptive charged particle optics [81, 82], especially as they can usually be operated in a very high frequency range.
A peculiar phase plate type are so-called Hilbert phase plates [83]. They produce a different kind of phase contrast by introducing a phase shift of π in one half of the electron beam in Fourier space. Electrostatic thin film Hilbert phase plates are comparably straight forward to be fabricated by focused ion beam milling [76].

Magnetic Phase Plates

While the electrostatic phase shift is inversely proportional to the primary electron velocity (c.f. Eq. (2.104)), the respective magnetic one is independent, which is referred to as isochromaticity. Magnetic elements are therefore better suited for applications at higher particle acceleration voltages, as in conventional TEMs. There have been various attempts to construct magnetic Zernicke-type phase plates, which feature a ferromagnetic ring supporting a vortex magnetization pattern. The electrons passing through such a ring acquire a phase shift proportional to the magnetic flux enclosed in the ring [84]. By tuning the ring's material and shape and placing it around the zero beam in an electron microscope a Zernicke phase plate can be realized. Magnetic Hilbert phase plates can be manufactured either by a thin straight magnetic needle or a closed loop magnet, extending half way into the beam in far field [85, 86]. With the notable exception of [87], there are no adaptive magnetic phase plates reported in literature so far. The suchlike obtained phase shift, however, were comparably small, as the exploited magnetic field was generated by a current through a sub micron sized wire, without any (soft) ferromagnetic material amplifying the field.

Electromagnetic Phase Plates

Electromagnetic phase plates exploit stimulated Compton scattering of photons at the beam electrons. In standing light waves, the resulting ponderomotive force leads to the desired phase shift, which is referred to as the Kapitza-Dirac effect, predicted already in 1933 [88]. Its experimental validation, however, took until 1987 [89], where sufficiently intense (laser) light sources were available. As the underlying stimulated Compton scattering is a second order process, huge laser intensities are required to generate the desired phase shifts, which is still very challenging inside electron microscopes. Therefore, the attainable phase shifts obtained with available in house laser systems is comparably low. The largest phase shifts (38°) within an electron microscope were generated by a one dimensional standing laser wave, where an optical

cavity was used to enhance the laser intensity [90]. In principle more complex higher dimensional waves can be generated using spatial light modulators, which , however, is technologically very challenging at the desired laser power. Laser-based optical elements can be operated in very high frequency regimes, if pulsed lasers are employed. This, however, requires synchronous electron emission, in turn leading to much smaller integrated intensities.

Electron Vortex Beam Generation

Aside from enhancing phase contrast, adaptive electron optics and aberration correction [91], another promising application of the various types of phase plates is electron beam shaping. One contemporary example is the generation of electron vortex beams (EVBs), electron beams that have non-zero orbital angular momentum (OAM), similarly to circularly polarized light carrying a spin angular momentum of $\pm\hbar$ [92]. First electron vortex beams were produced by suitable thin films with an azimuthally increasing thickness [93]. Subsequently, fork-shaped Fresnel zone plates were used [94], where an amplitude mask with consecutive wave propagation yields the desired phase at the specimen position. Recently, an adaptive electrostatic vortex phase plate was realized by two nano wires aligned in parallel, at which an antisymmetric electrostatic potential was applied [95]. Attempts for EVB generation using the magnetic field of a micro-sized magnetized nickel needle showed very promising results [96], however, no functional magnetic vortex phase plate with variable OAM was reported in literature so far. In chapter 4.1 of this thesis, the realization of a novel adaptive magnetic EVB phase plate manufactured with self-assembled micro coils is explained in detail.

Outline

This thesis is structured in the following way: After an introduction to a Hamiltonian formalism (Sec. 2.1) for charged particle optics and the following derivation of Gaussian matrix optics (Sec. 2.2), transfer matrices for thin magnetic quadrupoles and assemblies of which are established and analyzed. In section 2.4 scaling laws for the miniaturization of charged particle optical elements are derived, which serve as a starting point for the analysis of systems of µCPOs, as well as a motivation for their application. The following chapter 3 introduces the polymer-based self-assembling micro coils that are the backbone of the technology used to produce µCPO elements in this work. After a short introduction to the self-assembly process (Sec. 3.1) the results of finite element method (FEM) simulations of the magnetic fields in the micro coils are displayed (Sec. 3.2). Measurements of the magnetic behavior of the employed soft-magnetic micro wires, which are used as pole pieces inside the micro coils, are analyzed in section 3.3. An introduction to the production process for the self-assembled micro coils is given in section 3.4. The electron optical properties of the accordingly manufactured elements are analyzed in chapter 4, which is composed of three sections for the different types of fabricated elements, single pole EVB phase plates (Sec. 4.1), 1D dipole and 2D vectormagnet deflectors (Sec. 4.2), as well as anisotropically focusing quadrupole lenses (Sec. 4.3). This experimental chapter is completed by the analysis of the high-frequency behavior of the miniaturized µCPO elements in section 4.4. In the final chapter 5 several promising applications based on the developed µCPO elements are proposed and evaluated briefly.

2 Charged Particle Optics

The rigorous description of a generalized charged particle optical system would be based on a quantum mechanical formalism, either solving the corresponding wave equations [97, 98, 99, 100, 101, 102] or the Feynman path integrals [103] for the pertaining electromagnetic fields and initial quantum states. The spin of the charged particles can be ignored in most cases, as the spin-orbit coupling is negligible in CPO systems for fast particles. Considering the wave equation approach, this means the Klein-Gordon Equation [104] or the (relativistically corrected) Schrödinger equation [105] can be put in place of the Dirac equation.

A semi-classical treatment, however, is precise enough for most calculations regarding optics, where the characteristic length scales of the external fields are much larger than the considered wavelengths. In that regard, the charged particle wave fronts are approximated to be perpendicular to the classical charged particle trajectories (in magnetic field free domains). Purely wave optical phenomena, such as resolution limiting diffraction effects at non-transparent boundaries, can be introduced in an *a-posteriori* fashion by means of an according effective theory.

For practical system design and analysis, however, the quantum character may be completely neglected. The corresponding classical simulations can either be done in an analytical fashion by solving the pertaining classical equations of motion (e.g. [106]) or by numerical ray tracing (e.g. [107]).

2.1 Hamiltonian Formalism

Classical approaches discuss the particle trajectories within phase space (i.e. Hamiltonian mechanics), or generalized coordinates (i.e. Lagrange formalism). In the following, Hamiltonian mechanics operating in 6 dimensional phase space is employed, with three position components and three canonical momentum components, $\mathbf{r} = (x, y, z)^\mathsf{T}$ and $\mathbf{p} = \left(p_x, p_y, p_z\right)^\mathsf{T}$, respectively. So in this sense, every state of the system is exactly described by one state vector in phase space:

$$\mathbf{x} = \begin{pmatrix} x \\ y \\ z \\ p_x \\ p_y \\ p_z \end{pmatrix} . \tag{2.1}$$

Following the principle of least action, the time evolution of the system is given by Hamiltonian equations of motion (HEOM), where the Hamiltonian vector field reads:

$$\mathbf{X}_{\mathbf{x}(t)} = \frac{\mathrm{d}\mathbf{x}}{\mathrm{d}t} = \begin{pmatrix} \frac{d\mathbf{r}}{dt} \\ \frac{d\mathbf{p}}{dt} \end{pmatrix} = \begin{pmatrix} \frac{\partial \mathcal{H}}{\partial \mathbf{p}} \\ -\frac{\partial \mathcal{H}}{\partial \mathbf{r}} \end{pmatrix} = \{\mathbf{x}, \mathcal{H}\} , \tag{2.2}$$

with the Poisson bracket denoted as $\{\cdot, \cdot\}$ and the Hamilton function $\mathcal{H}$, corresponding to the system's total energy.

The non-relativistic Hamiltonian may be written as:

$$\mathcal{H}(\mathbf{r}, \mathbf{p}, t) = \frac{(\mathbf{p} - q\mathbf{A}(\mathbf{r}, t))^2}{2m} + q\Phi(\mathbf{r}, t) \ , \tag{2.3}$$

whereas the relativistic one, commonly employed in charged particle optics, is given by:

$$\mathcal{H}(\mathbf{r}, \mathbf{p}, t) = c\sqrt{m^2c^2 + (\mathbf{p} - q\mathbf{A}(\mathbf{r}, t))^2} + q\Phi(\mathbf{r}, t) \tag{2.4}$$

with c being the speed of light in vacuum, γ the relativistic Lorentz factor, $\mathbf{A}(\mathbf{r}, t)$ the magnetic vector potential, $\Phi(\mathbf{r}, t)$ the electrostatic potential and m and q the rest mass and charge of the particle, respectively. The Hamiltonian vector field $\mathbf{X}_{\mathbf{x}(t)} = \left(\frac{\partial\mathcal{H}}{\partial\mathbf{p}}, -\frac{\partial\mathcal{H}}{\partial\mathbf{r}}\right)^T$ can be constructed by taking the partial derivative of $\mathcal{H}$ with respect to $\mathbf{x}$ and $\mathbf{p}$, respectively, i.e. Hamilton's equations. In the non-relativistic case this reads:

$$\mathbf{X}_{\mathbf{x}(t)} \coloneqq \begin{pmatrix} \frac{\mathbf{p}-q\mathbf{A}}{m} \\ \frac{q}{m}\frac{\partial A_i}{\partial\mathbf{r}}(p_i - qA_i) - q\frac{\partial\Phi}{\partial\mathbf{r}} \end{pmatrix} . \tag{2.5}$$

While it is:

$$\begin{aligned} \mathbf{X}_{\mathbf{x}(t),\,\mathrm{rel}} &= \begin{pmatrix} \frac{\mathbf{p} - q\mathbf{A}}{\sqrt{m^2 + \frac{1}{c^2}(\mathbf{p} - q\mathbf{A})^2}} \\ q\frac{\partial A^i}{\partial\mathbf{r}}\frac{p_i - qA_i}{\sqrt{m^2 + \frac{1}{c^2}(\mathbf{p} - q\mathbf{A})^2}} - q\frac{\partial\Phi}{\partial\mathbf{r}} \end{pmatrix} \\ &= \begin{pmatrix} \frac{\mathbf{p} - q\mathbf{A}}{\gamma m} \\ q\frac{\partial A_i}{\partial\mathbf{r}}\frac{p_i - qA_i}{\gamma m} - q\frac{\partial\Phi}{\partial\mathbf{r}} \end{pmatrix} , \end{aligned} \tag{2.6}$$

in the relativistic case. Einstein's sum convention is employed and coordinate arguments are dropped in both formulations and from now on to condense the notation.

In order to solve the Hamiltonian equation of motion (Eq. (2.2)), it is convenient to identify one solution as a design trajectory, commonly called the optical axis, $\mathbf{x}_{\mathrm{ref}}(t)$. This reference trajectory can be either straight, e.g. in case of round lenses, quadrupoles and higher order multipoles or the Wien filter, or curved, e.g. for dipole like arrangements, like the sector magnet in a magneto dispersive energy filter commonly employed for EELS in TEM, or in particle collider rings. This optical axis can either be calculated analytically or, for more complex systems, numerically by ray tracing. The reference trajectory should always be chosen such that it reflects the maximum amount of symmetries of the field configuration.

Starting from here, all relevant solutions for the complete CPO system $\mathbf{y}(t)$ can be constructed as deviations from the design trajectory $\mathbf{x}_{\mathrm{ref}}(t) = \mathbf{x}(t)$, as a deviation vector $\delta\mathbf{x}(t)$[108]:

$$\mathbf{y}(t) = \mathbf{x}(t) + \delta\mathbf{x}(t) \ . \tag{2.7}$$

The corresponding HEOM (c.f. Eq. (2.2)) is then given by:

$$\frac{d(\mathbf{x} + \delta\mathbf{x})}{dt} = \mathbf{X}_{\mathbf{x}+\delta\mathbf{x}} \ , \tag{2.8}$$

yielding the following expression for the time derivative of the deviation vector $\delta\mathbf{x}(t)$:

$$\begin{aligned} \frac{d(\delta\mathbf{x})}{dt} &= \frac{d(\mathbf{x} + \delta\mathbf{x})}{dt} - \frac{d\mathbf{x}}{dt} \\ &= \mathbf{X}_{\mathbf{x}+\delta\mathbf{x}} - \mathbf{X}_{\mathbf{x}} \ , \end{aligned} \tag{2.9}$$

which can be expanded by means of a multidimensional Taylor series:

$$\begin{aligned} \frac{d\left(\sum_n \varepsilon^n \delta x_i^{(n)}\right)}{dt} &= \left(\frac{\partial X_i}{\partial x_j}\right)_{\mathbf{x}(t)} \sum_n \varepsilon^n \delta x_j^{(n)} \\ &\quad + \frac{1}{2}\left(\frac{\partial^2 X_i}{\partial x_{j_1} \partial x_{j_2}}\right)_{\mathbf{x}(t)} \sum_{n_1} \varepsilon^{n_1} \delta x_{j_1}^{(n_1)} \sum_{n_2} \varepsilon^{n_2} \delta x_{j_2}^{(n_2)} + \ldots \qquad (2.10a) \\ &= \sum_{n=1}^{\infty} \frac{1}{n!} \sum_{|j|=n} \binom{n}{j} \left(D^j X_i\right)_{\mathbf{x}(t)} \left(\sum_m \varepsilon^m \delta x^{(m)}\right)^j . \qquad (2.10b) \end{aligned}$$

In Eq. (2.10a) an auxiliary small parameter $\varepsilon = 1$ was introduced in an additional series expansion of $\delta\mathbf{x} = \sum_n \varepsilon^n \delta\mathbf{x}^{(n)}$. Multiindex notation $j = (j_1, \ldots, j_6)$ was employed In Eq. (2.10b) with:

$$D^j = \frac{\partial^{|j|}}{\partial x_1^{j_1} \ldots \partial x_6^{j_6}} \text{ and } \binom{n}{j} = \frac{n!}{\prod_{i=1}^{6} j_i!} \ . \tag{2.11}$$

In this series, different powers of ε reflect the various orders of trajectories and their aberrations, where $\delta x_j^{(1)}$ is usually called the Gaussian trajectory. All higher orders ($n > 1$) can be interpreted as deviations from the Gaussian trajectories $\mathbf{x}(t)$, for which $\delta x_j^{(n>1)}$ is set to zero by definition, and describe the different orders of aberrations. It is important to mention that chromatic as well as geometric aberrations are included in this notation, in contrast to other common descriptions of aberrations, where chromatic aberrations usually have to be additionally inserted in an *ad hoc* manner [109]. Additionally, the considered fields can be time-dependent rendering, e.g., the incorporation of electromagnetic elements straight forward as long as the features of the respective fields are large compared to the beam wavelengths, which means that the semi-classical approximation holds.

2.2 Gaussian Matrix Optics

Starting from here, the important characteristics of any CPO can be calculated by the analysis of the different terms in Eq. (2.10b). If the reference trajectory is already known, through symmetry principles or numerical ray tracing, the next step is usually to find the principal planes, focal lengths and (intermediate) image planes. All of which can be computed within Gaussian optics. The calculation of aberrations, i.e. deviations of the real trajectories from the Gaussian ones, is merely possible if the first order Gaussian characteristics are already known. In that regard Gaussian optics is also the backbone of the deeper analytical analysis of every CPO system.

The ultimate goal in Gaussian optics is to set up linear relations between position $\mathbf{x}$ and momentum $\mathbf{p}$ of the considered entities, usually formulated in a very convenient matrix form. These linear relations are conventionally defined as the deviation of $\mathbf{x}$ and $\mathbf{p}$ from the predefined design trajectory. They can be calculated through the Jacobi variational equation (JVE), the $n = 1$ term in the series expansion in Eq. (2.10b):

$$\begin{aligned} \frac{\mathrm{d}\left(\delta x_i\left(t\right)\right)}{\mathrm{d}t} &\approx \left(\frac{\partial X_i}{\partial x_j}\right)_{\mathbf{x}(t)} \delta x_j\left(t\right) \\ &= \chi_{ij}\left(t\right) \delta x_j\left(t\right) \,, \end{aligned} \tag{2.12}$$

where $\chi_{ij}\left(t\right)$ is defined as the Jacobian of the Hamiltonian vector field $\mathbf{X}_{\mathbf{x}(t)}$ (c.f. Eq. (2.5) and Eq. (2.6)). This paraxial approximation already yields the expressions for the focal lengths of optical elements or systems, the locations of their principal planes and their magnification. By employing the Lie derivative $\mathcal{L}_{\mathbf{X}}$ (see [110] for an introduction and more details in the notation) of the deviation vector $\delta\mathbf{x}$

$$\begin{aligned} \left(\mathcal{L}_{\mathbf{X}}\delta\mathbf{x}\right)_i &= \frac{\partial\delta\mathbf{x}^i}{\partial x^j}X^j - \frac{\partial X_i}{\partial x_j}\left(\delta\mathbf{x}\right)_j \\ &= \frac{\mathrm{d}\left(\delta\mathbf{x}\right)_i}{\mathrm{d}t} - \frac{\partial X_i}{\partial x_j}\left(\delta\mathbf{x}\right)_j \,, \end{aligned} \tag{2.13}$$

the JVE (Eq. (2.12)) can be rewritten as:

$$\mathcal{L}_{\mathbf{X}}\left(\delta\mathbf{x}\right) = 0\,. \tag{2.14}$$

Deviation vectors fulfilling this equation are forming so-called invariant vector fields. In this notation Liouville's theorem is given by:

$$\mathcal{L}_{\mathbf{X}}\omega\left(\delta\mathbf{x}, \delta\mathbf{x}'\right) = \frac{\mathrm{d}}{\mathrm{d}t}\omega\left(\delta\mathbf{x}, \delta\mathbf{x}'\right) = 0\,, \tag{2.15}$$

for any Poincaré 2-form $\omega\left(\delta\mathbf{x}, \delta\mathbf{x}'\right)$, measuring the preserved phase space volume spanned by the invariant vector fields $\delta\mathbf{x}$ and $\delta\mathbf{x}'$ along the optical axis. The conservation of transverse phase space volume leads to the so-called Helmholtz-Lagrange invariants, finally also yielding Abbe's sine condition, the statement that the real space magnification of some imaging system behaves reciprocally to its angular magnification.

The JVE for the non-relativistic CPO is given by:

$$\begin{aligned}\frac{\mathrm{d}\left(\delta \mathrm{x_i}\left(\mathrm{t}\right)\right)}{\mathrm{dt}} &\approx \left(\frac{\partial \mathrm{X_i}}{\partial \mathrm{x_j}}\right)_{\mathbf{x}(\mathrm{t})} \delta \mathrm{x_j}\left(\mathrm{t}\right) \\ &= \frac{\mathrm{q}}{\mathrm{m}} \left(\begin{array}{c|c} -\frac{\partial A_i}{\partial r_j} & \frac{1}{q}\delta_{ij-3} \\ \hline \frac{\partial^2 A_k}{\partial r_{i-3}\partial r_j}\left(p_k - qA_k\right) - q\frac{\partial A_k}{\partial r_{i-3}}\frac{\partial A_k}{\partial r_j} - m\frac{\partial^2 \Phi}{\partial r_{i-3}\partial r_j} & \frac{\partial A_{j-3}}{\partial r_{i-3}} \end{array}\right)_{\mathbf{x}(\mathrm{t})} \delta \mathrm{x_j}\left(\mathrm{t}\right), \end{aligned} \tag{2.16}$$

while it reads:

$$\begin{aligned}&\frac{\mathrm{d}\left(\delta \mathrm{x_i}\left(\mathrm{t}\right)\right)}{\mathrm{dt}} \approx \\ &\frac{\mathrm{q}}{\gamma \mathrm{m}} \left(\begin{array}{c|c} -\frac{\partial \mathrm{A_i}}{\partial \mathrm{r_j}} + \frac{\partial \mathrm{A_k}}{\partial \mathrm{r_j}}\frac{\mathrm{p_k}-\mathrm{qA_k}}{\mathrm{c}^2(\gamma \mathrm{m})^2}\left(\mathrm{p_i} - \mathrm{qA_i}\right) & \frac{1}{\mathrm{q}}\left(\delta_{\mathrm{ij}-3} - \frac{\left(\mathrm{p_i}-\mathrm{qA_i}\right)\left(\mathrm{p_{j-3}}-\mathrm{qA_{j-3}}\right)}{\mathrm{c}^2(\gamma \mathrm{m})^2}\right) \\ \hline \frac{\partial^2 \mathrm{A_k}}{\partial \mathrm{r_i}\partial \mathrm{r_{i-3}}}\left(\mathrm{p_k} - \mathrm{qA_k}\right) - \frac{\partial \mathrm{A_k}}{\partial \mathrm{r_{i-3}}}\frac{\partial \mathrm{A_k}}{\partial \mathrm{r_j}} & \frac{\partial \mathrm{A_{j-3}}}{\partial \mathrm{r_{i-3}}} - \frac{\partial \mathrm{A_k}}{\partial \mathrm{r_{i-3}}}\frac{\mathrm{p_k}-\mathrm{qA_k}}{\mathrm{c}^2(\gamma \mathrm{m})^2}\left(\mathrm{p_j} - \mathrm{qA_j}\right) \\ \frac{\partial \mathrm{A_k}}{\partial \mathrm{r_{i-3}}}\left(\mathrm{p_k} - \mathrm{qA_k}\right)\frac{\partial \mathrm{A_l}}{\partial \mathrm{r_j}}\frac{\mathrm{p_l} - \mathrm{qA_l}}{\mathrm{c}^2\left(\gamma \mathrm{m}\right)^2} - \gamma \mathrm{m}\frac{\partial^2 \Phi}{\partial \mathrm{r_{i-3}}\partial \mathrm{r_j}} & \end{array}\right)_{\mathbf{x}(\mathrm{t})} \delta \mathrm{x_j}\left(\mathrm{t}\right) \end{aligned} \tag{2.17}$$

for the full relativistic case. The latter may be simplified for optical elements that preserve the kinetic energy of the considered charged particles, such as purely magnetic elements:

$$\frac{\mathrm{d}\left(\delta \mathrm{x_i}\left(\mathrm{t}\right)\right)}{\mathrm{dt}} \approx \frac{\mathrm{q}}{\gamma \mathrm{m}} \left(\begin{array}{c|c} -\frac{\partial \mathrm{A_i}}{\partial \mathrm{r_j}} & \frac{1}{\mathrm{q}}\delta_{\mathrm{ij}-3} \\ \hline \frac{\partial^2 \mathrm{A_k}}{\partial \mathrm{r_{i-3}}\partial \mathrm{r_j}}\left(\mathrm{p_k} - \mathrm{qA_k}\right) - \mathrm{q}\frac{\partial \mathrm{A_k}}{\partial \mathrm{r_{i-3}}}\frac{\partial \mathrm{A_k}}{\partial \mathrm{r_j}} - \gamma \mathrm{m}\frac{\partial^2 \Phi}{\partial \mathrm{r_{i-3}}\partial \mathrm{r_j}} & \frac{\partial \mathrm{A_{j-3}}}{\partial \mathrm{r_{i-3}}} \end{array}\right)_{\mathbf{x}(\mathrm{t})} \delta \mathrm{x_j}\left(\mathrm{t}\right), \tag{2.18}$$

which has the same structure as the non-relativistic result, with the substitution $\mathrm{m} \rightarrow \gamma \mathrm{m}$ accounting for relativistic effects.

The formal solution to these JVEs can be calculated by a time-ordered integration of $\chi_{\mathrm{ij}}\left(\mathrm{t}\right)$:

$$\delta \mathrm{x_i}\left(\mathrm{t}\right) = \underbrace{\mathcal{T} \exp\left\{\int_0^{\mathrm{t}} \chi_{\mathrm{ij}}\left(\mathrm{t_1}\right) \mathrm{dt_1}\right\}}_{\mathcal{M}_{\mathrm{ij}}} \delta \mathrm{x_j}\left(0\right), \tag{2.19}$$

where time ordering is achieved by the time ordering operator $\mathcal{T}$. The desired linear relations between initial and final position $\mathbf{x}$ and momentum $\mathbf{p}$ is then given by the transfer matrix $\mathcal{M}_{ij}$. These canonical transfer matrices are not gauge invariant. For most systems a transformation of canonical to kinetic momentum is necessary to retrieve Gauge independent transfer matrices. The real space transfer matrices in Gaussian matrix optics, used to characterize the first order characteristics of an optical system, defined

by real space coordinates and kinetic momenta, for example need to be gauge invariant. In some systems, however, a gauge can be found that ensures the equality of canonical and kinetic momentum in planes of interest, rendering the aforementioned transformation unnecessary[8]. The time ordering operator vanishes if χ_{ij} commutes for all times. As this is not given in the general case, $\mathcal{M}_{ij}$ can be approximated by the so-called Magnus expansion [111, 108]:

$$\mathcal{M}_{ij} = \exp\left(\sum_{k=1}^{\infty} \Omega_k\right). \tag{2.20}$$

The first two terms are given by:

$$\Omega_1 = \int_0^t \chi_{ij}(t_1)\, dt_1 \tag{2.21}$$

and

$$\Omega_2 = \frac{1}{2}\int_0^t dt_1 \int_0^{t_1} \left[\chi_{ij}(t_1), \chi_{ij}(t_2)\right] dt_2\,, \tag{2.22}$$

where $[\cdot,\cdot]$ stands for the commutator. One important characteristic of this expansion is that it preserves the symplectic phase space structure in every step. Thereby additional information about the optical system is directly incorporated into the equations, simplifying their numerical evaluation.

Finally, the equations of motion for the position coordinate can be computed as the second derivative of the top three (position-type) components of

$$\frac{d(\delta x_i(t))}{dt} \approx \chi_{ij}(t)\,\delta x_j(t)\,. \tag{2.23}$$

The equations of motion read:

$$\begin{aligned} m\frac{d^2(\delta x_i(t))}{dt^2} &= -q\frac{\partial A_i}{\partial r_j}\frac{d\left(\delta x_j(t)\right)}{dt} - q\frac{\partial^2 A_i}{\partial r_j \partial r_k}\frac{dr_k}{dt}\left(\delta x_j(t)\right) + \frac{d(\delta x_{i+3}(t))}{dt} \\ &= -qF_{ij}\frac{d\left(\delta x_j(t)\right)}{dt} - q\frac{\partial F_{ij}}{\partial r_j}\frac{dr_k}{dt}\left(\delta x_j(t)\right) + q\frac{\partial E_i}{\partial r_j}\left(\delta x_j(t)\right) \end{aligned} \tag{2.24}$$

for the non-relativistic and:

$$\gamma m\frac{d^2(\delta x_i(t))}{dt^2} = -qF_{ij}\frac{d\left(\delta x_j(t)\right)}{dt} - q\frac{\partial F_{ij}}{\partial r_j}\frac{dr_k}{dt}\left(\delta x_j(t)\right) \tag{2.25}$$

for the relativistic case, with the components of the electric field E_i and the electromagnetic field tensor F_{ij}, and $i, j = 1, 2, 3$. It is important to note that the expressions for the JVE are not gauge invariant, while the equations of motion (Eq. (2.24) and Eq. (2.25)), solely containing physical constants, the electromagnetic field tensor F_{ij} and the relativistic gamma factor, are gauge invariant. The comparison of the real space

[8] c.f. [108] for examples of how such transformations are implemented

equations of motion (Eqs. (2.24) and (2.25)) to the Hamiltonian equations of motion (Eqs. (2.5) and (2.6)) shows that the generalized CPO problem can be posed in different formulations. On the one hand, as a second order differential equation system for 3 position components, the real space equations of motion. On the other hand, as a first order differential equation system for 6 canonical phase space components.

2.3 Transfer Matrices of Magnetic Elements

The transfer matrices $\mathcal{M}_{ij}$ of quadrupole lenses will be derived in the following section. Additionally, transfer matrices for arrangements of quadrupole lenses will be computed. Quadrupoles exhibit an anisotropic focusing behavior when acting on an incident parallel electron beam. The optical power of such quadrupole lenses is proportional to B_0 and not B_z^2 as for round magnetic lenses, hence their focusing action is called strong focusing[9]. Assemblies of quadrupoles are promising candidates as building blocks of μCPO systems for that reason. If not noted differently, the elements of all optical systems considered in this work are aligned along the z-axis, resembling the optical axis.

2.3.1 Single Quadrupole

The magnetic field configuration of an ideal quadrupole of length l with hyperbolic poles can be parameterized as:

$$\mathbf{B}(\mathbf{r}) = F(z)\nabla B_0 \begin{pmatrix} y \\ x \\ 0 \end{pmatrix}, \tag{2.26}$$

where pole orientation is rotated by $\pi/4$ with respect to the coordinate system (c.f. Fig. 1). The quadrupole strength is given by means of the normalized field difference along the pole orientation axis $\nabla B_0 = \frac{2B_0}{a}$, at a pole gap of a, in this idealized model. The unit free field distribution function $F(z)$ describes the field distribution along the optical axis, it is usually parameterized by some Gaussian, Lorentzian or rectangle function, each resembling different approximations to the real field distribution.

In the field region, the corresponding vector potential in Coulomb gauge, ensuring the equality of canonical and kinetic momentum, reads:

$$\mathbf{A} = \frac{1}{2} F(z) \nabla B_0 \begin{pmatrix} 0 \\ 0 \\ y^2 - x^2 \end{pmatrix}. \tag{2.27}$$

[9] c.f. Sec. 2.4.3 for a detailed analysis

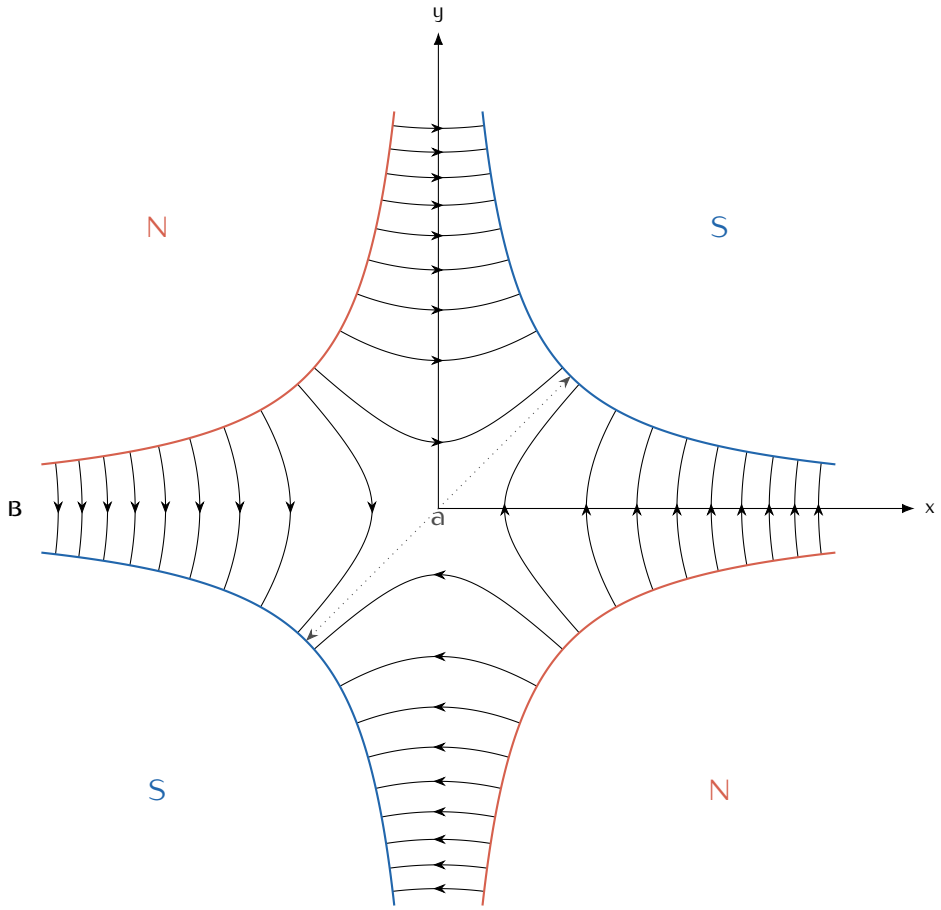

Figure 1: Two-dimensional field distribution in an ideal magnetic quadrupole with hyperbolic pole pieces and focusing action in the x-direction for electrons moving into the paper plane.

By plugging this vector potential into the equation for the non-relativistic Gaussian JVE (Eq. (2.16)) one readily obtains:

$$\frac{d\left(\delta x_i\left(t\right)\right)}{dt} \approx \underbrace{\left(\begin{array}{ccc|ccc} & & & \frac{1}{\gamma m} & 0 & 0 \\ & 0 & & 0 & \frac{1}{\gamma m} & 0 \\ & & & 0 & 0 & \frac{1}{\gamma m} \\ \hline -qF\left(z\right)\nabla B_0 v_z & 0 & 0 & & & \\ 0 & qF\left(z\right)\nabla B_0 v_z & 0 & & 0 & \\ 0 & 0 & 0 & & & \end{array}\right)}_{\chi_{ij}} \delta x_j\left(t\right), \tag{2.28}$$

with particle velocity along the optical axis v_z and the substitution $\gamma m \rightarrow m$ yielding the non-relativistic result. The 3D transfer matrices can be integrated directly from χ_{ij}:

$$\mathcal{M}_{ij} \;=\; \mathcal{T}\exp\left\{\int_0^t \chi_{ij}\left(t_1\right)dt_1\right\}, \tag{2.29}$$

if the first order Magnus expansion is employed (c.f. Eqs. (2.20) and (2.21)):

$$\mathcal{M}_{ij} = \exp\left\{\int_0^t \chi_{ij}(t_1)\,dt_1\right\}, = \exp\left(\begin{array}{ccc|ccc} & & & \frac{l}{\gamma m v_z} & 0 & 0 \\ & 0 & & 0 & \frac{l}{\gamma m v_z} & 0 \\ & & & 0 & 0 & \frac{l}{\gamma m v_z} \\ \hline -q\nabla B_{0,proj} & 0 & 0 & & & \\ 0 & q\nabla B_{0,proj} & 0 & & 0 & \\ 0 & 0 & 0 & & & \end{array}\right), \quad (2.30)$$

with the element length $l = v_z t$ and ∇B projected along the optical axis:

$$\nabla B_{0,proj} = \int_0^l F(z)\,\nabla B_0 dz \quad (2.31)$$

The three-dimensional transfer matrices may be split up into transfer matrices for the individual Cartesian planes, as there are no off-diagonal elements in its sub matrices:

$$\mathcal{M}_x = \exp\begin{pmatrix} 0 & \frac{l}{\gamma m v_z} \\ -q\nabla B_{0,proj} & 0 \end{pmatrix}, \quad (2.32)$$

$$\mathcal{M}_y = \exp\begin{pmatrix} 0 & \frac{l}{\gamma m v_z} \\ q\nabla B_{0,proj} & 0 \end{pmatrix}, \quad (2.33)$$

and

$$\mathcal{M}_z = \exp\begin{pmatrix} 0 & \frac{l}{\gamma m v_z} \\ 0 & 0 \end{pmatrix}, \quad (2.34)$$

respectively. Using

$$\exp\begin{pmatrix} 0 & b \\ c^- & 0 \end{pmatrix} = \begin{pmatrix} \cos(\sqrt{|bc^-|}) & \frac{b\sin(\sqrt{|bc^-|})}{\sqrt{|bc^-|}} \\ c^- \frac{\sin(\sqrt{|bc^-|})}{\sqrt{|bc^-|}} & \cos(\sqrt{|bc^-|}) \end{pmatrix}, \quad (2.35)$$

for $(b, c^-) \in \mathbb{R}$ and $bc^- < 0$, as well as

$$\exp\begin{pmatrix} 0 & b \\ c^+ & 0 \end{pmatrix} = \begin{pmatrix} \cosh(\sqrt{bc^+}) & \frac{b\sinh(\sqrt{bc^+})}{\sqrt{bc^+}} \\ c^+ \frac{\sinh(\sqrt{bc^+})}{\sqrt{bc^+}} & \cosh(\sqrt{bc^+}) \end{pmatrix}, \quad (2.36)$$

for $(b, c^+) \in \mathbb{R}$ and $bc^+ > 0$ from [112] and the substitutions:

$$b = \frac{l}{\gamma m v_z}\,, \tag{2.37}$$

$$c^{\pm} = \pm q \nabla B_{0,\mathrm{proj}}\,, \tag{2.38}$$

and

$$\sqrt{bc^+} = \sqrt{|bc^-|} = \sqrt{\left|\frac{q\nabla B_{0,\mathrm{proj}}}{\gamma m v_z l}\right|}\, l = kl = \sqrt{\left|\frac{2qlB_{0,\mathrm{proj}}}{a\gamma m v_z}\right|} \tag{2.39}$$

the quadrupole transfer matrices can be brought to their commonly known from [113, 114, 115]:

$$\mathcal{M}_x = \begin{pmatrix} \cos(kl) & \frac{1}{\gamma k m v_z}\sin(kl) \\ -\gamma k m v_z \sin(kl) & \cos(kl) \end{pmatrix}\,, \tag{2.40}$$

$$\mathcal{M}_y = \begin{pmatrix} \cosh(kl) & \frac{1}{\gamma k m v_z}\sinh(kl) \\ \gamma k m v_z \sinh(kl) & \cosh(kl) \end{pmatrix}\,, \tag{2.41}$$

and

$$\mathcal{M}_z = \begin{pmatrix} 1 & \frac{l}{\gamma m v_z} \\ 0 & 1 \end{pmatrix}\,. \tag{2.42}$$

Note that $\nabla B_{0,\mathrm{proj}} = l\nabla B_0$, if the sharp cutoff approximation is employed and

$$B_{0,\mathrm{proj}} = \int_0^l F(z)\, B_0 dz = \frac{1}{2} a \nabla B_{0,\mathrm{proj}}\,. \tag{2.43}$$

For positively charged particles, $\mathcal{M}_x$ describes the focusing action in x-direction, $\mathcal{M}_y$ the defocusing action in y-direction (vice versa negatively for charged particles) and $\mathcal{M}_z$ the propagation along the direction of the optical axis. As the common form of the transfer matrices is based on the following definition of the two-dimensional positions and the angles with respect to the optical axis, as[10]:

$$\mathbf{x} = \begin{pmatrix} x \\ y \\ \alpha_x \\ \alpha_y \end{pmatrix}\,, \tag{2.44}$$

the corresponding kinetic momentum entries have to be divided by the modulus of the momentum $p = mv$, according to $\tan(\alpha_i) \simeq \alpha_i = p_i/p$, in the paraxial regime. Finally, the likewise normalized transfer matrices read:

$$\mathcal{M}_x = \begin{pmatrix} \cos(kl) & \frac{1}{k}\sin(kl) \\ -k\sin(kl) & \cos(kl) \end{pmatrix} \tag{2.45}$$

[10] opposed to $\left(x, y, z, p_x, p_y, p_z\right)^T$, as it was defined in Eq. (2.1)

and

$$\mathcal{M}_y = \begin{pmatrix} \cosh(kl) & \frac{1}{k}\sinh(kl) \\ k\sinh(kl) & \cosh(kl) \end{pmatrix} . \tag{2.46}$$

Noting the oscillating behavior of the trigonometric functions and the monotonically increasing behavior of the hyperbolic functions, respectively, the focusing action in x- and defocusing action in y-direction becomes obvious, according to Eq. (2.26)

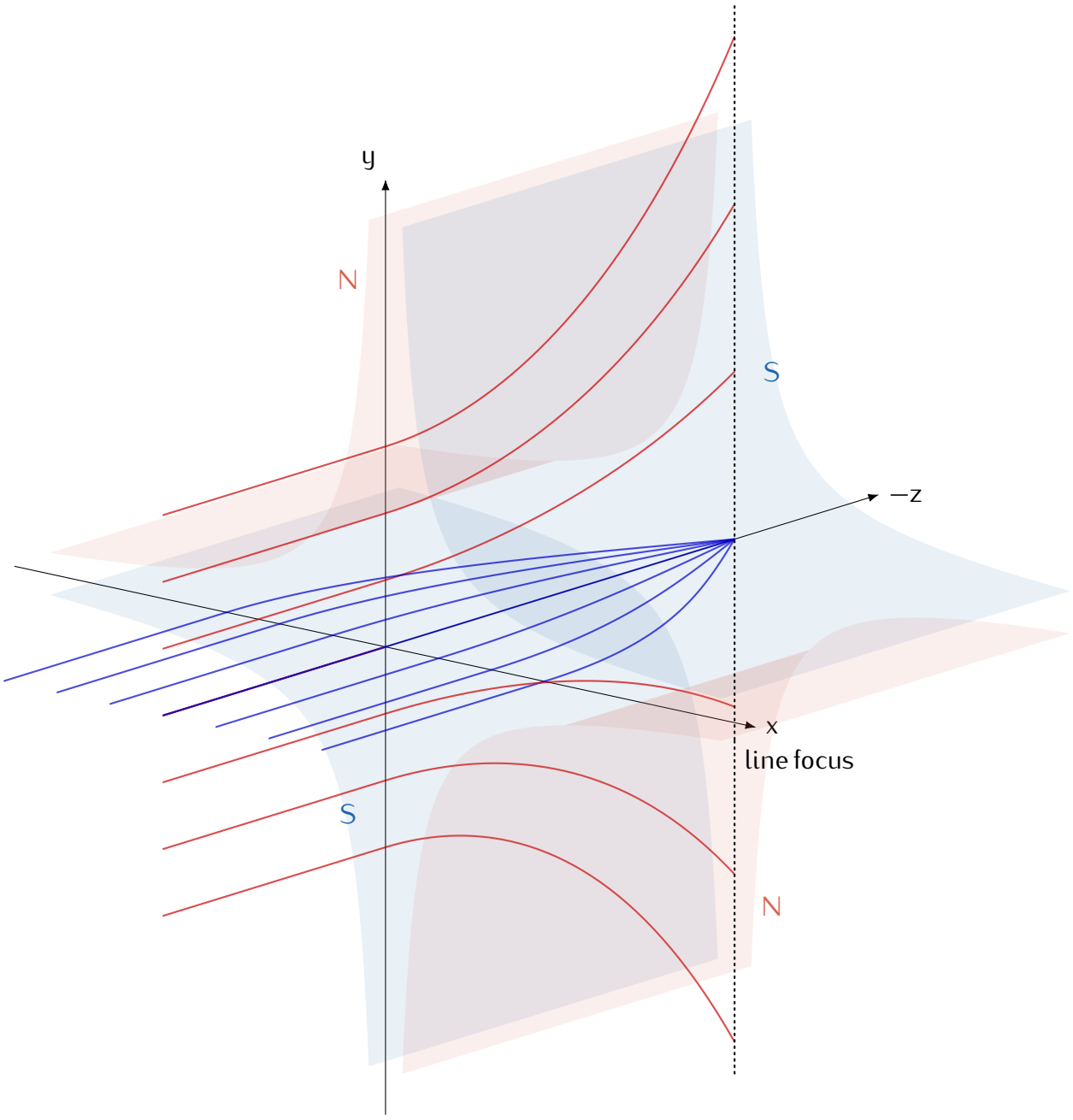

Figure 2: Schematic path of rays for a quadrupole focusing negatively charged particles in x-direction and defocusing them in y-direction. Trajectories incident along the x-axis are given in blue, trajectories along the y-axis in red. Negatively charged particles are moving with negative v_z to be focused in x-direction.

In order to focus beams of charged particles isotropically assemblies of multiple quadrupoles are necessary. These assemblies of quadrupoles aligned subsequently along the optical axis are referred to according to the number of elements they comprise, or multiplets, in general.

2.3.2 Quadrupole Multiplets

In order to simplify the expressions for the quadrupole multiplets, the individual quadrupole elements will be treated in the thin element approximation, being valid for small kl. For thin elements $\mathcal{M}_{12}$ can be approximated to zero, since $l \to 0$. As k^2 is usually very large in $\mathcal{M}_{21}$, being relevant for the focusing action, l can not be neglected there. The thin element approximation has to be handled with caution, it is a very good approximation, however, in case of the miniaturized quadrupoles considered in this work[11]. The corresponding transfer matrices read:

$$\mathcal{M}_x \longrightarrow \begin{pmatrix} 1 & 0 \\ -lk^2 & 1 \end{pmatrix} , \tag{2.47}$$

$$\mathcal{M}_y \longrightarrow \begin{pmatrix} 1 & 0 \\ lk^2 & 1 \end{pmatrix} , \tag{2.48}$$

and

$$\mathcal{M}_z \longrightarrow \begin{pmatrix} 1 & 0 \\ 0 & 1 \end{pmatrix} . \tag{2.49}$$

In this approximation the front and back focal lengths of the considered thin element have the same extension and the principal planes are coinciding with the midpoint of the quadrupole. The focal length f for the thin quadrupole can be deduced by comparison with the well known transfer matrix for a thin lens:

$$\mathcal{M}_{tl} = \begin{pmatrix} 1 & 0 \\ -\frac{1}{f} & 1 \end{pmatrix} , \tag{2.50}$$

as

$$f = \frac{1}{lk^2} = \frac{mv_z}{q\nabla B_{proj}} = \frac{amv_z}{2qB_{proj}} . \tag{2.51}$$

Note that the analytical expressions significantly simplify for thin quadrupole elements, such as the miniaturized elements in this work. This may enable and streamline the design of novel miniaturized electron optical systems (c.f. Sec. 2.3.2.3), but also complicates the direct comparison to conventional systems.

[11] c.f. [115] where thin element approximation is said to be reasonably correct as a starting point for CPO system analysis and design as long as $kl < 1 \approx 0.8$. The miniaturized elements in this work are well below $kl \simeq 0.03$ for electrons accelerated with 300 kV

In the following, different quadrupole assemblies of optical significance will be introduced. Starting from the quadrupole doublet, which facilitates an anamorphic point focus from an extended illumination. The system's transfer matrix for an arrangement of different elements $\mathcal{M}_{sys}$ can be calculated in a straight forward fashion via matrix multiplication, if all the individual transfer matrices $\mathcal{M}_j$ are known:

$$\mathcal{M}_{sys} = \prod_{j=1}^{m} \mathcal{M}_j = \mathcal{M}_{p,n+1} \prod_{i=1}^{n} \mathcal{M}_{QP,i} \mathcal{M}_{p,i} \,, \tag{2.52}$$

where

$$\mathcal{M}_{p,i} = \begin{pmatrix} 1 & d_i \\ 0 & 1 \end{pmatrix} \tag{2.53}$$

are the free space propagations of distance d_i, in between the thin quadrupoles

$$\mathcal{M}_{QP,i} = \begin{pmatrix} 1 & 0 \\ -\frac{1}{f_i} & 1 \end{pmatrix} . \tag{2.54}$$

The following an alternating focusing action of the quadrupoles (i.e. $c_1 f_1 = -c_2 f_2 = c_3 f_3 = -c_4 f_4 \ldots$ $\forall c_i, f_i \in \mathbb{R}^+$) and an initial focusing action in the x-direction will be considered to simplify the expressions without loss of generality.

2.3.2.1 Quadrupole Doublet

The explicit formula for the quadrupole doublet is given by:

$$\mathcal{M}_{QPD} = \mathcal{M}_{p,3} \mathcal{M}_{QP,2} \mathcal{M}_{p,2} \mathcal{M}_{QP,1} \mathcal{M}_{p,1} \,, \tag{2.55}$$

where $\mathcal{M}_{QP,1}$ and $\mathcal{M}_{QP,2}$ are the transfer matrices for the considered quadrupoles. The corresponding matrices for the x- and y-direction read:

$$\mathcal{M}_{QPD,x} = \begin{pmatrix} \frac{d_3}{f_2} - \frac{d_3 + d_2\left(\frac{d_3}{f_2}+1\right)}{f_1} + 1 & d_1 + d_2\left(1 - \frac{d_1}{f_1}\right) d_3 \left(-d_1\left(\frac{\frac{d_2}{f_2}+1}{f_1} - \frac{1}{f_2}\right) + \frac{d_2}{f_2} + 1\right) \\ \frac{1}{f_2} - \frac{\frac{d_2}{f_2}+1}{f_1} & -d_1\left(\frac{\frac{d_2}{f_2}+1}{f_1} - \frac{1}{f_2}\right) + \frac{d_2}{f_2} + 1 \end{pmatrix} \tag{2.56}$$

and

$$\mathcal{M}_{QPD,y} = \begin{pmatrix} \frac{d_3 - d_2\left(\frac{d_3}{f_2}-1\right)}{f_1} - \frac{d_3}{f_2} + 1 & d_1 + d_2\left(1 + \frac{d_1}{f_1}\right) + d_3\left(-d_1\left(\frac{\frac{d_2}{f_2}-1}{f_1} + \frac{1}{f_2}\right) - \frac{d_2}{f_2} + 1\right) \\ -\frac{\frac{d_2}{f_2}-1}{f_1} - \frac{1}{f_2} & -d_1\left(\frac{\frac{d_2}{f_2}-1}{f_1} + \frac{1}{f_2}\right) - \frac{d_2}{f_2} + 1 \end{pmatrix} , \tag{2.57}$$

where the first quadrupole is focusing in x- and defocusing in y-direction while the second one has an opposite optical action. The action of such a quadrupole doublet can be analytically treated for various cases, of which the following are the most important:

1. Anamorphic focusing of a parallel beam.

2. Elliptical collimation of a point source.

3. Imaging of a point source.

All of which will be presented in the following. For the next paragraphs it is important to keep in mind that $\mathcal{M}_{sys,11}$ defines how the real space beam position in the initial plane x_i influences the real space beam position in the final plane x_f[12]. $\mathcal{M}_{sys,22}$ defines how the initial angles with respect to the optical axis $\alpha_{x,i}$ affect the corresponding angles in the final plane $\alpha_{x,f}$. $\mathcal{M}_{sys,12}$ defines how the angles in the initial plane $\alpha_{x,i}$ alter the respective beam positions in the final plane x_f and vice versa for $\mathcal{M}_{sys,21}$. This can be directly seen in the expanded matrix form, here for the x-direction:

$$\begin{pmatrix} x_f \\ \alpha_{x,f} \end{pmatrix} = \begin{pmatrix} \mathcal{M}_{sys,11} & \mathcal{M}_{sys,12} \\ \mathcal{M}_{sys,21} & \mathcal{M}_{sys,22} \end{pmatrix} \begin{pmatrix} x_i \\ \alpha_{x,i} \end{pmatrix} = \begin{pmatrix} \mathcal{M}_{sys,11} x_i + \mathcal{M}_{sys,12} \alpha_{x,i} \\ \mathcal{M}_{sys,21} x_i + \mathcal{M}_{sys,22} \alpha_{x,i} \end{pmatrix} , \tag{2.58}$$

with initial states having index i and final ones index f.

Anamorphic Focusing of a Parallel Beam

This first action is achieved if $\mathcal{M}_{QPD,11}$, the element in the transfer matrix that transforms the position coordinates from initial to final plane, is zero in both $\mathcal{M}_{QPD,x}$ and $\mathcal{M}_{QPD,y}$. The other entries do not have to be considered in this case, as the incident angles are assumed to be zero for parallel illumination (c.f. Fig. 3).

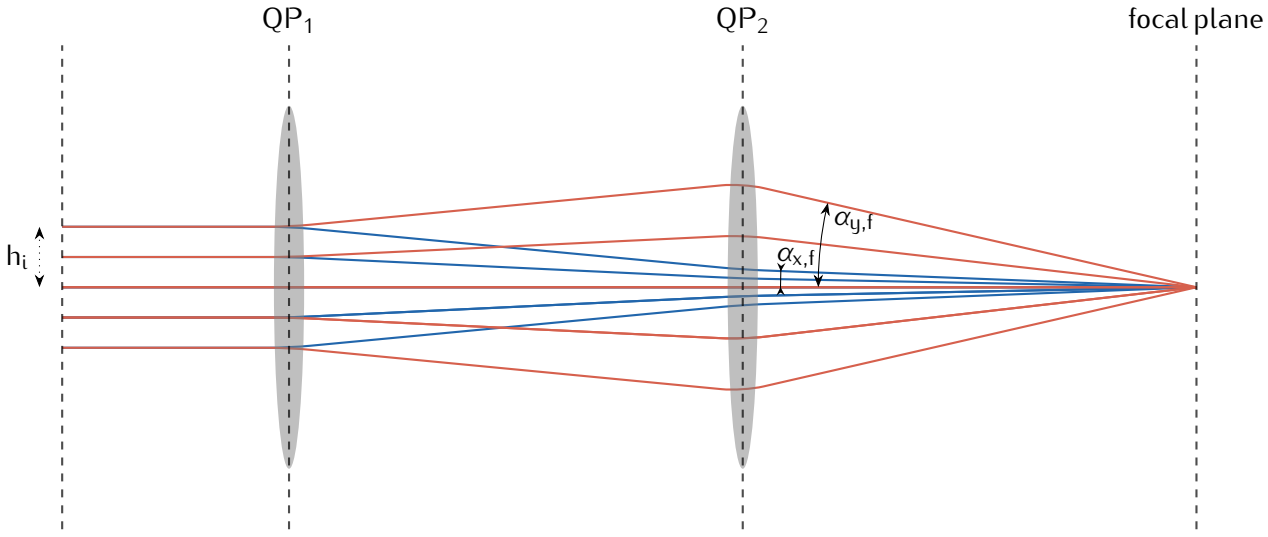

Figure 3: Path of rays for an anamorphically focusing quadrupole doublet with a parallel incident beam of negatively charged particles. The blue rays show the behavior in the x-direction, the red ones the behavior in the y-direction.

For the same reason, d_1 does not have to be considered. The conditions

$$\mathcal{M}_{QPD,x,11} = 0; \mathcal{M}_{QPD,y,11} = 0 \tag{2.59}$$

[12]The initial plane is generally considered as the object plane, the final plane as the image plane

are fulfilled if:

$$d_2 = \sqrt{f_1 (f_1 - f_2)} \tag{2.60}$$

and

$$d_3 = \frac{\sqrt{f_1} f_2}{\sqrt{f_1 - f_2}}, \tag{2.61}$$

under the condition $f_1 - f_2 > 0$. Eq. (2.60) shows that (anamorphic) focusing of a parallel beam is not possible in a symmetrically exited thin doublet (i.e. $f_1 = f_2$), for a finite d_2.
The angles of the beam with respect to the optical axis in the focal point are given by:

$$\alpha_{x,f} = x_i \mathcal{M}_{QPD,x,21} = x_i \frac{1}{f_1 f_2} \left(f_1 - \sqrt{f_1 (f_1 - f_2)} - f_2 \right) \tag{2.62}$$

and

$$\alpha_{y,f} = y_i \mathcal{M}_{QPD,y,21} = y_i \frac{1}{f_1 f_2} \left(-f_1 - \sqrt{f_1 (f_1 - f_2)} + f_2 \right). \tag{2.63}$$

For a symmetric parallel illumination (i.e. $x_i = y_i$ and $\alpha_{x,i} = \alpha_{y,i} = 0$) the difference in illumination angles in the focal point can be calculated by:

$$\alpha_{x,f} - \alpha_{y,f} = \mathcal{M}_{QPD,x,21} - \mathcal{M}_{QPD,y,21} = 2 \frac{f_1 - f_2}{f_1 f_2}, \tag{2.64}$$

from which the anamorphic character the Quadrupole doublet can be seen directly.

Elliptical Collimation of a Point Source

Parallel collimation of a point source is accomplished if $\alpha_{x,f}$, $\alpha_{y,f}$ after the considered system vanish for all beams emitted under various angles (c.f. Fig. 4).

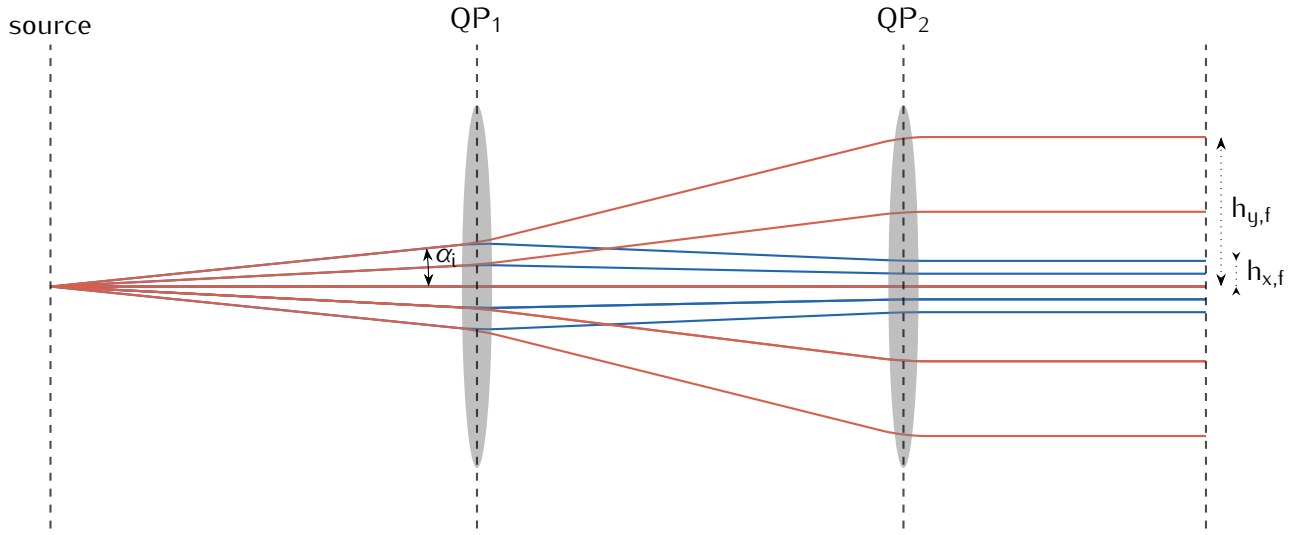

Figure 4: Path of rays for quadrupole doublet elliptically collimating the rays from a point source of negatively charged particles. The blue rays show the behavior in the x-direction, the red ones the behavior in the y-direction.

This is guaranteed if $\mathcal{M}_{QPD,22} = 0$, for both directions:

$$\mathcal{M}_{QPD,x,22} = 0; \mathcal{M}_{QPD,y,22} = 0 \tag{2.65}$$

Solving these equations yields:

$$d_1 = \frac{-f_1 d_2}{f_1 - f_2}\,, \tag{2.66}$$

and

$$d_2 = \sqrt{-f_2\,(f_1 - f_2)}\,. \tag{2.67}$$

Accordingly, f_1 must be smaller than f_2 and parallel focusing of a point source is not possible in a symmetrically exited thin doublet (i.e. $f_1 = f_2$), for a finite d_2.
The distances of the final rays to the optical axis read:

$$h_{x,f} = \alpha_{x,i}\mathcal{M}_{QPD,x,12} = \alpha_{x,i}\left(d_1 + d_2\left(1 - \frac{d_1}{f_1}\right)\underbrace{-d_1 d_3\left(\frac{\frac{d_2}{f_2}+1}{f_1} - \frac{1}{f_2}\right) + \frac{d_2 d_3}{f_2} + d_3}_{d_3\mathcal{M}_{QPD,x,22}=0}\right), \tag{2.68}$$

and:

$$h_{y,f} = \alpha_{y,i}\mathcal{M}_{QPD,y,12} = \alpha_{y,i}\left(d_1 + d_2\left(1 + \frac{d_1}{f_1}\right)\underbrace{-d_1 d_3\left(\frac{\frac{d_2}{f_2}-1}{f_1} + \frac{1}{f_2}\right) - \frac{d_2 d_3}{f_2} + d_3}_{d_3\mathcal{M}_{QPD,y,22}=0}\right). \tag{2.69}$$

The according relative size difference of the beam between the x- and y-direction, after the second element, for symmetrical incidence angles (i.e. $\alpha_{x,i} = \alpha_{y,i}$) reads:

$$\frac{h_{x,f} - h_{y,f}}{\alpha_{x,i}} = \frac{\alpha_{x,i}\mathcal{M}_{QPD,x,12} - \alpha_{x,i}\mathcal{M}_{QPD,y,12}}{\alpha_{x,i}} = -2\frac{d_1 d_2}{f_1}\,, \tag{2.70}$$

which describes the eccentricity of the resulting parallel elliptical illumination.

Imaging of a Point Source

Point to point focusing by a quadrupole doublet (c.f. Fig. 5) is realized when:

$$\mathcal{M}_{\mathrm{QPD,x,12}} = 0; \mathcal{M}_{\mathrm{QPD,y,12}} = 0 \tag{2.71}$$

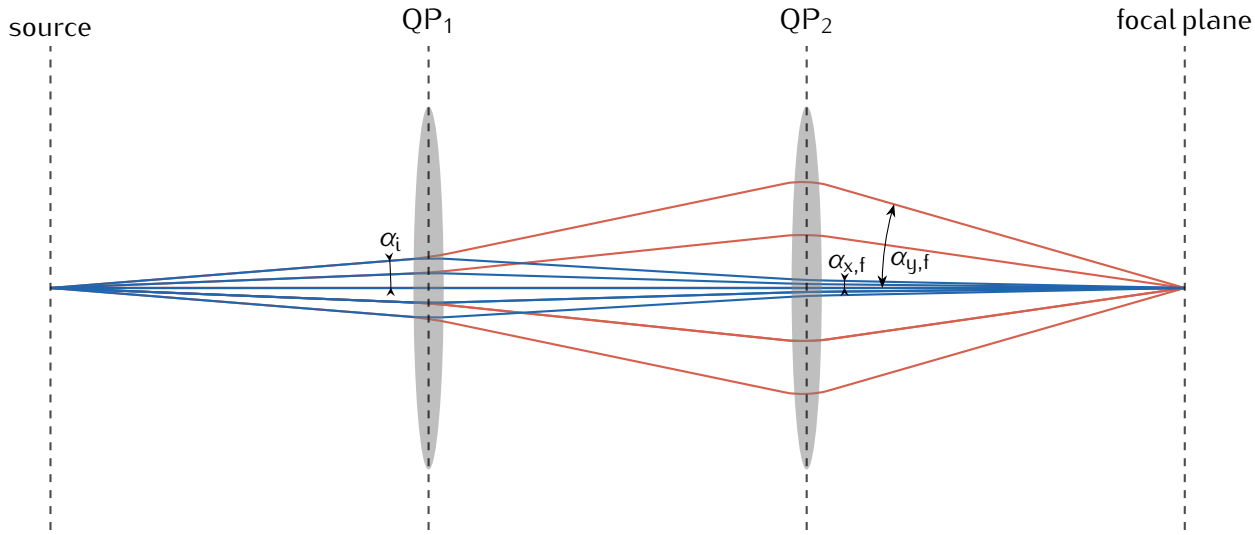

Figure 5: Path of rays for quadrupole doublet anamorphically imaging a point source of negatively charged particles. The blue rays show the behavior in the x-direction, the red ones the behavior in the y-direction.

From which the following expressions for the respective distances can be derived:

$$d_1 = \frac{f_1 d_2 \left(f_1 \pm \sqrt{d_2^2 + f_1 f_2} \right)}{-f_1^2 + f_1 f_2 + d_2^2}, \tag{2.72}$$

and

$$d_3 = \frac{f_2 d_2 \left(f_2 \pm \sqrt{d_2^2 + f_1 f_2} \right)}{-f_2^2 + f_1 f_2 + d_2^2}, \tag{2.73}$$

where the upper or the lower symbol is chosen in order to ensure the positivity of the expressions. Negative distances are forbidden here, as the underlying matrices do not commute. The corresponding focal lengths can be calculated in a similar manner:

$$f_1 = d_1 \sqrt{\frac{d_2 \left(d_2 + d_3 \right)}{\left(d_1 + d_2 \right) \left(d_1 + d_2 + d_3 \right)}} \tag{2.74}$$

and

$$f_2 = \frac{d_3 \left(d_1 + d_2 \right) \sqrt{\frac{d_2 (d_2 + d_3)}{(d_1 + d_2)(d_1 + d_2 + d_3)}}}{d_2 + d_3}. \tag{2.75}$$

The corresponding expressions for a symmetrically exited doublet (i.e. $f_1 = f_2 = f$) are significantly less complicated. From Eqs. (2.72-2.73) follows:

$$d_1 = d_3\,, \tag{2.76}$$

$$d_2 = \frac{2d_1 f^2}{d_1^2 - f^2} \tag{2.77}$$

and

$$f = d_1\sqrt{\frac{d_2}{(2d_1 + d_2)}}\,. \tag{2.78}$$

The corresponding angular magnifications for x- and y-direction, M_{α_x} and $M_{\alpha_y}$are given by $\mathcal{M}_{\mathrm{QPD,x,22}}$ and $\mathcal{M}_{\mathrm{QPD,y,22}}$. In the general case they can be calculated by:

$$M_{\alpha_x} = \underbrace{-d_1\left(\frac{\frac{d_2}{f_2}+1}{f_1} - \frac{1}{f_2}\right) + \frac{d_2}{f_2} + 1}_{\mathcal{M}_{\mathrm{QPD,x,22}}} = \frac{1}{d_3}\left(\underbrace{\mathcal{M}_{\mathrm{QPD,x,12}}}_{=0} - d_1 + d_2\left(\frac{d_1}{f_1} - 1\right)\right) = -\frac{d_1}{d_3} + \frac{d_2}{d_3}\left(\frac{d_1}{f_1} - 1\right), \tag{2.79}$$

and:

$$M_{\alpha_y} = \underbrace{-d_1\left(\frac{\frac{d_2}{f_2}-1}{f_1} + \frac{1}{f_2}\right) - \frac{d_2}{f_2} + 1}_{\mathcal{M}_{\mathrm{QPD,y,22}}} = \frac{1}{d_3}\left(\underbrace{\mathcal{M}_{\mathrm{QPD,y,12}}}_{=0} - d_1 - d_2\left(\frac{d_1}{f_1} + 1\right)\right) = -\frac{d_1}{d_3} - \frac{d_2}{d_3}\left(\frac{d_1}{f_1} + 1\right). \tag{2.80}$$

Following Abbe's sine condition, the real space magnification in small angle approximation given is by:

$$M_x = \frac{1}{M_{\alpha_x}} = \frac{d_3 f_1}{-d_1 f_1 + d_2\,(d_1 - f_1)} \tag{2.81}$$

and

$$M_y = \frac{1}{M_{\alpha_y}} = \frac{d_3 f_1}{-d_1 f_1 - d_2\,(d_1 + f_1)}\,. \tag{2.82}$$

Therefore, stigmatic imaging of a point source by a quadrupole doublet is also anamorphic as Eqs. (2.81) and (2.82) show that $M_x \neq M_y$ for all non-trivial cases.

As all the examples of simple optical systems with two quadrupoles show, the achievable degrees of freedom in the path of rays are quite limited. This is most evident in the case of anamorphically illuminated foci, which cannot be made orthomorphic as the degree of freedom to adjust the convergence angles in x- and y direction independently is missing. The missing degree of freedom can be introduced by subsequently adding another quadrupole to the optical system.

2.3.2.2 Quadrupole Triplet

According to formula (2.52) the transfer matrix of the thin lens quadrupole triplet reads:

$$\mathcal{M}_{QPD} = \mathcal{M}_{p,4}\mathcal{M}_{QP,3}\mathcal{M}_{p,3}\mathcal{M}_{QP,2}\mathcal{M}_{p,2}\mathcal{M}_{QP,1}\mathcal{M}_{p,1}\,, \tag{2.83}$$

where $\mathcal{M}_{QP,1}$, $\mathcal{M}_{QP,2}$ and $\mathcal{M}_{QP,3}$ are the transfer matrices for the considered quadrupoles. The pertaining matrices for the x- and y-direction are:

$$\mathcal{M}_{QPT,x} = \begin{pmatrix} \sigma_{1,x} & d_4 + d_1\sigma_{1,x} + d_2\left(\sigma_{5,x} - \frac{d_4}{f_3} + 1\right) - \sigma_{3,x} \\ \sigma_{2,x} - \sigma_{4,x} - \frac{1}{f_3} & 1 - d_2\left(\sigma_{4,x} + \frac{1}{f_3}\right) - d_1\left(\sigma_{4,x} - \sigma_{2,x} + \frac{1}{f_3}\right) - \frac{d_3}{f_3} \end{pmatrix} \tag{2.84}$$

and

$$\mathcal{M}_{QPT,y} = \begin{pmatrix} \sigma_{1,y} & d_4 + d_1\sigma_{1,y} + d_2\left(\frac{d_4}{f_3} - \frac{d_4 + d_3\left(\frac{d_4}{f_3}+1\right)}{f_2} + 1\right) + d_3\left(\frac{d_4}{f_3}+1\right) \\ \sigma_{2,y} & d_1\sigma_{2,y} - d_2\left(\frac{\frac{d_3}{f_3}+1}{f_2} - \frac{1}{f_3}\right) + \frac{d_3}{f_3} + 1 \end{pmatrix}, \tag{2.85}$$

with the following substitutions in order to simplify the expressions:

$$\sigma_{1,x} = 1 - \frac{d_4 + d_2\left(\frac{d_4-\sigma_3}{f_2} - \frac{d_4}{f_3} + 1\right) - \sigma_{3,x}}{f_1} - \frac{d_4}{f_3} + \sigma_{5,x}\,,\ \sigma_{2,x} = \frac{\frac{d_3}{f_3} + d_2\left(\sigma_{4,x} + \frac{1}{f_3}\right) - 1}{f_1}\,, \tag{2.86}$$

$$\sigma_{3,x} = d_3\left(\frac{d_4}{f_3} - 1\right),\ \sigma_{4,x} = \frac{\frac{d_3}{f_3} - 1}{f_2}\,,\ \sigma_{5,x} = \frac{d_4 - d_3\left(\frac{d_4}{f_3} - 1\right)}{f_2}\,,$$

$$\sigma_{1,y} = \frac{d_4}{f_3} - \frac{d_4 + d_3\left(\frac{d_4}{f_3}+1\right)}{f_2} + \frac{d_4 + d_2\left(\frac{d_4}{f_3} - \frac{d_4 + d_3\left(\frac{d_4}{f_3}+1\right)}{f_2} + 1\right) + d_3\left(\frac{d_4}{f_3}+1\right)}{f_1} + 1 \tag{2.87}$$

and

$$\sigma_{2,y} = \frac{\frac{d_3}{f_3} - d_2\left(\frac{\frac{d_3}{f_3}+1}{f_2} - \frac{1}{f_3}\right) + 1}{f_1} - \frac{\frac{d_3}{f_3}+1}{f_2} + \frac{1}{f_3}\,. \tag{2.88}$$

Here, the first quadrupole is again assumed to be focusing in x- and defocusing in y-direction. The subsequent quadrupoles are assumed to have alternating focusing behavior. Some cases of the quadrupole triplet action can be treated analytically, for example the orthomorphic focusing of a parallel beam[13] and the imaging of a point source with isotropic magnification.

[13] which is inversion symmetric to the isotropic parallel focusing of a point source

Focusing of a Parallel Beam

Orthomorphic focusing of a parallel beam (c.f. Fig. 6) is achieved if all rays intercept at the same point (Eq. (2.89)) and rays with the same initial distance to the optical axis intercept it under the same angle (Eq. (2.90)).

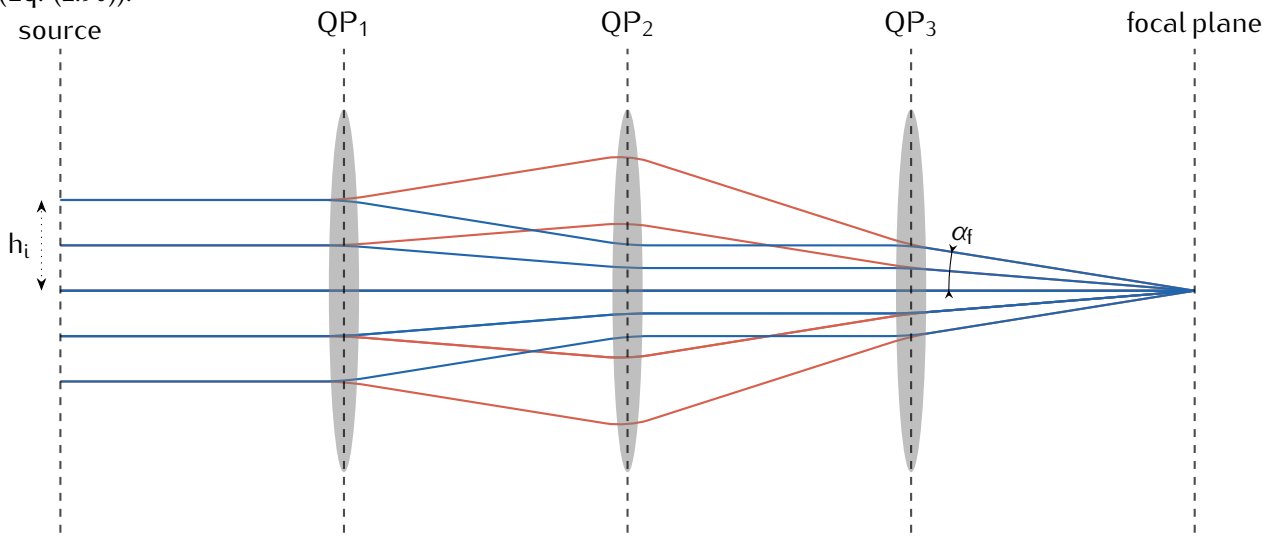

Figure 6: Path of rays for a symmetric quadrupole triplet (according to Eq. (2.94)) focusing a parallel incoming beam of negatively charged particles orthomorphically. The blue rays show the behavior in the x-direction, the red ones the behavior in the y-direction.

In the transfer matrix formulation this reads:

$$\mathcal{M}_{QPT,x,11} = 0 \quad ; \quad \mathcal{M}_{QPT,y,11} = 0 \tag{2.89}$$

and

$$\mathcal{M}_{QPT,x,21} = \mathcal{M}_{QPT,y,21}\,. \tag{2.90}$$

For a symmetric quadrupole triplet ($d_2 = d_3$) this equation system yields the following expressions:

$$d_2 = \sqrt{-f_2\,(f_3 - 2f_2)} \tag{2.91}$$

$$d_4 = -\frac{f_3\sqrt{-f_2\,(f_3 - 2f_2)}}{f_3 - 2f_2} \tag{2.92}$$

$$f_1 = 2f_2 \tag{2.93}$$

The maximum convergence angle giving the greatest resolving power in the diffraction limited case is achieved if, $f_2 = f_3 = d_2 = d_3 = d_4$ is satisfied as well [116]. Here, the expressions simplify dramatically:

$$d_2 = d_3 = d_4 = \frac{1}{2}f_1 = f_2 = f_3\,, \tag{2.94}$$

while d_1 does not have to be considered for parallel illumination. The path of rays for the isotropic ($h_{x,f} = h_{y,f}$) collimation of the rays of a point source are inversion symmetric, hence the corresponding expressions are also symmetric.

Imaging of a Point Source

When imaging a point source, the quadrupole triplet can produce an orthomorphic image, in contrast to the quadrupole doublet.

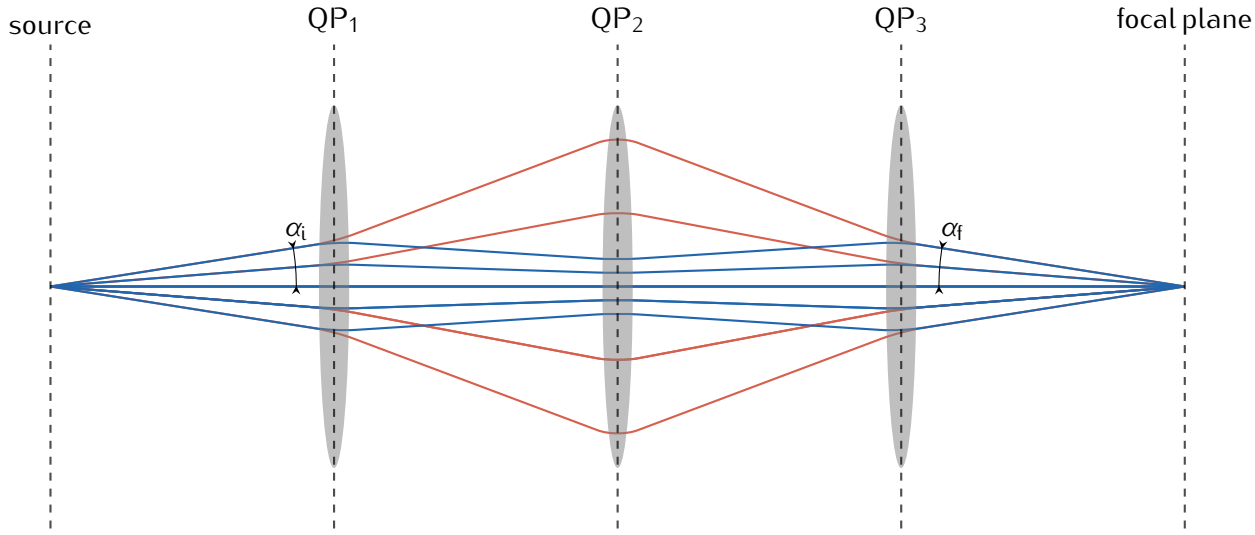

Figure 7: Path of rays for a symmetric quadrupole triplet (according to Eq. (2.100)) imaging a source of negatively charged particles orthomorphically. The blue rays show the behavior in the x-direction, the red ones the behavior in the y-direction.

Imaging is achieved if:

$$\mathcal{M}_{QPT,x,12} = 0 \quad ; \quad \mathcal{M}_{QPT,y,12} = 0\,. \tag{2.95}$$

In this case, an orthomorphic image is produced if:

$$M_{\alpha_x} = \mathcal{M}_{QPT,x,22} = \mathcal{M}_{QPT,y,22} = M_{\alpha_y}\,. \tag{2.96}$$

For a symmetric quadrupole triplet ($d_2 = d_3$) these conditions are fulfilled for:

$$d_1 = -\frac{d_2^3 - 4d_2f_2^2 + d_2f_2f_3}{d_2^2 - 2f_2^2 + f_2f_3} \tag{2.97}$$

$$d_4 = -\frac{d_2f_3}{f_3 - 2f_2} \tag{2.98}$$

$$f_1 = -\frac{d_2^2 - 4f_2^2 + f_2f_3}{f_2}\,. \tag{2.99}$$

In case of a symmetric excitation of the quadrupoles ($f_1 = f_2 = f_3$) the distances between the quadrupoles become equal to the distance between object and first quadrupole, and image and last quadrupole, respectively. The focal lengths are then equal to the distances times $\sqrt{2}$:

$$d_1 = d_2 = d_3 = d_4 = \sqrt{2}f_1 = \sqrt{2}f_2 = \sqrt{2}f_3\,. \tag{2.100}$$

2.3.2.3 Higher Order Quadrupole Multiplets

There are various further quadrupole multiplet configurations, all of which being relevant for different applications. Their important 1st order properties can be found by a transfer matrix treatment, either considering thin or thick elements. Most examples that can be found in literature concentrate on thick elements, as this description yields the most accurate description for macroscopic quadrupole systems. The characteristics, however, greatly differ, if conventional thick elements are considered, as opposed to the thin elements discussed here. An orthomorphic image can be also formed, for example, by a thick quadrupole doublet[14], as long as it is not required that the focal point or image is in the field free regions [113, 117].

There are some more important instances of higher order quadrupole multiplets with especially high symmetry that shall be introduced briefly:

1. The thin quadrupole quadruplet, consisting out of two quadrupole doublets mirrored at the central plane along the optical axis, with a FDDF (subsequent Focusing, Defocusing, Defocusing, Focusing) action in the x-direction. The first doublet produces an elliptical parallel beam from a point source, the second doublet focuses the elliptical beam back to a point in an orthomorphic fashion, if:

$$d_1 = d_5 = \frac{f_1 d_2 (f_1 - f_2)}{-f_1^2 + f_1 f_2 + d_2^2} \tag{2.101}$$

   and $d_2 = d_4$. The distance between the quadrupole doublets d_3 is free of choice, as there should be an elliptical beam, parallel to the optical axis. In real systems, however, d_3 should be minimized to reduce external influences and deviations due to misalignment.

2. Two point-to-point focusing quadrupole doublets forming an orthomorphically focusing quadruplet, if the product of the corresponding individual magnifications (Eqs. (2.81) and (2.82)) are equal in x- and y-direction.

3. A quadrupole quintuplet with the symmetry planes rotated by 45° with respect to their normal orientation can be used to rotate an image by 90° [118]. It was initially designed in a symmetric arrangement for the use in an energy loss spectrometer.

4. A thick quadrupole quintuplet can be used as an objective lens, where the object is ideally located in a field free region and high magnifications are mandatory. This combination is usually hard to accomplish with thick quadrupole systems. In an electrostatic quadrupole system the pole potential was shown to be 3 % to 7 % of the acceleration voltage, enabling much larger magnifications, as the commonly employed round lenses [117, 119].

[14] within rectangular field approximation

2.4 Scaling Laws for Charged Particle Optics

In order to gain insights into optical properties and to assess whether the miniaturization of some device is attractive, a discussion of scaling laws is usually a fruitful first step. Scaling laws denote the behavior of equations, describing the (macroscopic) behavior of some instrument or physical phenomenon, with respect to the system's size. In isotropic scaling considerations[15] all properties are proportional to the considered device's extension and powers of which are scaling with the corresponding power of the scaling factor α (c.f. [120] for a general introduction and [121] for an introduction to magnetic scaling laws). For the investigation of more complex CPO systems it is necessary to carve out the most important limiting factors, e.g., electrical breakthrough or limited heat dissipation, to predict their behavior correctly and define the scaling laws accordingly. The analysis of the scaling laws cannot replace a thorough investigation of the system. It might, however, allow to derive some rules of thumb for the design of the system and motivate a deeper investigation. It is furthermore important to note that all scaling laws eventually break down at a small enough system size, where, e.g., quantum mechanical phenomena become relevant.

2.4.1 Thin Film

Thin film phase plates are not limited by power dissipation or by some breakdown voltage, but by their transparency for the incident particles, described by the particle's mean free path length λ_{mfpl} in the thin film material of thickness t. The mean free path length for the single scattering case can be derived by making the assumption that the local attenuation of the particle beam's intensity is directly proportional to the product of the attenuation coefficient $\mu = \frac{1}{\lambda_{\mathrm{mfpl}}}$ and the local intensity $I(z)$:

$$\frac{dI(z)}{dz} = -\mu I(z) \ . \tag{2.102}$$

Upon integration, one obtains the so-called Lambert-Beer law:

$$I(t) = I_0 e^{-\mu t} = I_0 e^{-\frac{t}{\lambda_{\mathrm{mfpl}}}} \ . \tag{2.103}$$

So on the one hand the thickness of the thin film should be well below the mean free path length, in order to minimize unwanted elastic and inelastic scattering, responsible for charging, contamination and a loss of intensity. On the other hand, the thickness of the material needs to be sufficiently large to produce the desired phase shift[16] [122]:

$$\varphi = \frac{q}{\hbar v} \int_0^t V(z)\, dz \, , \tag{2.104}$$

[15] Isotropic scaling is commonly considered, although anisotropic scaling could be investigated to explore the full potential that lies in the miniaturization of CPO systems.

[16] The term for the magnetic phase shift can be ignored for common thin film phase plate materials

with q being the charge of the considered particles, $\hbar = h/2\pi$ the reduced Planck's constant and $\frac{1}{t}\int_0^t V(z)\,dz$ the mean inner electrostatic potential (MIP). According to Eq. (2.104) the magnitude of the phase shift can be tuned by changing the particle velocity, the material's thickness, or the MIP. The velocity might be changed by altering the acceleration voltage or by using particles of different mass but the same kinetic energy. The MIP can differ due to charging, contamination[17] or through the deliberate use of different materials. An increase in the MIP of the thin film material, as well as an increase in its thickness, are mostly reducing the mean free path length λ_{mfpl} of the beam in the material, leading to unwanted diffuse scattering and a loss of usable intensity. This fact, together with stability and longevity issues, limits the widespread use of thin film materials as general electron optical elements. The ease of their fabrication and tunability[18], however, makes them applicable as phase plates, wherever modest phase shifts are sufficient.

2.4.2 Electrostatic Scaling Laws

The optical strength of electrostatic CPO elements is mostly limited by their breakdown voltage, as long as direct current (DC) systems are considered. The breakdown voltage U_{bd} is given by the dielectric strength E_d of the materials between the electrodes (at a distance d):

$$U_{bd} = E_d d\,. \tag{2.105}$$

Usually there is some dielectric material in the relevant region, for which E_d is a material's constant, as well as residual gas for which the breakdown voltage is described by the Paschen's law for gas discharge [123, 124]:

$$U_{bd} = \frac{Bpd}{\ln(Apd) - \ln\left(\ln\left(1+\frac{1}{\gamma_{sc}}\right)\right)}\,, \tag{2.106}$$

with the experimentally determined parameters A and B that are related to the saturation ionization in the gas at particular values of field strength over pressure E/p and excitation/ionization energies, respectively. The number of produced secondary electrons per gas ion is given by the secondary electron emission coefficient γ_{sc}. One can find the maximum voltage for a certain gas type by setting the derivative of U_{bd} with respect to the pressure-distance product to zero, which gives:

$$pd = \frac{e\ln\left(1+\frac{1}{\gamma_{sc}}\right)}{A}\,, \tag{2.107}$$

[17] The working principle of so-called Volta phase plates [78]

[18] Either by changing the materials thickness or the incident intensity an thereby the charging of the material

where e is Euler's number. Considering phase plates, the maximum attainable phase shift is given by Eq. (2.104), when inserting $\int_0^t V(z)\,dz = U_{bd}d$, for the relevant breakdown scenario, either for break down through residual gases (Eq. (2.106)) or through a dielectric material. For homogeneous fields and a constant dielectric strength the applicable voltages are scaling linearly with the system's size:

$$E_d d = U \sim \alpha\,, \tag{2.108}$$

if the electrostatic system is only limited by voltage breakdown. In the following discussion of the scaling laws for CPO the acceleration voltages will not be scaled according to α, as the acceleration system could be scaled differently to maintain the large voltages of conventional state-of-the-art systems. Novel acceleration schemes could possibly be utilized as an alternative route towards high acceleration voltage in miniaturized systems [125, 126, 127, 128]. Comparably large acceleration voltages, difficult to attain with accelerators isotropically scaled down to the micrometer regime, are mandatory for many applications, such as high resolution lithography, microscopy and manipulation of samples with beams of charged particles. As noted before, it is important to keep in mind that the investigation of the scaling laws just gives a first impression on the behavior of a system, which will inevitably break down at some scale. The scaling laws for electrostatic electron optical systems developed here are merely valid down to the micrometer regime, where a $1/\sqrt{\alpha}$ scaling of the breakdown voltage becomes manifest. For systems in the single-digit and sub-micrometer regime the breakdown voltage finally becomes even scale independent for a large range of dielectrics commonly used for electrical isolation [129].

Electrostatic Deflector

The electrostatic deflector can be discussed in terms of a plate capacitor (of length l and plate distance d) as a simplified model. The achievable deflection angle is then given by:

$$\vartheta_{max} = \frac{U_{bd} l}{2 d U_a} = \frac{E_d l}{2 U_a}\,, \tag{2.109}$$

with the acceleration voltage U_a. It is scaling linearly with the considered system size:

$$\vartheta_{max} \sim \alpha\,, \tag{2.110}$$

as E_d and U_a are considered as scale independent. Accordingly, miniaturization of electrostatic deflectors is not favorable for systems where large deflection angles are necessary. In case of isotropic scaling of some CPO device similar deflection angles are usually required to sustain the characteristics of the device. Nevertheless, miniaturized electrostatic deflectors might be interesting in use cases where non-isotropic scaling is possible, ultimate deflection power is not necessary, high frequency transfer is the main goal, or power dissipation through joule heating is an issue. If the acceleration voltage is scaled with the same factor, however, the attainable deflection angles will remain constant.

Electrostatic Aperture Lens

Considering optics there are mainly two common types of circularly symmetric electrostatic lenses, namely immersion lenses and einzel lenses[19]. Both lens types are composed of multiple electrodes with aperture bores around the optical axis. The focusing action arises from the axial field gradient between surfaces of different potential [130], inevitably leading also to a bending of the field lines at the bores (c.f. [131]), of diameter D. An immersion (or Butler) lens is composed of two subsequent electrodes at a distance L aligned perpendicular to the optical axis, at which two different potentials are applied: U_a, between the particle source and the first electrode and U_2 between the electrodes. This configuration changes the velocity of the respective charged particles. The front and back focal lengths, f_f and f_b, are given by [132]:

$$f_f = \frac{4L\left(\sqrt{\frac{U_2}{U_a}}+1\right)}{\frac{U_a}{U_2}+\frac{U_2}{U_a}-2} \tag{2.111}$$

and

$$f_b = \frac{4L\left(\sqrt{\frac{U_a}{U_2}}+1\right)}{\frac{U_2}{U_a}+\frac{U_a}{U_2}-2}\,, \tag{2.112}$$

for $D \ll L$ [131]. Approximate numerical solutions for breakdown limited scaling laws of f_f and f_b can be found, for instance by limiting U_2 to 10 % of U_a:

$$f_f \sim 9\alpha^{\frac{5}{2}} \tag{2.113}$$

and

$$f_b \sim 8\alpha^{\frac{5}{3}}\,. \tag{2.114}$$

An electrostatic einzel lens is an assembly of three electrodes with aperture bores, where the two outermost electrodes share the same potential, $U_3 = U_1$. For that reason the velocities of the charged particles are not altered by the einzel lens as the particles are symmetrically accelerated and decelerated (or *vice versa)* within the lens. An approximation for the front and back focal length of an einzel lens geometrically symmetric to its middle plane perpendicular to the optical axis can be obtained in a simplified piece-wise linear model [133]:

$$\frac{l}{f} = \frac{3}{4}\left(\frac{U_2}{U_a}-1\right)\left(4-3\sqrt{\frac{U_a}{U_2}}-\sqrt{\frac{U_2}{U_a}}\right). \tag{2.115}$$

Considering the same approximation as before ($U_2 \leq 0.1U_a$), the approximate numerical solution for the scaling law of the breakdown limited case is given by:

$$f \sim 2.5\alpha^2\,. \tag{2.116}$$

[19] "einzel" is the German word for single

These scaling laws render electrostatic einzel lenses very suitable for miniaturization, as their optical power greatly increases for miniaturized systems. Note, however, that it is difficult to find general expressions for the optical properties of electrostatic lenses, as they often vary strongly with the considered geometries. The scaling laws, derived here, are just meant to give a first rough estimate of whether miniaturization efforts are worthwhile. If the acceleration voltage is not considered scale independent and scaled with the same factor, the respective focal lengths of these two types of lenses would scale linearly with the scaling factor α.

Electrostatic Quadrupole Lens

The focusing action of an electrostatic quadrupole of length l can be described analogous to the corresponding magnetic one. The field configuration for focusing negatively charged particles in y-direction (for $F(z) > 0$) reads:

$$\mathbf{E}(\mathbf{r}) = F(z)\nabla E_0 \begin{pmatrix} x \\ -y \\ 0 \end{pmatrix}. \tag{2.117}$$

Here, the in-plane components of the electric field have to increase linearly in their respective Cartesian coordinate (c.f. Fig. 8) for a focussing action in y-direction for negative particles, as opposed to the magnetic case (Eq. (2.26)) where components are flipped, as the Lorentz force is acting perpendicular to the field.

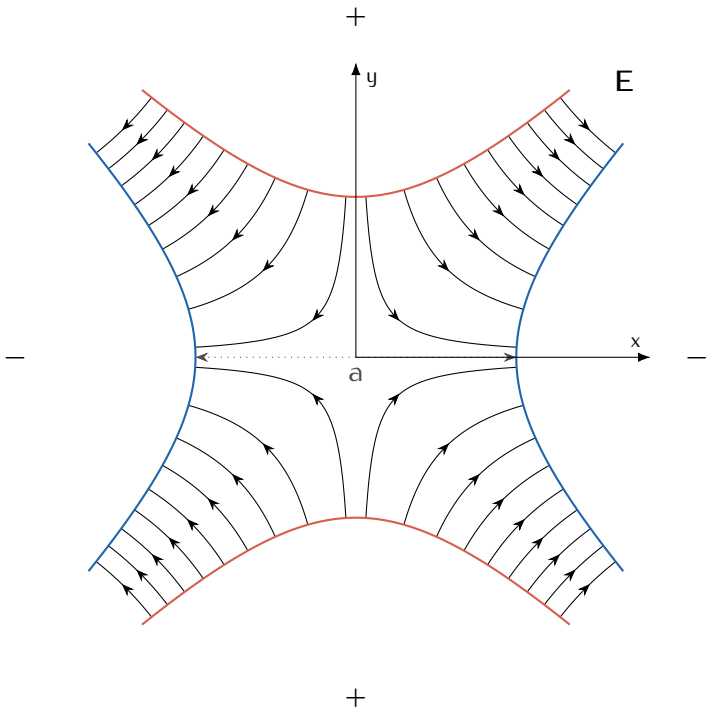

Figure 8: Two-dimensional field distribution in an ideal electrostatic quadrupole with hyperbolic pole pieces and focusing action in the y-direction for negatively charged particles.

Accordingly, the poles are aligned parallel to the Cartesian axes, in contrast to the magnetic quadrupole, where the poles are rotated by $\pi/4$. The corresponding focal length for non-relativistic charged particles reads:

$$f = \frac{mv^2}{q\nabla E_{proj}}\,, \tag{2.118}$$

where the terms for the particle's kinetic energy $E_{kin} = 1/2 mv^2$ and $\nabla E_{proj} = \frac{2E_{proj}}{a}$ can be replaced by the terms for the corresponding potential differences, the acceleration voltage $U_a = 1/q E_{kin}$ and the projected pole potential $U_{proj} = \int_0^l F(z)\, U_p dz = E_{proj} a$, respectively:

$$f = \frac{2U_a a^2}{U_{proj}}\,. \tag{2.119}$$

E_{proj} is the electric field projected along the optical axis z of the optical element of length l: $E_{proj} = \int_0^l E dz$. Substituting $U_p = U_{bd} = E_d a$[20] for the pole gap a yields the minimal focal length:

$$f_{min} = \frac{2U_a a}{E_{d,proj}}. \tag{2.120}$$

The minimal focal length is scale invariant for isotropic scaling, as the contributions of a and l cancel out:

$$f_{min} \sim \text{const}\,, \tag{2.121}$$

which indicates that isotropic scaling of electrostatic quadrupole lenses conserves optical power, while increasing the high frequency transfer [38]. Additionally, electrostatic elements are more easily fabricated as their counterparts based on electromagnets. The focal length in systems with accordingly scaled acceleration voltage is scaling linearly with α.

2.4.3 Magnetic Scaling Laws

Regarding scaling laws for CPOs based on magnetic elements, two logical classes can be distinguished, namely elements based on permanently magnetized ferromagnets and elements using a current through some conducting material in order to generate the desired magnetic flux. In real systems most electromagnets used in charged particle optics also incorporate some soft ferromagnet to enhance and guide the magnetic field. Permanent magnets that are polarized by a short intense current pulse through some external conductor[21] are another example where both logical classes are implemented in one device.
The magnetic vector potential **A** of a magnetic element of thickness t alters the phase of an impinging charged particle wave according to [134, 135]:

$$\varphi = -\int_0^t \frac{q}{\hbar} A_z(z)\, dz\,, \tag{2.122}$$

[20] and $U_{proj} = U_{bd,proj} = E_{d,proj} a$, accordingly
[21] or the magnet itself by spin transfer torque

which is also considered as the magnetic Aharonov-Bohm phase.

Permanent Magnets

The scaling laws for CPOs based on ferromagnets realively straight forward to derive. The magnetic induction is defined as the magnetic flux density, which stays constant at the pole surface if the material is scaled isotropically [121]:

$$\mathbf{B} \sim \text{const}\,. \tag{2.123}$$

Assuming a constant acceleration voltage the Lorentz force acting on the considered charged particles is then also scale independent:

$$\mathbf{F}_L \sim \text{const}\,. \tag{2.124}$$

leading to the beneficial scaling laws for the subsequent optical elements.

Electromagnets

For most miniaturized systems[22] based on electromagnets the main limiting factor is the maximum power dissipation P_d of the power generated by joule heating P_J. Usually there are different power dissipation routes present, e.g.:

1. Heating of the surrounding gases or liquids and subsequent convection, optionally aided externally by fans or pumps
2. Heat conduction through electrical conduction paths and contact areas to substrates
3. Heat radiation

In case of microelectronic systems operating in vacuum at room temperature, like the miniaturized electron optical elements in this work, the most relevant power dissipation path is number two. The scaling laws for CPO systems driven by electromagnets are given by the maximal attainable magnetic fields B_{max}, which are limited by the maximal current through some conductor of resistance R:

$$B_{max} \sim I_{max} = \sqrt{\frac{P_J}{R}}\,. \tag{2.125}$$

The system remains in thermal equilibrium as long as $P_d \geq P_J$. The system will heat up to its critical temperature T_c, ultimately getting damaged, if the heating power exceeds the maximum power dissipation. For dynamic systems, e.g. in pulsed operation, P_J can surpass P_d momentarily as long as the total heat brought into the system is lower than the critical heat Q_c, corresponding to T_c.
Considering miniaturized electrical components operated in vacuum at ambient temperature the main heat dissipation mechanism is conduction of heat through electrical connections and the substrate, as discussed before (c.f. Sec. 2.4). The respective rate of heat transfer is given by Fourier's law:

[22] The limiting factor for the optical power of macroscopic CPO systems is mostly the saturation magnetization of pole piece material, which is usually not reached in miniaturized systems.

$$\dot{Q} = \frac{-\kappa A \triangle T}{d} = P_d \,, \tag{2.126}$$

with the heat conductivity of the considered material κ, its cross-section area A and the temperature difference with respect to some macroscopic reservoir at distance d. This reservoir can either be the substrate, external connections or cooling units. The respective scaling law is:

$$P_d \sim \alpha \,, \tag{2.127}$$

as κ and $\bigtriangleup T$ can be regarded constant in thermal equilibrium and $A \sim \alpha^2$ and $d \sim \alpha$, respectively. The corresponding maximal current is scaling according to:

$$I_{max} \sim \alpha, \tag{2.128}$$

because the resistance of a conductor of length $l_R \sim \alpha$, cross-section $A_R \sim \alpha^2$ and specific electrical resistivity ρ_{el} is scaling as:

$$R = \rho_{el} \frac{l_R}{A_R} \sim \frac{1}{\alpha} \,. \tag{2.129}$$

Most CPO systems are based on some kind of solenoid, the important field component is usually B_a, which is oriented along the solenoid's symmetry axis $\mathbf{e}_a$. A corresponding scaling law for $B_{a,max}$ can be derived by using the analytical expression for B_a in the center of the coil [136]:

$$B_{a,max}(x_a) = \frac{\mu_0 N I_{max}}{2l} \left(\frac{x_a + l/2}{\sqrt{R^2 + (x_a + l/2)^2}} - \frac{x_a - l/2}{\sqrt{R^2 + (x_a - l/2)^2}} \right) \mathbf{e}_a \,, \tag{2.130}$$

where N, l and R is the winding of the solenoid, its length and radius, respectively. The vacuum permeability μ_0 may be multiplied by the scale-independent permeability of some soft magnetic pole piece μ_r. The according isotropic scaling is scale independent like in the case of permanent magnets:

$$B_{a,max} \sim \text{const} \,, \tag{2.131}$$

because the linear contributions of x_a, I_{max}, R and l cancel out. In reality, however, the scaling behavior of CPO systems driven by electromagnets might drastically differ from the behavior of their permanent magnetic counterparts, the main reasons are that anisotropic scaling is widely applied, different heat dissipation schemes are taking effect at larger scales[23] and the polarization dynamics of the pole pieces differ remarkably for miniaturized systems.

[23] especially the feasibility of external (water) cooling is totally different, while it is very common in macroscopic devices it is difficult to realize in miniaturized systems. Note, however, that thermoelectric cooling schemes might be an suitable alternative for such miniaturized elements.

Magnetic Vortex Phase Plates

The orbital angular momentum, the optical transparency as well as the purity of the produced vortex state are the important characteristics of a vortex phase plate. An ideal vortex beam could be produced by a hypothetical magnetic monopole [137, 96]. The orbital angular momentum, the transmitted intensity and the purity of the quantum state produced by one ideal monopole would be unity. One end of an (also hypothetical) Dirac string[24] [138, 96] would produce an analogous result. The phase of a round charged particle beam, impinging on any of these systems, is increasing with the polar angle after the interaction. For topological reasons, the integral of the phase along a closed loop must vanish except for a 2π ambiguity [138]:

$$\oint \varphi \mathrm{ds} = \mathrm{n}2\pi;\ \mathrm{n} \in \mathbb{N}\,. \tag{2.132}$$

At the position of the monopole the amplitude vanishes to ensure continuity of the wave function and the phase becomes ill defined. This point is commonly called the vortex core.

An approximate realization of such a Dirac string is a current-carrying coil of infinite length and infinitesimal radius, terminating in the region of interaction with the charged particle beam, which could be approached with miniaturized electromagnet systems. It is convenient to guide and enhance the flux density generated by the miniaturized coil by a polarized soft magnet, at whose tip the field lines are emerging, resembling the end of a Dirac string. Alternatively, an infinitely long permanent magnet could approximate such a Dirac string. The orbital angular momentum L of such a device is given by the magnetic flux $\mathbf{B}$ enclosed in the area $\iint \mathrm{d}\mathbf{S}$ within the ring integral $\oint \mathrm{d}\mathbf{s}$ around the soft magnetic needle[139] (c.f. Fig. 9):

$$\mathrm{L} = \frac{\mathrm{e}}{\mathrm{h}} \oint \mathbf{A}\mathrm{d}\mathbf{s} = \frac{\mathrm{e}}{\mathrm{h}} \iint \mathbf{B}\mathrm{d}\mathbf{S}\,. \tag{2.133}$$

Here, Stokes' theorem was applied in order to convert the expression for the vector potential $\mathbf{A}$ to an expression depending on the magnetic flux density $\mathbf{B}$.

The corresponding scaling law for the OAM of a magnetic vortex aperture in terms of enclosed magnetic flux is:

$$\mathrm{L} \sim \alpha^2\,, \tag{2.134}$$

as $\mathbf{B}$ is scale independent and the area $\iint \mathrm{d}\mathbf{S}$ along the magnet axis is scaling proportional to α^2.

[24] a one dimensional curve connecting two magnetic monopoles of opposite charge

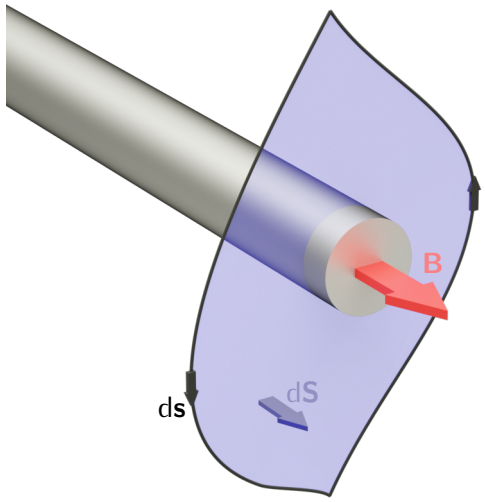

Figure 9: Principle geometry of an electron wave obtaining a phase shift by enclosing a magnetic magnetic flux originating from a magnetized wire.

The optical transparency and thus the element's transmittance is scale independent, if the beam is scaled accordingly. The purity of the vortex state is also benefiting from miniaturization, as the effect of partial coherence is reduced with interaction area, eventually vanishing at an interaction area size comparable to the coherence length. This compromise between current density and illuminated area, is described by the Van Cittert–Zernike theorem [140].

Magnetic Deflectors

The deflection angle of a charged particle in a homogeneous magnetic field B of length l is given by:

$$\vartheta = \frac{eBl}{p_z}\,, \tag{2.135}$$

if the initial momentum p_z is large compared to the momentum in the deflection direction p_x. For a constant acceleration voltage, p_z remains constant in a scaled system and the deflection angle scales according to:

$$\vartheta \sim \alpha\,, \tag{2.136}$$

as the magnetic flux density is scale independent for permanent magnets and isotropically scaled electromagnets. If the acceleration voltage scales with α as well, the resulting deflection angle is scale independent. Considering this simplified isotropic scaling law a magnetic deflector would essentially scale similarly to an electrostatic deflector.

Magnetic Lenses

Regarding magnetic charged particle lenses there are two common types, namely axisymmetric and quadrupole lenses. The focusing action of axisymmetric magnetic lenses is essentially a second order process. The charged particles to-be-focused are forced to rotate about the optical axis by the radial part of the magnetic field B_r at first. The corresponding force reads:

$$F_\phi = q v_z B_r \,. \tag{2.137}$$

In the second step, the axial field B_z is bending the rotating particles towards the optical axis. As B_r increases with the distance to the optical axis, the rotation velocity v_ϕ increases accordingly, causing a proportional force in radial direction, hence the focusing action:

$$F_r = q v_\phi B_z \,. \tag{2.138}$$

The optical power of an axisymmetric charged particle lens with effective field length l can be approximated by [141]:

$$\frac{1}{f_r} = \frac{q}{8 m U_a} \int_0^l B_z^2 dz \,. \tag{2.139}$$

The corresponding scaling law for the focal length is given by the scaling of the effective field length, as B_z is scale independent:

$$f_r \sim \frac{1}{\alpha} \,. \tag{2.140}$$

It becomes scale independent, however, if the acceleration voltage U_a is scaled accordingly.

Magnetic Quadrupole Lenses

The anisotropic focusing behavior of a magnetic quadrupole lens is different: The focusing is a direct first order effect, as the optical axis is perpendicular to the main orientation of the magnetic fields. The optical power reads (c.f. Sec 2.3.2):

$$\frac{1}{f_{qp}} = \frac{2 q B_{0,proj}}{a m v_z} \,. \tag{2.141}$$

For isotropic scaling the focal length is scale independent, as the projection length for $B_{0,proj}$ is scaling similarly the pole gap (i.e. a):

$$f_{qp} \sim \text{const} \,. \tag{2.142}$$

Considering non-relativistic dynamics, the particle velocity v_z along the optical axis is scaling quadratically with the acceleration voltage U_a:

$$U_a \sim v_z^2 \,. \tag{2.143}$$

Consequently, for a linear scaling of the acceleration voltage $U_a \sim \alpha$, the focal length of a magnetic quadrupole lens is scaling as:

$$f_{qp} = \sqrt{\alpha}\,. \tag{2.144}$$

The behavior of f_r and f_{qp} for different acceleration voltages U_a and magnetic flux densities B is given in Fig. 10.

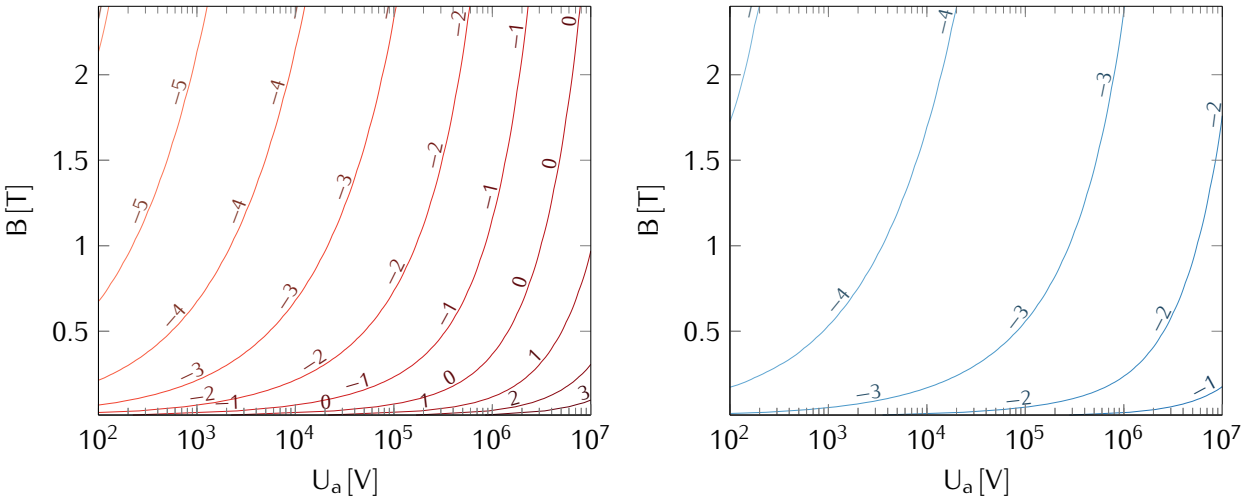

(a) $\log_{10}\left(f_r/m\right)$ (b) $\log_{10}\left(f_{qp}/m\right)$

Figure 10: Attainable focal lengths for a miniaturized magnetic round lens (f_r) and magnetic quadrupole lens (f_{qp}), for practically important values of B and U_a given in their unit free decadic logarithm. The specific charge q/m of electrons was used for the numerical calculations. A rectangular field model of length $l = 1\,\text{mm}$ was assumed for both cases, the pole gap of the quadrupole was assumed to be $a = 1\,\text{mm}$, as well.

3 Design and Fabrication of Miniaturized Electron Optics

Following the scaling laws from chapter 2.4 miniaturized magnetic CPOs have very intriguing properties, enabling the manipulation of fast charged particle beams for various desirable applications. The great advantage of elements incorporating electromagnets compared to pure permanent magnetic ones is their tunability. Permanent magnetic devices can also be tuned, similar to most light optical devices, but here a mechanical movement is necessary, deteriorating the accuracy and precision of the adjustments, and the longevity of the device. Especially for charged particle microscopy where a delicate control of the charge particle beam is necessary, systems based on electromagnets are indispensable. There are some approaches for adaptive miniaturized magnetic CPOs, some of which are limited by the achievable miniaturization factors [142], others by the quality of the deposited conducting layers in the coils. Poor quality of the conduction paths leads to large Joule heating and eventually to thermal damage of the coils. Especially for FIB-based approaches [143] the quality of the deposited conductive metal layers becomes a limiting factor for the achievable optical performance. Another factor that limits the optical performance of adaptive miniaturized magnetic CPOs is that they have to be operated in (high) vacuum. This makes power dissipation through convection negligible, which rendered a self-assembling InGaAs/GaAs micro coil system [144] that was initially used in the beginning of this work, unsuitable for CPO. The direct current that coils of this system could withstand in the high vacuum within a TEM were limited to a few µA.

In this work a novel approach towards adaptive miniaturized magnetic CPO elements is proposed, namely self-assembled micro coils with tapered soft magnetic CoFeSiB micro wires used as pole pieces. In this approach the quality of the conducting layers is ensured by their deposition in a single fabrication step. The 3D solenoid structure is formed in the subsequent self-assembly process. Other techniques often require very complicated and production yield limiting processes with multiple intermediate steps to form some kind of 3D solenoid [71, 72, 145, 146]. The small achievable length scales of the solenoid in this work are rendered possible by combining “top down” micro patterning of the planar structures by lithography with a “bottom up” self-assembly process [147]. The use of special magnetically soft micro wires as pole pieces ensures their polarizability and hence the tunability of the elements while enhancing the attainable fields.

In the following, only the fundamentals of the polymer-based self-assembly process are described, where the emphasis of this thesis is in the design and the evaluation of the electron optical properties of the miniaturized CPO elements that were produced at Institute for Integrative Nanosciences (IIN) at the Leibniz-Institute for Solid State and Materials Research Dresden (IFW) in a collaborative research effort. A detailed description of the chemical foundations and the technological realization of the micro-fabrication process can be found in the dissertations of our collaboration partners Daniil Karnaushenko [148], Dmitriy D. Karnaushenko [149] and Renato Huber[25], as well as in their previous publications [150, 151, 152, 153,

[25] not submitted at the time this thesis was handed in

154, 155, 156, 157, 158, 159, 160, 161, 162, 163, 164, 165, 166, 167], where the self-assembly process is used in order to fabricate (magnetic) microelectromechanical systems for different purposes. The technical complexity of the self-assembly scheme is mostly ignored in this chapter. The following chapter just serves to get a basic idea about underlying mechanisms of the fabrication process.

3.1 Basics of Polymer-Based Self-Assembly Technology

The foundation of the polymeric self-assembly process consist of three different polymers that are sequentially spin coated onto some substrate, p-doped silicon in our case, and subsequently directly structured using UV photo lithography. Direct structuring of the polymer layers renders the applications of extra photoresists unnecessary, reducing the overall production steps and consequently increasing the final production yield. The three polymeric layers are:

1. A sacrificial layer, ideally completely dissolving in the rolling process, where the planar structures are forming the 3D solenoids, in this work made from photosensitized lanthanum acrylate

2. A hydrogel layer, which swells volumetrically in the rolling solution, consisting out of N-2-hydroxyethyl acrylamide (HEAA) and polyethylene-alt-maleic anhydride (PEMA) forming polymeric chains in N,N-dimethyl acetamide (DMA) solution

3. A rigid layer, which serves as an anchor for the 3D structure on the substrate, as well as connection between the conductors and the hydrogel layer; this rigid layer facilitates the rolling by releasing volumetric stress of the swollen hydrogel layer by getting strained itself. In this work a photosensitized polyimide made from 3,3',4,4'-benzophenonetetracarboxylic dianhydride (BPDA) and 3,3'-diaminodiphenyl sulfone (DADPS) in N,N-dimethyl acetamide solution modified with dimethylaminoethyl methacrylate (DMAEMA) was used as a rigid layer.

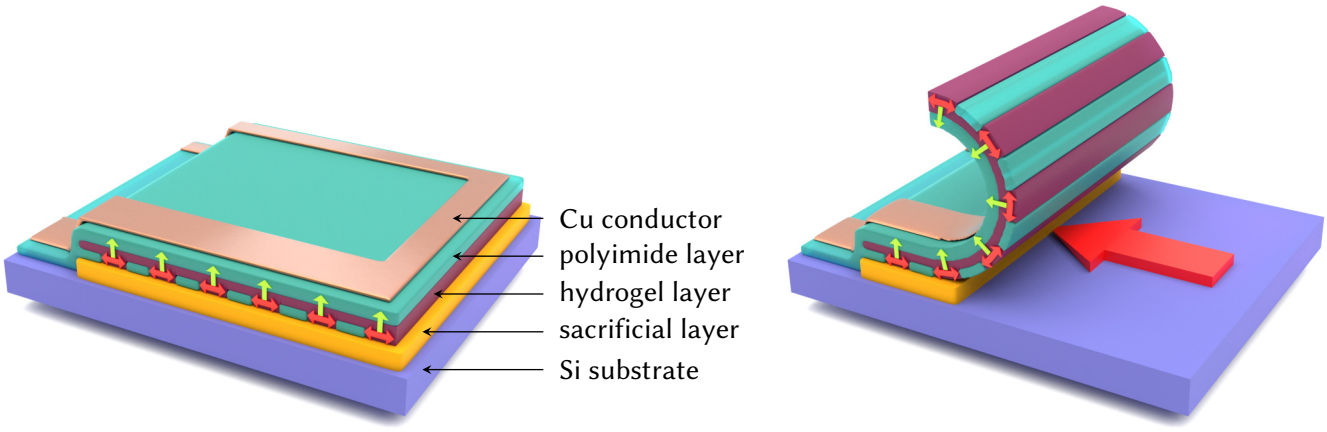

(a) planar structure (b) rolling process

Figure 11: Schematics of the planar structures and the rolling process. The small red arrows indicate the swelling of the hydrogel stripes, the small green arrows the according motion, which leads to the rolling process. The big red arrow indicates the rolling direction.

Details on the synthesis and the polymers are given in [155]. A conducting copper layer is deposited on top of the rigid layer prior to the rolling process. A lift-off process involving an additional photoresist has to be used for patterning in this step. The adhesion between the different layers, as well as their uniformity and quality is crucial for the whole production process. The final diameter of the produced coils can be adjusted by the pH value of the rolling solution, because the hydrogel layer is swelling due to the response of the incorporated carboxylic groups to hydroxide anions [149]. It is also possible to adjust the diameter after a first finished rolling attempt, by immersing the samples into the rolling solution with an altered pH.

3.2 Basic Coil Design and Magnetic Field Simulations

In order to get an approximate value for the magnetic field strengths attainable with the self-assembled micro coils finite element method (FEM) simulations using *Ansys* Electromagnetics were conducted. The physical dimensions of the self-assembled CPO elements in this work are limited by the restricted space inside a TEM, where they are tested and characterized. The contacting and *in-situ* biasing of the manufactured elements is realized with a *Protochips* Fusion Select TEM specimen holder. The holder accepts chips of 4 mm by 6 mm and determines the electron transparent region (c.f. Fig. 12), thereby giving restrictions to overall design of the CPO elements.

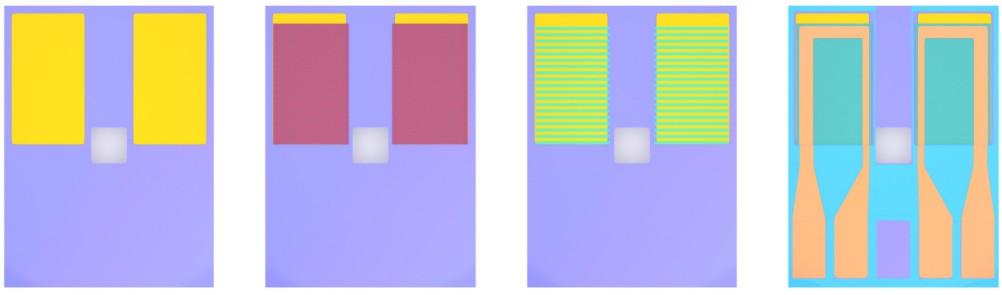

(a) sacrificial layer (b) hydrogel layer (c) polyimide layer (d) complete chip

Figure 12: Planar layout of the chips with the to-be-rolled micro coils in dipole configuration. The layout of the vector magnet and quadrupole configuration is given in Fig. 32. The different layers have the same colors as in Fig. 11. The dimensions are not to scale, for better visibility of the different structures.

FEM simulations were performed to evaluate the fields achievable with the micro coils, whose geometrical parameters are determined by the chip dimensions. In this particular design the maximum length of the to-be-rolled conductors is 2.6 mm resulting in about 3 turns for an inner coil radius of 140 µm. A "Swiss-role" type coil geometry is used in order to maximize the magnetic field for a given current density, ultimately limited by the element's power dissipation.

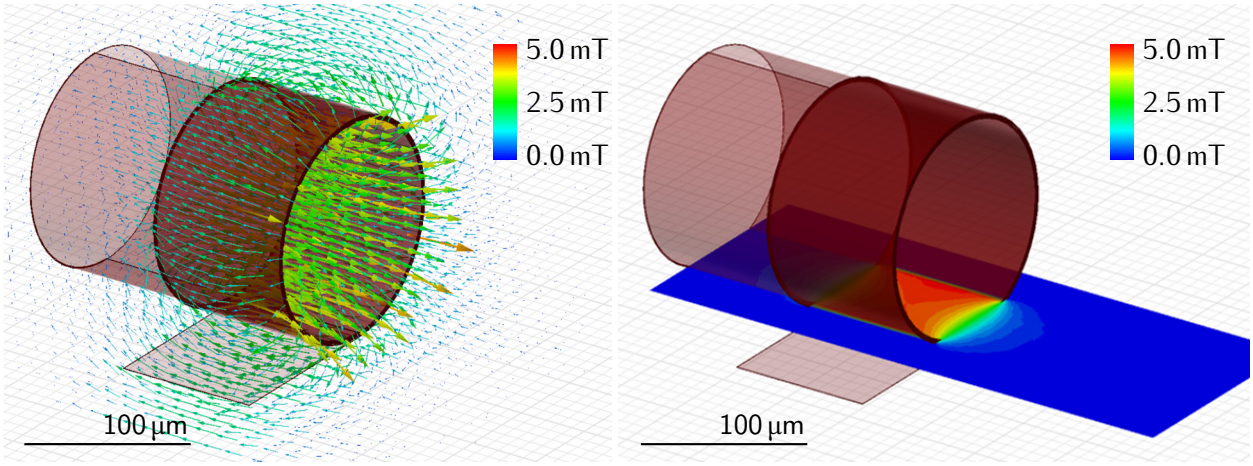

(a) **B** (b) B_a

Figure 13: FEM simulations of solenoids with the geometry of the self-assembled micro coils as determined by the *Protochips* Fusion chip design. The 3D distribution of the magnetic field **B** (a) as well as its axial component in the relevant plane B_a (b), where the soft magnetic micro wires are going to be introduced (c.f. Sec. 3.3) is given for a current of 100 mA. For the considered conductor cross-section of 100 µm x 300 nm this current corresponds to a current density of about 3.3 kA/mm^2. The micro coils can sustain this relatively large current density, equal to the melting current density of copper [168], indicating the quality of the deposited material layers and the large dissipation of heat in the system. For the simulation an inner radius of 140 µm and a pitch in between the "Swiss-role" layers of 0.6 µm was assumed. *Ansys* Electromagnetics was used for the FEM simulations, the overall simulation volume was 225 x 225 x 400 µm and adaptive meshing was employed.

The FEM simulations (Fig. 13) suggest an axial magnetic field B_a of about 3 mT - 4 mT in the vicinity of the conductor for the considered coil geometry at 100 mA current, which is the maximum current that *Protochips* recommends for the Fusion Select holder. The FEM simulation closely resembles the analytical result for the axial field given in Eq. (2.130) with an on axis maximum value of about 1.27 mT for the considered geometry (c.f. Fig 13a).

As these values are by far insufficient for charged particle optical applications, a soft magnetic material has to be introduced inside the coils to enhance and shape the resulting magnetic field. In order to polarize a ferromagnetic pole piece with such small magnetic fields, the magnet has to be very soft, i.e. it has to possess very low remanent magnetization and coercive field. Pyrex encapsulated core-shell CoFeSiB micro wires are reported to fulfill the aforementioned requirements [169]. These micro wires achieve the ultra soft behavior by the interplay between their stressed Pyrex shell and their magnetic CoFeSiB core. More details on their magnetic properties are given in the next section, their polarization behavior was measured using vibration sample magnetometry (VSM) (c.f. Sec. 3.3).

3.3 CoFeSiB-Pyrex Core-Shell Micro Wires

All Pyrex coated amorphous ferromagnetic micro wires are made from similar ferromagnetic alloys comprising transition metals (TM) as well as metalloids (M) and commonly share the same structure formula:

$$TM_xM_{(1-x)}\,, \tag{3.1}$$

with x ranging from 0.7 to 0.8. The commonly used transition metals are iron, cobalt and nickel, which give rise to the ferromagnetic behavior of the wires, the used metalloids are typically silicon and boron [169].

There are mainly three different types of Pyrex coated ferromagnetic micro wires [169, 170]:

1. Micro wires with negative magnetostriction (magnetostrictive constant λ_{ms} of about -10^{-6}), which are mostly made from CoFeB alloys and exhibit a circular easy axis due to the stress distribution. Accordingly, these wires display a circular domain structure and a very soft, non-hysteretic linear magnetization behavior.

2. Micro wires with low or balanced magnetostriction (λ_{ms} in the order of -10^{-6} to -10^{-7}) that are usually made from CoFeSiB alloys with 3–5% Fe content. Here, the emanating magnetic behavior is characterized by circular domains near the glass alloy interface and an axially magnetized core. These types of wires generally have a small coercive field and remanent magnetization, and a high initial differential permeability.

3. Micro wires with positive magnetostriction (λ_{ms} of about $1 - 3 \cdot 10^{-5}$), which are made either from FeSiB or FeSiBCuNb alloys. These wires commonly have a single axial domain in the central part, if short enough, and a radial magnetization in the outer part of the ferromagnetic core. Their magnetization behavior exhibits a rectangular hysteresis curve with a single large Barkhausen jump at the switching field H_{sw}. Their magnetization effectively has just two values, $\pm$ the saturation magnetization M_s.

Three contributions to the magnetic energy are present in these amorphous magnetic micro wires: (i) the exchange coupling which leads to the ferromagnetic behavior of the alloys, regardless of their geometry, (ii) the magnetoelastic anisotropy, critically determined by the internal stresses due to the rapid solidification in the production process (further details are given below), and (iii) the demagnetizing field energy due to the wire's geometry. The magneto crystalline anisotropy, commonly present in (micro) crystalline ferromagnetic materials is not existent because the alloy in the core of the wires is amorphous, due to the quenching process.

The soft magnetic micro wires, used in this work, are of an amorphous CoFeSiB-Pyrex core-shell structure They exhibit low negative to vanishing magnetostriction (λ_{ms} is about -10^{-6} to -10^{-7} [169, 170]) and internal stresses of several hundred MPa, induced by the Pyrex coating [169]. This internal stress is a result of the drawing and quenching production process[26], referred to as the Taylor-Ultivsky technique [171, 172, 173, 174]. In this production scheme, the considered magnetic alloy is inductively heated inside a Pyrex capillary until the Pyrex is melting and forming a droplet, which is subsequently fixed onto a rotating coil, which draws the emanating micro wire. The material is quenched in a water jet at a rate of about 10^5 K/s [170], which amplifies the internal stresses during drawing. The diameter of the amorphous ferromagnetic core, as well as of the Pyrex shell, can be controlled by the temperature of the materials, the drawing speed, the employed alloy, and the initial thickness of the Pyrex capillary. The such produced wires can have a length of several kilometers. The diameter of core and shell, however, can vary considerably, even in one batch. The micro wires used in this work were produced by the *Nanomagnetism and Magnetization Processes Group* under the supervision of Manuel Vázquez at the *Instituto de Ciencia de Materiales de Madrid* (ICMM). The nominal diameters of the used wires, if not stated otherwise, are 15.5 µm ± 3.5 µm for the CoFeSiB core and 19.5 µm ± 5.5 µm for the whole wire with glass coating. These numbers from the suppliers were also confirmed by SEM measurements. Note that the diameter of the magnetic core varies by over 20%, which significantly alters the magnetic behavior of the different micro wires, although they are from the same batch. A micro magnetic model for such glass coated soft magnetic micro wires, taking into account the exchange interaction, as well as the magnetoelastic anisotropy energy, is given in [175]. The application of this calculations to the wires in this work, however, is challenging due to the variations in their diameter and possible fluctuations in the composition of the soft ferromagnetic alloy.

Vibrating Sample Magnetometer Measurements

The magnetization behavior of the amorphous ferromagnetic micro wires, used in this work, was analyzed with the vibrating sample magnetometer (VSM) installed within the physical properties measurement system (PPMS) from *Quantum Design*. The micro wire for the VSM measurement had a length of 0.27 cm with a ferromagnetic core radius of 4.7 µm, as measured from SEM images. Additionally, various minor hysteresis loops were recorded without significant deviations from the initial complete loop. Hysteresis effects in the ferromagnets of the VSM coils were corrected according to the procedure described in [176]. To that end, the external field value in the measurements was offset by -15.45 mT. It is important to note that the VSM measurements are not directly comparable to magnetization behavior of the wires inside the self-assembled micro coils. The former applies a homogeneous external field to the complete wire, while the latter one only encloses part of the wire, hence applying an inhomogeneous field, which is decaying toward the wire tip approaching the electron beam.

[26] There are three different stress inducing mechanisms in Pyrex coated micro wires[169]: 1. Thermoelastic stress stemming from the temperature gradient during quenching. 2. Drawing stress of tensile nature from the mechanical forces during the drawing. 3. Thermal stress originating from the different thermal expansion coefficients of core and shell.

Despite the different experimental situation in the VSM measurements compared to the one in the µCPO devices, these measurements yield some important insights in the magnetization behavior of the CoFeSiB micro wires in their later application: The measurements depicted in Fig. 14 show that the magnetization process is linear with respect to the external magnetic field between -0.3 mT and 0.3 mT. The wire is completely polarized at about ±1 mT.

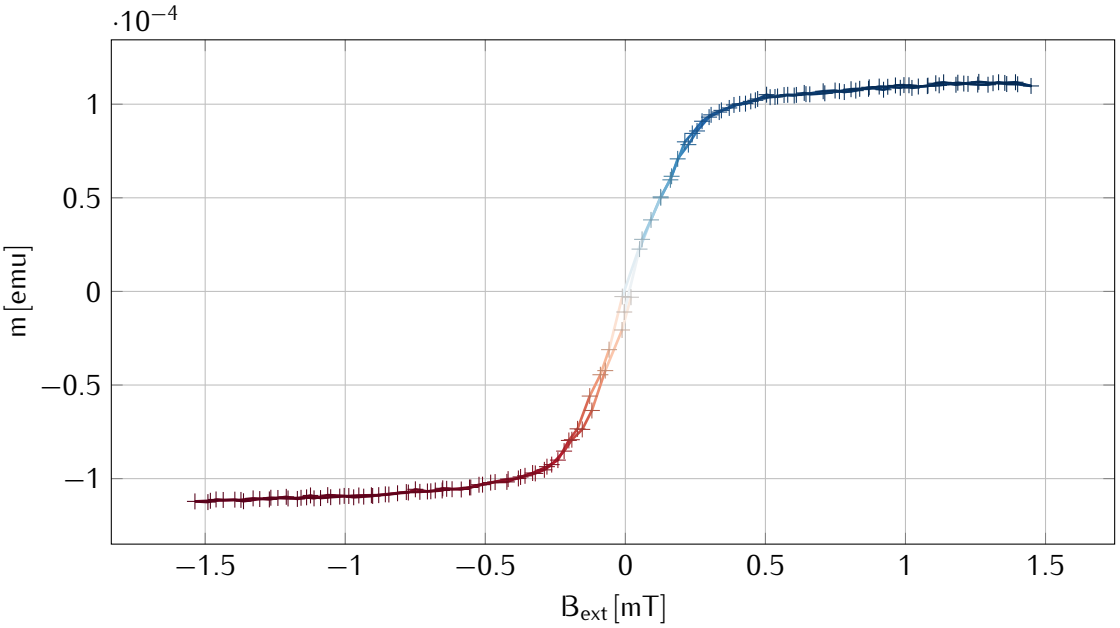

Figure 14: VSM measurements of a CoFeSiB micro wire with a length of 2.7 mm and a radius of the ferromagnetic core of 4.7 µm. The corresponding maximum flux density in axial direction at the end of the wire is about 0.76 T.

A quantitative evaluation of the magnetization behavior of the micro wires inside the inhomogeneous field generated by the micro coils by classical techniques, such as micro Hall or magnetomechanic measurements, is challenging due to the small size of the assembly. Magnetooptic Kerr microscopy measurements are also difficult, due to reflections on the Pyrex coating. The direct measurement of the deflection of an electron beam inside the µCPO device, however, provides the necessary information about the miniaturized CPO elements in a very direct manner. There are various TEM techniques that render the measurement of the deflection of the microscope's electron beam possible, most of which with sub-nanometer spatial resolution and micro radian angular resolution. In order to measure the projected magnetic fields within a field of view (FOV) of several 10 µm - 100 µm, and to minimize charging issues, a differential phase contrast (DPC) technique, in a special low magnification mode with a magnetic-field-free specimen plane, was developed and employed. The results of the experimental characterization of the electron optical properties of the fabricated µCPO devices are reported in chapter 4 of this thesis.

3.4 Fabrication of Self-Assembled Micro Coil Devices

As mentioned before, the fabrication process of the self-assembled micro coil devices was developed by our collaboration partners Renato Huber, Dr. Dmitriy Karnaushenko, Dr. Daniil Karnaushenko and Prof. Oliver G. Schmidt, at the IIN. The responsible person for the fabrication was Renato Huber, therefore more details on the process can be found in his doctoral thesis, which is not submitted at the time this thesis was handed in.
The self-assembled micro coils were designed with a geometry similar to the model for the magnetic simulations shown in Fig. 13. According to the VSM measurements (c.f. Sec. 3.3), the calculated field strengths are sufficient to polarize the CoFeSiB micro wires. As a first step, the chromium masks for the photo lithography process were designed and produced in a lift-off process using a *Heidelberg Instruments* MLA100. The photoresist was removed by rinsing the mask with a mixture of acetone and isopropyl alcohol.

Preparation of the Substrate

The silicon wafer was prepared by depositing 40 nm Al_2O_3 with an atomic layer deposition (ALD) FlexAL from *Oxford Instruments Plasma Technology*. This layer's function is mainly to electrically isolate the copper conduction paths from the silicon substrate but also to serve as a stopping layer for the Bosch process (see below for more details on this process). Additionally, a structured SU8 photoresist layer is applied from the backside that acts as a hard mask for the Bosch process. The layers on both sides of the wafer were aligned with the help of the backside alignment technique as implemented in the *Süss MicroTec* Mask Aligner MA 6. The hard mask needs to be applied on the backside of the wafer as it is not possible to apply it on top of the polymeric structures and remove it again without damaging the top layers. In a final step of the wafer preparation the Al_2O_3 coated side of the wafer is silanized, to enhance the adhesion of the polymers to the substrate, after being plasma cleaned in oxygen plasma (in a GIGAbatch 310M from *PVA Metrology & Plasma Solutions* for 15 minutes at 600W with O2 flow of 200 sccm). The wafer is silanated by baking at 150°C for two hours in a vacuum oven, where 200 µL 3-Methacrylpropyltrimethoxysilane (MAPTMS) were placed adjacent in a glass dish.

Polymer Layers

The three different polymeric layers were spin coated onto a 3" or 6" p-doped silicon wafer, by using a SPIN 150i from *SPS-Europe,* and subsequently soft baked on a hotplate. The parameters used for the spin coating process are given in table 1. The polymeric layers were subsequently structured using a *Süss MicroTec* Mask Aligner MA 6 and developed in DI water (deionized water), DEGMEE (Diethylenglykol-monoethylether) or a NEP (1-Ethyl-2-pyrrolidon) based solution (NEP-DEGMEE-ethanol in 4:2:1 volumetric parts). The developed structures are rinsed with acetate (*Micro Resist Technology* MR Dev 600 for 10 seconds) and dried with an air gun. After hard baking at 220°C on a hotplate, the thickness of the structured polymeric layers was evaluated with a *Bruker* DektakXT stylus profilometer, by analyzing representative edges. The different polymeric layers were aligned by using predefined alignment marks that were deposited as part of the structure. For the quadrupoles and vector magnets in this work the swelling

layer is partly structured with rigid polyimide stripes in-between to ensure rolling by wrinkling of the membrane (inspired by [177]), regardless of the large aspect ratio of 1.48. The aspect ratio of the planar structures is given by $r = h/w$, where h is the length of the polymeric layers along the rolling direction and w the corresponding length in the perpendicular direction.

step	spin coating rotations [rpm]	soft bake [°C]	soft bake [min]	exposure [mJ/cm^2]
sacrificial layer	1500	35	10	280
rigid stripes	3000	50	5	600
swelling layer	4000	40	5	450
rigid layer	3000	50	5	660

step	developer	develop time [s]	hard bake [°C]	hard bake [min]	thickness [nm]
sacrificial layer	di water	30	220	10	300±100
rigid stripes	NEP solution	240	220	5	600±100
swelling layer	DEGMEE	90	220	10	600±100
rigid layer	NEP solution	180	220	5	600±100

Table 1: Parameters for the spin-coating of the polymer layers. The rigid stripes were just used in the vector magnet and quadrupole samples due to their different aspect ratio of the planar structures [178].

Conducting Layer

After the finalization of the rigid polyimide layer, the conducting Ti-Cu-Ti layer was sputtered onto a spin coated *MicroChemicals* AZ 5214E image reversal photoresist, baked on a hotplate at 90°C for 5 minutes, and finally structured in a lift-off process using the *Süss MicroTec* Mask Aligner MA 6 (exposure: 45 mJ/cm^2). Before the development of the photoresist in AZ 726 MIF and rinsing with deinoized water it is baked on a hot plate at 120°C for 2 minutes and subsequently flood exposed at 300 mJ/cm^2. The conducting Ti-Cu-Ti layer is then sputtered on the structured photoresist with a HZM-P4 (*Von Ardenne*). The 5 nm ± 2 nm titanium layers enhance the adhesion to the rigid polyimide layer and protect the structures. The 300 nm ± 100 nm copper layer is the main conduction path in the self-assembled micro coils. In a final step of the metallization, the AZ 5214E sacrificial layer, with the unwanted part of the metal layers on top, is removed by immersing the wafer in acetone. The wafer with the finished planar structures is then cleaned with isopropanol and dried with an air gun.

Bosch Process

The window for the TEM electron beam was etched from the backside into the silicon substrate by a Bosch process [179] using SU8 photoresist, as a final step before dicing of the chips and rolling of the micro coils. In order to protect the planar structures, before the Bosch process, a layer of AZ 520 D photoresist (*MicroChemicals*) is applied by spin coating with a SPIN 150i at 2000 rpm for 30 seconds and afterwards dried on a hotplate for 10 minutes at 90°C.

Further details on the Bosch process and the employed parameters can be found in [178] and the dissertation of Renato Huber, which is not published at the time this thesis was handed in.

Self-Assembly

In order to dice the wafer into the individual chips, which can be inserted into the *Protochips* Fusion Select TEM specimen holder, the wafer is loaded to a semi-automatic SS10 Dicing Machine from *Accretech* and pre-diced with a depth of 100 µm. The AZ 520 D protection layer can now be removed with acetone, before the wafer with the planar structures is finally cleaned with isopropanol and dried with an air gun. The initial etching solution for dissolving the sacrificial layer is a 1:30 (mass ratio) ethylenediaminetetraacetic acid (EDTA) ($[CH_2N(CH_2CO_2H)_2]_2$) solution in water slightly alkalinized with NaOH to a pH of 6.9. Subsequently, $C_6H_5N_3$ was adjoined in 1:10 mass ratio to EDTA and finally ethanol in a 1:9 volume ratio to water. As soon as the sacrificial polymeric layer is dissolved, the pH of the solution is increased to about 10 by adding 2 % NaOH solution. In this geometry, the final diameter of the micro coils can be adjusted between 80 and 160 µm with the pH of the rolling solution. After the self-assembly process the samples are rinsed with 1:4 volumetric ratio solution of ethanol in water and dried on lab wipes.

Pole-Piece Installation

The soft ferromagnetic micro wires are inserted after the rolling process manually, and fixed in place by a vacuum stable polymeric instant adhesive. After the hardening of the instant adhesive on a hot plate at 70° C for several hours, the micro wires were shaped in a *Zeiss* 1540XB CrossBeam and a *Zeiss* NVision40 focused gallium ion beam machine. The FIB was mostly operated at 10 nA and 30 kV, which results in a spatial resolution in the 100 nm regime. An increased resolution can be achieved, however, by decreasing the semi-convergence angle through changing the aperture to a smaller size, thus reducing the beam current, as well as the resolution-limiting aberrations. A resolution in the single digit nanometer regime is possible with state-of-the-art FIB machines.

4 Optical Properties of Self-Assembled Miniaturized Electron Optics

The optical properties of a CPO element can be determined by various experimental techniques, either in a direct manner through the deflection and deformation of an incident electron beam or indirectly by measuring the relevant field distribution within the element from which the corresponding optical properties can be calculated. The fields in magnetic elements can be measured in manifold ways, e.g., by probing the force on some permanent magnet or current-carrying conductor within the field, or by measuring the voltage induced in a moving conductor of a fluxgate magnetometer, across some magnetoresistive material, by the Hall effect, or across the Josephson junction in a superconducting quantum interference device (SQUID). The magnetization of the ferromagnetic pole pieces could also be directly determined by magneto optical Kerr microscopy of the pole pieces or by magnetic force microscopy (MFM). In the case of the miniaturized electron optical elements that were produced within the frame of this work, however, it is very challenging to measure the field distribution, employing any of the above noted methods due to the small size of the elements and the required resolution in real space. Kerr microscopic and MFM measurements of the pole pieces are rendered difficult, due to reflections on the Pyrex shell, the three-dimensional structure of the devices, and the paramagnetic behavior of the Pyrex shell.

The direct determination of the deflection of an electron beam does not suffer from the aforementioned difficulties. There are various experimental setups allowing to measure the deflection of an electron beam, which fulfill the requirements of nanometer spatial resolution, micro radian angular resolution, and projected field resolution in the sub-nano Tm regime. In this work, a differential phase contrast (DPC) technique is employed within a TEM. This method is commonly used to measure projected electrostatic and magnetic fields down to sub nanometer resolution [180, 181, 182]. In combination with tomographic techniques, three-dimensional fields can be reconstructed from different projections along different axes [183].

Differential Phase Contrast

In the following sections, the DPC technique is applied in a TEM that is operated in a dedicated low magnification mode. In this mode, the ultimate spatial resolution is sacrificed for a larger field of view and magnetic-field-free conditions in the sample plane. The latter is necessary to operate the miniaturized electron optical elements unperturbed from the magnetic field of the microscope's objective lens. Highest resolution is not necessary for the mapping of the deflection of the microscope's electron beam, as the considered fields in the bore of the µCPOs do not exhibit modulations at sub micrometer length scales. In the employed DPC scheme the focused TEM electron beam is scanned over the considered sample in a scanning TEM (STEM) fashion and the corresponding diffraction disk is recorded with a pixelated detector in the far field of the specimen plane (see Fig. 15).

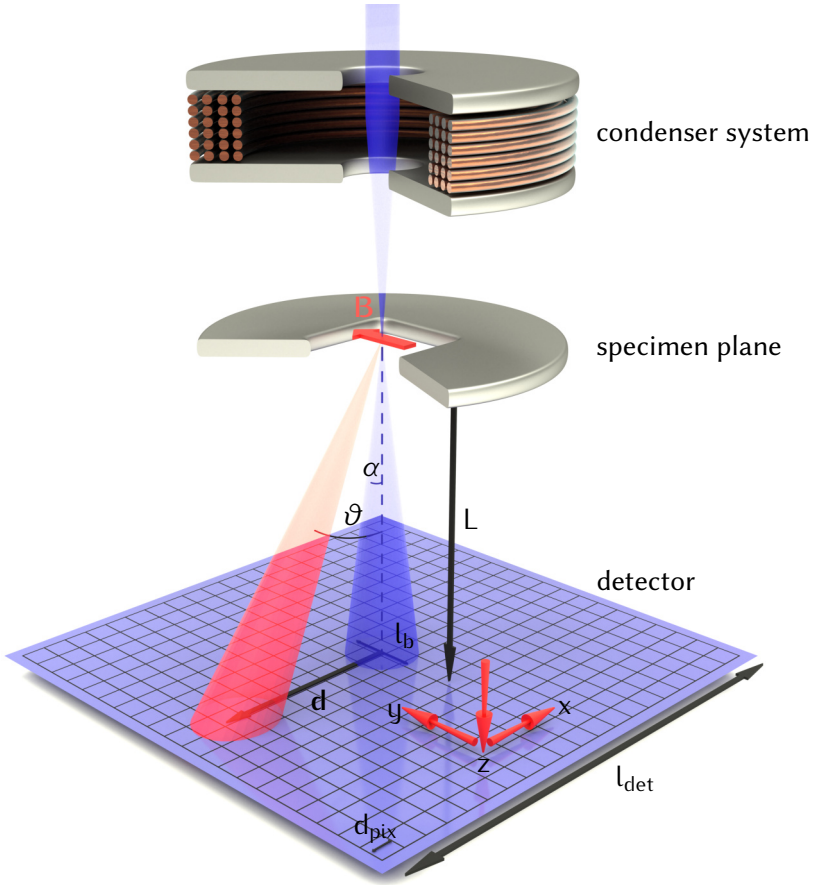

Figure 15: Simplified principle of the differential phase contrast measurement setup with one condenser lens and without any optics beneath the sample position.

Various different detector types for DPC in a TEM exist, namely pixelated [184, 185] or segmented [186] ones, which are specially adopted either for recording speed or large angular resolution. In this work, a *Gatan* Ultrascan 1000 CCD camera with 2048 x 2048 14 µm pixels was used in a double corrected *FEI* (now *Thermofisher Scientific*) Titan^3 80-300, operated at 300 kV acceleration voltage. In the DPC measurements for this work, only the deflection of the focused electron beam in the vacuum next the soft magnetic wires is analyzed, as the wires are too thick for the electron beam to be transmitted. An electron beam with a convergence angle in the 100 µrad range was employed, ensuring that the scan step size, which is in the µm range, is larger than the probe size. Therefore, artifacts due to optical vignetting, which is redistribution of intensity in the diffraction disk due to partial blocking of the convergent electron beam, are limited to the reconstructed pixels in the direct vicinity of the wires. See [187] and the corresponding supplementary information for a detailed explanation of optical vignetting. Moreover, the intensity in the diffraction disks is not redistributed due to mutual interference of coherently scattered partial waves (c.f. [188]). Hence, the information in the recorded diffraction disks can be evaluated in a straight forward manner as the

displacement **d** of the center of mass (COM) of the intensity distribution is given by [189, 190]:

$$\mathbf{d} = eL \int_0^l \left(\frac{1}{p_z} \mathbf{e}_z \times \mathbf{B}_\perp \right) dz + \frac{eL}{\mathbf{p} \cdot \mathbf{v}} \int_0^l \mathbf{E}_\perp dz \,, \tag{4.1}$$

where l is the effective length of the field region, e the elementary charge, $\mathbf{p}$ the relativistic electron momentum along the microscope's optical axis $\mathbf{e}_z$, $\mathbf{v}$ the electron velocity, $\mathbf{B}_\perp$ the magnetic in-plane flux density and $\mathbf{E}_\perp$ the in-plane electric field to-be-measured. The angular offset between the scan and detector orientation due to the Larmor rotation of the TEM's magnetic lenses was measured in advance and corrected numerically.

The electrostatic field term can be neglected for the measurement of magnetic stray fields. There is, however, always a non-zero electric field adjacent to materials in or next to the beam, as all samples accumulate charges under the electron beam when illuminated directly and also from diffuse scatted electrons when been not illuminated directly. This charging is usually of positive nature, as it is caused by the emission of secondary electrons from the sample. The contribution of the electrostatic field could be separately determined and subtracted by recording two sets of DPC scans, where the sample is flipped and the detector axis perpendicular to the flip axis is numerically inverted for the second scan [191]. This procedure indirectly exploits the different behavior of the electrostatic potential $V(z)$ and the magnetic vector potential $\mathbf{A}(z)$ under the time reversal operation ($t \to -t$):

$$V(z) \overset{t \to -t}{\to} V(z) \tag{4.2}$$

$$\mathbf{A}(z) \overset{t \to -t}{\to} -\mathbf{A}(z) \,, \tag{4.3}$$

by the two flipping operations that mimic the same experiment reversed in time [192]. The corresponding phase shift of the electron wave [122]:

$$\varphi_t = \frac{q}{\hbar} \left(\frac{1}{v} \int_0^t V(z) - \int_0^t A_z(z)\, dz \right) , \tag{4.4}$$

is altered accordingly upon time reversal:

$$\varphi_t \overset{t \to -t}{\to} \varphi_{-t} = \frac{q}{\hbar} \left(\frac{1}{v} \int_0^t V(z) + \int_0^t A_z(z)\, dz \right) , \tag{4.5}$$

By subtracting φ_{-t} from φ_t the contribution of the electrostatic field should ideally vanish and only twice the magnetic part remains:

$$\varphi_{mag} = \varphi_t - \varphi_{-t} = -2\frac{q}{\hbar} \int_0^t A_z(z)\, dz \,. \tag{4.6}$$

The *Protochips* Fusion Select specimen holder, used in this work, does not allow the flipping of the sample, while keeping it contacted, so the subtraction technique could not be employed, unfortunately. The electrostatic contributions due to electron beam induced charging should not be significant, however, because the analyzed FOVs and magnetic fields are very large[27]. Moreover the scanning procedure with the long dwell and readout times in the 100 ms regime additionally limits the effects of charging. The DPC maps are symmetric with respect to the wire axis, if an additional electrostatic component is completely absent and the deflection is assumed to be solely caused by magnetic fields, even in the nearly unmagnetized state (e.g. Fig. 28).

If only the components of $\mathbf{B}$ perpendicular to $\mathbf{p}$ are considered:

$$\int_0^l \frac{1}{p_z}\mathbf{e}_z \times \mathbf{B}_\perp dz = \frac{\mathbf{B}_{proj}}{p_z}\,, \tag{4.7}$$

the modulus value of $\mathbf{d}$ reads:

$$d = |\mathbf{d}| = \left|\frac{e\mathbf{B}_{proj}}{p_z} L\right|. \tag{4.8}$$

The deflection in small angle approximation is then given by:

$$\vartheta = \arctan\left(\frac{d}{L}\right) \approx \left|\frac{e\mathbf{B}_{proj}}{p_z}\right|. \tag{4.9}$$

In a sharp cut off approximation $\left(\mathbf{B}_{proj} = \mathbf{B}_\perp t\right)$, the corresponding quantities read:

$$\int_0^l \frac{1}{p_z}\mathbf{e}_z \times \mathbf{B} dz = \frac{\mathbf{B}_\perp t}{p_z}\,, \tag{4.10}$$

$$d = |\mathbf{d}| = \left|\frac{e\mathbf{B}_\perp t}{p_z} L\right| \tag{4.11}$$

and

$$\vartheta = \arctan\left(\frac{d}{L}\right) \approx \left|\frac{e\mathbf{B}_\perp t}{p_z}\right|, \tag{4.12}$$

for an element of optical thickness t.

Accordingly, the spatially resolved projected field $\mathbf{B}_\perp t$ can be readily determined by measuring the deflection angle in COM DPC measurements, which is sufficient for the evaluation of the optical characteristics of the µCPOs (as they can be treated as thin elements (c.f. Sec. 2.3.2). An additional deflection from not perfectly pivotized scan units was corrected by acquiring an additional scan without the sample and a subsequent numerical subtraction of the fields reconstructed from this reference scan. This numerical correction was performed for all DPC measurements in this work.

[27] which reduces charging form diffuse scattered electrons

The effective camera length L for the DPC measurements in this work, i.e. the electron optical distance between the sample plane and the detector in the far field, was determined to 13.2 m ± 0.8 m (if not explicitly stated differently) by recording a diffraction pattern of a standardized gold cross grating (2160 $^{\text{lines}}/_{\text{mm}}$). A shorter camera length is not available in the low magnification mode that has to be employed for magnetic field free imaging in the specimen plane. The pixel-level precision of the determined projected magnetic fields $B_{proj,min}$ with this camera length can be estimated to 2.23 Tnm for the used 300 kV acceleration voltage and 14 µm pixel size d_{pix}:

$$B_{proj,min} = \frac{d_{pix} p_z}{eL} . \tag{4.13}$$

The actual precision for sub pixel determination of the COM can be some orders of magnitude higher, if the overall dose is not a limiting issue [193, 188]. The maximally resolvable projected field is given by the detector size l_{det} minus the beam diameter l_b in the far field, which is determined by the semi-convergence angle of the used illumination:

$$B_{proj,max} = \frac{(l_{det} - l_b)\, p_z}{eL} . \tag{4.14}$$

In the used setup the maximum projected magnetic field is about 2 Tµm for both deflection directions. The beam size on the detector l_b is given by the semi-convergence angle α of the illumination and the used camera length L:

$$l_b = \tan(\alpha)\, L \approx \alpha L . \tag{4.15}$$

In the diffraction limited case, the spatial resolution d_{diff} is solely depending on the electron wavelength λ and the semi-convergence angle α and given by the Rayleigh Criterion [194]:

$$d_{diff} = 0.61 \frac{\lambda}{\sin(\alpha)} . \tag{4.16}$$

Accordingly, the bandwidth product of real space resolution and precision of the reconstructed fields is a constant for a given optical system. It only depending on the pixel and detector size:

$$B_{proj,min} d_{diff} = 0.61 \frac{d_{pix} p_z \lambda}{eL \sin(\alpha)} \approx 0.61 \frac{d_{pix} h}{e l_b} , \tag{4.17}$$

as the contributions p_z and λ depending on the electron energy cancel out according to the de Broglie relation. A similar expression can be found for the interplay between maximum detectable projected field $B_{proj,max}$ and the diffraction limited spatial resolution d_{diff}:

$$B_{proj,max} = \frac{p_z}{e} \left(\tan \alpha_{det} - \tan \left(\arcsin \left(0.61 \frac{\lambda}{d_{diff}} \right) \right) \right) \approx \frac{p_z}{e} \alpha_{det} - 0.61 \frac{h}{e d_{diff}} , \tag{4.18}$$

where $\tan(\alpha_{det}) = {}^{l_{det}}/_{L} \approx \alpha$ is the angular size of the detector. For the setup used in this work, however, the attainable spatial resolution should be some orders of magnitude lower than the diffraction limit, as there is no aberration corrected setup for the probe corrector when operated in low magnification mode. The spatial resolution of the reconstructed projected field maps is additionally limited by sample drift during the acquisition time, which is determined by the camera's readout speed in our case. For the reconstruction of magnetic fields in free space, however, ultimate spatial resolution is not necessary, as the fields are smooth and can be interpolated subsequently.

In the following, this electron optical characteristics of the various produced µCPO elements are put on display and analyzed.

4.1 Electron Vortex Phase Plate

The conceptually most simple µCPO element, regarding its design and assembly, is a single solenoid with a tapered pole piece that acts as an electron vortex phase plate, if placed in the center of a round parallel electron beam (c.f. Sec 2.4.3). It is beneficial to taper the pole piece in order to concentrate the axial magnetic flux density within the soft magnetic micro wire and in order to reduce the interaction area with the electron beam. The effect of partial coherence is diminished if the interaction area is smaller than the coherence length of the illumination and thus a vortex quantum state of high purity can be generated. The final shape as well as the distance of the tip to the micro coil, however, also determines the magnetization behavior of the tip. To illustrate this point, two extreme cases of taper geometries are discussed here: an angulated taper towards the tip (c.f. Fig 16a) and a plane-parallel lamella (c.f. Fig 16b).

(a) tapered design (b) lamella design

Figure 16: Renderings of the two analyzed pole piece geometries, the tapered design and the lamella design.

In both geometries, the micro wire is tapered in the plane perpendicular to the optical axis and unmodified along the optical axis, as only the projected fields are of interest in first order. The emanating fields from both tip geometries is measured via COM DPC, the results are shown in section 4.1.1. The characteristics of the electron vortex beam (EVB) produced by the corresponding tip geometries is analyzed in section 4.1.2.

4.1.1 Projected Magnetic Fields

Both types of EVB phase plates were produced in the same fashion as outlined in Sec. 3.4 and the micro wires were from the same batch. The only difference between the two types of phase plates is the different taper, that the chips were from different batches with sightly different micro coils, and that an adhesive was used to fix the lamella-shaped wire micro wires in place. SEM overview images of the two taper variants are given in Fig. 17.

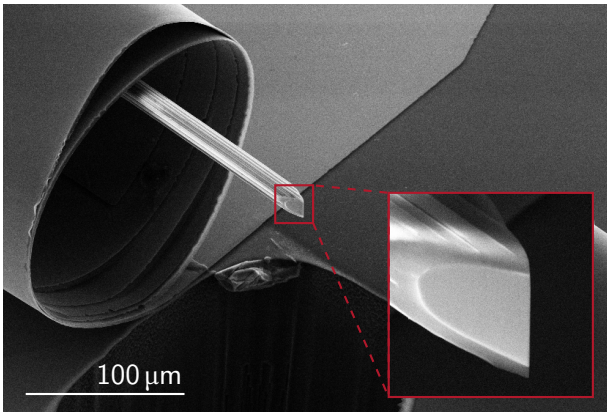

(a) tapered design

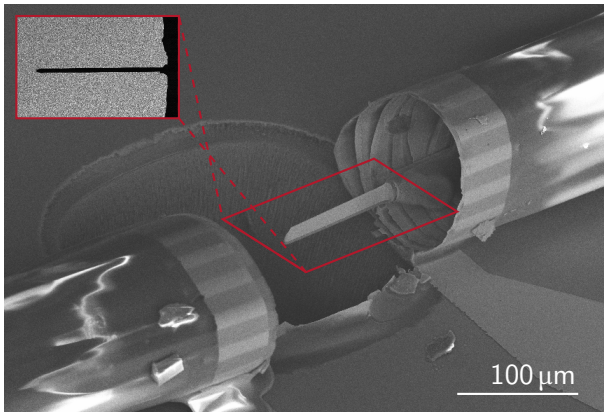

(b) lamella design

Figure 17: SEM overview images of the produced magnetic electron vortex beam phase plates driven by self-assembled micro coils with two different FIB taperings of the soft ferromagnetic micro wire pole pieces. The inset in (b) is an STEM image recorded with an HAADF detector.

In order to analyze the magnetization behavior of the EVB phase plate pole piece, DPC maps with varying excitation current through the miniaturized coils were acquired for both tip geometries. The maximum current was determined by monitoring a constant electrical resistance, as a rise in DC resistance should be caused by an increased temperature, which could ultimately degrade the device. The current was generated using a *Keithley* 2636B System Sourcemeter in constant current mode, as in all the measurements with DC excitation shown in this work. The accordingly estimated maximum current I_{max} is 66 mA for the EVB phase plate with the lamella-shaped pole piece and 100 mA for the tapered device. The corresponding DPC maps for excitations from $-I_{max}$ to I_{max} are given in Fig. 21b.

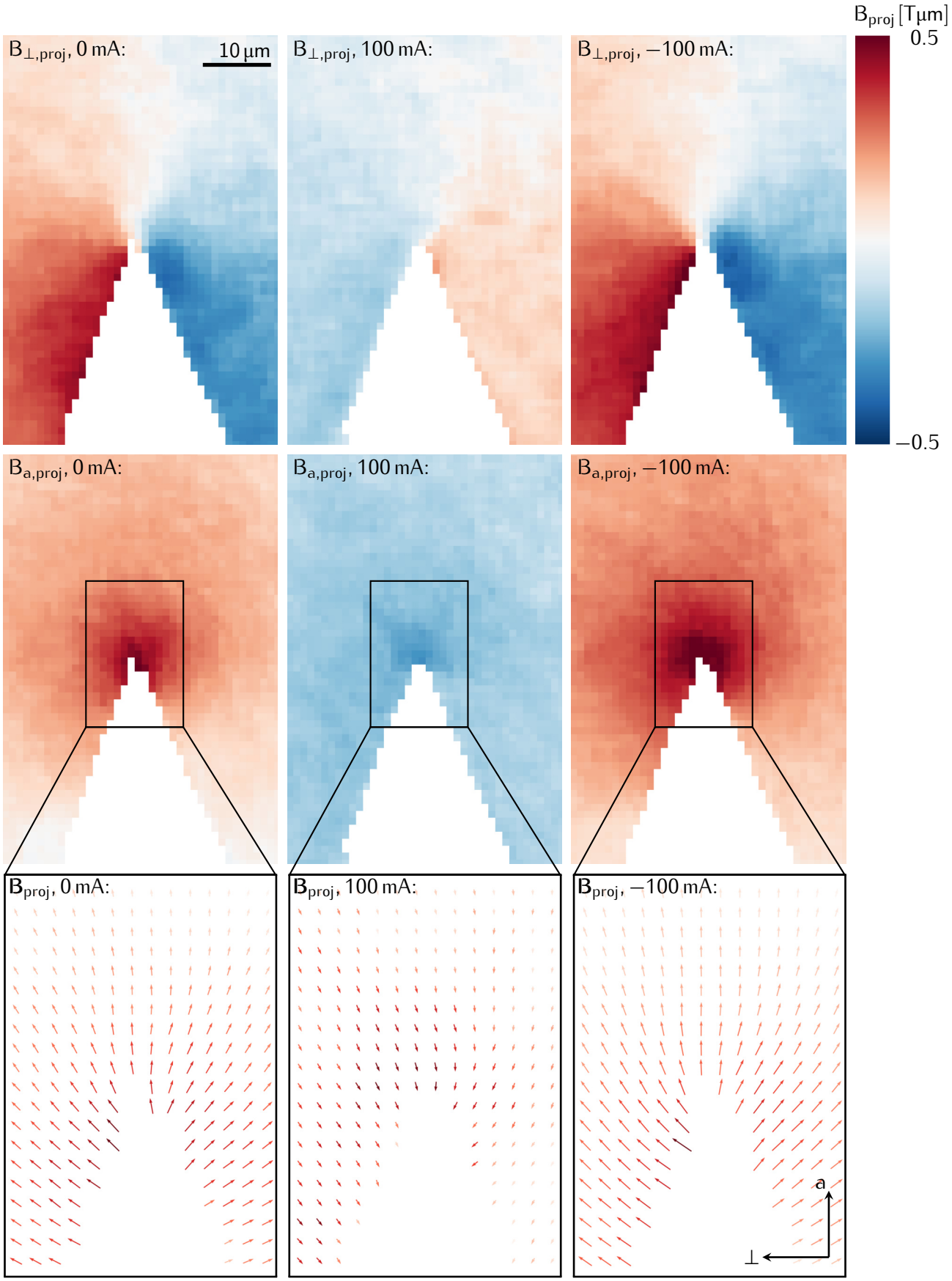

Figure 18: Maps of the projected magnetic fields emanating from the pole piece tips of the tapered micro coil electron vortex phase plates driven by self-assembled micro coils for different excitation currents. The projected fields were reconstructed by means of COM DPC. The upper row shows the axial field $B_{\perp,\mathrm{proj}}$, the middle row the field perpendicular to the axis $B_{a,\mathrm{proj}}$, and the lower one the corresponding vector plot $\mathbf{B}_{\mathrm{proj}}$.

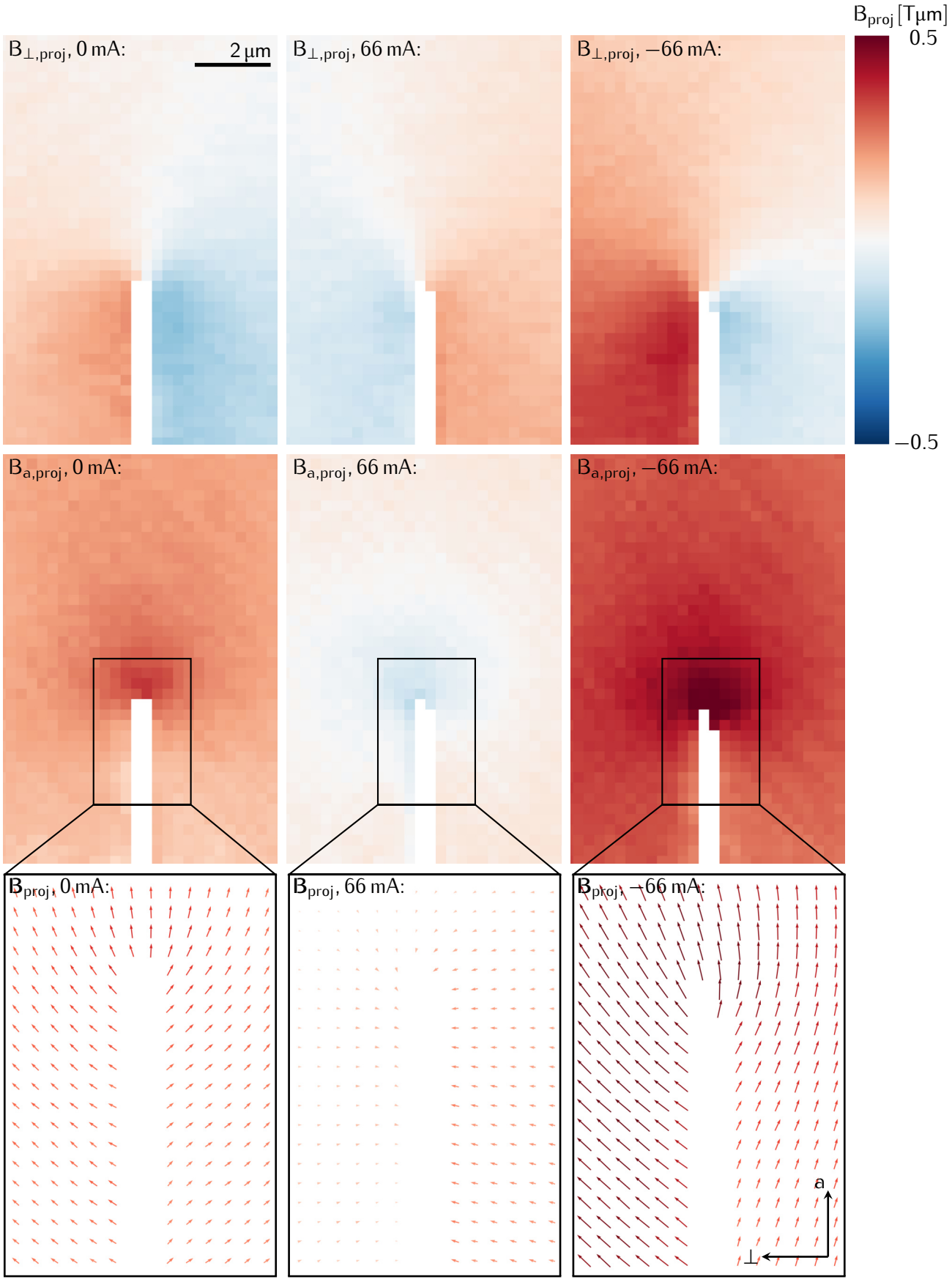

Figure 19: Maps of the projected magnetic fields emanating from the pole piece tips of the lamella-shaped micro coil electron vortex phase plates driven by self-assembled micro coils for different excitation currents. The projected fields were reconstructed by means of COM DPC. The upper row shows the axial field $B_{\perp,proj}$, the middle row the field perpendicular to the axis $B_{a,proj}$ and the lower one the corresponding vector plot $\mathbf{B}_{proj}$

The DPC measurements clearly show that the self-assembled micro coils are able to polarize the soft magnetic micro wires, in both taper geometries. The lamella shape can be regarded most challenging to polarize, because almost all the Pyrex coating is removed in the FIB papering process[28] and the resulting geometry yields a drastically enhanced magnetic shape anisotropy. The maps for the projected magnetic field, especially the ones perpendicular to the solenoid axis $B_{\perp,proj}$, indicate that the fields show a severe deviation from a monopole like field, required for EVB creation. The most significant deviations occur in the half-plane between the tip of the micro wire and the micro coil assembly, while the other half-plane appears reasonably monopole-like. It is important to note that these discrepancies with respect to ideal monopole field are more pronounced in the lamella-shaped geometry. Tomographic measurements that reveal the three-dimensional field distribution would be necessary to properly clarify the underlying magnetization of the soft magnetic micro wire.

There is an obvious remanent magnetic field in the non-excited state, which direction always points away from the micro coil assembly, regardless of the wire's magnetic history. This remanent behavior may be attributed to pinning of domain walls due to the removal of the Pyrex coating, as it was clearly visible in all produced single pole devices, although to a different extent. Additional deflection from electrostatic charging can be excluded as an origin of the deviations from an ideal monopole field shape, as this would introduce a vortex magnetic like field distribution when treated as deflection by a magnetic field.

For a more detailed analysis of the magnetic behavior, a hysteresis measurement was conducted by means of a DPC deflection series with varying current at an increment of 10 mA. The distribution of the reconstructed axial magnetic flux density $B_{a,proj}$ in direct vicinity of the tip for a series of excitation currents from $-I_{max}$ to I_{max} is shown in Fig. 20. The measurements were averaged over 3 pixels, oriented perpendicular to the axial direction from the obtained DPC maps. The magnetization curve barely shows any hysteretic behavior, but a clear remanent state. Therefore, the non-magnetized state is shifted towards positive excitation currents (resulting in axial magnetic fields pointing towards the micro coil assembly), as compared to non-tapered micro wires in a homogeneous field [175]. The measurement of the tapered microwire shows significantly more noise in the reconstructed fields, presumably because of small mechanical movements of the micro wire, which were eliminated in subsequent experiments by using an adhesive that fixes the micro wires in the micro coil. This movement is also observable in the summed transmitted intensity, which was used as a threshold for the masking of the pole region in the DPC maps (white areas in Fig. 18 and Fig. 19). The data indicates that the micro coil assembly is able to change the polarization of the micro wire at around -80 mA and -60 mA for the tapered and lamella-shaped tapered microwire, respectively.

[28] Magnetostriction induced by the Pyrex shell is important for the soft magnetic behavior of the micro wires (c.f. Sec. 3.3)

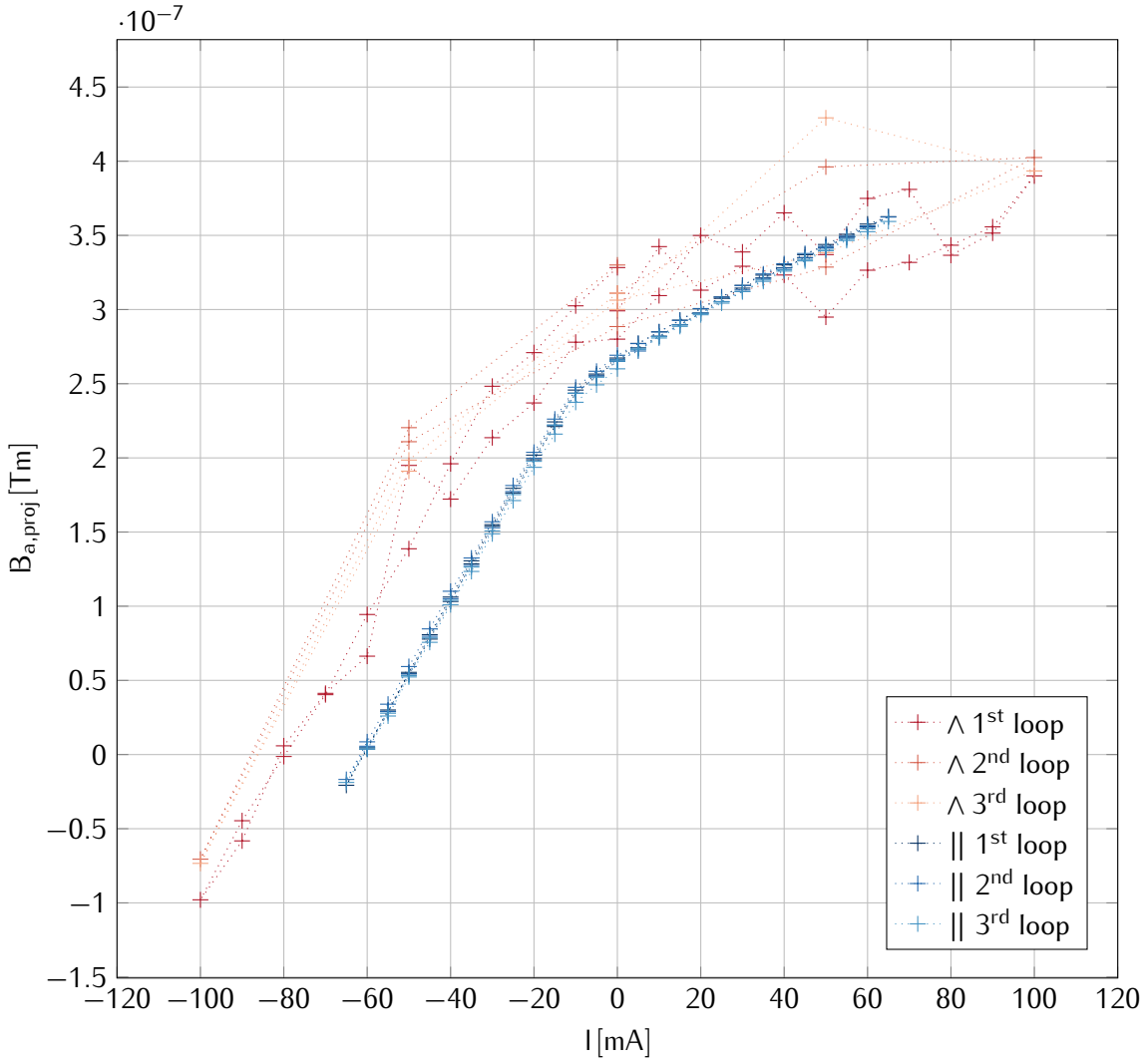

Figure 20: Averaged axial projected magnetic fields $B_{a,proj}$ emanating from the pole piece tips of the electron vortex phase plates driven by self-assembled micro coils at different excitation currents, reconstructed by means of COM DPC. The curves for the tapered pole tip are denoted by ∧, the curve for lamella-shaped pole piece by ||.

The magnitude of the projected fields in the Tμm regime indicates that a corresponding electron vortex beam would have several thousand ħ orbital angular momentum according to Eq. (2.133). The numerical evaluation of Eq. (2.133) by means of integrating the projected fields according to [195]:

$$\frac{\hbar}{e}\partial_x\varphi = \int_{-\infty}^{+\infty} B_y dz \tag{4.19}$$

and, equivalently:

$$\frac{\hbar}{e}\partial_y\varphi = -\int_{-\infty}^{+\infty} B_x dz\,, \tag{4.20}$$

is given in Fig. 21. The OAM in the reconstructed phase distribution is about one order of magnitude above the currently published numbers for the largest OAM of an electron vortex beam [196, 197].

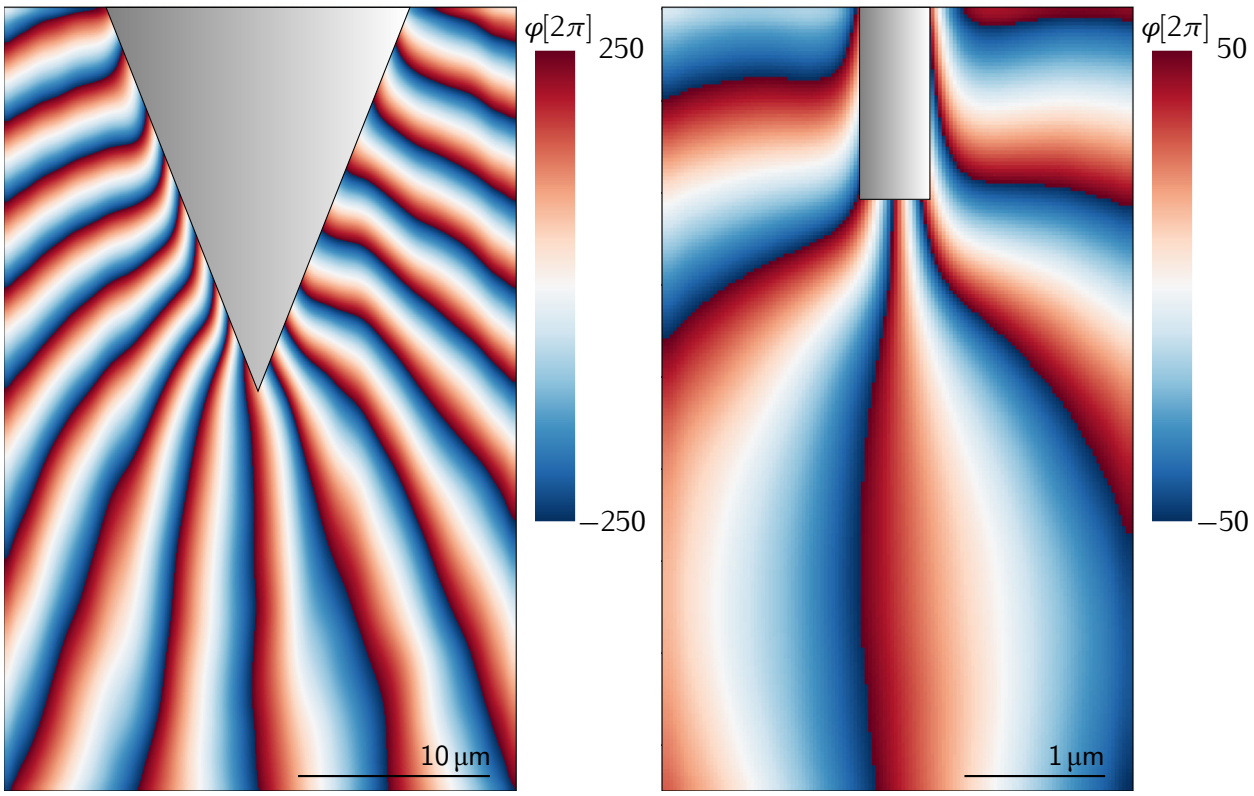

(a) tapered pole piece

(b) lamella-shaped pole piece

Figure 21: Reconstructed electron phase after the EVB phase plate at an excitation of I_{max}, i.e 100 mA for the phase plate with the tapered pole piece and 66 mA for the phase plate with the lamella-shaped pole piece. Depending on its size, an impinging electron beam can accumulate a phase shift of several thousand π by the interaction with the tapered pole's magnetic field and a corresponding OAM. The corresponding phase shift for the lamella-shaped pole are several hundred π. The projected magnetic fields were smoothed with a Gaussian filter (σ of one pixel) before the numerical integration, and interpolated subsequently. The bending of the phase contours near the poles can be attributed to the filtering. An offset in the projected fields of 20 Tnm for $B_\perp$ and of 50 Tnm for B_a was applied in Fig. 21a and an offset of 30 Tnm for $B_\perp$ and of 300 Tnm for B_a in Fig. 21b.

4.1.2 Vortex Beam Characteristics

In order to evaluate the characteristics of the electron vortex beam generated by the two different taper geometries, data series at varying excitation currents and defoci were acquired. To that end the EVB phase plate was illuminated with a parallel electron beam and the corresponding diffraction disks were recorded in the far field of the phase plate. Defocusing of the EVB was accomplished by altering the excitation of the intermediate diffraction lens, which was calibrated using the diffracted parallel beam without the EVB phase plate. The far field beam intensities for a set of different defoci and currents through the micro coils are given in Fig. 22 and Fig. 23. Images at different defocus values show the propagation of the electron vortex beam. A variety of different electron beam intensity patterns can be obtained by changing the defocus and current through the micro coils. A clear rotation is visible, which also indicates the variation of OAM of the produced vortex beam. Two parts with vanishing electron probability density are present in the images, the vortex core where the phase singularity appears, and additionally the region where the tapered micro wire blocks the beam, giving rise to a peculiar intensity distribution.

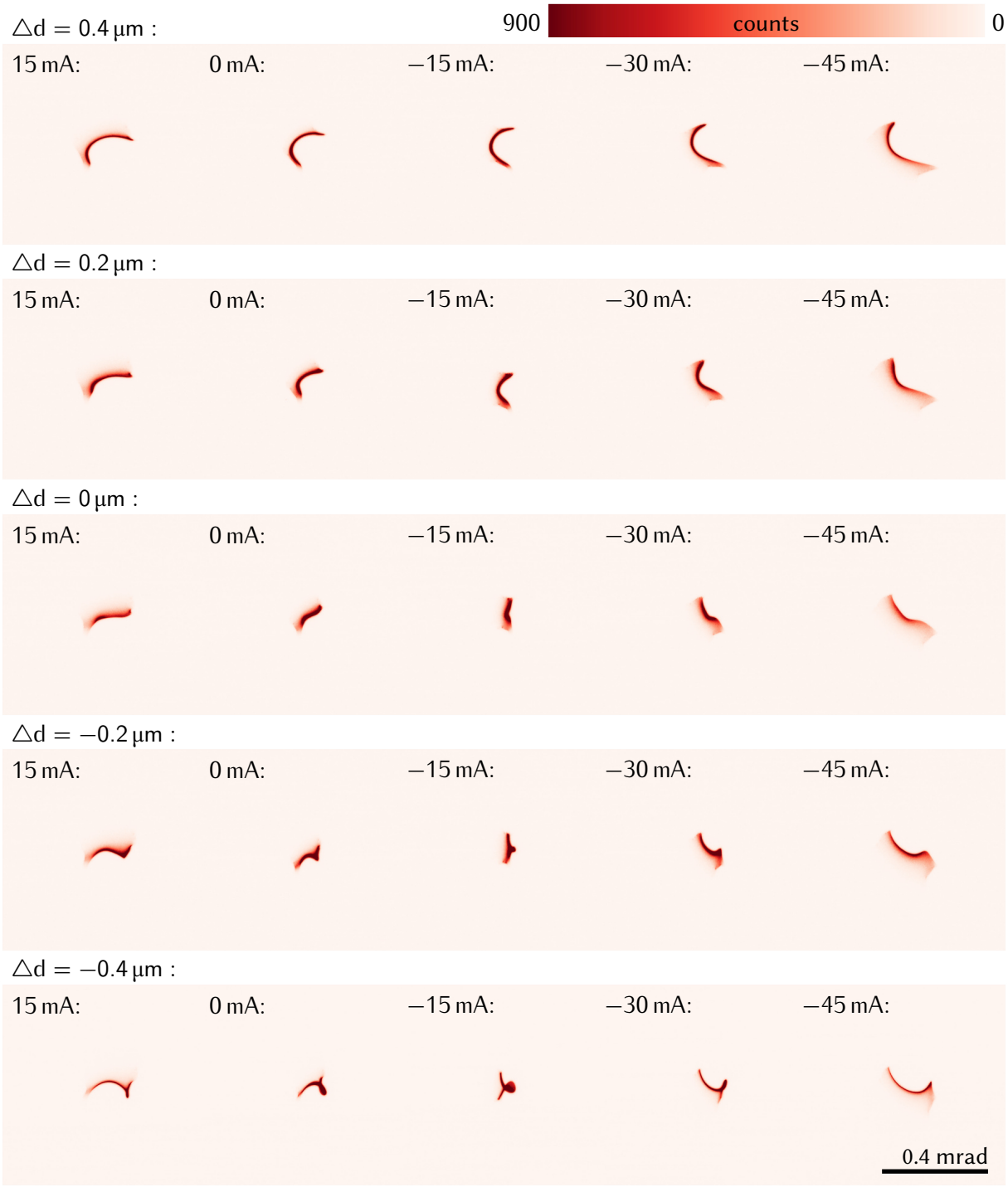

Figure 22: Electron vortex beams produced by the self-assembled micro coil device with a tapered pole piece, recorded in the far field of the object plane, for a set of different stimulation currents and indicated defoci △d.

Some deviations with respect to simulations of EVBs produced by magnetic needles (c.f. [96]) are present in the data sets. These deviations may be attributed to charging of the remaining Pyrex coating, as simulated in [198] as well as non-zero magnetic fields $B_\perp$ emanating from the tip perpendicular to the axial direction (c.f. Fig. 18 and Fig. 19). Note that charging effects are assumed to be more pronounced in these experiments employing a broad parallel illumination, as compared to the DPC scan with a focused electron beam.

Figure 23: Electron vortex beams produced by the self-assembled micro coil device with a plane-parallel structured pole piece, recorded in the far field of the object plane, for a set of different stimulation currents and indicated defoci △d. Note that at about 36 mA the projected magnetic field and hence the OAM nearly vanishes (c.f. Fig. (19)).

The contribution of the electrostatic charging to the far field beam profile could additionally be reduced by coating the micro wire with an electrically conducting layer subsequent to the FIB milling. Note, that the aforementioned imperfections of the vortex beams are more pronounced in beams produced by the phase plate with the tapered pole, compared to the ones produced by the lamella-shaped pole piece.

Some applications of large OAM electron vortex beams in literature such as rotation of metallic nanoparticles [199], measuring of in-plane magnetic fields in a TEM [200, 201, 202] or electron optical tweezers [203] may be rather difficult to accomplish with EVBs produced by this type of phase plate, due to the imperfect shape of the produced EVB. The strong deviations from an ideal vortex beam shape and the large OAM combined with a low purity of the quantum state, also renders the fabricated phase plate unsuitable to create EVBs for EMCD measurements. The unprecedented large OAM of the EVBs produced with this type of devices may, however, outweigh the special shape of the EVB for certain applications. These applications include the determination of longitudinal magnetic fields through the measurement of the Zeeman splitting of an EVB [202], or the probing of electrical fields via the deflection of an EVB through the orbital spin Hall effect [139]. The Zeeman splitting is linearly scaling with the beam's OAM, hence a superior signal-to-noise ratio (SNR) is expected for large OAM beams, if the difficulties originating from non-purity of the OAM quantum states could be overcome.

4.2 Miniaturized Deflector

Deflectors are essential optical elements in almost any CPO system. In circular particle accelerators and colliders beam, bending elements are indispensable to keep the particle beam on the desired trajectory. In straight CPO systems deflectors are essential for the mutual alignment of adjacent optical elements. Deflecting elements are also used to create electromagnetic synchrotron radiation from charged particle beams in wigglers, undulators or free electron lasers. Additionally, many specialized routines in design, tuning and maintenance of CPO systems rely on deflecting elements, such as aberration determination and correction in electron microscopes. Scan units, fundamental for any kind of scanning charged particle beam technique, are essentially also deflectors, which can operate very fast and precise. The attainable scan speed is merely limited by the electronic high-frequency (HF) passband of the deflecting element, and the corresponding circuitry and connectors. The greatest advantage of miniaturization of deflection elements driven by electromagnets lies in the corresponding linear scaling of their inductance [38], facilitating the transmission of HF signals.

The miniaturized charged particle deflectors in this work are built in two different designs, i.e. a dipole deflector for 1D deflection and a vector magnet assembly with 4 poles for 2D deflection (c.f. Fig. 24 and Fig. 25).

The dipole design is based on the same planar structures as the electron vortex phase plate (c.f. Sec. 4.1), the only difference is that for the dipole deflector two soft magnetic poles were inserted in the two self-assembled coils next to the electron passage, instead of one. In the FIB treatment the pole faces were cut straight and polished afterwards, in order to have a smooth field distribution. SEM overview images of the manufactured miniaturized dipole and vector magnet charged particle deflectors are given in Fig. 26.

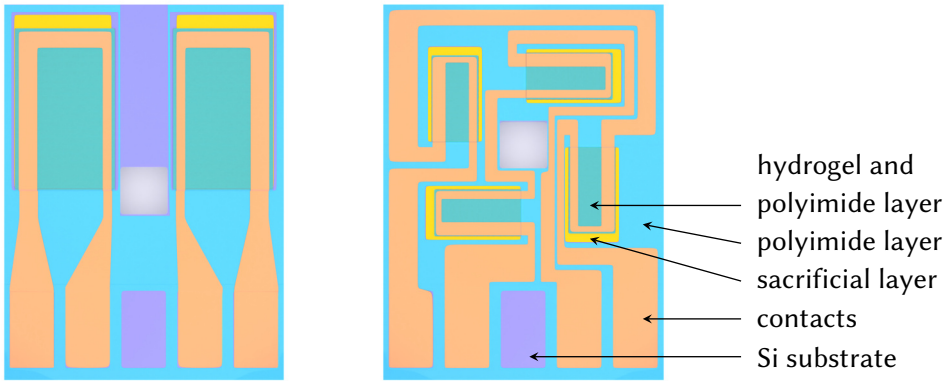

(a) dipole (b) vector magnet

Figure 24: Planar layout of the chips with the to-be-rolled micro coils in dipole and vector magnet configuration. The different layers have the same color coding as in Fig. 11. The dimensions of the different structures are not to scale, for better visibility.

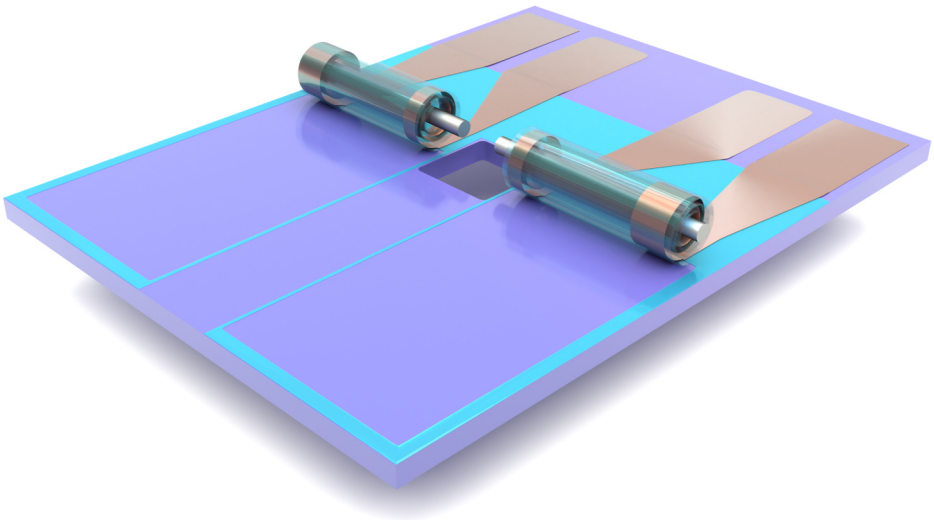

(a) dipole

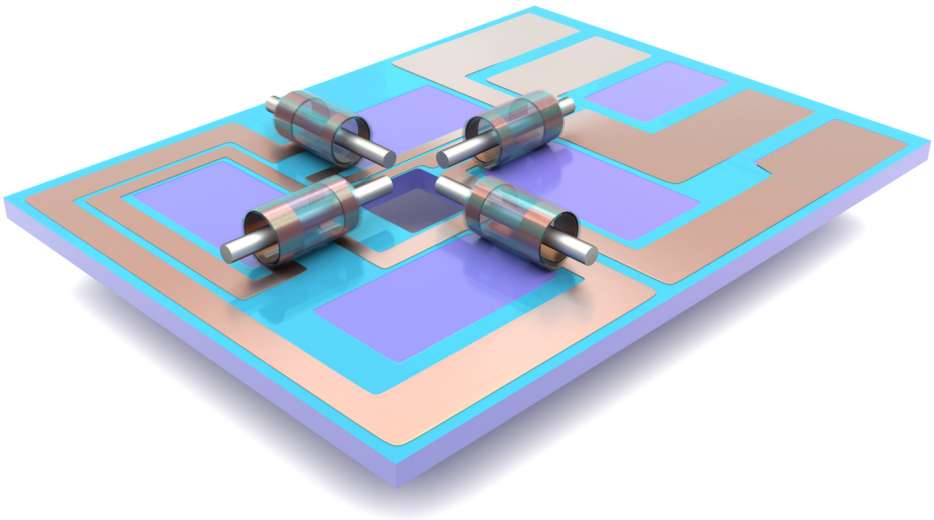

(b) vector magnet

Figure 25: 3D renderings of the chips with the self-assembled micro coils in dipole and vector magnet configuration. The different layers have the same color coding as in Fig. 11. The dimensions of the different structures are not to scale, for better visibility.

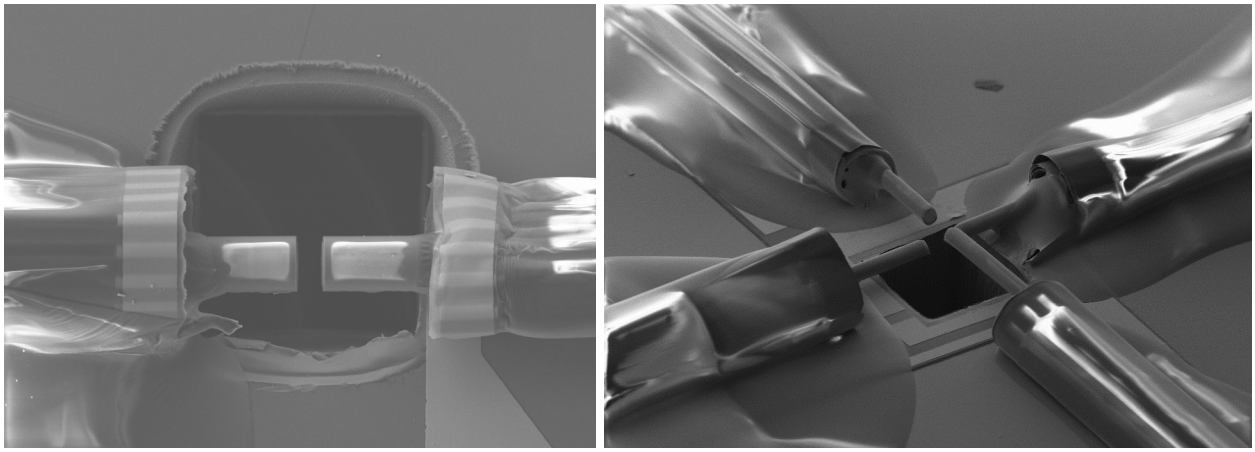

(a) dipole (b) vector magnet

Figure 26: SEM overview images of the produced magnetic deflectors driven by self-assembled micro coils with FIB structured soft ferromagnetic micro wire pole pieces. The dipolar 1D deflector is given in (a), the four pole 2D deflector in (b)

For the vector magnet assembly slightly different planar structures were used in order to fit four self-assembled coil pairs onto one chip that complies to the spatial dimension boundaries of the *Protochips* Fusion Select platform that is used for the electron optical characterization of the miniaturized deflection elements within an *FEI* Titan^3 TEM. The reduced planar space per coil pair causes a reduced winding number for each coil, leading to an overall reduction in the attainable magnetic field per current. The maximum current specification for this holder is 100 mA DC. This explains the larger attainable deflection for the dipolar design. Note, however, that these restrictions can be lifted if the manufacturing process is adjusted slightly by expanding the planar to-be-rolled structures outside the 4 x 6 mm boundaries from the chips. The fit to the *Protochips* Fusion Select platform can still be ensured by dicing the chips subsequent to the rolling process.

DPC Maps

The first order Gaussian optical characteristics (c.f. Sec. 2.2) of the dipole assembly can completely be determined by means of DPC measurements. The most important quantity of interest for a deflector is the attainable deflection for different excitation currents and beam positions within the soft magnetic micro wire pole piece gap. It can be directly obtained by several DPC scans over the pole area for different applied currents, as the shift of the COM of an electron diffraction disc $\mathbf{d}$ allows the direct computation of the deflection angle ϑ if the effective camera length L is known:

$$\vartheta = \arctan\left(\frac{\mathbf{d}}{L}\right). \tag{4.21}$$

Additionally, the projected magnetic field is obtained through the following relation:

$$\vartheta = \arctan\left(\frac{\mathbf{d}}{L}\right) \approx \frac{1}{p_z}\mathbf{e}_z \times e\mathbf{B}_{\text{proj}}\,. \tag{4.22}$$

The in-plane components of the magnetic field can be calculated from the projected field, if some field distribution is assumed. In the sharp cutoff approximation the in-plane magnetic field **B** is given by $\mathbf{B}t \approx \mathbf{B}_{\mathrm{proj}}$, with the micro wire thickness t. The corresponding DPC maps for a current series from 0 mA to 100 mA to -100 mA and back to 0 mA in 50 mA steps are depicted in Fig. 27. The experimental parameters are the same as for the DPC measurements of the produced electron vortex phase plate (c.f. Sec. 4.1.1). Fig. 28 shows reconstructed projected magnetic fields of the same sample as in Fig. 27 at higher spatial resolution for the maximum excitation current $I_{\mathrm{max}} = \pm 100\,\mathrm{mA}$, which is the maximum DC current permitted by the *Protochips* Fusion Select TEM specimen holder.

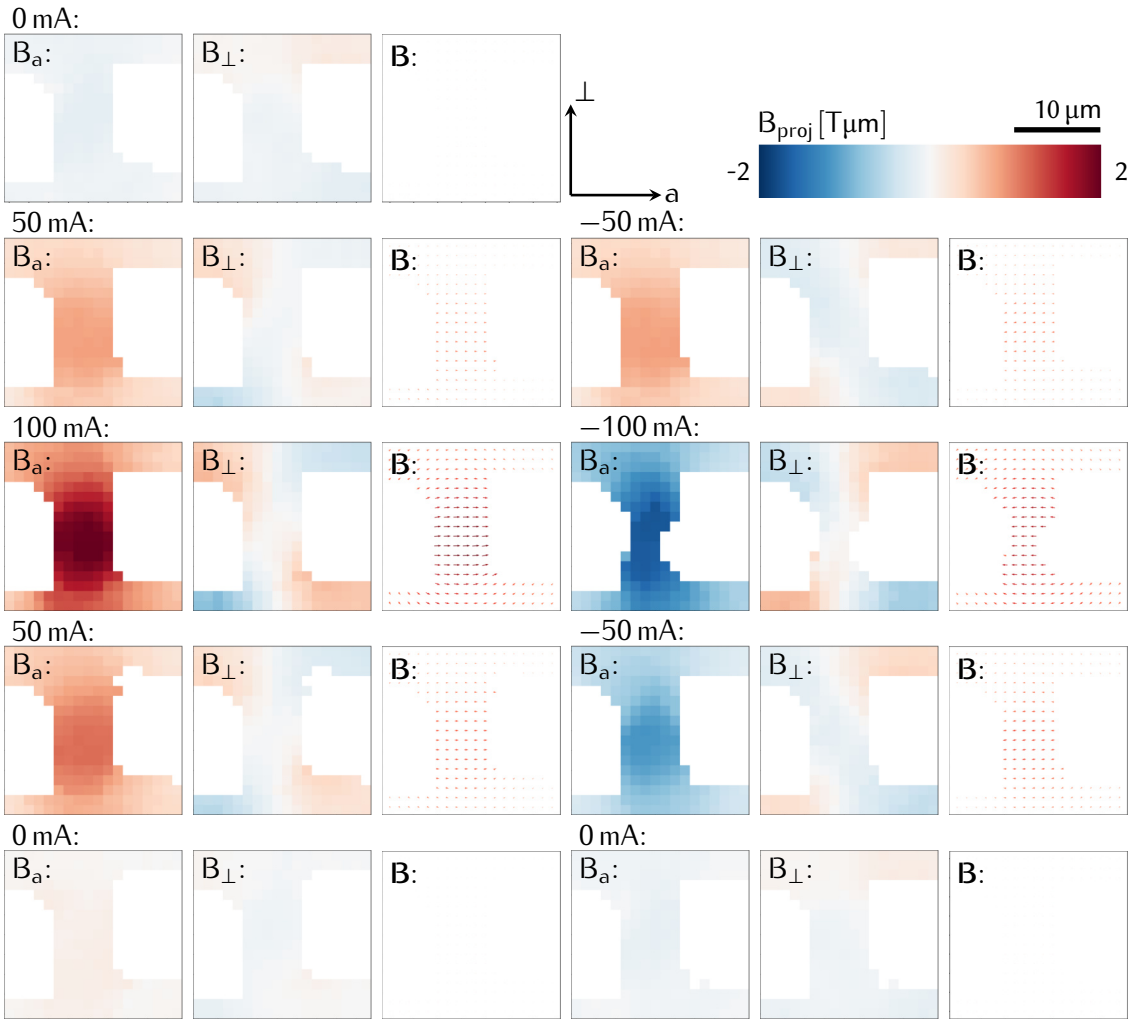

Figure 27: Reconstructed magnetic fields $\mathbf{B}_{\mathrm{proj}}$ of a miniaturized dipole assembly, driven by self- assembled micro coils, for different excitation currents and incidence positions. The reconstructed axial magnetic fields $B_{a,\mathrm{proj}}$ are shown in (a), the fields in the direction perpendicular to the coil axis $B_{\perp,\mathrm{proj}}$ in (b). Both components of $\mathbf{B}_{\mathrm{proj}}$ are additionally given as a quiver plot in (c). The used micro wire has a total diameter of about 25 µm with a magnetic core of about 20 µm, which was used for the estimation of the in-plane components of the magnetic field **B** from the measured projected field in sharp cut off approximation. The DPC scans were acquired in the following order: From top left to bottom left, and subsequently from top right to bottom right.

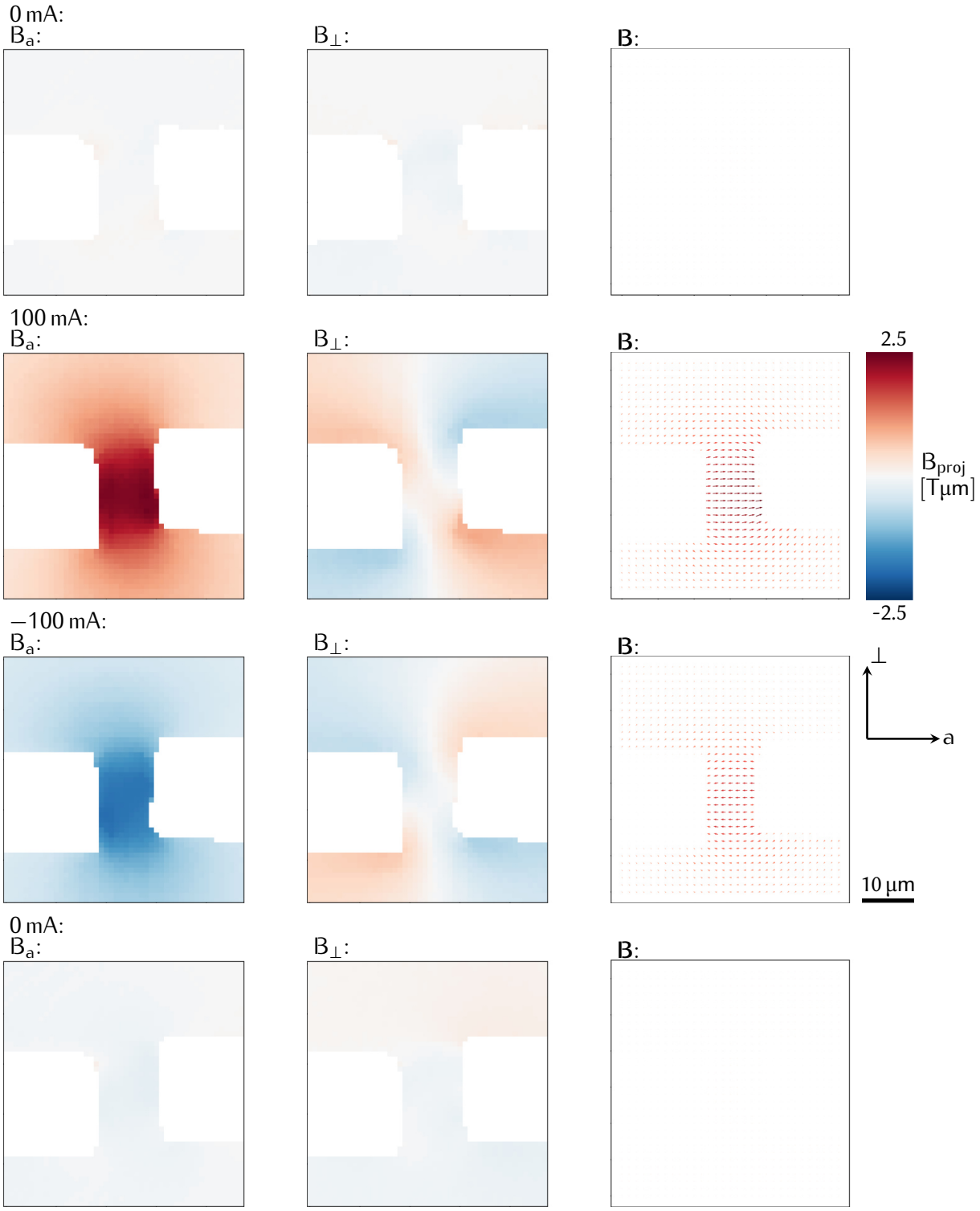

Figure 28: Reconstructed magnetic fields $\mathbf{B}_{proj}$ attainable with a miniaturized dipole assembly for $I_{max} = \pm 100$ mA excitation current, the incidence positions are better resolved in this experiment as compared to the one shown in Fig. 27, while the other experimental parameters and the sample are identical. The DPC scans were acquired from top to bottom.

The DPC data (Fig. 27 and Fig. 28) shows that the maximum deflection angle perpendicular to the coil axis

$$\vartheta_\perp \approx \frac{eB_a}{p_z}\,, \tag{4.23}$$

ranges from -1.04 mrad at 100 mA to 0.64 mrad at -100 mA, in the middle of the poles. The corresponding projected magnetic fields $\mathbf{B}_{proj}$ are between -2.20 Tµm for 100 mA and 1.51 Tµm for -100 mA. The according in-plane axial magnetic field B_a in sharp cutoff approximation is ranging from -110 mT at 100 mA to 76 mT at -100 mA, for a diameter of the magnetic core of about 20 µm.

Hysteresis in the Magnetic Polarization

In addition to the spatially resolved maps, the DPC data can also be evaluated to illustrate the hysteresis in the magnetic polarization process. To that end, the central part of another DPC scan with fewer scan points, is averaged over 2x3 centrally located reconstructed pixels (approximately 9.5 µm x 14.2 µm in real space), the result is shown in Fig. 29.

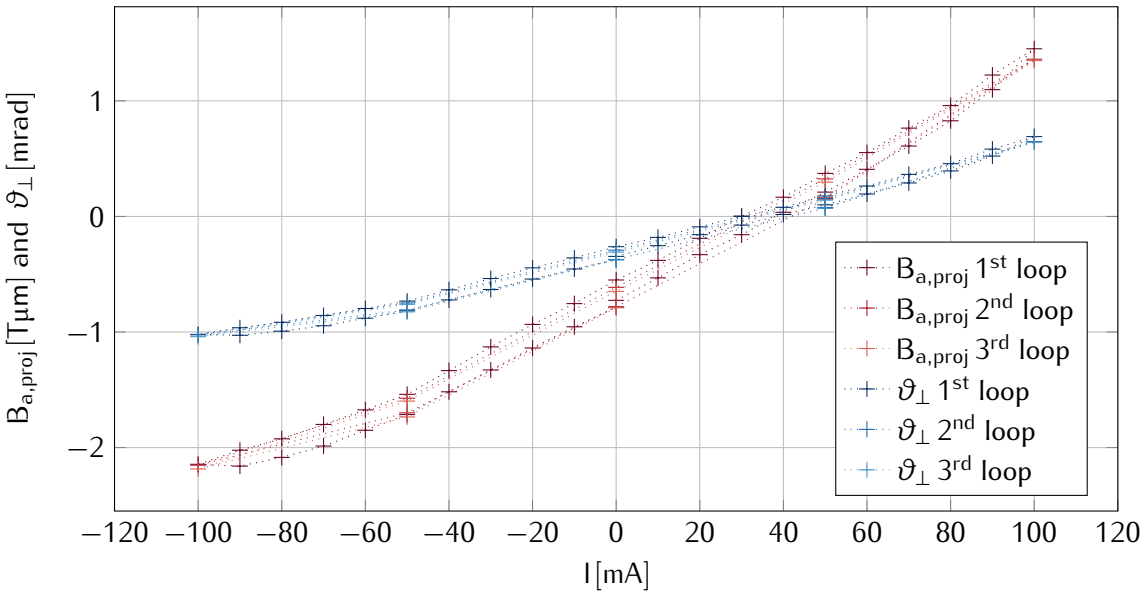

Figure 29: Hysteresis measurement of the dipole assembly, reconstructed from a series of COM DPC measurements for varying excitation currents, locally averaged over six scanning positions. The action of the dipole is given by means of deflection perpendicular to the coil axis $\vartheta_\perp$, as well as by the corresponding projected field $B_{a,proj}$.

The hysteresis measurements of the attainable deflection perpendicular to the coil axis $\vartheta_\perp$ (and accordingly the respective projected magnetic fields $B_{a,proj}$) for different excitation currents I exhibits negligible nonlinearities and deviations between the different loops. There is, however, a clearly visible remanent projected field (c.f. Figs 27 and 28) of about 0.7 Tµm. The corresponding bias is reached at about 30 mA - 40 mA excitation of the micro coils. This behavior has been already reported in literature, for the same

type of wires, although to a far smaller extent [204] and for similar wires made out of a magnetic FeCrSiB alloy [205]. The exaggeration of the remanent field as compared to [204] may be attributed to the different wire geometry, inhomogeneities in the external magnetic field and in the magnetic material within the wire, surface irregularities from the FIB processing or asymmetries in the self-assembled micro coils.

Wire Thickness Effects

As the soft magnetic behavior of the FeCoSiB micro wires is caused by the magnetostriction induced by their Pyrex shell, wires of different thickness exhibit different magnetization properties. Most experiments were conducted with wires of a total diameter of 25.4 µm and a 20.1 µm magnetic core diameter, respectively. Wires with total diameters of 50 µm and 86 µm, and corresponding core diameters of 41.1 µm and 72.8 µm, respectively, are analyzed in this paragraph. For the determination of the magnetic properties of the µCPOs with different wire diameters, DPC measurements with the same optical setup as for Figs. 27 - 29 were conducted. The reconstructed projected magnetic fields, as measured by COM DPC, are shown in Fig. 30 and Fig. 31, for the µCPOs with 50 µm and 86 µm wires[29], respectively. The comparison between the 25 µm and 50 µm wires shows an almost linear relation between wire diameter and projected fields at -50 mA coil excitation, from 1.6 Tµm to about 3.8 Tµm[30], respectively. An additional increase in diameter to 86 µm is not altering the projected field significantly in our measurements, the attained projected field values were about 3.6 Tµm[31] in the center between the poles. The corresponding magnetic flux densities in sharp cutoff approximation, are similar for the 25 µm and 50 µm wires at a value of about 80 mT and 92 mT, respectively, and smaller for the 86 µm micro wire at about 49 mT.

It is important to mention, however, that the measured values are already at the detection limit of the COM DPC method in the used *FEI* Titan^3, when employing an operation mode with magnetic field-free sample plane (objective lens switched off). The maximal detectable projected field could be increased by reducing the effective camera length, which is at this microscope only possible by exciting the objective lens or by setting up a special mode for the imaging corrector. The excitation of the objective lens would lead to a strong external magnetic field in the specimen area (of about 2 T in the conventional operation mode), perturbing the magnetic configuration of the µCPOs.

[29] The lower edge of these scans is white, because the total intensity in the diffraction disks is below the threshold masking value, due to the diffraction disk leaving the detector. This is not caused by the deflection by the micro coil assembly, but due to imperfect descan correction, which has a greater effect at larger fields of view.

[30] Note that the maximum detectable projected magnetic field of about ±2 Tµm (see Sec. 4.1.1 for the derivation) is by far exceeded in this measurement for the -50 mA coil excitation. The mentioned value was calculated by a single measurement were the offset to the reference scan was measured separately, allowing larger $\mathbf{B}_{\mathrm{proj,max}}$ values to be determined.

[31] This value also exceeds the detectable ±2 Tµm margin in this microscope setup by far. For the computation of the mentioned value (-50 mA in Fig. 31) the beam was shifted off center to compensate for the larger deflection, effectively shifting the measurement range to about -4 Tµm - 0 Tµm. For this offset an additional shifted reference scan was acquired and subsequently subtracted.

The magnetization at a positive coil excitation currents exhibits a different behavior compared to the 25 µm wires. Here, the bias was reached between 30 mA and 40 mA, while excitation currents of almost 100 mA and far beyond 50 mA were necessary to polarize the 50 µm and 86 µm micro wires, respectively. The remanent fields for the 50 µm and 86 µm poles both range slightly below the 2 Tµm margin. For the 25 µm micro wires the remanent field stays well below 0.8 Tµm, rendering these wires better suited for most µCPO applications, although the projected fields are not the largest attainable ones.

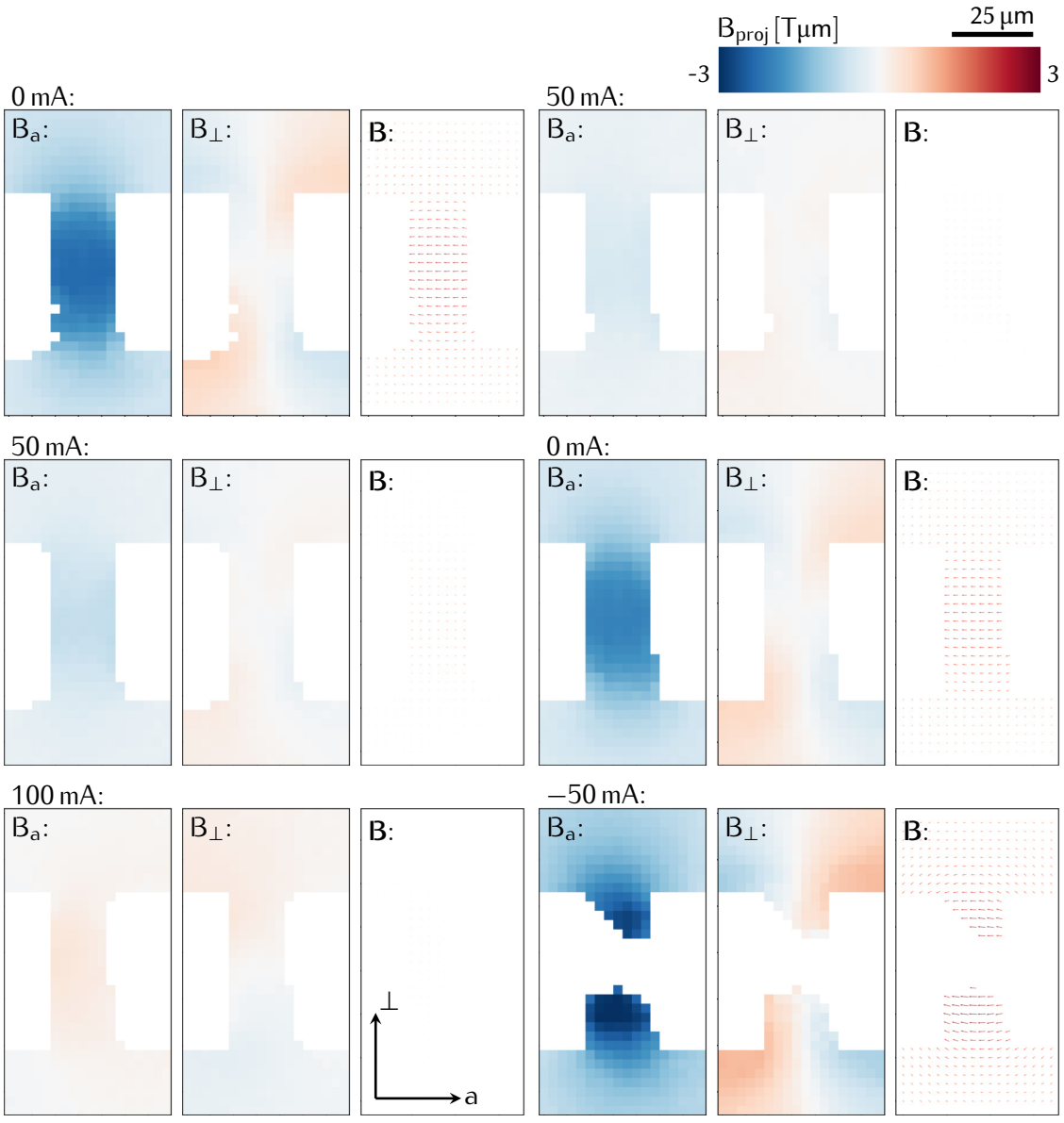

Figure 30: COM DPC measurements of a µCPO device with micro wires of 50 µm diameter as pole pieces for varying excitation currents. Note that the maximum detectable projected magnetic field of about ±2 Tµm (see Sec. 4.1.1 for the derivation) is by far exceeded in this measurement for the -50 mA coil excitation. The scan positions where the measurement range is exceeded are displayed white (like the pole pieces) as there the total intensity threshold value in the diffraction disks was not reached. The DPC scans were acquired in the following order: From top left to bottom left, and subsequently from top right to bottom right.

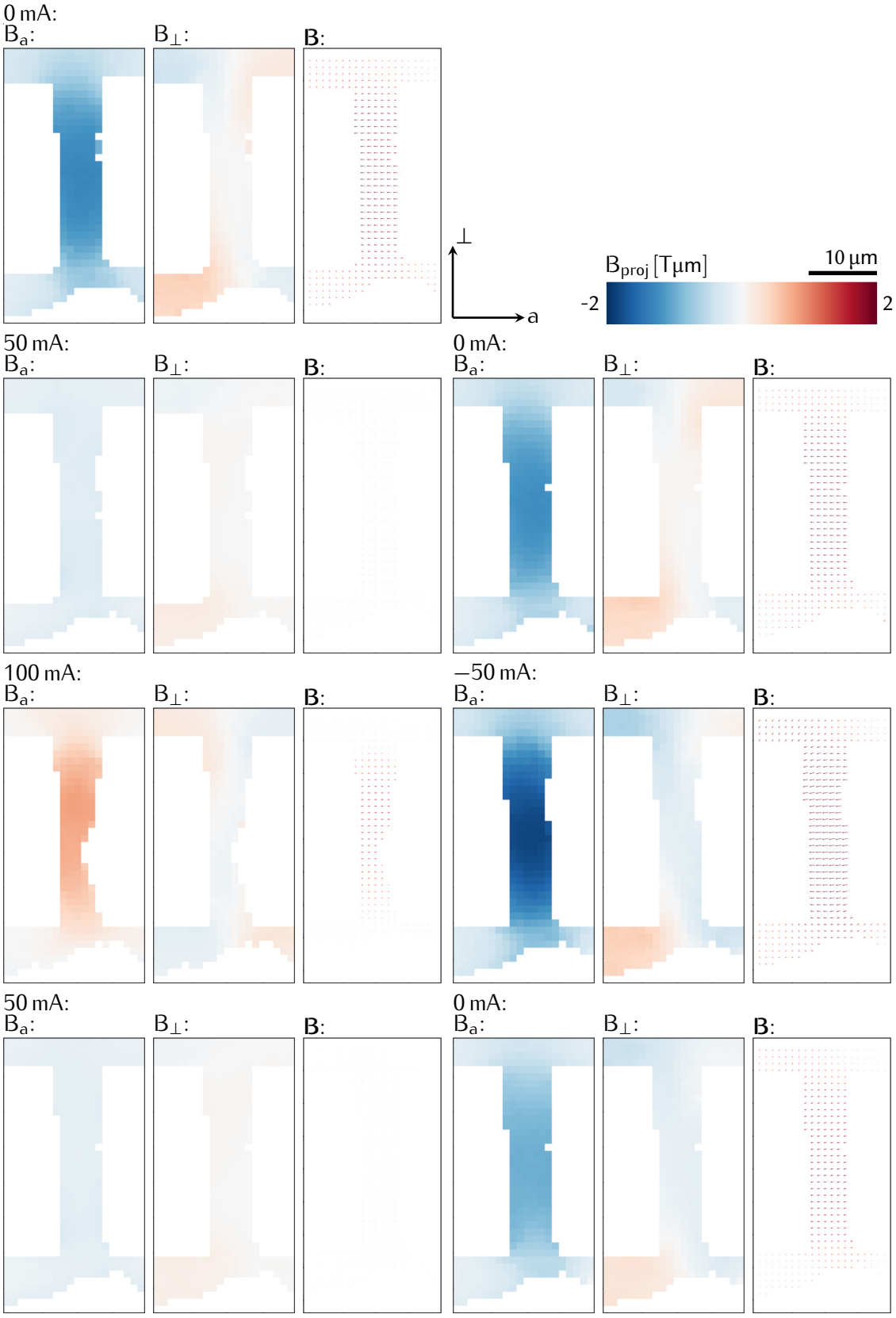

Figure 31: COM DPC measurements of a μCPO device with 80 μm micro wires as pole pieces for varying excitation currents. Note that the maximum detectable projected magnetic field of about ±2 Tμm (see Sec. 4.1.1 for the derivation) is by far exceeded in this measurement for the -50 mA coil excitation. For this reason, the diffraction disk was additionally shifted at -50 mA by using the diffraction alignment coils of the microscope. The thereby introduced offset was corrected by acquiring another reference scan that was subsequently subtracted. This shift technique essentially moves the measurement range from about -2 - 2 Tμm to about -4 - 0 Tμm. The DPC scans were acquired in the following order: From top left to bottom left, and subsequently from top right to bottom right.

4.3 Quadrupole Focusing Optic

Magnetic quadrupole lenses exhibit a very promising scaling behavior with respect to their focal length upon isotropic miniaturization (c.f. Sec. 2.4.3) and additionally possess the strong focusing characteristic, rendering them ideal for miniaturization of CPOs for fast charged particles. The miniaturized magnetic quadrupole lenses in this work share the polymeric platform with the aforementioned four pole deflectors. The only difference is that the conduction paths are modified (c.f. Fig. 32), because an antiparallel field direction is required for opposing coils as compared to the parallel one for the deflectors. As the *Protochips* Fusion Select has just four electrical contacts, the four coils cannot be excited individually, but only in pairs. For that reason, the conduction paths must be modified as compared to the four pole deflector (c.f. Fig. 32 and Fig. 33).

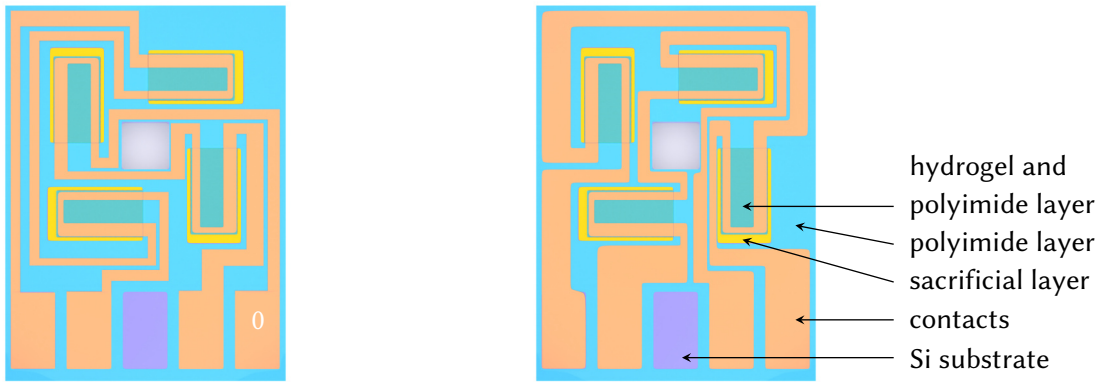

(a) quadrupole (b) vector magnet

Figure 32: Planar layout of the chips with the to-be-rolled micro coils in quadrupole and vector magnet configuration. The different layers have the same color coding as in Fig. 11. The dimensions of the different structures are not to scale, for better visibility.

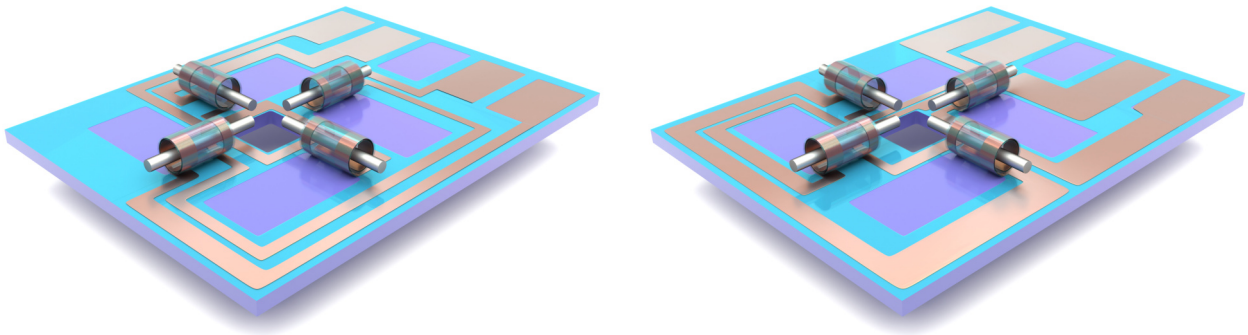

(a) quadrupole (b) vector magnet

Figure 33: 3D renderings of the chips with the self-assembled micro coils in vector magnet and quadrupole configuration. The different layers have the same color coding as in Fig. 11. The dimensions of the different structures are not to scale, for better visibility.

The focusing characteristics and the optical power of a magnetic quadrupole (Eq. (2.141), see Eq. (2.51) and above for the derivation):

$$\frac{1}{f_{qp}} = \frac{2qB_{0,proj}}{amv_z} \tag{4.24}$$

is assessed by three different means:

(i) DPC deflection measurements from which $\nabla B_{0,proj} = {}^{2B_{0,proj}}/_{a}$ (c.f. Eq. (2.43)) can be determined directly by taking the numerical derivative.

(ii) The ray optical analysis of the beam focused in the Fourier plane of the excited quadrupole.

(iii) From the deformation of the intensity distribution in the Fourier plane of the main imaging lens.

Position dependent deviations from the first order Gaussian trajectories could also be analyzed from the DPC data, but this is beyond the scope of this thesis. Higher order incidence angle dependent aberrations could in principle also be obtained from DPC measurements with a pixelated detector, here the whole intensity distribution needs to be evaluated, not just the intensity's COM. In the current experimental setup with semi-convergence angles in the 100 µrad range, however, the precise determination of the aberrations may ultimately run into SNR issues. Off-axial aberrations could be determined by an analysis of the projected fields at some distance to the optical axis, most straight forward by a multipolar expansion and a subsequent fitting to suitable aberration functions.
As the aberrations of the individual elements determine the important specifications of a CPO system, it is a crucial point for the further development of the µCPO elements to assess and minimize them. The first routes for a minimization of the aberrations would be to improve fabrication techniques to reduce the parasitic aberrations from misalignment of the pole pieces. Additionally, milling the pole piece surfaces to a more elaborated shape that produces an ideal hyperbolic field distribution in projection [206] would help to reduce aberrations. Currently, the pole pieces are milled to a planar shape in the FIB, which yields a projected field at the pole piece surface of the form:

$$B_{a,proj} = \int_{-\sqrt{r^2-r_\perp^2}}^{+\sqrt{r^2-r_\perp^2}} B_{a,0}\,dz = 2B_{a,0}\sqrt{r^2 - r_\perp^2}, \tag{4.25}$$

if a uniform magnetization of maximal value $B_{a,0}$ is assumed, with r being the diameter of the soft magnetic material in the micro wire and the distance to the wire in the direction perpendicular to the wire axis $r_\perp$. This projected field distribution is already a very similar to the projected field distribution from an ideal hyperbolic pole piece (c.f. Fig. 34).
SEM overview images of the produced quadrupole assemblies are given in Fig. 35. Note the misalignment of the poles along the optical axis, which is stemming from the manual insertion of the poles as two complete wires, which are subsequently milled in the FIB. The assessment of the parasitic aberrations stemming from this misalignment needs further investigation. In principle the wires could also be inserted one by one with intermediate FIB milling, to minimize the misalignment along the optical axis, which would, however, add another step to the fabrication process.

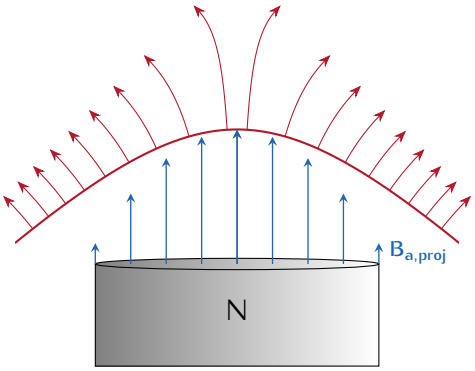

Figure 34: Two-dimensional projected field distribution B_{ideal} of one pole in an ideal magnetic quadrupole with a hyperbolic pole piece (depicted in red) and the projected field distribution $B_{a,proj}$ of a homogeneously magnetized wire (depicted in blue).

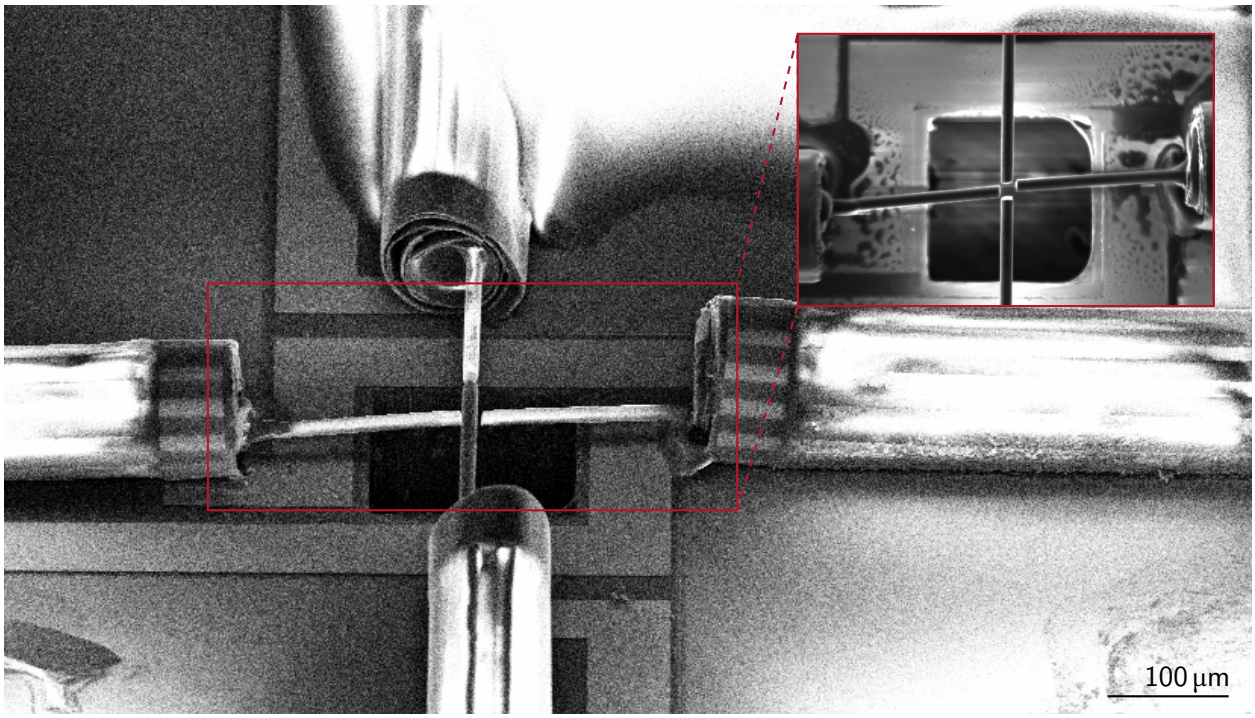

Figure 35: SEM overview images of the produced magnetic quadrupole lenses driven by self-assembled micro coils with FIB structured soft ferromagnetic micro wire pole pieces.

DPC Maps

COM DPC measurements allow the direct computation of the first order Gaussian characteristics of the miniaturized quadrupoles for different currents applied to the self-assembled micro coils. The experimental setup for the acquisition of the DPC maps of the miniaturized quadrupole assembly is the same as for the single pole and dipole ones: The chip containing the micro coils and milled micro wires is placed in the specimen plane of a *FEI* Titan^3 TEM using a *Protochips* Fusion Select biasing holder. The microscope is operated in a low magnification mode with the objective lens switched off to ensure magnetic field free conditions. The electron beam is scanned over a sample region of about 75 µm x 75 µm with a convergence

angle of about 230 µrad. A reference scan without sample was acquired to correct for additional deflection from the non-ideally pivotized scan unit. The effective electron optical camera length was 13.2 m ± 0.8 m and the far field diffraction disks were recorded with a *Gatan* Ultrascan 1000 CCD camera with a 14 µm pixel pitch. Soft magnetic micro wires with an external diameter of 25 µm and a core diameter of 20 µm were used, because the measurements on the dipoles suggested these wires as the most promising candidates (c.f. Sec. 4.2). The DPC measurements were conducted for 0 mA, 50 mA and -50 mA, the reconstructed projected fields are shown in Fig 36.

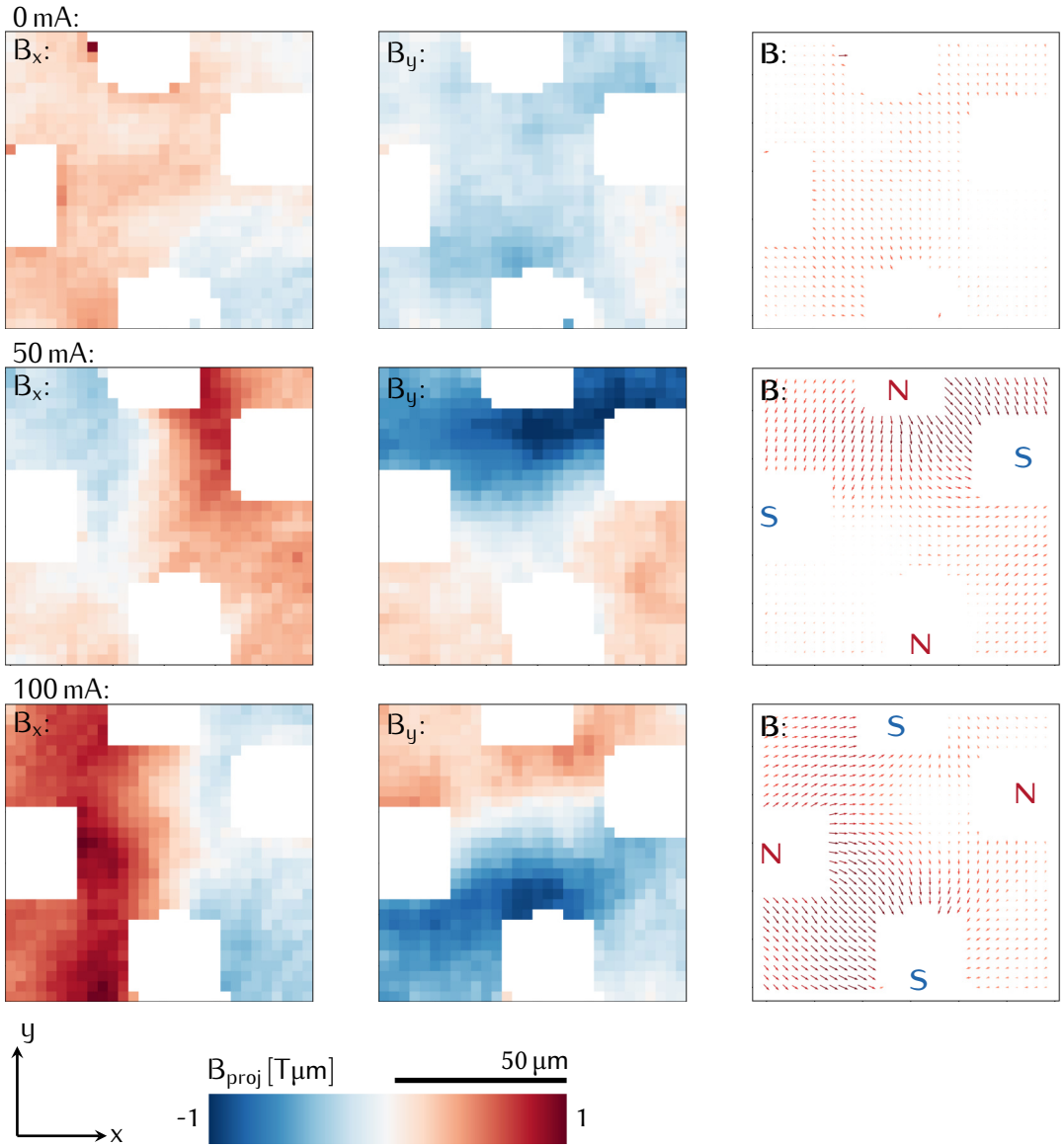

Figure 36: Projected magnetic fields within a miniaturized magnetic quadrupole lens, without an applied current (1st row) and with 50 mA (2nd row) and -50 mA (3rd row) applied current through the self-assembled micro coils. The soft magnetic pole pieces are not electron transparent, consequently they are displayed as white overlay according to a threshold in the overall intensity in the diffraction disks. The two components of the projected magnetic fields are shown separately (1st and 2nd column) and combined as a quiver plot (3rd column).

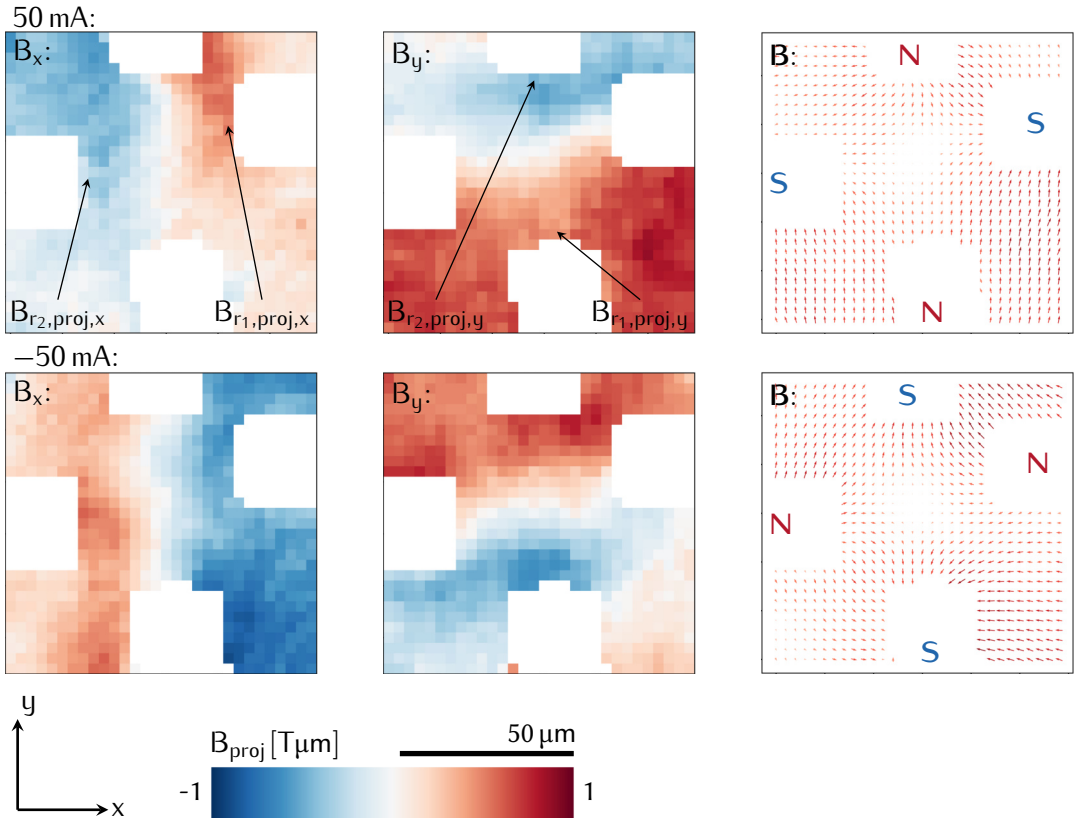

Figure 37: Projected magnetic fields within a miniaturized magnetic quadrupole lens at 50 mA (1st row) and -50 mA (2nd row) applied current. The two components of the projected magnetic fields are shown separately (1st and 2nd column) and combined as a vector plot (3rd column). The projected fields in this figure are corrected and offset of -0.2 Tμm in x-direction and 0.5 Tμm in y-direction for 50 mA, and -0.4 Tμm in the x-direction and 0.3 Tμm for -50 mA.

The different distances of the pole ends to the respective coil are causing an asymmetry in the projected fields. The first order in an aberration series expansion is a linear offset in the projected magnetic field in some direction that just acts as an additional deflection, which may be corrected numerically. Note, that the projected field in the non-excited state is less strong than for the dipole and single pole devices, which may be attributed to differences in the soft magnetic micro wires, or to the interaction of the different poles. Fig. 37 shows the DPC measurements in the relevant region between the poles with a linear offset correction of -0.2 Tμm in x-direction and 0.5 Tμm in y-direction for 50 mA, and -0.4 Tμm in the x-direction and 0.3 Tμm in the y-direction for -50 mA. Considering these values, the hysteresis bias of this assembly is roughly one half of that of the dipole employing similar wires (see Fig. 27 and Fig. 29).The optical power (Eq. (2.141)) of the miniaturized quadrupoles can be calculated from the reconstructed projected fields from two opposing points close to the poles $B_{r_1,proj}$ and $B_{r_2,proj}$ at a distance a, according to:

$$\frac{1}{f_{qp}} = \frac{2q\left(B_{r_1,proj} - B_{r_2,proj}\right)}{amv_z}. \tag{4.26}$$

The corresponding focal lengths are approximately 6.5 cm for a pole piece gap of 50 μm, 300 kV electrons and $B_{r_1,proj,y}$ and $B_{r_2,proj,y}$ in the 0.4 Tμm region for the y-direction. The corresponding projected fields in x-direction $B_{r_1,proj,x}$ and $B_{r_2,proj,x}$ are slightly smaller at about 0.3 Tμm, as is the pole piece gap with 43 μm. The according focal length is about 7.5 cm. The corresponding quadrupole strength ∇B_0 is 800 $^{T}/_{\mu m}$ and 700 $^{T}/_{\mu m}$, respectively, in sharp cutoff approximation.

The lowest attainable foci within the DPC data are in the 6 cm region, here evaluation points closer to the optical axis are chosen, which reduces a as well as $B_{r_1,proj}$ and $B_{r_2,proj}$. Variations of the focal length at different distances to the optical axis indicate the presence of non-negligible aberrations. It may, however, also be attributed to the limiting SNR in the DPC measurements. For that reason, additional measurements based on ray optical considerations were conducted.

Ray Optical Analysis of Far Field Diffraction Disks

The electron optical characteristics of the miniaturized quadrupole assembly can additionally be evaluated by analyzing the intensity distribution of an initially parallel electron beam in the far field behind the element. The Fourier plane of the quadrupole was imaged to that end, which was achieved by varying the excitation of the intermediate diffraction lens. In Fig. 38 a series of these far field diffraction pattern is shown for different coil currents, as well as a reference beam without quadrupole.

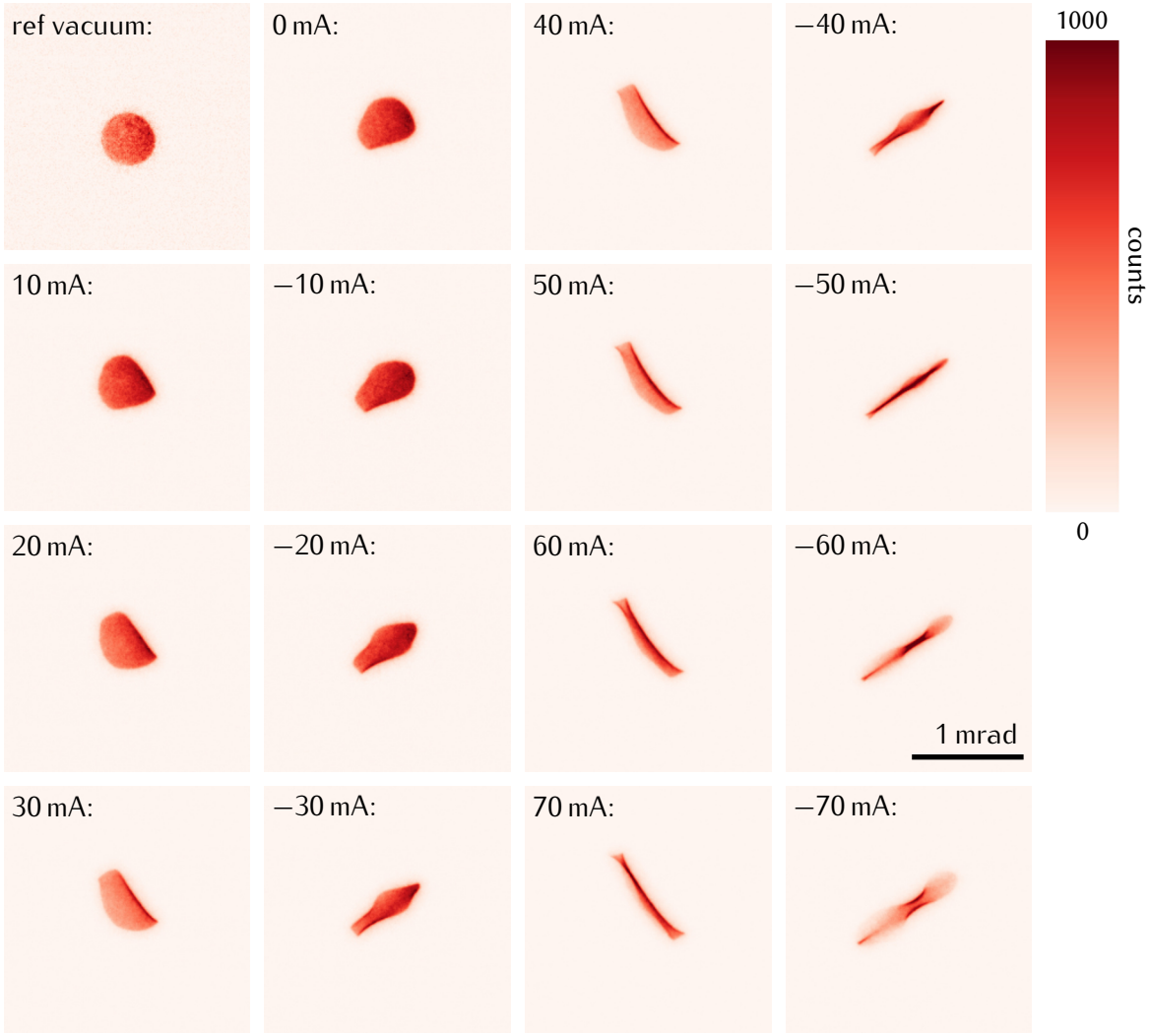

Figure 38: Stigmatic focusing of the electron beam in a TEM by the miniaturized quadrupole lens assembly. The electron beam intensity is recorded in the Fourier plane of the excited assembly. The intensity distribution is given for different excitation currents, as well as for the reference without the quadrupole inserted in the microscope.

Here, the stigmatic focusing characteristics in a plane inclined by 45° with respect to the pole-axes of the micro quadrupole are clearly obvious. The series shows that line foci in both directions can be generated, although a stronger excitation of 70 mA is needed in the negative current direction. The measurement additionally shows clear deviations from a perfect line focus, presumably stemming from parasitic aberrations due to the non-ideal alignment of the poles. The intensity profile of the unexcited quadrupole is also slightly distorted, as compared to the reference beam, due to the remanent fields that are also visible in the DPC measurements (c.f. Fig 37).

In addition to this analysis of the beam in the Fourier plane of the quadrupole the beam can be analyzed in a more quantitative way in the Fourier plane of the main imaging lens at a camera length L = 1.418 m ± 0.001 m. This plane was adjusted by focusing a parallel electron beam before inserting the quadrupole. The incident beam is now stigmatically focused by the quadrupole assembly. As the diameter of the illumination d_{ill}, and the size of the beam on the detector d_{det} can be measured directly[a], the focal length f of the quadrupole can be computed by ray optical considerations. To that end, the geometric intercept theorem is employed, the relations are illustrated in Fig. 39 and Fig. 40. Accordingly, the measured focal length is given by:

$$f_{qp,+} = \frac{d_{ill} L}{d_{det} + d_{ill}} \tag{4.27}$$

for the focusing direction (c.f. Fig 39) and by:

$$f_{qp,-} = \frac{d_{ill} L}{d_{det} - d_{ill}} \tag{4.28}$$

for the defocusing direction (c.f. Fig 40). The electron optical distance between the object plane and the detector L was determined beforehand by exploiting the known scattering angle in the Debye-Scherrer rings from electrons diffracted at a gold sample. Accordingly, an ellipse, whose the semi-major and semi-minor axes are swapped when in inverting the current, is expected for an aberration free quadrupole assembly in this measurement.

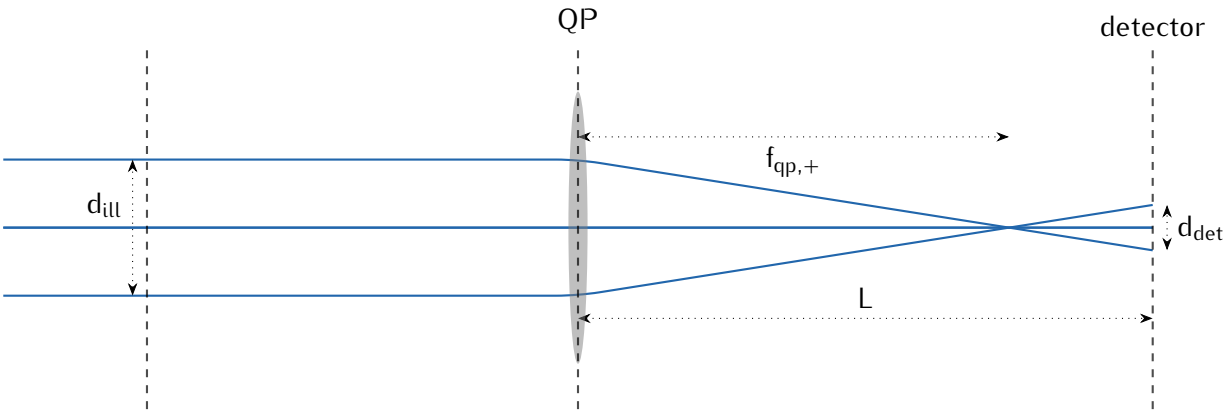

Figure 39: Geometrical relations for the ray optical analysis of the focal length of the self-assembled quadrupoles in focusing direction using the intercept theorem. An initially parallel electron beam of known radius is focused stigmatically by the quadrupole lens.

[a] for this routine the imaging mode needs to calibrated properly, which was checked with a standardized gold cross grating of 2160 $^{lines}/_{mm}$.

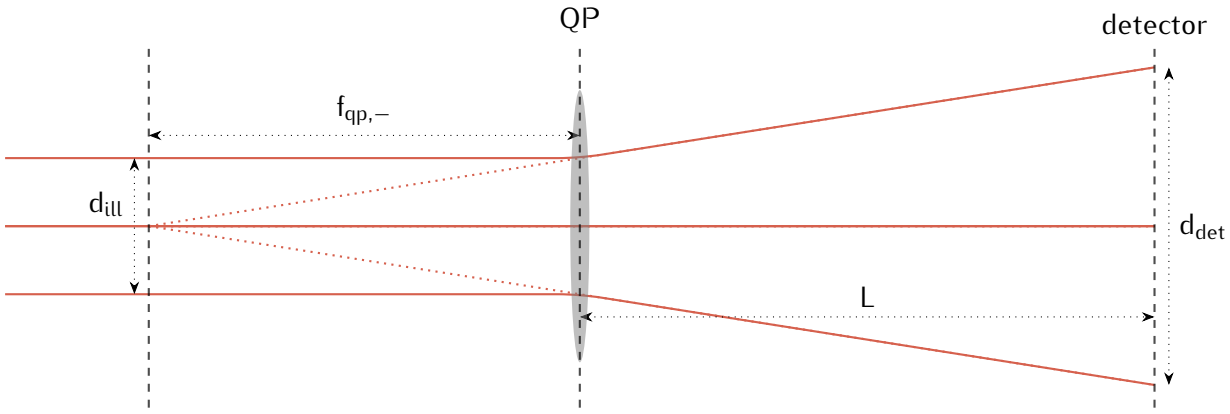

Figure 40: Geometrical relations for the ray optical analysis of the focal length of the self-assembled quadrupoles in defocusing direction using the intercept theorem. An initially parallel electron beam of known radius is defocused stigmatically by the quadrupole lens.

The accuracy and precision of this method for the determination of the quadrupole's focal length is limited by various factors:

1. The incident beam was adjusted to be as round as possible in the image of the sample plane where the quadrupole is located. Subsequently, the calibration of the microscope was checked with a standardized gold cross grating. By comparing the two directions of the cross grating a clear anisotropic magnification can be seen, the corresponding axes in the illumination are 37 µm and 38.7 µm. This anisotropy of 4.5 % may be additionally enhanced by electron optical distortion due to the unconventional setup, a slight (local) tilt of the cross grating, inhomogeneities in the cross grating due to degradation, and distortion due to the fiber optics in the detector. These factors not only contribute to uncertainties in the measurement of the illuminating beam, which could be compensated, but additionally also to inaccuracies in the determination of the size of the focused beam in the far field, which are much harder to correct.

2. Aberrations, mainly of parasitic nature, that induce higher scattering angles, as the ones that contribute to the first order Gaussian behavior. Their presence is clearly visible in the diffuse edges of the diffracted beam in the far field; without aberrations the beam should have an elliptical profile with an almost binary intensity distribution. The diffuse part of the intensity profile, presumable stemming from aberrations, are occupying up to 25 % of its lateral extension. The minimization of these aberrations is beyond the scope of this thesis, but the most important step would be to minimize the parasitic aberrations by reducing the misalignment of the poles.

These inaccuracies render the disentanglement of the two focal directions difficult as the relative difference of the principal axes is only 7 % for a camera length of 1.4 m and d_{ill} of 37 µm (c.f. Eqs. (4.27) and (4.28)). For that reason also the intensity profiles for opposite coil current directions look very similar. Fig. 41 shows the corresponding measurements for coil currents of ±50 mA and ±100 mA.

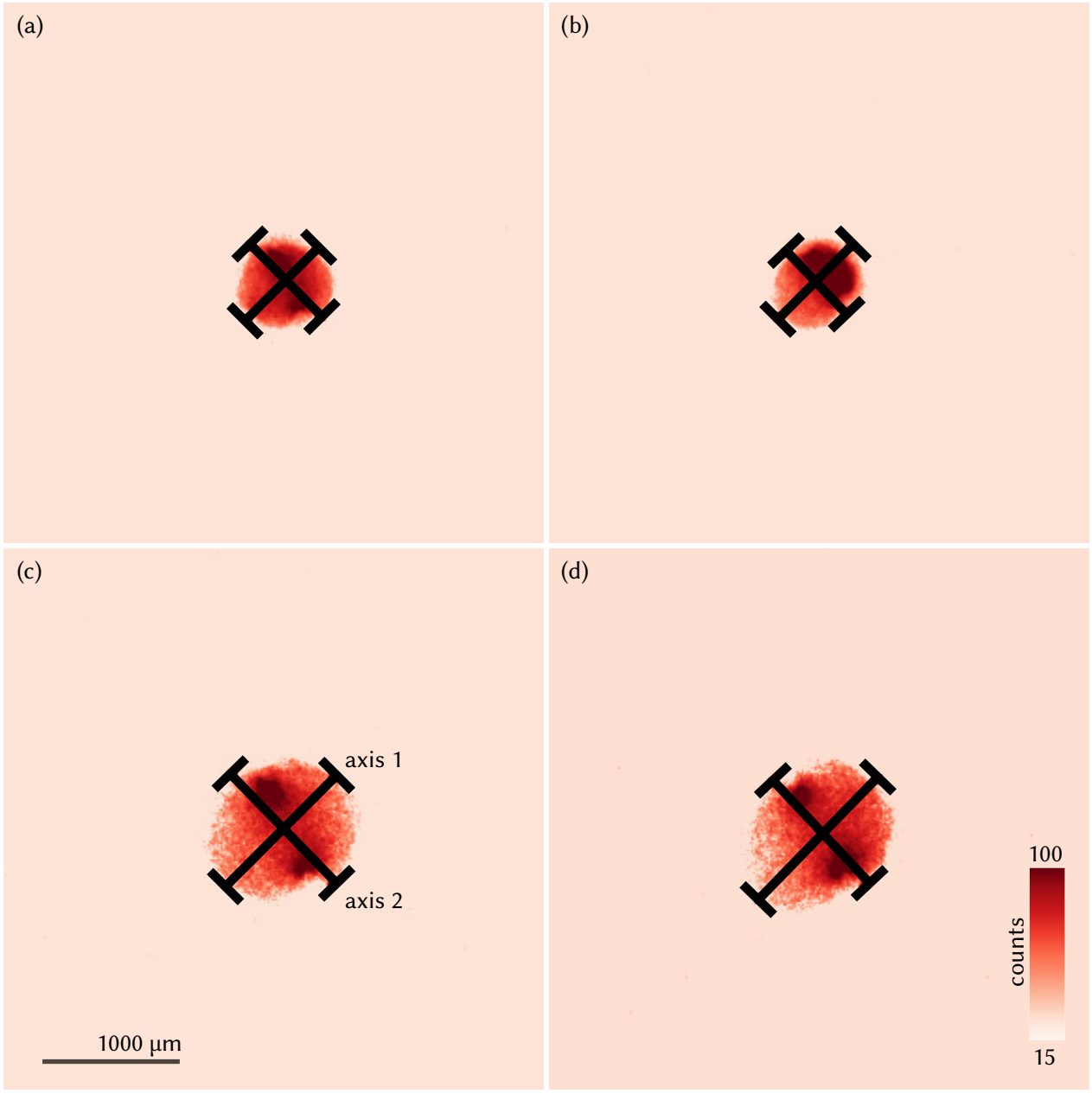

Figure 41: Diffraction disks recorded in the far field of the specimen plane, where the miniaturized quadrupole assembly is located. The self-assembled coils are stimulated with ±50 mA in (a) and (b) and ± 100 mA in (c) and (d), respectively. The different extensions of the diffraction disks are evaluated to compute the focal lengths of the quadrupole lenses.

The lengths of the principal axes, as determined by the outermost part of the intensity profile are, given in Tab. 2. The measurements show that there is a significant offset in the deflection angles for the two axes. In fact, axis 1 is always slightly longer than axis 2. This behavior may be attributed to the (parasitic) aberrations of the system, as their effect is scaling with the stimulation current. Nonetheless, there is a clear trend in the relative difference $\triangle_{\text{rel}}$ between the axis lengths visible, which are much larger for positive stimulation currents than for negative ones. For that reason, it can be assumed that the quadrupole is focusing in direction of axis 2 and defocusing in direction of axis 1 for a positive current and vice versa for a negative current.

	+50 mA	-50 mA	+100 mA	-100 mA
axis 1	812 µm	806 µm	1376 µm	1237 µm
axis 2	673 µm	796 µm	1100 µm	1189 µm
$\triangle_{abs}$	139 µm	10 µm	276 µm	48 µm
$\triangle_{rel}$	18.7 %	1.2 %	21.6 %	4.0 %
$f_{qp,+}$	75 mm	64 mm	47 mm	42 mm
$f_{qp,-}$	69 mm	71 mm	40 mm	46 mm

Table 2: Data of the measurements shown in Fig. 41, together with their computed absolute and relative differences, $\triangle_{abs}$ and $\triangle_{rel}$, respectively. The focal lengths for the focusing direction $f_{qp,+}$ and defocusing direction $f_{qp,-}$ are computed according to Eq. (4.27) and Eq. (4.28).

Corresponding to the aforementioned focusing directions the averaged focal lengths for a 100 mA and 50 mA stimulation read 44 mm $\pm$ 3mm and 70mm $\pm$ 5mm, respectively. The errors in this comparison account for the anisotropy in between the poles. If only one focusing direction is considered, the deviations for different current orientations become much smaller; about $\pm$1 mm for $\pm$ 100 mA and about $\pm$ 3 for 50 mA. This anisotropy is expected to reduce further if the alignment of the poles is improved.

Concluding this section about the miniaturized quadrupole assembly based on the self-assembled micro coils, it can be inferred that we were able to miniaturize a quadrupole lens assembly by several orders of magnitude compared to the quadrupoles used for example in conventional TEMs or EEL Spectrometers that operate in the same electron energy range. The achieved focal lengths of the miniaturized quadrupoles are in the same order of magnitude as conventional magnetic round and magnetic quadrupole lenses used in the aforementioned devices, which underscores the validity of the scaling laws for charged particle optics outlined in Sec. 2.4. The remaining milestones for this technology are mainly the assessment and minimization of the electron optical aberrations of the quadrupole lenses. The first important step here is to improve the manufacturing process, because the parasitic aberrations, stemming from the mutual misalignment of the coils, are presumably the strongest contribution. If the aberrations can be minimized to a degree similar to that of comparable macroscopic systems, however, the outlined minimization of the quadrupole lenses driven by self-assembled micro coils opens the door to a world of previously unthinkable charged particle devices.

4.4 High Frequency Characteristics of Self-Assembled Electron Optics

In addition to the electron optical properties of the miniaturized CPO elements their high frequency characteristics also play a fundamental role for many envisioned applications. These applications range from fast scanning units for possible miniaturized SEMs, TEMs or lithography machines to fast deflection units for stroboscopic measurements of dynamic processes in various types of electron microscopes. Interesting phenomena that could be studied *in-situ* in an electron microscope while being stimulated with an HF electromagnet, such as spin waves [207, 208, 209, 210] or dynamics of magnetic textures [211, 212], require a stimulation of the sample in the GHz regime (more examples are given in Sec. 5.3).

The miniaturized electromagnets could be additionally used for *in-situ* application of dynamic magnetic fields within the restricted sample space in SEMs or TEMs. Retrofitting existing electron microscopes with macroscopic fast deflectors for stroboscopic imaging [213] or with devices for *in-situ* application of magnetic fields [214] is typically a very challenging, costly and time-consuming procedure. The HF cutoff frequencies, essential for the functionality of the aforementioned devices, are expected to benefit from miniaturization [38], especially when magnetic fields are involved. The throughput of miniaturized SEMs and lithography machines is almost linearly scaling with the HF cutoff frequency, if the current density is not the limiting factor [215]. In stroboscopic measurements, the achievable temporal resolution as a function of repetition rate and dose is also linearly increasing with the HF cutoff frequency.
The overall HF characteristics of the miniaturized electromagnet systems are depending on three main parts: 1. the self-assembled micro coils, 2. the soft magnetic micro wires, and 3. the electric connections to a function generator stimulating the whole assembly. It is very challenging to disentangle the individual contributions from electronical measurements and use them to draw conclusions about the polarization and the magnetic flux densities at the tip of the micro wire poles. For that reason, this work focuses on an *in-situ* approach for the direct measurement of the HF characteristics through the deflection of an electron beam. Further details on the electrical HF characterization of the chips and the holder assembly, like the measurement of the impedance of the chips and an equivalent circuit diagram can be found in the doctoral thesis of Renato Huber[32].

In-Situ TEM Measurements

The miniaturized electromagnets are installed in a *FEI* Titan^3 TEM for this approach. The electron beam is placed in between the poles of the electromagnet in biaxial vector magnet configuration, which is stimulated with an HF signal generator. The deflection of the electron is then measured by two different means, as an angular deflection in the far field of the micro coil device location and in real space in a plane conjugate to the device, which allows to draw conclusions about the HF properties (e.g. cut-off frequency) and possible stroboscopic measurement modes in the TEM.
For this approach, the micro coil assembly was inserted in the C3 condenser aperture plane of a *FEI* Titan^3 80-300 using a specially modified *ThermoFisher* aperture holder based on the *ThermoFisher* NanoEx i/v specimen holder. To enable a large HF passband the original wires and connectors of the aperture holder were replaced with rg-178 coaxial cables and SMA (Subminiature version A) plugs, respectively. Due to the limited space inside the holder tube only four coaxial cables could be fitted. For that reason, the two opposing coils of the vector magnet are excited with the same signal. The electrical connector pads of the chip with the fabricated micro coil vector magnet were wire bonded to the coaxial cables. The whole assembly was protected against diffuse electron irradiation by a specially laser cut copper shield. Images of the whole assembly are shown in Fig. 42. In order to vacuum seal the whole assembly, a KF 40 plate with four integrated SMA connectors was mounted to the original KF 16 flange of the aperture holder, using a custom-built adapter, which allowed to install the modified holder in the limited space of the housing of a low base *FEI* Titan^3.

[32] Which is not submitted at the time this thesis was handed in

top view with wire-bonded sample:

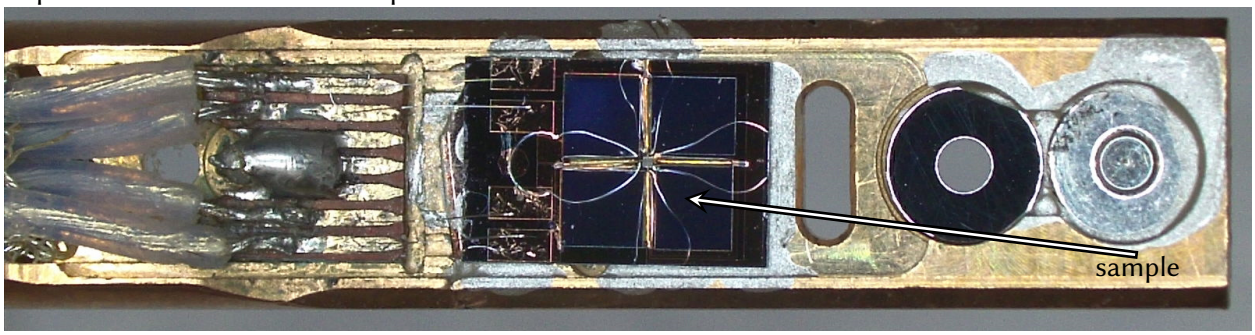

back view:

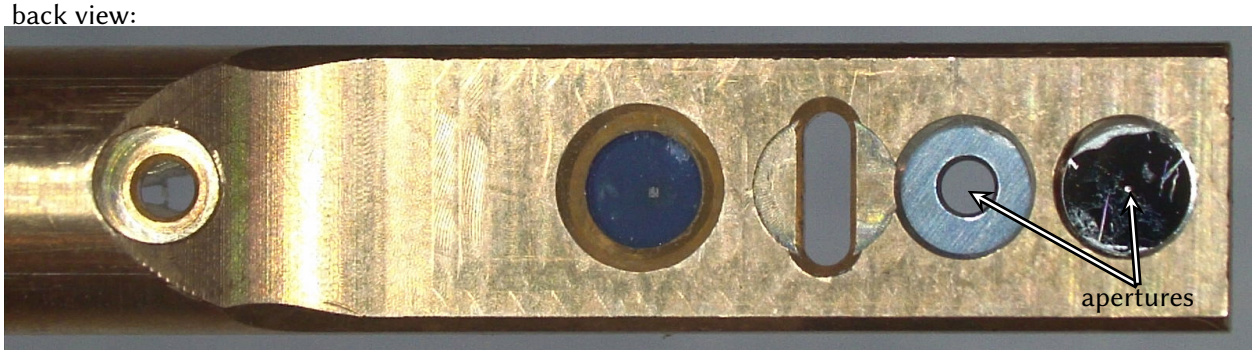

top view with protective shield:

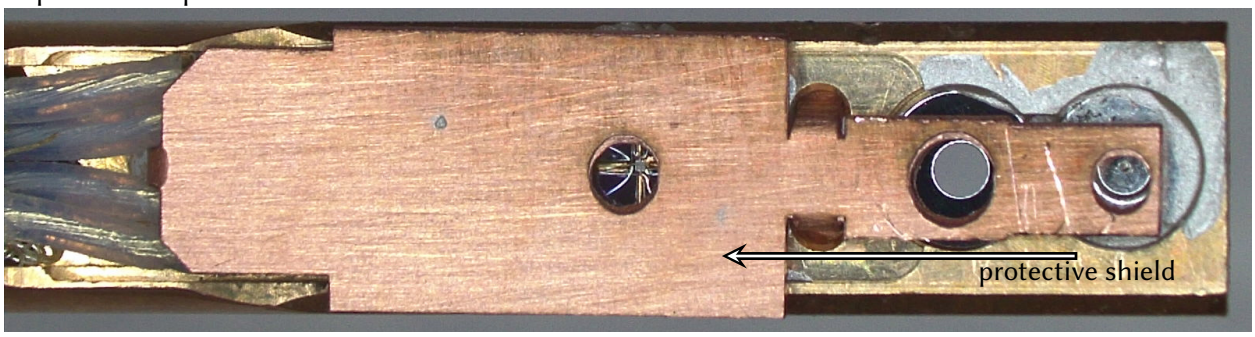

side view with protective shield:

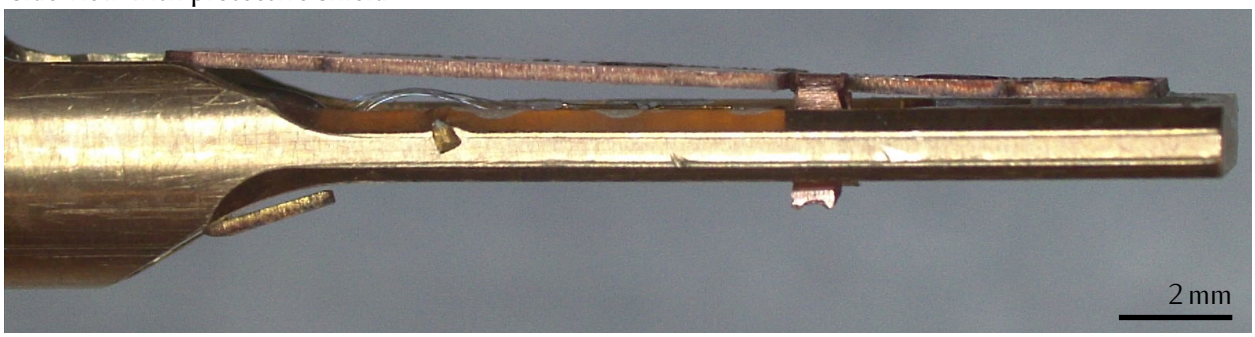

side view with protective shield:

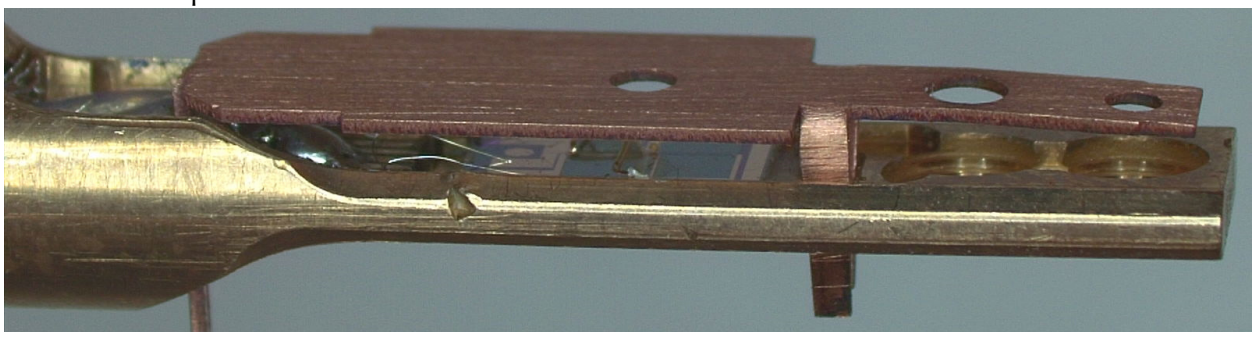

Figure 42: Images of the modified C3 condenser aperture holder based on a *ThermoFisher* NanoEx i/v specimen holder with the chip containing the miniaturized electromagnets, driven by the self-assembled micro coils. The original 50 µm and 1000 µm apertures are placed in the first two aperture positions to allow the microscope to be used in the original setting.

Angular Deflection

The instrument was operated in a special mode, where the *CEOS* CESCOR probe corrector was used as a transfer system magnifying the deflection produced by the micro coil device in the specimen plane. Specifically, this specially developed mode provides a magnification of 1.43 between the C3 aperture plane and the specimen plane, as measured by the comparison of the image of the poles with a cross grating of 2160 $^{\text{lines}}/_{\text{mm}}$ in the specimen plane. The corresponding angular magnification of a deflection in the C3 aperture plane is than 0.7, according to the Helmholtz-Lagrange invariant.

The angular deflection was measured in the far field of the specimen plane, where the temporally integrated electron beam intensity is recorded on the detector at an effective electron optical camera length of 13.2 m $\pm$ 0.8 m. A simplified path of rays of this experimental setup is depicted in Fig. 43.

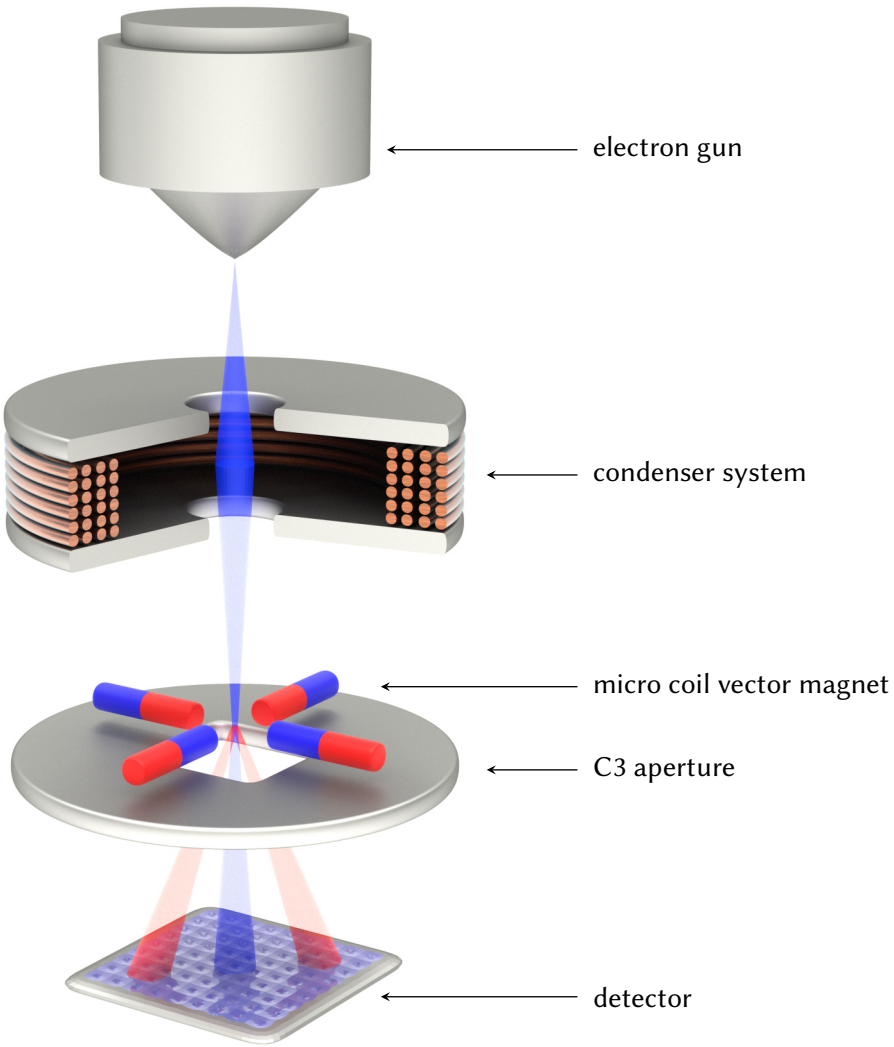

Figure 43: Simplified path of rays of the measurement setup, which is used to determine the high frequency angular deflection of the electron beam

For a harmonic excitation of the micro electromagnet assembly with amplitude **A**, phase ϕ, and angular frequency ω_0 and hence a displacement of the electron beam

$$\mathbf{r}\,(t) = \mathbf{A}\sin\left(\omega_0 t + \phi\right)\,, \tag{4.29}$$

the corresponding density distribution along the oscillation direction r,

$$P_{harm}\,(r) = \frac{1}{2\pi A\sqrt{1-\left(\frac{r}{A}\right)^2}}\,, \tag{4.30}$$

can be found according to:

$$P_{harm}\,(r)\,dr = \frac{dt}{T} = \frac{\omega dt}{2\pi}\,, \tag{4.31}$$

with:

$$dr = A\omega\cos\left(\omega t\right)dt = A\omega\sqrt{1-\sin^2\left(\omega t\right)}dt = A\omega\sqrt{1-\left(\frac{r}{A}\right)^2}dt\,. \tag{4.32}$$

The accumulated counts of the electron beam on the detector for an exposure time t_{exp} are then given by:

$$N\left(\mathbf{r}\right) = \left(P_{harm}\left(\mathbf{r}\right) \otimes I_0\left(\mathbf{r}\right)\right) t_{exp}\,, \tag{4.33}$$

with the probe intensity $I_0\left(\mathbf{r}\right)$ and the convolution denoted by $\otimes$. The corresponding intensity profiles for a frequency range between 0.25 MHz and 500 MHz are shown in Fig. 44. Outside that region, there are no measurable deviations compared to the profiles at 0.25 MHz and 500 MHz, respectively. A *Keysight Technologies* 33600A Series Trueform Waveform generator was used for the stimulation up to 32 MHz, a *Rhode Schwarz* SMR 27 for the frequency range from 16 MHz to 500 MHz. The *Keysight Technologies* 33600A operates as a constant voltage source and is adjusted in Volts peak-to-peak (Vpp), while the *Rhode Schwarz* SMR 27 is adjusted in terms of output power in dbm. The *Rhode Schwarz* SMR 27 was operated at 19 dbm (79mW). The *Keysight Technologies* 33600A was operated at 4.6 Vpp for coil pair 1, and at 4.8 Vpp for coil pair 2. The signal level of the *Keysight Technologies* 33600A was adjusted such that the beam deflection matches the one of the *Rhode Schwarz* SMR 27 at 19 dbm in the overlapping data points at 16 MHz, 32 MHz and 64 MHz. As the intensity profiles in Fig. 44 do not exactly match the distribution from Eq. (4.33), it can be assumed that the oscillation has a non-negligible anharmonicity, given by [178]:

$$r\,(t) = A\sin\left(\omega t\right) + \epsilon\frac{A^2}{6\omega^2}\left(3 - 4\sin\left(\omega t\right) - \cos^2\left(\omega t\right) + \sin^2\left(\omega t\right)\right)\,, \tag{4.34}$$

with a perturbation parameter ϵ. The corresponding probability density distribution (see. [178] for the dervation)

$$P_{an}\,(r) = \frac{1}{2\pi\sqrt{1-\left(\frac{r}{A}\right)^2}\left(1+\alpha\left(\frac{r}{A}-1\right)\right)}\,, \tag{4.35}$$

with $\alpha = {}^{2\epsilon}/_{3\omega^2}$ can be found similarly to the derivation for the harmonic oscillation (Eq. (4.31)).

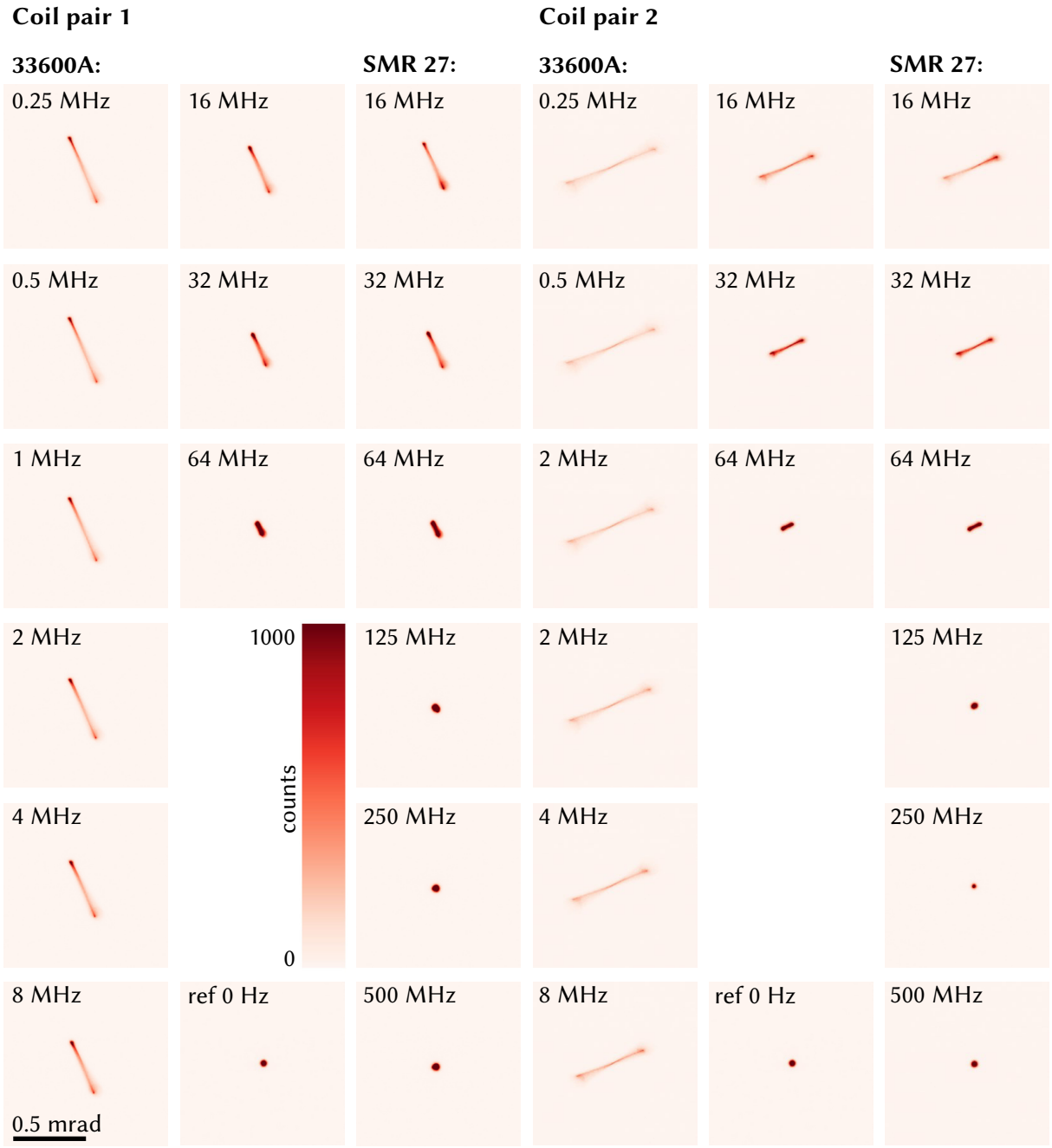

Figure 44: Electron intensity profiles for sinusoidal deflection by the two axially aligned coil pairs of a micro vector magnet driven by self-assembled micro coils. The corresponding stimulation frequencies are indicated, a reference without stimulation is given additionally under the label 'ref 0 Hz'. In the different series the oscillation was generated by the *Keysight Technologies* 33600A Series Trueform Waveform generator (labeled as '33600A') and by *the Rhode Schwarz* SMR 27 (labeled as 'SMR 27').

For the further numerical evaluation of the data from Fig. 44 the profiles have been fitted to the anharmonic probability distribution Eq. (4.35). To that end, the images were rotated to align the oscillation to one image axis and shifted to the image center in a first step. The suitable rotation angle as well as the necessary shift was calculated from the positions of the two peaks in the intensity profiles, which

were detected by a local maximum detection algorithm. In a next step, the projection along the direction perpendicular to the oscillation is computed. Eq. (4.35) convoluted with the additionally acquired and accordingly rotated and shifted probe intensity is then fitted to the projected intensity with A, α, and the total intensity as free parameters, using a Nelder-Mead minimization algorithm [216]. The accordingly fitted oscillation amplitudes for different stimulation frequencies are shown in Fig. 45.

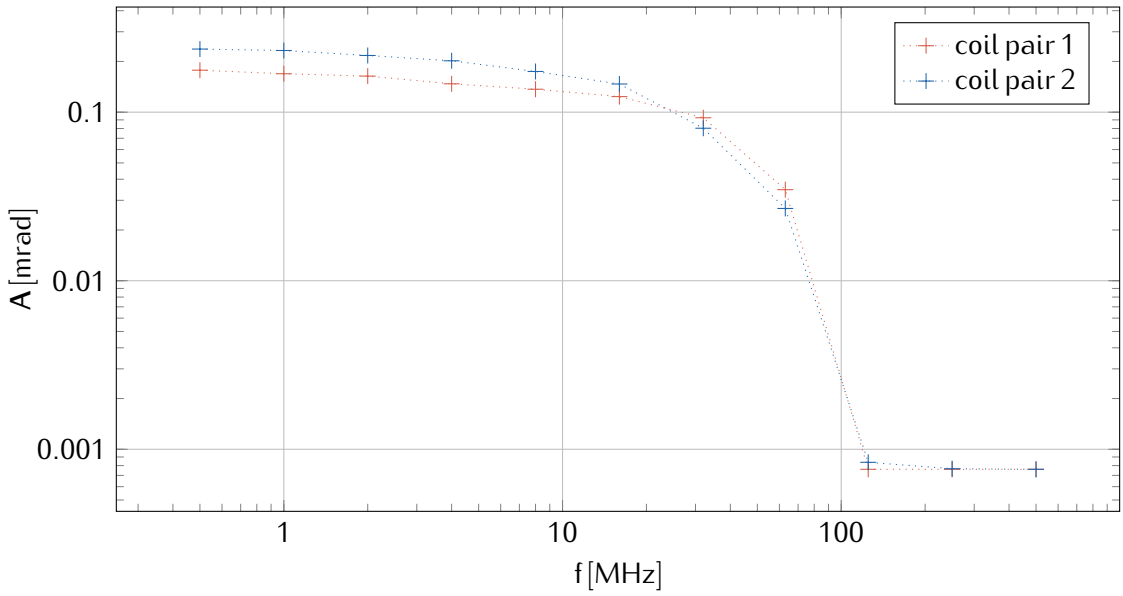

Figure 45: Oscillation amplitudes for different stimulation frequencies as obtained from the data shown in Fig. 44.

The fitted data (Fig. 45) indicates an onset of the HF dampening at about 250 kHz and a sigmoidal drop towards the cutoff at about 250 MHz. There is a relative difference in amplitude between the two oscillation directions of about 25 % for frequencies below 10 MHz, presumably stemming from the different distances of the pole tips to the micro coils (c.f. Fig 35). The aforementioned anharmonicities, particularly pronounced at lower frequencies, become manifest as inhomogeneities of the profiles towards larger deflections and an additional smearing of the intensity profile. Presumably they are also stemming from tolerances in the manufacturing process, nonlinearities in the magnetization behavior or aberrations in the subsequent optics, whose impact intensifies through the tilt of the electron beam.

Real Space Deflection

In addition to the angular deflection, the attainable real space deflection in the aforementioned optical setup of the microscope is another interesting property, in particular for the development of stroboscopic imaging modes in a TEM. A simplified path of rays of a corresponding experimental setup is depicted in Fig. 46.

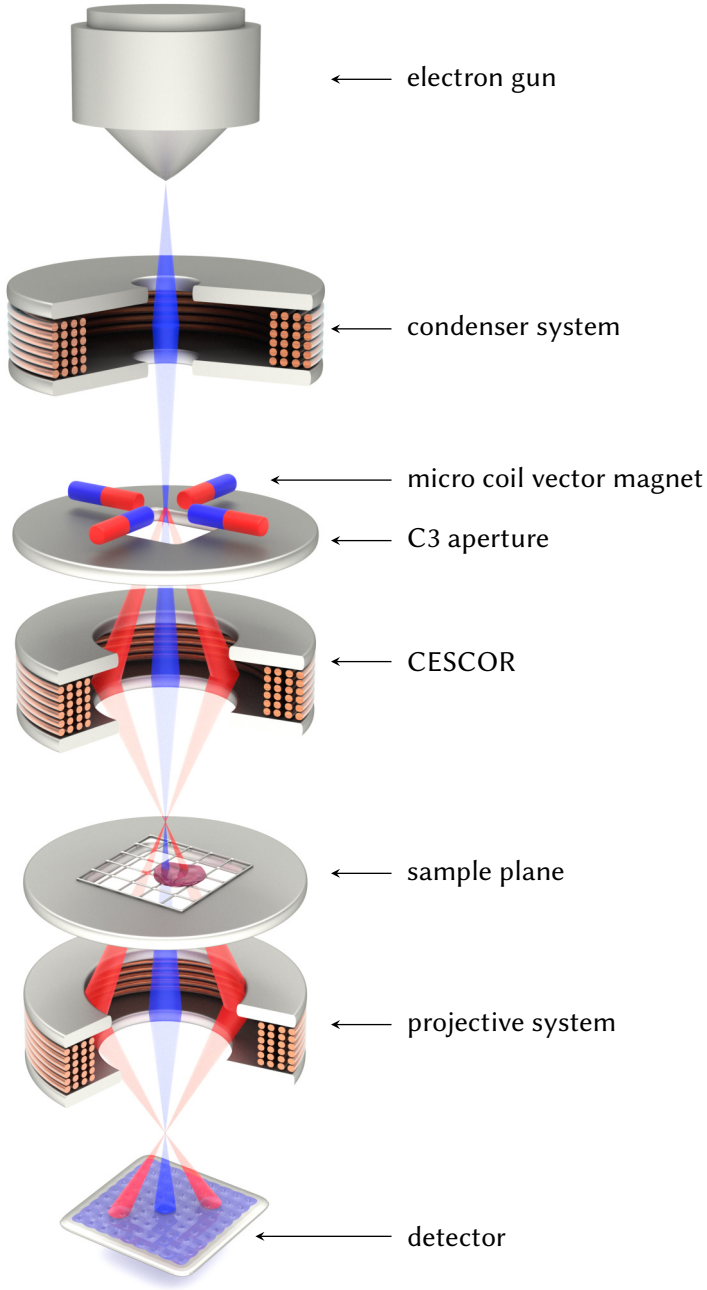

Figure 46: Simplified path of rays of the measurement setup, which is used to determine the high frequency real space deflection of the electron beam in the specimen plane.

The pulse length Δt in a stroboscopic setup is the time that the electron beam illuminates a region of interest of length r_{ROI}. For a sinusoidal oscillation of the electron beam, whose center of mass obeys:

$$r(t) = A \sin(\omega_0 t) \ , \tag{4.36}$$

with amplitude A and angular frequency ω_0, the stroboscopic pulse length for an ROI centered at the origin of the oscillation reads:

$$\Delta t = \frac{T}{\pi} \arcsin\left(\frac{r_{ROI}}{A}\right) \ , \tag{4.37}$$

if the electron beam size along the oscillation direction is equal to r_{ROI}. In order to test the developed stroboscopic setup and to measure the attainable deflection, averaged real space images of the oscillating beam over a gold cross grating with 2160 $^{lines}/_{mm}$ were recorded. A series of such images for different stimulation frequencies is shown in Fig. 47. The oscillation was generated, again, by a *Keysight Technologies* 33600A and a *Rhode Schwarz* SMR 27, for frequencies up to 32 MHz and above 16 MHz, respectively. The 33600A was operated at 2.5 Vpp below 4 MHz, as the attained real space deflection was larger than the microscopic field of view in that setup. Above 2 MHz 5 Vpp were used at for the 33600A, the overlap in frequency was used to numerically stitch the graph together. There is a notable discontinuity between the two graphs for 2.5 Vpp and 5 Vpp, which may be attributed to the internal electronics of the *Keysight Technologies* 33600A. The graphs at 5 Vpp of the 33600A and 19 dbm at the SMR 27 were stitched together with a numerical offset of the SMR 27 values by a factor of 0.9. The maximum bandwidth-amplitude product is attained at 32 MHz, at about 450 Hzm, which corresponds to a pulse width of 0.7 ns for a 1 µm sized ROI and beam diameter. In the described setup there is always a trade-off between the attainable FOV (and the corresponding dose rate per area) and pulse length. A pulse width of 0.7 ps could be obtained for a FOV of 1 nm, which comes at the expense of a factor of 10^3 of usable dose.

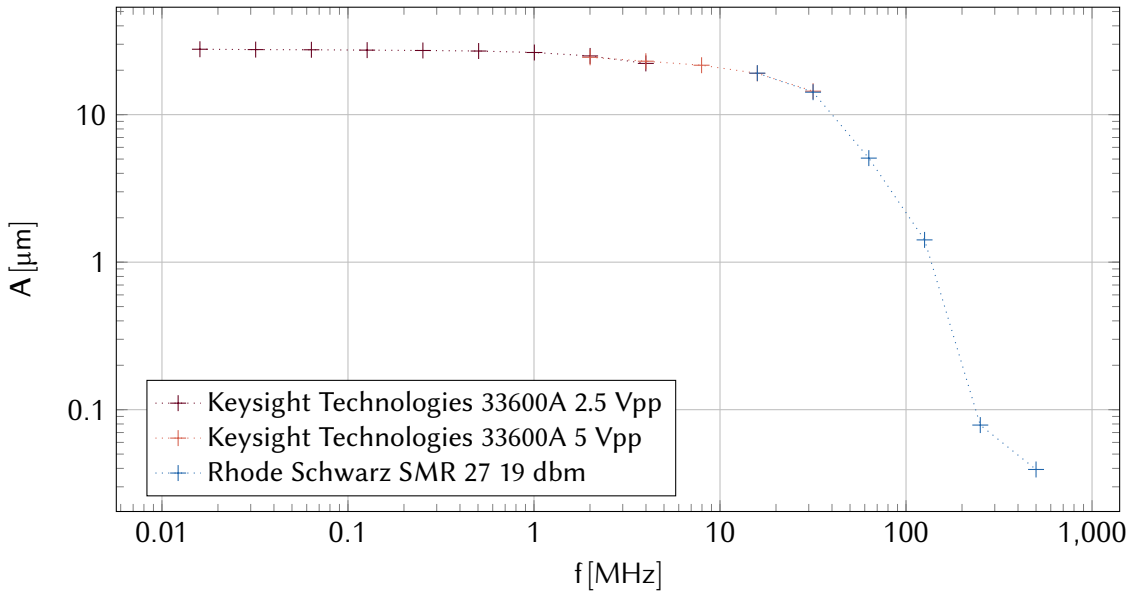

Figure 47: Temporally averaged deflection amplitude of the developed stroboscopic setup, where the electron beam is oscillating over the sample deflected by a micro vector magnet located in the C3 aperture plane. The CESCOR scanning corrector is operated in a special transfer setup that allows to maximize the real space deflection in the specimen plane for a given angular deflection. The deflection values from *Keysight Technologies* 33600A at 2.5 Vpp and *Rhode Schwarz* SMR 27 were multiplied by 1.75 and by 0.9, respectively, in order to match the differences in the excitation.

5 Summary and Outlook

The goal of this work was to design, fabricate and evaluate miniaturized electron optical elements produced through a polymeric self-assembly process that was developed by our collaboration partners at the Institute for Integrated Nanosciences. The scaling laws for charged particle optical elements (developed in Sec. 2.4) indicate a very favorable scaling of the electron optical properties of transverse magnetic elements upon miniaturization. Transmission electron microscopy offers the unique possibility for the *in-situ* measurement of projected magnetic fields of the electron optical elements with Tnm precision at a spatial resolution in the nanometer regime. All the miniaturized electron optical elements were fit to the geometrical and electrical constraints given by the commercially available specimen and aperture holders, to permit their characterization in a TEM. Magnetic finite element method simulations (c.f. Sec. 3.2) were conducted to match the design of the micro coils to these holders and to the soft magnetic CoFeSiB micro wires that are employed as pole pieces. The magnetic properties of the micro wires were investigated beforehand by VSM measurements (c.f. Sec. 3.3). Three different kinds of miniaturized electron optical elements were designed, fabricated and characterized:

1. A magnetic electron vortex phase plate, the first such tunable device reported in literature. The attainable orbital angular momentum has an unprecedented value of several 1000 ħ at a coil current of 100 mA.

2. Two variants of deflectors for charged particles: An axially aligned micro electromagnet pair for one dimensional deflection and a two-dimensionally deflecting micro vector magnet. The deflector can produce a projected magnetic field of up to 2 Tμm at 100 mA coil excitation. The attainable deflection is more than 1 mrad for 300 keV electrons.

3. An anisotropic focusing quadrupole optic with a focal length of 44 mm and an according quadrupole strength of 800 Tμm at 100 mA coil stimulation.

The electron optical characterization of the aforementioned elements was mainly performed by differential phase contrast measurements. For these measurements, a dedicated STEM mode with magnetic field free specimen position had to be developed to ensure an unperturbed operation of the miniaturized elements. The characteristics of the magnetic vortex phase plate were additionally analyzed by the investigation of the propagation of the generated electron vortex beam in defocus series at different currents (c.f. Sec. 4.1.2). The focal length of the miniaturized quadrupole was calculated from the projected fields, which were reconstructed from the differential phase contrast measurements, and verified by measurements based on ray optical considerations (c.f. Sec. 4.3).
Currently, all the mentioned multi pole devices suffer from a mutual misalignment of the poles, which is especially obvious in the non-negligible parasitic aberrations of the quadrupole. The most promising strategy to minimize this misalignment is to deposit a soft magnetic material directly in the fabrication process, as opposed to the currently employed manual insertion procedure after the rolling process. In such a deposition approach, however, the soft magnetic micro wires, used in this work, can not be applied anymore. Another route to minimize the misalignment of the poles is to match the size of the coil to the

size of the wires, either by using larger micro wires or by reducing the coils size. The fabricated dipoles with 50 µm and 86 µm wires already showed improvements in that regard. The unfavorable polarization behavior of the thicker wires (c.f. Sec. 4.2) might be rendered irrelevant, if currents larger than 100 mA could be applied. As this limit is given by the employed *Protochips* Fusion Select biasing holder, it is necessary to develop a holder that permits larger currents for this approach.

Due to the linear scaling of the inductance with system size, all aforementioned elements can be switched at least in the 100 MHz regime, rendering plenty of HF applications possible. For first applications, a stroboscopic measurement setup was developed, in which a temporal resolution of 0.7 ns for a FOV of 1 µm could be realized (c.f. Sec. 4.4). The temporal resolution can easily be further increased at the expense of FOV and illumination dose. Corresponding simulations from our collaboration partners suggest that the measured frequency passband is limited by the contacting of the chips through wire bonding, and the circuit paths on the chips, and not by the micro coils. Consequently, in order to reach the single or even double-digit GHz regime the contacting and the design of the chips presumably have to be altered, e.g., by incorporating a more elaborated shielding of the chip to prevent losses due to emission.

The combination of the mentioned properties renders the developed optical elements very promising for envisioned applications outlined in the final sections.

5.1 Applications of Electron Vortex Beams with Large OAM

For most currently envisioned applications of electron vortex beams, large orbital angular momenta are not necessary. For example, in electron magnetic chiral dichroism (EMCD) measurements a precise adjustment of the OAM and a quantum state of high purity is of much greater importance. EMCD measurements may, however, benefit from a tunable vortex phase plate generating lower quanta of OAM. It was not the scope of this work to produce such an EVB phase plate. It might, however, be possible to produce tunable EVB phase plates suitable for EMCD with thinner soft magnetic wires or magnetically different poles where the shape anisotropy can be overcome.

The most interesting applications of EVBs, where large quanta of OAM are desirable, are:

1. The measurement of out-of-plane $\mathbf{B}$ fields in a TEM employing a novel measurement scheme; this novel setup outlined in [202] exploits the Zeeman interaction of the electron beam with the sample's magnetic field, where the signal is directly proportional to the OAM of the incident beam.

2. The rotation of nanoparticles [199] by EVBs benefits in particular from larger quanta of OAM, as the underlying mechanism is absorption of the electron and hence the transfer of the electron's OAM to the sample conserving, the overall angular momentum [139]

Besides that, there are other envisioned applications, such as electron optical tweezers [203] that might benefit from a larger OAM of the electron beam.

5.2 Optics of Large Optical Power for Pulsed Instruments

The optical power of the miniaturized electron optical elements produced within the frame of this work is limited by Joule heating. Therefore, their optical power may be further enhanced in a pulsed operation mode with current peaks above the DC value, which is given by temporally averaged power dissipation. Pulsed miniaturized electron optical elements could, e.g., be applied in systems with a (laser) pulsed electron gun [22]. These instruments are mainly used to facilitate measurements in the time domain, with attainable temporal resolution down to the attosecond regime [217]. Although the elements produced in this work are merely switchable in the 10 MHz regime, they may still be employed in systems with much shorter pulses of the electron gun, if the electron-emission repetition rate is not exceeding the repetition rate attainable by the element. The optical power of the miniaturized elements is expected to increase drastically in pulsed operation, if suitable pole pieces with high saturation magnetization are used. Following to the arguments in Sec. 2.4.3 the attainable magnetic flux density B_{max} is given by the system's ability to dissipate the power generated through joule heating P_J.

For the system to be able to dissipate P_J, the total heat Q within the system must not rise above the critical heat Q_c destroying the device. That can be reached within a single pulse or through a pulse-wise heating of the device, if the heat dissipation P_d is smaller than the temporally averaged Joule heating (c.f. Sec. 2.4.3)

$$\overline{P_J} = \int_0^T P_J dt \,. \tag{5.1}$$

While it is very challenging to quantify Q_c, especially if HF pulses are employed, a value for P_d can be calculated easily from the resistance of the coils and the maximum current they can withstand. With the average maximum current of 93.0 mA ± 12.7 mA and the average Ohmic DC resistivity of 8.45 Ω ± 1.52 Ω (see [178] for more details) a heat dissipation P_d of 73 mW ± 13 mW can be calculated. If the heat generated by a single pulse is smaller than Q_c, the attainable current in a T_p = 31.3 ns pulse (corresponding to one oscillation at 32 MHz) at repetition rate of 250 kHz ($T_r = 4$ µs) can reach 23.5 A according to:

$$\overline{P_J} = \frac{1}{T_r} \int_0^{T_r} I(t)^2 R dt \simeq I_{max}^2 \frac{T_p}{T_r} R \,, \tag{5.2}$$

if an impedance of about 17 Ω is assumed at 32 MHz following to the HF measurements in Sec. 4.4. According to the FEM simulations, the corresponding attainable flux density then reaches values of about 0.82 T in the center of the micro coil, more than enough to polarize the currently used micro wires. For repetition rates in the 40 kHz regime peak currents of 57 A would be attainable, generating 2 T in the current coil design, which would even be sufficient to polarize magnetically hard permanent magnets. The resulting focal lengths at the saturation magnetization of 0.7 T (see Sec. 3.3) would be about 1.8 mm for 300 keV electrons for the manufactured quadrupoles. Sub millimeter values could be obtained by using thicker wires of 86 µm in diameter that were already tested but could hardly be polarized with 100 mA DC (c.f. Fig.31). These short focal lengths are necessary if envisioned electron optical instruments should be miniaturized isotropically, i.e. also along the optical axis. The enhanced optical power additionally

opens up paths towards devices that employ higher electron energies. It is important to note that some kind of ferromagnetic material as pole piece is mandatory for most miniaturized magnetic electron optical elements, for example to reach fields in the 100 mT regime with a miniaturized coil with a radius of 20 µm and a length of 100 µm a current of about 8 A would be necesarry according to formula Eq. 2.130

5.3 Stroboscopic TEM Measurements

A miniaturized vector magnet can be used to set up a stroboscopic measurement scheme, outlined in Sec. 4.4, in almost every conventional TEM. The only preconditions are that the instrument can be operated in a mode that has a magnetic field-free condenser aperture position and that a HF capable aperture holder is available. With the currently employed setup, sub nanosecond pulses on a to-be-measured 1 µm FOV can be achieved, which can be used to analyze reversible or oscillating phenomena with a corresponding temporal resolution. The stroboscopic field of view of 1 µm along the oscillation direction can be sacrificed for even smaller pulse lengths, as both quantities are related linearly, if the oscillation amplitude is much larger than the FOV (c.f. Eq. (4.37)). The established stroboscopic setup can be used for imaging of various dynamic phenomena, for example: The imaging of skyrmion dynamics [218] in several material systems, where their velocity is in the 100 $^{m}/_{s}$ regime, such as in MnSi nano wires [219], thin Co films [220] or Pt, CoFeB, MgO hetero structures [221]. Another interesting phenomenon that could be analyzed by the stroboscopic TEM method are the dynamics of domain walls, which serve as interesting candidates for next generation memory devices, so-called racetrack memory [222]. Velocities of current driven domain walls in permalloy nano wires are also in the 100 $^{m}/_{s}$ regime [211, 223], making the dynamics accessible by the developed stroboscopic setup. Additionally, magnetic systems may be also stimulated by the magnetic fields from the micro electromagnet assembly for various *in-situ* measurements. Usually the TEM's objective lens is used for such measurements, the corresponding field, however, is always oriented along the optical axis of the microscope. The produced micro electromagnets could be used for applications where variable fields in the 100 mT regime perpendicular to the optical axis are sufficient, e.g., for the stabilization of a skyrmionic phase. A benefit of this setup would be that the micro magnets can be rotated together with the sample, which facilitates various tomographic setups, similar to the holder manufactured in [224], but with more than four times the magnetic flux density. To that end, the produced chips can be easily adopted in almost any TEM, without the need for modifications of the instrument.

5.4 Miniaturized Wigglers, Undulators and Free Electron Lasers

Emission of Bremsstrahlung, by charged particles on curved trajectories, is commonly employed, e.g. for the generation of X-rays. A very elaborate way to produce electromagnetic radiation through this principle is to use a large number of aligned bending magnets in wigglers or undulators. While wigglers emit a very intense and broad spectrum, in an undulator the phase of the electron oscillation is matched to the undulator period $\lambda_u = {}^{2\pi}/_{k_u}$, which generates electromagnetic waves of much larger brilliance. The

common classification [225] for wigglers and undulators is based on the undulator strength parameter:

$$K = \frac{\gamma \lambda_u}{2\pi R} = \frac{\lambda_u e B}{2\pi m c}, \tag{5.3}$$

with the relativistic Lorentz factor γ, the elementary charge e, the speed of light c and the bending radius R within the magnetic field of maximum value B. For K values much larger than unity the bending magnet assembly is considered a wiggler, for values much smaller an undulator. The usually dominant first order emission wavelength of an undulator is given by the resonance condition:

$$\lambda_{em} = \frac{\lambda_u}{2\gamma^2} \left(1 + \frac{K^2}{2} + \theta^2 \gamma^2 \right) , \tag{5.4}$$

with θ being the emission angle off the undulators axis. According to these simplified approximations a miniaturized undulator with λ_u= 100 µm and B = 100 mT would emit at a resonance frequency that corresponds to an optical wavelength of 20 µm for 300 kV electrons, in the visible range above 3 MeV and in the soft X-ray regime for 35 MeV electrons. As the aforementioned values are in reach using the micro coil technology employed within this work, miniaturized undulators and free electron lasers could be built, if suitable miniaturized electron sources and accelerators can be developed. Most electron sources are already quite small by design, and routes towards miniaturized electron accelerators are already envisioned and partially realized. Examples are inverse free electron lasers [128] and laser based acceleration through optical near fields at dielectric structures [127] or in plasma wake fields [125, 126]. Specifications similar to the ones of the fabricated self-assembled microcoils are attainable with already existing permanent magnet undulators [226, 227] and tunable surface-micromachined electromagnets [71, 72]. Both approaches, however, could not show the generation of electromagnetic radiation by the undulators up to now. A mIniaturized undulator based on permanent magnets placed at a distance of 5 mm producing soft X-ray radiation at 17 nm from 200 MeV electrons has already been demonstrated in literature [228].

5.5 Towards Integrated Electron Optical Systems

The demonstrated parallelized fabrication procedure of up to 2428 micro coils on a 6-inch wafer (c.f. Fig 48) with a production yield of 91.4 % is also a good vantage point for the development of multibeam charged particle devices. The unique prospects of such devices include:

- Operation with fast charged particles through the utilization of magnetic elements, potentially increasing the attainable resolution

- Increase in resolution through scaling of the optical aberrations with the relevant element size [229, 57] if parasitic aberrations are well-behaved

- Design of multibeam instruments in a multi column fashion, greatly reducing the beam broadening through space charges by the Boersch effect [53]

- Large number of mutually independent beams, with accordingly increasing throughout compared to single beam devices; beam counts of more than 10^4 are attainable at a device footprint of conventional single beam devices
- Low cost of auxiliary installations through eased vacuum requirements, no need for external water cooling and low requirements with respect to mechanical support
- Lower impact of mechanical vibrations and external magnetic stray fields through the reduced system size
- Fast scanning, focusing and beam blanking facilitated by the large HF passband

A conceptually very simple, yet highly useful instrument would be a multibeam scanning electron microscope that could also be used for electron beam lithography. Five elements are in principle sufficient for such a device: an electron gun, an accelerator, a condenser system, intermediate deflectors and some kind of detector. The most straight forward design of such a multibeam device would be based on the wafers currently used for the production of the miniaturized elements.

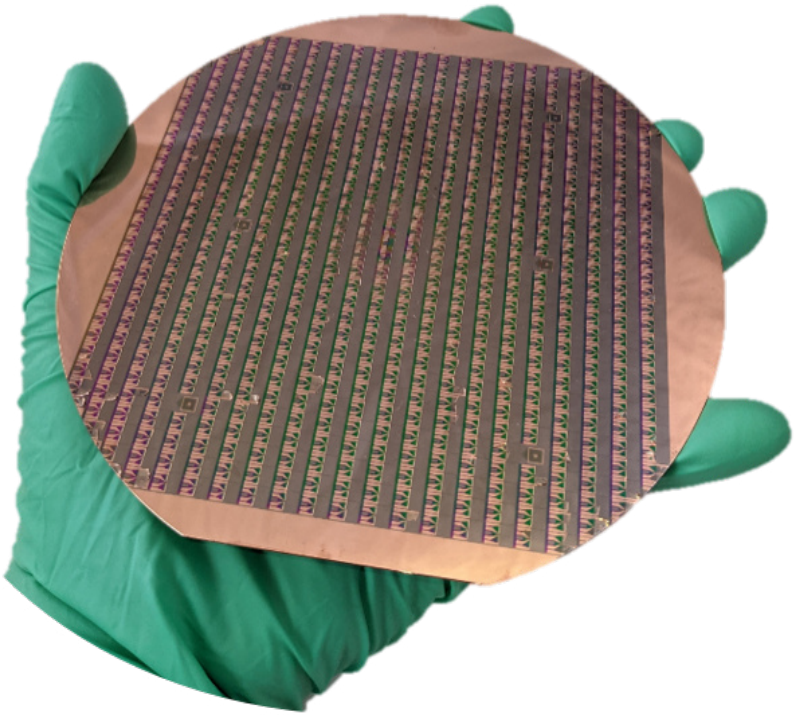

Figure 48: An as-fabricated 6-inch wafer with self-assembled miniaturized dipole deflectors. Courtesy of Renato Huber.

To minimize transverse misalignment, the wafers could be used without being diced, resulting in a device with more than 10^3 beams. To achieve this large number of beams in an integrated device, the pole pieces must be structured directly on the device, not be inserted manually after the rolling process. An appropriate anamorphic focusing system (c.f. Sec. 2.3.2) can be realized by two wafers with miniaturized

quadrupoles successively arranged along the optical axis. Additional planes with scanning and alignment deflectors could be inserted, but a more elegant incorporation of the deflection could be realized by modulating the quadrupole's excitation. To that end, the quadrupole stimulation would be a superposition of quadrupole and vector magnet contributions. The currently missing elements would be:

- Electron sources, which were already produced in large arrays with a very low form factor (exceeding packing densities of 10^6 $1/mm^2$ [230]) as Spindt type field emitter arrays [231], offering a brightness of $3.2 \cdot 10^7$ A/cm^2 at 98 V primary acceleration [230]
- An accelerator, which could either be produced conventionally, by applying a high voltage between the source and additional electrodes, or by employing inverse free electron lasers [128] or laser based acceleration at dielectric structures through optical near fields [127]
- An electron detector; a very simple secondary electron detector could be realized by incorporating a photo diode on the backside of the wafer adjacent to the sample

Summing up, the miniaturized electron optical elements produced within the frame of this work offer unique possibilities to develop unprecedented instruments that could potentially revolutionize micro- and nanocharacterization and manufacturing techniques, much desired for future advances in the natural sciences, as well as in the micro-fabrication industry.

List of Figures

1 Two-dimensional field distribution in an ideal magnetic quadrupole with hyperbolic pole pieces and focusing action in the x-direction for electrons moving into the paper plane. . 15

2 Schematic path of rays for a quadrupole focusing negatively charged particles in x-direction and defocusing them in y-direction. 18

3 Path of rays for an anamorphically focusing quadrupole doublet with a parallel incident beam of negatively charged particles. 21

4 Path of rays for quadrupole doublet, elliptically collimating the rays from a point source of negatively charged particles. 22

5 Path of rays for quadrupole doublet, anamorphically imaging a point source of negatively charged particles. 24

6 Path of rays for a symmetric quadrupole triplet focusing a parallel incoming beam of negatively charged particles orthomorphically. 27

7 Path of rays for a symmetric quadrupole triplet imaging a source of negatively charged particles orthomorphically. 28

8 Two-dimensional field distribution in an ideal electrostatic quadrupole with hyperbolic pole pieces and focusing action in the y-direction for negatively charged particles. 34

9 Principle geometry of an electron wave obtaining a phase shift by enclosing a magnetic magnetic flux originating from a magnetized wire. 39

10 Attainable focal lengths for a miniaturized magnetic round lens and magnetic quadrupole lens. 41

11 Schematics of the planar structures and the rolling process. 43

12 Planar layout of the chips with the to-be-rolled micro coils in dipole configuration. 44

13 FEM simulations for solenoids with the geometry of the self-assembled micro coils in the dimensions given by the *Protochips* Fusion platform. 45

14 VSM measurements of a CoFeSiB micro wire with a length of 2.7 mm and a radius of the ferromagnetic core of 4.7 µm. 48

15 Simplified principle of the differential phase contrast measurement setup with one condenser lens and without any optics beneath the sample position. 53

16 Renderings of the two analyzed pole piece geometries, the tapered design and the lamella design. 57

17 SEM overview images of the produced magnetic electron vortex beam phase plates driven by self-assembled micro coils with two different FIB taperings of the soft ferromagnetic micro wire pole pieces. 58

18 Maps of the projected magnetic fields emanating from the pole piece tips of the tapered micro coil electron vortex phase plates driven by self-assembled micro coils for different excitation currents. 59

19 Maps of the projected magnetic fields emanating from the pole piece tips of the lamella-shaped micro coil electron vortex phase plates driven by self-assembled micro coils for different excitation currents. . . . 60
20 Averaged axial projected magnetic fields $B_{a,proj}$ emanating from the pole piece tips of the electron vortex phase plates driven by self-assembled micro coils at different excitation currents, reconstructed by means of COM DPC. . . . 62
21 Reconstructed electron phase after the EVB phase plate at an excitation of I_{max}. . . . 63
22 Electron vortex beams produced by the self-assembled micro coil device with a tapered pole piece, recorded in the far field of the object plane, for a set of different stimulation currents and indicated defoci $\triangle$d. . . . 64
23 Electron vortex beams produced by the self-assembled micro coil device with a plane-parallel structured pole piece, recorded in the far field of the object plane, for a set of different stimulation currents and indicated defoci $\triangle$d. Note that at about 36 mA the projected magnetic field and hence the OAM nearly vanishes (c.f. Fig. (19)). . . . 65
24 Planar layout of the chips with the to-be-rolled micro coils in dipole and vector magnet configuration. . . . 67
25 3D renderings of the chips with the self-assembled micro coils in dipole and vector magnet configuration. . . . 67
26 SEM overview images of the produced magnetic deflectors driven by self-assembled micro coils with FIB structured soft ferromagnetic micro wire pole pieces. . . . 68
27 Reconstructed magnetic fields $\mathbf{B}_{proj}$ of a miniaturized dipole assembly, driven by self- assembled micro coils, for different excitation currents and incidence positions. . . . 69
28 Reconstructed magnetic fields $\mathbf{B}_{proj}$ attainable with a miniaturized dipole assembly for $I_{max} = \pm 100$ mA excitation current in higher resolution. . . . 70
29 Hysteresis measurement of the dipole assembly, reconstructed from a series of COM DPC measurements for varying excitation currents. . . . 71
30 COM DPC measurements of a µCPO device with micro wires of 50 µm diameter as pole pieces for varying excitation currents. . . . 73
31 COM DPC measurements of a µCPO device with 80 µm micro wires as pole pieces for varying excitation currents. . . . 74
32 Planar layout of the chips with the to-be-rolled micro coils in quadrupole and vector magnet configuration. . . . 75
33 3D renderings of the chips with the self-assembled micro coils in vector magnet and quadrupole configuration. . . . 75
34 wo-dimensional projected field distribution B_{ideal} of one pole in an ideal magnetic quadrupole with a hyperbolic pole piece and the projected field distribution $B_{a,proj}$ of a homogeneously magnetized wire. . . . 77
35 SEM overview images of the produced magnetic quadrupole lenses driven by self-assembled micro coils with FIB structured soft ferromagnetic micro wire pole pieces. . . . 77

36 Projected magnetic fields within a miniaturized magnetic quadrupole lens. 78
37 Projected magnetic fields within a miniaturized magnetic quadrupole lens, offset corrected 79
38 Stigmatic focusing of the electron beam in a TEM by the miniaturized quadrupole lens assembly. 80
39 Geometrical relations for the ray optical analysis of the focal length of the self-assembled quadrupoles in focusing direction by the intercept theorem. 81
40 Geometrical relations for the ray optical analysis of the focal length of the self-assembled quadrupoles in defocusing direction by the intercept theorem.. 82
41 Diffraction disks recorded in the far field of the specimen plane, where the miniaturized quadrupole assembly is located. 83
42 Images of the modified C3 condenser aperture holder based on a *ThermoFisher* NanoEx i/v specimen holder with the chip containing the miniaturized electromagnets, driven by the self-assembled micro coils. 86
43 Simplified path of rays of the measurement setup, which is used to determine the high frequency angular deflection of the electron beam 87
44 Electron intensity profiles for sinusoidal deflection by the two axially aligned coil pairs of a micro vector magnet driven by self-assembled micro coils. 89
45 Oscillation amplitudes for different stimulation frequencies as obtained from the data shown in Fig. 44. 90
46 Simplified path of rays of the measurement setup, which is used to determine the high frequency real space deflection of the electron beam in the specimen plane. 91
47 Temporally averaged deflection amplitude of the developed stroboscopic setup, where the electron beam is oscillating over the sample deflected by a micro vector magnet located in the C3 aperture plane. 92
48 As fabricated 6-inch wafer with self-assembled miniaturized dipole deflectors. 98

List of Tables

1 Parameters for the spin-coating of the polymer and photoresist layers. 50
2 Values for the measurements shown in Fig. 41, together with their computed absolute and relative differences, $\triangle_{abs}$ and $\triangle_{rel}$, respectively. 84

List of Publications

- R. Huber[1] F. Kern[1], D. D. Karnaushenko, E. Eisner, P. Lepucki, A. Thampi, A. Mirhajivarzaneh, C. Becker, T. Kang, Baunack, B. Büchner, D. Karnaushenko, O. G. Schmidt, A. Lubk
  Tailoring electron beams with high-frequency self-assembled magnetic charged particle micro optics, Nature Communications (in review) (2021).

- F. Kern, J. Krehl, A. Thampi, A. Lubk
  A Hamiltonian mechanics framework for charge particle optics in straight and curved systems, Optik, Volume 242, 2021, DOI: https://doi.org/10.1016/j.ijleo.2021.167242

- F. Kern, M. Linck, D. Wolf, N. Alem, H. Arora, S. Gemming, A. Erbe, A. Zettl, B. Büchner, A. Lubk
  Autocorrected off-axis holography of two-dimensional materials, Physical Review Research, Volume 4, 2020, DOI: https://doi.org/10.1103/PhysRevResearch.2.043360

- F. Kern, M. Linck, D. Wolf, T. Niermann, H. Arora, N. Alem, A. Erbe, S. Gemming, A. Lubk
  Direct Correction of Residual Symmetric Aberrations in Electron Holograms of Weak Phase Objects, Microscopy and Microanalysis, Volume 25, 2019, https://doi.org/10.1017/S1431927619001223

- F. Börrnert, F. Kern, F. Harder, T. Riedel, H. Müller, B. Büchner, A. Lubk
  The Dresden in-situ (S) TEM special with a continuous-flow liquid-helium cryostat, Ultramicroscopy, Volume 203, 2019, DOI: https://doi.org/10.1016/j.ultramic.2019.01.005

- F. Seifert, F. Kern, I. Kézsmárki, U. Rößler, D. Wolf, S. Schneider, D. Pohl, B. Büchner, A. Lubk
  Cryogenic TEM Studies of Bloch and Neel Skyrmion Textures in Lacunar Spinels and Cubic Helimagnets, Microscopy and Microanalysis, Volume 24, 2018,
  DOI: https://doi.org/10.1017/S1431927618005226

- F. Kern, D. Wolf, P. Pschera, A. Lubk
  Quantitative determination of elastic and inelastic attenuation coefficients by off-axis electron holography, Ultramicroscopy, Volume 171, 2016, DOI: https://doi.org/10.1016/j.ultramic.2016.08.011

- A. Lubk, D. Wolf, F. Kern, F. Röder, P. Prete, N. Lovergine, H. Lichte
  Nanoscale three-dimensional reconstruction of elastic and inelastic mean free path lengths by electron holographic tomography, Applied Physics Letters, Volume 105, 2014, DOI: http://dx.doi.org/10.1063/1.4900406

[1]Both Authors contributed equally to this work

References

[1] J. J. Thomson, Cathode rays, The London, Edinburgh, and Dublin Philosophical Magazine and Journal of Science 44 (269) (1897) 293–316. doi:10.1080/14786449708621070. (Cited on pages 1 and 2.)

[2] J. Franck, G. Hertz, Über Zusammenstöße zwischen Elektronen und Molekülen des Quecksilberdampfes und die Ionisierungsspannung desselben, Verhandlungen der Deutschen Physikalischen Gesellschaft 16 (1914) 457–467. (Cited on page 1.)

[3] G. P. Thomson, A. Reid, Diffraction of cathode rays by a thin film, Nature 119 (3007) (1927) 890–890. doi:10.1038/119890a0. (Cited on page 1.)

[4] C. J. Davisson, L. H. Germer, Reflection of electrons by a crystal of nickel, Proceedings of the National Academy of Sciences 14 (4) (1928) 317–322. doi:10.1073/pnas.14.4.317. (Cited on page 1.)

[5] B. v. Borries, E. Ruska, H. Ruska, Bakterien und Viren in Übermikroskopischer Aufnahme, Klinische Wochenschrift 17 (27) (1938) 921–925. (Cited on page 1.)

[6] G. E. Palade, A small particulate component of the cytoplasm, The Journal of Biophysical and Biochemical Cytology 1 (1) (1955) 59–68. doi:10.1083/jcb.1.1.59. (Cited on page 1.)

[7] B. T. Wimberly, D. E. Brodersen, W. M. Clemons, R. J. Morgan-Warren, A. P. Carter, C. Vonrhein, T. Hartsch, V. Ramakrishnan, Structure of the 30S ribosomal subunit, Nature 407 (6802) (2000) 327–339. doi:10.1038/35030006. (Cited on page 1.)

[8] N. Ban, P. Nissen, J. Hansen, P. B. Moore, T. A. Steitz, The complete atomic structure of the large ribosomal subunit at 2.4 Å resolution, Science 289 (5481) (2000) 905–920. doi:10.1126/science.289.5481.905. (Cited on page 1.)

[9] W. C. Röntgen, On a new kind of rays, Nature 53 (1369) (1896) 274–276. (Cited on page 1.)

[10] G. Geloni, E. Saldin, L. Samoylova, E. Schneidmiller, H. Sinn, T. Tschentscher, M. Yurkov, Coherence properties of the european XFEL, New Journal of Physics 12 (3) (2010) 035021. doi:10.1088/1367-2630/12/3/035021. (Cited on page 1.)

[11] R. W. McAllister, R. Hofstadter, Elastic scattering of 188-MeV electrons from the proton and the alpha particle, Phys. Rev. 102 (1956) 851–856. doi:10.1103/PhysRev.102.851. (Cited on page 1.)

[12] E. D. Bloom, D. H. Coward, H. DeStaebler, J. Drees, G. Miller, L. W. Mo, R. E. Taylor, M. Breidenbach, J. I. Friedman, G. C. Hartmann, H. W. Kendall, High-energy inelastic $e - p$ scattering at 6° and 10°, Phys. Rev. Lett. 23 (1969) 930–934. doi:10.1103/PhysRevLett.23.930. (Cited on page 1.)

[13] M. Breidenbach, J. I. Friedman, H. W. Kendall, E. D. Bloom, D. H. Coward, H. DeStaebler, J. Drees, L. W. Mo, R. E. Taylor, Observed behavior of highly inelastic electron-proton scattering, Phys. Rev. Lett. 23 (1969) 935–939. doi:10.1103/PhysRevLett.23.935. (Cited on page 1.)

[14] J. E. Augustin, A. M. Boyarski, M. Breidenbach, F. Bulos, J. T. Dakin, G. J. Feldman, G. E. Fischer, D. Fryberger, G. Hanson, B. Jean-Marie, R. R. Larsen, V. Lüth, H. L. Lynch, D. Lyon, C. C. Morehouse, J. M. Paterson, M. L. Perl, B. Richter, P. Rapidis, R. F. Schwitters, W. M. Tanenbaum, F. Vannucci, G. S. Abrams, D. Briggs, W. Chinowsky, C. E. Friedberg, G. Goldhaber, R. J. Hollebeek, J. A. Kadyk, B. Lulu, F. Pierre, G. H. Trilling, J. S. Whitaker, J. Wiss, J. E. Zipse, Discovery of a narrow resonance in e^+e^- annihilation, Phys. Rev. Lett. 33 (1974) 1406–1408. doi:10.1103/PhysRevLett.33.1406. (Cited on page 1.)

[15] J. J. Aubert, U. Becker, P. J. Biggs, J. Burger, M. Chen, G. Everhart, P. Goldhagen, J. Leong, T. McCorriston, T. G. Rhoades, M. Rohde, S. C. C. Ting, S. L. Wu, Y. Y. Lee, Experimental observation of a heavy particle J, Phys. Rev. Lett. 33 (1974) 1404–1406. doi:10.1103/PhysRevLett.33.1404. (Cited on page 1.)

[16] S. W. Herb, D. C. Hom, L. M. Lederman, J. C. Sens, H. D. Snyder, J. K. Yoh, J. A. Appel, B. C. Brown, C. N. Brown, W. R. Innes, K. Ueno, T. Yamanouchi, A. S. Ito, H. Jöstlein, D. M. Kaplan, R. D. Kephart, Observation of a dimuon resonance at 9.5 GeV in 400-GeV proton-nucleus collisions, Phys. Rev. Lett. 39 (1977) 252–255. doi:10.1103/PhysRevLett.39.252. (Cited on page 1.)

[17] UA1 Collaboration, Experimental observation of isolated large transverse energy electrons with associated missing energy at s=540 GeV, Physics Letters B 122 (1) (1983) 103–116. doi:https://doi.org/10.1016/0370-2693(83)91177-2. (Cited on page 1.)

[18] UA2 Collaboration, Observation of single isolated electrons of high transverse momentum in events with missing transverse energy at the CERN pp collider, Physics Letters B 122 (5) (1983) 476–485. doi:https://doi.org/10.1016/0370-2693(83)91605-2. (Cited on page 1.)

[19] ATLAS Collaboration, Observation of a new particle in the search for the standard model higgs boson with the ATLAS detector at the LHC, Physics Letters B 716 (1) (2012) 1–29. doi:https://doi.org/10.1016/j.physletb.2012.08.020. (Cited on page 1.)

[20] CMS Collaboration, Observation of a new boson at a mass of 125 GeV with the CMS experiment at the LHC, Physics Letters B 716 (1) (2012) 30–61. doi:https://doi.org/10.1016/j.physletb.2012.08.021. (Cited on page 1.)

[21] A. Feist, N. Bach, N. Rubiano da Silva, T. Danz, M. Möller, K. E. Priebe, T. Domröse, J. G. Gatzmann, S. Rost, J. Schauss, S. Strauch, R. Bormann, M. Sivis, S. Schäfer, C. Ropers, Ultrafast transmission electron microscopy using a laser-driven field emitter: Femtosecond resolution with a high coherence electron beam, Ultramicroscopy 176 (2017) 63–73, 70th Birthday of Robert Sinclair and 65th Birthday of Nestor J. Zaluzec PICO 2017 – Fourth Conference on Frontiers of Aberration Corrected Electron Microscopy. doi:https://doi.org/10.1016/j.ultramic.2016.12.005. (Cited on page 1.)

[22] F. Houdellier, G. Caruso, S. Weber, M. Kociak, A. Arbouet, Development of a high brightness ultrafast transmission electron microscope based on a laser-driven cold field emission source, Ultramicroscopy 186 (2018) 128–138. doi:https://doi.org/10.1016/j.ultramic.2017.12.015. (Cited on pages 1 and 95.)

[23] R. Srinivasan, V. Lobastov, C.-Y. Ruan, A. Zewail, Ultrafast electron diffraction (UED), Helvetica Chimica Acta 86 (6) (2003) 1761–1799. doi:https://doi.org/10.1002/hlca.200390147. (Cited on page 1.)

[24] P. Baum, A. H. Zewail, Breaking resolution limits in ultrafast electron diffraction and microscopy, Proceedings of the National Academy of Sciences 103 (44) (2006) 16105–16110. doi:10.1073/pnas.0607451103. (Cited on page 1.)

[25] F. Zhou, J. Williams, C.-Y. Ruan, Femtosecond electron spectroscopy in an electron microscope with high brightness beams, Chemical Physics Letters 683 (2017) 488–494, ahmed Zewail (1946-2016) Commemoration Issue of Chemical Physics Letters. doi:https://doi.org/10.1016/j.cplett.2017.03.019. (Cited on page 1.)

[26] E. Pomarico, Y.-J. Kim, F. J. García de Abajo, O.-H. Kwon, F. Carbone, R. M. van der Veen, Ultrafast electron energy-loss spectroscopy in transmission electron microscopy, MRS Bulletin 43 (7) (2018) 497–503. doi:10.1557/mrs.2018.148. (Cited on page 1.)

[27] M. Plücker, Observations on the electrical discharge through rarefied gases, The London, Edinburgh, and Dublin Philosophical Magazine and Journal of Science 16 (109) (1858) 408–418. doi:10.1080/14786445808642591. (Cited on page 2.)

[28] A. Schuster, The discharge of electricity through gases, Proceedings of the Royal Society of London 47 (1890) 526–559. (Cited on page 2.)

[29] L.-V. de Broglie, Recherches sur la theorie des quanta, Ph.D. thesis, Universitet de Paris (1924). (Cited on page 2.)

[30] H. Busch, Berechnung der Bahn von Kathodenstrahlen im axialsymmetrischen elektromagnetischen Felde, Annalen der Physik 386 (25) (1926) 974–993. doi:10.1002/andp.19263862507. (Cited on page 2.)

[31] H. Busch, Über die Wirkungsweise der Konzentrierungsspule bei der Braunschen Röhre, Archiv für Elektrotechnik 18 (6) (1927) 583–594. doi:10.1007/BF01656203. (Cited on page 2.)

[32] E. Ruska, M. Knoll, Die magnetische Sammelspule für schnelle Elektronenstrahlen, Z. techn. Physik. 12 (1931) 389–400. (Cited on page 2.)

[33] C. J. Davisson, C. J. Calbick, Electron lenses, Phys. Rev. 38 (1931) 585. doi:10.1103/PhysRev.38.579. (Cited on page 2.)

[34] R. Wideröe, Über ein neues Prinzip zur Herstellung hoher Spannungen, Archiv für Elektrotechnik 21 (4) (1928) 387–406. doi:10.1007/BF01656341. (Cited on page 2.)

[35] O. Scherzer, Über einige Fehler von Elektronenlinsen, Zeitschrift für Physik 101 (9-10) (1936) 593–603. doi:10.1007/BF01349606. (Cited on page 2.)

[36] M. Haider, S. Uhlemann, E. Schwan, H. Rose, B. Kabius, K. Urban, Electron microscopy image enhanced, Nature 392 (1998) 768. (Cited on page 2.)

[37] J. Gaskin, T. Abbott, S. Medley, K. Patty, D. Gregory, K. Thaisen, B. Ramsey, G. Jerman, A. Sampson, R. Harvey, L. Taylor, Miniaturized scanning electron microscope for in situ planetary studies, Earth and Space (2010) 1246–1257doi:10.1061/41096(366)113. (Cited on page 2.)

[38] Drexler, Nanosystems: Molecular Machinery, Manufacturing, and Computation, John Wiley & Sons, 1992. (Cited on pages 3, 35, 66, and 85.)

[39] T. H. P. Chang, D. P. Kern, L. P. Muray, Arrayed miniature electron beam columns for high throughput sub-100 nm lithography, Journal of Vacuum Science & Technology B: Microelectronics and Nanometer Structures Processing, Measurement, and Phenomena 10 (6) (1992) 2743–2748. doi:10.1116/1.585994. (Cited on page 3.)

[40] M. Mankos, S. Coyle, A. Fernandez, A. Sagle, P. Allen, W. Owens, J. Sullivan, T. H. P. Chang, Multisource optimization of a column for electron lithography, Journal of Vacuum Science & Technology B: Microelectronics and Nanometer Structures Processing, Measurement, and Phenomena 18 (6) (2000) 3010–3016. doi:10.1116/1.1321752. (Cited on page 3.)

[41] T. Chang, M. Mankos, K. Y. Lee, L. P. Muray, Multiple electron-beam lithography, Microelectronic Engineering 57-58 (2001) 117–135, micro- and Nano-Engineering 2000. doi:https://doi.org/10.1016/S0167-9317(01)00528-7. (Cited on page 3.)

[42] H. S. Kim, Y. B. Lee, S. W. Choi, H. W. Kim, D.-W. Kim, S. J. Ahn, T. S. Oh, Y.-H. Song, B. C. Park, S. J. Lim, Development of arrayed microcolumns and field emitters, Japanese Journal of Applied Physics 56 (6S1) (2017) 06GA02. doi:10.7567/jjap.56.06ga02. (Cited on page 3.)

[43] H. Yasuda, S. Arai, J. Kai, Y. Ooae, T. Abe, S. Maruyama, T. Kiuchi, Multielectron beam blanking aperture array system SYNAPSE-2000, Journal of Vacuum Science & Technology B: Microelectronics and Nanometer Structures Processing, Measurement, and Phenomena 14 (6) (1996) 3813–3820. doi:10.1116/1.588673. (Cited on page 3.)

[44] G. Winograd, V. Krishnamurthi, R. Garcia, L. H. Veneklasen, M. Mankos, F. Pease, Demonstration of multiblanker electron-beam technology, Journal of Vacuum Science & Technology B: Microelectronics and Nanometer Structures Processing, Measurement, and Phenomena 18 (6) (2000) 3052–3056. doi:10.1116/1.1321757. (Cited on page 3.)

[45] M. Muraki, S. Gotoh, New concept for high-throughput multielectron beam direct write system, Journal of Vacuum Science & Technology B: Microelectronics and Nanometer Structures Processing, Measurement, and Phenomena 18 (6) (2000) 3061–3066. doi:10.1116/1.1320798. (Cited on page 3.)

[46] M. Nakasuji, S. Yoshikawa, T. Satake, N. Noji, Feasibility study of multiple-beam scanning electron microscopy for defect inspection, Japanese Journal of Applied Physics 44 (7B) (2005) 5570–5574. doi:10.1143/jjap.44.5570. (Cited on page 3.)

[47] O. Kamimura, S. Tanimoto, H. Ohta, Y. Nakayama, M. Sakakibara, Y. Sohda, M. Muraki, S. Gotoh, M. Hosoda, Y. Someda, K. Tamamori, F. Hirose, K. Nagae, K. Kato, M. Okunuki, Optical properties of a multibeam column with a single-electron source, Journal of Vacuum Science & Technology B: Microelectronics and Nanometer Structures Processing, Measurement, and Phenomena 25 (1) (2007) 140–146. doi:10.1116/1.2429674. (Cited on page 3.)

[48] Y. Zhang, P. Kruit, High brightness 100-electron-beam source for high-resolution applications, Journal of Vacuum Science & Technology B: Microelectronics and Nanometer Structures Processing, Measurement, and Phenomena 25 (6) (2007) 2239–2244. doi:10.1116/1.2794073. (Cited on page 3.)

[49] A. Mohammadi-Gheidari, C. W. Hagen, P. Kruit, Multibeam scanning electron microscope: Experimental results, Journal of Vacuum Science & Technology B 28 (6) (2010) C6G5–C6G10. doi:10.1116/1.3498749. (Cited on page 3.)

[50] T. Ichimura, Y. Ren, P. Kruit, A large current scanning electron microscope with MEMS-based multibeam optics, Microelectronic Engineering 113 (2014) 109–113. doi:https://doi.org/10.1016/j.mee.2013.07.008. (Cited on page 3.)

[51] T. Doi, M. Yamazaki, T. Ichimura, Y. Ren, P. Kruit, A high-current scanning electron microscope with multi-beam optics, Microelectronic Engineering 159 (2016) 132–138, micro/Nano Devices and Systems 2015. doi:https://doi.org/10.1016/j.mee.2016.02.055. (Cited on page 3.)

[52] E. Slot, M. J. Wieland, G. de Boer, P. Kruit, G. F. ten Berge, A. M. C. Houkes, R. Jager, T. van de Peut, J. J. M. Peijster, S. W. H. K. Steenbrink, T. F. Teepen, A. H. V. van Veen, B. J. Kampherbeek, MAPPER: high throughput maskless lithography, in: F. M. Schellenberg (Ed.), Emerging Lithographic Technologies XII, Vol. 6921, International Society for Optics and Photonics, SPIE, 2008, pp. 517 – 525. doi:10.1117/12.771965. (Cited on page 3.)

[53] H. Boersch, K.-J. Hanszen, Abbildung von Verdampfungsquellen mit dem Lochkameraverfahren, Zeitschrift für Physik 139 (3) (1954) 243–250. doi:10.1007/BF01375185. (Cited on pages 3 and 97.)

[54] G. Liebmann, The symmetrical magnetic electron microscope objective lens with lowest spherical aberration, Proceedings of the Physical Society. Section B 64 (11) (1951) 972–977. doi:10.1088/0370-1301/64/11/305. (Cited on page 3.)

[55] G. Liebmann, The magnetic pinhole electron lens, Proceedings of the Physical Society. Section B 68 (9) (1955) 682–685. doi:10.1088/0370-1301/68/9/414. (Cited on page 3.)

[56] L. S. Hordon, R. F. W. Pease, Scanning tunneling microscope microlens with magnetic focusing, Journal of Vacuum Science & Technology B: Microelectronics Processing and Phenomena 8 (6) (1990) 1686–1690. doi:10.1116/1.585140. (Cited on page 3.)

[57] T. H. P. Chang, D. P. Kern, L. P. Muray, Microminiaturization of electron optical systems, Journal of Vacuum Science & Technology B: Microelectronics Processing and Phenomena 8 (6) (1990) 1698–1705. doi:10.1116/1.585142. (Cited on pages 3 and 97.)

[58] T. Tajima, J. M. Dawson, Laser electron accelerator, Phys. Rev. Lett. 43 (1979) 267–270. doi:10.1103/PhysRevLett.43.267. (Cited on page 3.)

[59] B. Jiang, G. Kirkman, N. Reinhardt, High brightness electron beam produced by a ferroelectric cathode, Applied Physics Letters 66 (10) (1995) 1196–1198. doi:10.1063/1.113855. (Cited on page 3.)

[60] R. Weingartner, M. Fuchs, A. Popp, S. Raith, S. Becker, S. Chou, M. Heigoldt, K. Khrennikov, J. Wenz, T. Seggebrock, B. Zeitler, Z. Major, J. Osterhoff, F. Krausz, S. Karsch, F. Grüner, Imaging laser-wakefield-accelerated electrons using miniature magnetic quadrupole lenses, Phys. Rev. ST Accel. Beams 14 (2011) 052801. doi:10.1103/PhysRevSTAB.14.052801. (Cited on page 3.)

[61] T. H. P. Chang, Proximity effect in electron-beam lithography, Journal of Vacuum Science and Technology 12 (6) (1975) 1271–1275. doi:10.1116/1.568515. (Cited on page 4.)

[62] E. D. Wolf, F. S. Ozdemir, W. E. Perkins, P. J. Coane, Response of the positive electron resist elvacite 204l to kilovolt electron beam exposure, Record of the 11th Symposium on Electron, Ion and Laser Beam Technology (1971) 331. (Cited on page 4.)

[63] A. N. Broers, Resolution, overlay, and field size for lithography systems, IEEE Transactions on Electron Devices 28 (11) (1981) 1268–1278. doi:10.1109/T-ED.1981.20599. (Cited on page 4.)

[64] W. Hu, G. Bernstein, K. Sarveswaran, M. Lieberman, Low temperature development of PMMA for sub-10-nm electron beam lithography, Third IEEE Conference on Nanotechnology (2003). doi:10.1109/NANO.2003.1230983. (Cited on page 4.)

[65] W. W. Hu, K. Sarveswaran, M. Lieberman, G. H. Bernstein, Sub-10 nm electron beam lithography using cold development of polymethylmethacrylate, Journal of Vacuum Science & Technology B: Microelectronics and Nanometer Structures 22 (4) (2004) 1711. doi:DOI:10.1116/1.1763897. (Cited on page 4.)

[66] I.-B. Baek, J.-H. Yang, W.-J. Cho, C.-G. Ahn, K. Im, S. Lee, Electron beam lithography patterning of sub-10 nm line using hydrogen silsesquioxane for nanoscale device applications, Journal of Vacuum Science & Technology B: Microelectronics and Nanometer Structures 23 (6) (2005) 3120. doi:https://doi.org/10.1116/1.2132328. (Cited on page 4.)

[67] K. Yamazaki, M. S. Saifullah, H. Namatsu, K. Kurihara, Sub-10-nm electron-beam lithography with sub-10-nm overlay accuracy (jul 2000). doi:10.1117/12.390084. (Cited on page 4.)

[68] V. R. Manfrinato, L. Zhang, D. Su, H. Duan, R. G. Hobbs, E. A. Stach, K. K. Berggren, Resolution limits of electron-beam lithography toward the atomic scale, Nano Letters 13 (4) (2013) 1555–1558. doi:10.1021/nl304715p. (Cited on page 4.)

[69] L.-C. Chang, C. Nien, J.-H. Ye, C.-H. Chung, V.-C. Su, C.-H. Wu, C.-H. Kuan, A comprehensive model for sub-10 nm electron-beam patterning through the short-time and cold development, Nanotechnology 28 (42) (2017) 425301. doi:https://doi.org/10.1088/1361-6528/aa8005. (Cited on page 4.)

[70] A. Cattoni, D. Mailly, O. Dalstein, M. Faustini, G. Seniutinas, B. Rösner, C. David, Sub-10 nm electron and helium ion beam lithography using a recently developed alumina resist, Microelectronic Engineering 193 (2018) 18–22. doi:10.1016/j.mee.2018.02.015. (Cited on page 4.)

[71] J. Harrison, A. Joshi, J. Lake, R. Candler, P. Musumeci, Surface-micromachined magnetic undulator with period length between 10 µm and 1 mm for advanced light sources, Physical Review Accelerators and Beams 15 (7) (2012) 070703. doi:10.1103/physrevstab.15.070703. (Cited on pages 4, 42, and 97.)

[72] J. Harrison, A. Joshi, Y. Hwang, O. Paydar, J. Lake, P. Musumeci, R. N. Candler, Surface-micromachined electromagnets for 100 µm-scale undulators and focusing optics, Physics Procedia 52 (2014) 19–26. doi:10.1016/j.phpro.2014.06.005. (Cited on pages 4, 42, and 97.)

[73] F. Zernicke, Das Phasenkontrastverfahren bei der mikroskopischen Beobachtung, Zeitschrift für technische Physik 16 (1935) 454–457. (Cited on page 4.)

[74] H. Boersch, Über die Kontraste von Atomen im Elektronenmikroskop, Zeitschrift für Naturforschung 2a (1947) 615–633. (Cited on page 4.)

[75] A. W. Agar, R. S. M. Revell, R. A. Scott, A preliminary report on attempts to realise a phase contrast electron microscope, European Regional Conference on Electron Microscopy, Delft 52 (1949) 1–3. (Cited on page 4.)

[76] R. Danev, K. Nagayama, Phase plates for transmission electron microscopy, Methods in Enzymology 481 (2010) 343–369. doi:https://doi.org/10.1016/S0076-6879(10)81014-6. (Cited on pages 4 and 5.)

[77] S. Hettler, E. Kano, M. Dries, D. Gerthsen, L. Pfaffmann, M. Bruns, M. Beleggia, M. Malac, Charging of carbon thin films in scanning and phase-plate transmission electron microscopy, Ultramicroscopy 184 (2018) 252–266. doi:https://doi.org/10.1016/j.ultramic.2017.09.009. (Cited on page 5.)

[78] R. Danev, B. Buijsse, M. Khoshouei, J. M. Plitzko, W. Baumeister, Volta potential phase plate for in-focus phase contrast transmission electron microscopy, Proceedings of the National Academy of Sciences 111 (44) (2014) 15635–15640. doi:10.1073/pnas.1418377111. (Cited on pages 5 and 31.)

[79] R. Danev, W. Baumeister, Cryo-EM single particle analysis with the Volta phase plate, eLife 5 (mar 2016). doi:10.7554/elife.13046. (Cited on page 5.)

[80] E. Majorovits, B. Barton, K. Schultheiß, F. Pérez-Willard, D. Gerthsen, R. Schröder, Optimizing phase contrast in transmission electron microscopy with an electrostatic Boersch phase plate, Ultramicroscopy 107 (2-3) (2007) 213–226. doi:10.1016/j.ultramic.2006.07.006. (Cited on page 5.)

[81] J. Verbeeck, A. Béché, K. Müller-Caspary, G. Guzzinati, M. A. Luong, M. D. Hertog, Demonstration of a 2 x 2 programmable phase plate for electrons, Ultramicroscopy 190 (2018) 58–65. doi:10.1016/j.ultramic.2018.03.017. (Cited on page 5.)

[82] H. Dohi, P. Kruit, Design for an aberration corrected scanning electron microscope using miniature electron mirrors, Ultramicroscopy 189 (2018) 1–23. doi:10.1016/j.ultramic.2018.03.009. (Cited on page 5.)

[83] R. Danev, K. Nagayama, Complex observation in electron microscopy: IV. reconstruction of complex object wave from conventional and half plane phase plate image pair, Journal of the Physical Society of Japan 73 (10) (2004) 2718–2724. doi:https://doi.org/10.1143/JPSJ.73.2718. (Cited on page 5.)

[84] N. Osagabe, S. Nomura, T. Matsuda, J. Endo, A. Tonomura, H. Umezaki, S. K, Phase contrast electron microscope (Jan. 1985). (Cited on page 5.)

[85] K. Nagayama, Development of phase plates for electron microscopes and their biological application, European Biophysics Journal 37 (4) (2008) 345–358. doi:https://doi.org/10.1007/s00249-008-0264-5. (Cited on page 5.)

[86] T. Tanji, H. Niimi, J. Usukura, Y. Yamamoto, S. Ohta, Electron differential phase microscopy with an A-B effect phase plate, Microscopy and Microanalysis 21 (S3) (2015) 1945–1946. doi:https://doi.org/10.1017/S1431927615010508. (Cited on page 5.)

[87] A. H. Tavabi, M. Beleggia, V. Migunov, A. Savenko, O. Öktem, R. E. Dunin-Borkowski, G. Pozzi, Tunable Ampere phase plate for low dose imaging of biomolecular complexes, Scientific Reports 8 (1) (apr 2018). doi:10.1038/s41598-018-23100-3. (Cited on page 5.)

[88] P. L. Kapitza, P. A. M. Dirac, The reflection of electrons from standing light waves, Mathematical Proceedings of the Cambridge Philosophical Society 29 (2) (1933) 297–300. doi:10.1017/s0305004100011105. (Cited on page 5.)

[89] P. H. Bucksbaum, M. Bashkansky, T. J. McIlrath, Scattering of electrons by intense coherent light, Physical Review Letters 58 (4) (1987) 349–352. doi:10.1103/physrevlett.58.349. (Cited on page 5.)

[90] O. Schwartz, J. J. Axelrod, S. L. Campbell, C. Turnbaugh, R. M. Glaeser, H. Müller, Laser phase plate for transmission electron microscopy, Nature Methods 16 (10) (2019) 1016–1020. doi:https://doi.org/10.1038/s41592-019-0552-2. (Cited on page 6.)

[91] R. Shiloh, R. Remez, P.-H. Lu, L. Jin, Y. Lereah, A. H. Tavabi, R. E. Dunin-Borkowski, A. Arie, Spherical aberration correction in a scanning transmission electron microscope using a sculpted thin film, Ultramicroscopy 189 (2018) 46–53. doi:https://doi.org/10.1016/j.ultramic.2018.03.016. (Cited on page 6.)

[92] R. A. Beth, Direct detection of the angular momentum of light, Physical Review 48 (5) (1935) 471–471. doi:10.1103/physrev.48.471. (Cited on page 6.)

[93] M. Uchida, A. Tonomura, Generation of electron beams carrying orbital angular momentum, Nature 464 (7289) (2010) 737–739. doi:10.1038/nature08904. (Cited on page 6.)

[94] J. Verbeeck, H. Tian, P. Schattschneider, Production and application of electron vortex beams, Nature 467 (7313) (2010) 301–304. doi:10.1038/nature09366. (Cited on page 6.)

[95] A. H. Tavabi, H. Larocque, P.-H. Lu, M. Duchamp, V. Grillo, E. Karimi, R. E. Dunin-Borkowski, G. Pozzi, Generation of electron vortices using nonexact electric fields, Physical Review Research 2 (1) (2020) 013185. doi:https://doi.org/10.1103/PhysRevResearch.2.013185. (Cited on page 6.)

[96] A. Béché, R. V. Boxem, G. V. Tendeloo, J. Verbeeck, Magnetic monopole field exposed by electrons, Nature Physics 10 (1) (2013) 26–29. doi:10.1038/nphys2816. (Cited on pages 6, 38, and 64.)

[97] R. Jagannathan, R. Simon, E. Sudarshan, N. Mukunda, Quantum theory of magnetic electron lenses based on the Dirac equation, Physics Letters A 134 (8) (1989) 457–464. doi:https://doi.org/10.1016/0375-9601(89)90685-3. (Cited on page 8.)

[98] R. Jagannathan, Quantum theory of electron lenses based on the Dirac equation, Phys. Rev. A 42 (1990) 6674–6689. doi:10.1103/PhysRevA.42.6674. (Cited on page 8.)

[99] R. Jagannathan, S. Khan, Quantum theory of the optics of charged particles, Advances in Imaging and Electron Physics 97 (1996) 257–358. doi:https://doi.org/10.1016/S1076-5670(08)70096-X. (Cited on page 8.)

[100] R. Jagannathan, S. A. Khan, Quantum Mechanics of Charged Particle Beam Optics, CRC Press, 2019. doi:10.1201/9781315232515. (Cited on page 8.)

[101] R. Jagannathan, Quantum mechanics of Dirac particle beam optics: single particle theory, 2020, pp. 568–577. doi:10.1142/9789812777447_0047. (Cited on page 8.)

[102] S. A. Khan, R. Jagannathan, Quantum mechanics of round magnetic electron lenses with Glaser and power law models of b(z), Optik 229 (2021) 166303. doi:https://doi.org/10.1016/j.ijleo.2021.166303. (Cited on page 8.)

[103] B. K. Jap, R. M. Glaeser, The scattering of high-energy electrons. i. Feynman path-integral formulation, Acta Crystallographica Section A 34 (1) (1978) 94–102. doi:https://doi.org/10.1107/S0567739478000170. (Cited on page 8.)

[104] A. Lubk, Quantitative off-axis electron holography and (multi-)ferroic interfaces, phdthesis, Technische Universität Dresden (2010). (Cited on page 8.)

[105] L. Reimer, H. Kohl, 3. Wave Optics of Electrons, Springer New York, New York, NY, 2008, pp. 43–74. doi:10.1007/978-0-387-40093-8_3. (Cited on page 8.)

[106] W. Glaser, Strenge Berechnung magnetischer Linsen der Feldform $H = \frac{H_0}{1+(z/a)^2}$, Zeitschrift für Physik 117 (1941) 285 – 315. (Cited on page 8.)

[107] G. Liebmann, An improved method of numerical ray tracing through electron lenses, Proceedings of the Physical Society. Section B 62 (1949) 753. doi:10.1088/0370-1301/62/12/301. (Cited on page 8.)

[108] F. Kern, J. Krehl, A. Thampi, A. Lubk, A hamiltonian mechanics framework for charge particle optics in straight and curved systems, Optik 242 (2021) 167242. doi:https://doi.org/10.1016/j.ijleo.2021.167242. (Cited on pages 10 and 13.)

[109] P. Hawkes, E. Kasper, Chapter 26 - chromatic aberrations, in: P. Hawkes, E. Kasper (Eds.), Principles of Electron Optics (Second Edition), second edition Edition, Elsevier, 2018, pp. 443–461. doi:https://doi.org/10.1016/B978-0-08-102256-6.00026-2. (Cited on page 10.)

[110] T. Frankel, The Lie Derivative, 3rd Edition, Cambridge University Press, 2011, p. 125–154. doi:10.1017/CBO9781139061377.009. (Cited on page 11.)

[111] W. Magnus, On the exponential solution of differential equations for a linear operator, Communications on Pure and Applied Mathematics 7 (4) (1954) 649–673. doi:https://doi.org/10.1002/cpa.3160070404. (Cited on page 13.)

[112] D. Bernstein, W. So, Some explicit formulas for the matrix exponential, IEEE Transactions on Automatic Control 38 (1993) 1228–1232. (Cited on page 17.)

[113] P. W. Hawkes, Quadrupole Optics, Springer Tracts in Modern Physics, Springer Berlin Heidelberg, 1966. (Cited on pages 17 and 29.)

[114] A. J. Dragt, Lectures on nonlinear orbit dynamics, AIP Conference Proceedings 87 (1) (1982) 147–313. doi:10.1063/1.33615. (Cited on page 17.)

[115] H. Wollnik, 3 - quadrupole lenses, in: H. Wollnik (Ed.), Optics of Charged Particles, Academic Press, 1987, pp. 48–88. doi:https://doi.org/10.1016/B978-0-12-762130-2.50006-6. (Cited on pages 17 and 19.)

[116] J. K. Lim, P. Frigola, G. Travish, J. B. Rosenzweig, S. G. Anderson, W. J. Brown, J. S. Jacob, C. L. Robbins, A. M. Tremaine, Adjustable, short focal length permanent-magnet quadrupole based electron beam final focus system, Phys. Rev. ST Accel. Beams 8 (2005) 072401. doi:10.1103/PhysRevSTAB.8.072401. (Cited on page 27.)

[117] H. D. Bauer, Ein elektrostatisches Vierpolsystem als Objektiv im Elektronenmikroskop, Naturwissenschaften 51 (24) (1964) 632–632. doi:10.1007/BF00623665. (Cited on page 29.)

[118] S. Kowalski, H. Enge, Beam rotator, in: Proceedings of The 4th International Conference on Magnet Technology, Upton, NY, 1972, p. 182. (Cited on page 29.)

[119] H. D. Bauer, Elektronenoptische Eigenschaften einer elektrostatischen Objektivlinse mit Vierpolsymmetrie, Optik 26 (6) (1965) 596–609. (Cited on page 29.)

[120] M. Wautelet, Nanotechnologie, Oldenbourg, 2008, Ch. 1. Die Revolution der Nanotechnologie, pp. 1 – 26. (Cited on page 30.)

[121] O. Cugat, J. Delamare, G. Reyne, Magnetic micro-actuators and systems (MAGMAS), IEEE Transactions on Magnetics 39 (6) (2003) 3607–3612. doi:10.1109/tmag.2003.816763. (Cited on pages 30 and 36.)

[122] H. Lichte, M. Lehmann, Electron holography - basics and applications, Reports on Progress in Physics 71 (1) (2008) 016102. (Cited on pages 30 and 54.)

[123] F. Paschen, Über die zum Funkenübergang in Luft, Wasserstoff und Kohlensäure bei verschiedenen Drucken erforderliche Potentialdifferenz, Annalen der Physik 273 (5) (1889) 69–96. doi:https://doi.org/10.1002/andp.18892730505. (Cited on page 31.)

[124] J. Townsend, Electricity in Gases, Clarendon Press, 1915. (Cited on page 31.)

[125] J. B. Rosenzweig, D. B. Cline, R. N. Dexter, D. J. Larson, A. W. Leonard, K. R. Mengelt, J. C. Sprott, F. E. Mills, F. T. Cole, Plasma wake field acceleration: A proposed experimental test, in: AIP Conference Proceedings, 1985. doi:https://doi.org/10.1063/1.35323. (Cited on pages 32 and 97.)

[126] J. B. Rosenzweig, D. B. Cline, B. Cole, H. Figueroa, W. Gai, R. Konecny, J. Norem, P. Schoessow, J. Simpson, Experimental observation of plasma wake-field acceleration, Physical Review Letters 61 (1) (1988) 98–101. doi:10.1103/physrevlett.61.98. (Cited on pages 32 and 97.)

[127] J. Breuer, P. Hommelhoff, Laser-based acceleration of nonrelativistic electrons at a dielectric structure, Physical Review Letters 111 (13) (2013) 134803. doi:10.1103/physrevlett.111.134803. (Cited on pages 32, 97, and 99.)

[128] J. Duris, P. Musumeci, M. Babzien, M. Fedurin, K. Kusche, R. K. Li, J. Moody, I. Pogorelsky, M. Polyanskiy, J. B. Rosenzweig, Y. Sakai, C. Swinson, E. Threlkeld, O. Williams, V. Yakimenko, High-quality electron beams from a helical inverse free-electron laser accelerator, Nature Communications 5 (1) (sep 2014). doi:10.1038/ncomms5928. (Cited on pages 32, 97, and 99.)

[129] C. Neusel, G. A. Schneider, Size-dependence of the dielectric breakdown strength from nano- to millimeter scale, Journal of the Mechanics and Physics of Solids 63 (2014) 201–213. doi:https://doi.org/10.1016/j.jmps.2013.09.009. (Cited on page 32.)

[130] F. Hinterberger, Ion optics with electrostatic lenses (2006). doi:10.5170/CERN-2006-012.27. (Cited on page 33.)

[131] F. Hinterberger, Ionenoptik mit elektrostatischen Linsen, Springer Berlin Heidelberg, Berlin, Heidelberg, 2008, pp. 211–238. doi:10.1007/978-3-540-75282-0_5. (Cited on page 33.)

[132] H. Liebl, Lenses: Basic Optics, Springer Berlin Heidelberg, Berlin, Heidelberg, 2008, pp. 1–43. doi:10.1007/978-3-540-71925-0_1. (Cited on page 33.)

[133] M. Szilagyi, 7 - electrostatic lenses, in: Electron and Ion Optics, Springer US, 1988, Ch. Motion of Charged Particles in Electric and Magnetic Fields, pp. 313–393. doi:10.1007/978-1-4613-0923-9. (Cited on page 33.)

[134] W. Ehrenberg, R. E. Siday, The refractive index in electron optics and the principles of dynamics, Proceedings of the Physical Society. Section B 62 (1) (1949) 8–21. doi:10.1088/0370-1301/62/1/303. (Cited on page 35.)

[135] Y. Aharonov, D. Bohm, Significance of electromagnetic potentials in the quantum theory, Phys. Rev. 115 (1959) 485–491. doi:10.1103/PhysRev.115.485. (Cited on page 35.)

[136] K. F. Müller, Berechnung der Induktivität von Spulen, Archiv für Elektrotechnik 17 (3) (1926) 336–353. doi:10.1007/bf01655986. (Cited on page 37.)

[137] J. Verbeeck, G. Van Tendeloo, Charged particle vortex wave generation (2011). (Cited on page 38.)

[138] P. Dirac, Quantised singularities in the electromagnetic field, Proceedings of the Royal Society of London. Series A, Containing Papers of a Mathematical and Physical Character 133 (821) (1931) 60–72. doi:10.1098/rspa.1931.0130. (Cited on page 38.)

[139] K. Bliokh, I. Ivanov, G. Guzzinati, L. Clark, R. Van Boxem, A. Béché, R. Juchtmans, M. Alonso, P. Schattschneider, F. Nori, J. Verbeeck, Theory and applications of free-electron vortex states, Physics Reports 690 (2017) 1–70, theory and applications of free-electron vortex states. doi:https://doi.org/10.1016/j.physrep.2017.05.006. (Cited on pages 38, 66, and 94.)

[140] P. van Cittert, Die Wahrscheinliche Schwingungsverteilung in Einer von Einer Lichtquelle Direkt Oder Mittels Einer Linse Beleuchteten Ebene, Physica 1 (1) (1934) 201–210. doi:https://doi.org/10.1016/S0031-8914(34)90026-4. (Cited on page 39.)

[141] R. F. Egerton, 2. Electron Optics, Springer US, Boston, MA, 2005, pp. 27–55. doi:10.1007/0-387-26016-1_2. (Cited on page 40.)

[142] A. Béché, B. Goris, B. Freitag, J. Verbeeck, Development of a fast electromagnetic beam blanker for compressed sensing in scanning transmission electron microscopy, Applied Physics Letters 108 (9) (2016) 093103. doi:10.1063/1.4943086. (Cited on page 42.)

[143] A. Béché, Dynamic generation of electron vortex beams in a (S)TEM, holography workshop in Berlin, not published (2018). (Cited on page 42.)

[144] D. Brick, V. Engemaier, Y. Guo, M. Grossmann, G. Li, D. Grimm, O. G. Schmidt, M. Schubert, V. E. Gusev, M. Hettich, T. Dekorsy, Interface adhesion and structural characterization of rolled-up GaAs/$In_{0.2}Ga_{0.8}As$ multilayer tubes by coherent phonon spectroscopy, Scientific Reports 7 (1) (jul 2017). doi:https://doi.org/10.1038/s41598-017-05739-6. (Cited on page 42.)

[145] J. Harrison, J. Wu, O. Paydar, Y. Hwang, E. Threlkeld, J. Rosenzweig, P. Musumeci, R. Candler, High-gradient MEMS electromagnets for particle beam manipulation, Solid-State Sensors, Actuators and Microsystems Workshop (Jun. 2014). doi:DOI:10.13140/2.1.4307.9365. (Cited on page 42.)

[146] J. Harrison, O. Paydar, Y. Hwang, J. Wu, E. Threlkeld, P. Musumeci, R. N. Candler, Fabrication process for thick-film micromachined multi-pole electromagnets, Journal of Microelectromechanical Systems 23 (3) (2014) 505–507. doi:10.1109/jmems.2014.2315763. (Cited on page 42.)

[147] B. K. Teo, X. H. Sun, From top-down to bottom-up to hybrid nanotechnologies: Road to nanodevices, Journal of Cluster Science 17 (4) (2006) 529–540. doi:10.1007/s10876-006-0086-5. (Cited on page 42.)

[148] D. Karnaushenko, Shapeable microelectronics, phdthesis, Technische Universität Chemnitz (Jan. 2016). (Cited on page 42.)

[149] D. Karnaushenko, Compact helical antenna for smartimplant applications, phdthesis, Technische Universität Chemnitz (May 2017). (Cited on pages 42 and 44.)

[150] D. Makarov, D. Karnaushenko, O. G. Schmidt, Printable magnetoelectronics, ChemPhysChem 14 (9) (2013) 1771–1776. doi:10.1002/cphc.201300162. (Cited on page 43.)

[151] M. Melzer, J. I. Mönch, D. Makarov, Y. Zabila, G. S. C. Bermúdez, D. Karnaushenko, S. Baunack, F. Bahr, C. Yan, M. Kaltenbrunner, O. G. Schmidt, Wearable magnetic field sensors for flexible electronics, Advanced Materials 27 (7) (2014) 1274–1280. doi:10.1002/adma.201405027. (Cited on page 43.)

[152] D. Karnaushenko, D. Makarov, M. Stöber, D. D. Karnaushenko, S. Baunack, O. G. Schmidt, High-performance magnetic sensorics for printable and flexible electronics, Advanced Materials 27 (5) (2014) 880–885. doi:10.1002/adma.201403907. (Cited on page 43.)

[153] M. Melzer, M. Kaltenbrunner, D. Makarov, D. Karnaushenko, D. Karnaushenko, T. Sekitani, T. Someya, O. G. Schmidt, Imperceptible magnetoelectronics, Nature Communications 6 (1) (jan 2015). doi:10.1038/ncomms7080. (Cited on page 43.)

[154] M. Melzer, D. Karnaushenko, G. Lin, S. Baunack, D. Makarov, O. G. Schmidt, Direct transfer of magnetic sensor devices to elastomeric supports for stretchable electronics, Advanced Materials 27 (8) (2015) 1333–1338. doi:10.1002/adma.201403998. (Cited on page 43.)

[155] D. Karnaushenko, N. Münzenrieder, D. D. Karnaushenko, B. Koch, A. K. Meyer, S. Baunack, L. Petti, G. Tröster, D. Makarov, O. G. Schmidt, Biomimetic microelectronics for regenerative neuronal cuff implants, Advanced Materials 27 (43) (2015) 6797–6805. doi:10.1002/adma.201503696. (Cited on pages 43 and 44.)

[156] D. D. Karnaushenko, D. Karnaushenko, D. Makarov, O. G. Schmidt, Compact helical antenna for smart implant applications, NPG Asia Materials 7 (6) (2015) e188–e188. doi:10.1038/am.2015.53. (Cited on page 43.)

[157] D. Karnaushenko, D. D. Karnaushenko, D. Makarov, S. Baunack, R. Schäfer, O. G. Schmidt, Self-assembled on-chip-integrated giant magneto-impedance sensorics, Advanced Materials 27 (42) (2015) 6582–6589. doi:10.1002/adma.201503127. (Cited on page 43.)

[158] D. Karnaushenko, N. Münzenrieder, D. D. Karnaushenko, B. Koch, A. K. Meyer, S. Baunack, L. Petti, G. Tröster, D. Makarov, O. G. Schmidt, Biomimetic microelectronics for regenerative neuronal cuff implants, Advanced Materials 27 (43) (2015) 6797–6805. doi:10.1002/adma.201503696. (Cited on page 43.)

[159] D. D. Karnaushenko, D. Karnaushenko, D. Makarov, O. G. Schmidt, Compact helical antenna for smart implant applications, NPG Asia Materials 7 (6) (2015) e188–e188. doi:10.1038/am.2015.53. (Cited on page 43.)

[160] D. D. Karnaushenko, D. Karnaushenko, H.-J. Grafe, V. Kataev, B. Büchner, O. G. Schmidt, Rolled-up self-assembly of compact magnetic inductors, transformers, and resonators, Advanced Electronic Materials 4 (11) (2018) 1800298. doi:10.1002/aelm.201800298. (Cited on page 43.)

[161] D. Karnaushenko, T. Kang, V. K. Bandari, F. Zhu, O. G. Schmidt, 3D self-assembled microelectronic devices: Concepts, materials, applications, Advanced Materials 32 (15) (2019) 1902994. doi:10.1002/adma.201902994. (Cited on page 43.)

[162] C. Becker, D. Karnaushenko, T. Kang, D. D. Karnaushenko, M. Faghih, A. Mirhajivarzaneh, O. G. Schmidt, Self-assembly of highly sensitive 3D magnetic field vector angular encoders, Science Advances 5 (12) (dec 2019). doi:10.1126/sciadv.aay7459. (Cited on page 43.)

[163] D. Karnaushenko, T. Kang, O. G. Schmidt, Shapeable material technologies for 3D self-assembly of mesoscale electronics, Advanced Materials Technologies 4 (4) (2019) 1800692. doi:10.1002/admt.201800692. (Cited on page 43.)

[164] V. K. Bandari, Y. Nan, D. Karnaushenko, Y. Hong, B. Sun, F. Striggow, D. D. Karnaushenko, C. Becker, M. Faghih, M. Medina-Sánchez, F. Zhu, O. G. Schmidt, A flexible microsystem capable of controlled motion and actuation by wireless power transfer, Nature Electronics 3 (3) (2020) 172–180. doi:10.1038/s41928-020-0384-1. (Cited on page 43.)

[165] W. Huang, Z. Yang, M. D. Kraman, Q. Wang, Z. Ou, M. M. Rojo, A. S. Yalamarthy, V. Chen, F. Lian, J. H. Ni, S. Liu, H. Yu, L. Sang, J. Michaels, D. J. Sievers, J. G. Eden, P. V. Braun, Q. Chen, S. Gong, D. G. Senesky, E. Pop, X. Li, Monolithic 7mT-level magnetic induction by self-rolled-up membrane technology, Science Advances 6 (3) (jan 2020). doi:10.1126/sciadv.aay4508. (Cited on page 43.)

[166] P. Lepucki, A. I. Egunov, M. Rosenkranz, R. Huber, A. Mirhajivarzaneh, D. D. Karnaushenko, A. P. Dioguardi, D. Karnaushenko, B. Büchner, O. G. Schmidt, H.-J. Grafe, Self-assembled rolled-up microcoils for nL microfluidics NMR spectroscopy, Advanced Materials Technologies 6 (1) (2020) 2000679. doi:10.1002/admt.202000679. (Cited on page 43.)

[167] Y. Lee, V. K. Bandari, Z. Li, M. Medina-Sánchez, M. F. Maitz, D. Karnaushenko, M. V. Tsurkan, D. D. Karnaushenko, O. G. Schmidt, Nano-biosupercapacitors enable autarkic sensor operation in blood, Nature Communications 12 (1) (aug 2021). doi:10.1038/s41467-021-24863-6. (Cited on page 43.)

[168] J. Ganz, I. Buresch, E. Vinaricky, J. Horn, Elektrische Kontakte, Werkstoffe und Anwendungen: Grundlagen, Technologien, Prüfverfahren, Engineering online library, Springer Berlin Heidelberg, 2016, Ch. 18. Dauerhafte Verbindungen, Steckverbindungen und Gleitkontaktsysteme, pp. 537 – 602. doi:10.1007/978-3-642-45427-1. (Cited on page 45.)

[169] M. Vázquez, Advanced Magnetic Microwires, John Wiley & Sons, 2007, pp. 1 – 29. arXiv:https://onlinelibrary.wiley.com/doi/pdf/10.1002/9780470022184.hmm418, doi:https://doi.org/10.1002/9780470022184.hmm418. (Cited on pages 45, 46, and 47.)

[170] R. El Kammouni, Single and biphase magneticmicrowires: Microwave behaviorand temperature dependence, Ph.D. thesis, Universidad Autónoma de Madrid (Mar. 2015). (Cited on pages 46 and 47.)

[171] G. F. Taylor, A method of drawing metallic filaments and a discussion of their properties and uses, Physical Review 23 (5) (1924) 655–660. doi:10.1103/physrev.23.655. (Cited on page 47.)

[172] A. A. A.V.Ulitovsky, I.M. Maianski, Method of continuous casting of glass coated microwire (1960). (Cited on page 47.)

[173] A. Ulitovski, N. Avernin, Method of fabrication of metallic microwire (1964). (Cited on page 47.)

[174] K.-Y. Wang, D.-X. Chen, J. Arcas, V. Larin, J. Velazquez, M. Vazquez, A. Hernando, Glass-coated hard-magnetic Fe-Co-Cr microwires, Journal of Physics: Condensed Matter 9 (43) (1997) L573–L576. doi:10.1088/0953-8984/9/43/001. (Cited on page 47.)

[175] J. Torrejón, A. Thiaville, A. Adenot-Engelvin, M. Vázquez, O. Acher, Cylindrical magnetization model for glass-coated microwires with circular anisotropy: Statics, Journal of Magnetism and Magnetic Materials 323 (3-4) (2011) 283–289. doi:10.1016/j.jmmm.2010.09.018. (Cited on pages 47 and 61.)

[176] Quantum Design, Magnetic Property Measurement System SQUID VSM User's Manual, 6325 Lusk BoulevardSan Diego, CA 92121 USA (Jan. 2009). (Cited on page 47.)

[177] P. Cendula, S. Kiravittaya, I. Mönch, J. Schumann, O. G. Schmidt, Directional roll-up of nanomembranes mediated by wrinkling, Nano Letters 11 (1) (2010) 236–240. doi:10.1021/nl103623e. (Cited on page 50.)

[178] R. Huber, F. Kern, D. D. Karnaushenko, E. Eisner, P. Lepucki, A. Thampi, A. Mirhajivarzaneh, C. Becker, T. Kang, Baunack, B. Büchner, D. Karnaushenko, O. G. Schmidt, A. Lubk, Tailoring electron beams with high-frequency self-assembled magnetic charged particle micro optics, Nature Communications (in review) (2021). (Cited on pages 50, 51, 88, and 95.)

[179] F. Laermer, A. Schilp, Method of anisotropically etching silicon (1996). (Cited on page 50.)

[180] N. Shibata, S. D. Findlay, Y. Kohno, H. Sawada, Y. Kondo, Y. Ikuhara, Differential phase-contrast microscopy at atomic resolution, Nature Physics 8 (8) (2012) 611–615. doi:10.1038/nphys2337. (Cited on page 52.)

[181] K. Müller, F. F. Krause, A. Béché, M. Schowalter, V. Galioit, S. Löffler, J. Verbeeck, J. Zweck, P. Schattschneider, A. Rosenauer, Atomic electric fields revealed by a quantum mechanical approach to electron picodiffraction, Nature Communications 5 (1) (dec 2014). doi:10.1038/ncomms6653. (Cited on page 52.)

[182] T. Seki, Y. Ikuhara, N. Shibata, Toward quantitative electromagnetic field imaging by differential-phase-contrast scanning transmission electron microscopy, Microscopy 70 (1) (2020) 148–160. doi:10.1093/jmicro/dfaa065. (Cited on page 52.)

[183] R. Ferrier, Y. Liu, J. Martin, T. Arnoldussen, Electron beam tomography of magnetic recording head fields, Journal of Magnetism and Magnetic Materials 149 (3) (1995) 387–397. doi:10.1016/0304-8853(95)00304-5. (Cited on page 52.)

[184] T. J. Pennycook, A. R. Lupini, H. Yang, M. F. Murfitt, L. Jones, P. D. Nellist, Efficient phase contrast imaging in STEM using a pixelated detector. part 1: Experimental demonstration at atomic resolution, Ultramicroscopy 151 (2015) 160–167. doi:10.1016/j.ultramic.2014.09.013. (Cited on page 53.)

[185] H. Yang, T. J. Pennycook, P. D. Nellist, Efficient phase contrast imaging in STEM using a pixelated detector. part II: Optimisation of imaging conditions, Ultramicroscopy 151 (2015) 232–239. doi:10.1016/j.ultramic.2014.10.013. (Cited on page 53.)

[186] N. Shibata, S. D. Findlay, T. Matsumoto, Y. Kohno, T. Seki, G. Sánchez-Santolino, Y. Ikuhara, Direct visualization of local electromagnetic field structures by scanning transmission electron microscopy, Accounts of Chemical Research 50 (7) (2017) 1502–1512. doi:10.1021/acs.accounts.7b00123. (Cited on page 53.)

[187] J. Krehl, G. Guzzinati, J. Schultz, P. Potapov, D. Pohl, J. Martin, J. Verbeeck, A. Fery, B. Büchner, A. Lubk, Spectral field mapping in plasmonic nanostructures with nanometer resolution, Nature Communications 9 (1) (oct 2018). doi:10.1038/s41467-018-06572-9. (Cited on page 53.)

[188] V. Boureau, M. Staňo, J.-L. Rouvière, J.-C. Toussaint, O. Fruchart, D. Cooper, High-sensitivity mapping of magnetic induction fields with nanometer-scale resolution: comparison of off-axis electron holography and pixelated differential phase contrast, Journal of Physics D: Applied Physics 54 (8) (2020) 085001. doi:10.1088/1361-6463/abc77d. (Cited on pages 53 and 56.)

[189] H. Rose, Phase contrast in scanning transmission electron microscopy, OPTIK 39 (4) (1974) 416–436. (Cited on page 54.)

[190] N. Dekkers, H. de Lang, Differential phase-contrast in a STEM, OPTIK 41 (4) (1974) 452–456. (Cited on page 54.)

[191] A. Tonomura, T. Matsuda, J. Endo, T. Arii, K. Mihama, Holographic interference electron microscopy for determining specimen magnetic structure and thickness distribution, Physical Review B 34 (5) (1986) 3397–3402. doi:10.1103/physrevb.34.3397. (Cited on page 54.)

[192] F. Arntzenius, Time reversal operations, representations of the Lorentz group, and the direction of time, Studies in History and Philosophy of Science Part B: Studies in History and Philosophy of Modern Physics 35 (1) (2004) 31–43. doi:10.1016/j.shpsb.2003.09.005. (Cited on page 54.)

[193] A. Lubk, J. Zweck, Differential phase contrast: An integral perspective, Physical Review A 91 (2) (2015) 023805. doi:10.1103/physreva.91.023805. (Cited on page 56.)

[194] B. R. J. W. Strutt, On the theory of optical images, with special reference to the microscope, Philosophical Magazine Series 5. 42 (Nr. 255) (1896) 167 – 195. doi:doi:10.1080/14786449608620902. (Cited on page 56.)

[195] M. Beleggia, T. Kasama, R. E. Dunin-Borkowski, The quantitative measurement of magnetic moments from phase images of nanoparticles and nanostructures - I. Fundamentals, Ultramicroscopy 110 (5) (2010) 425 – 432, hannes Lichte 65th Birthday. doi:https://doi.org/10.1016/j.ultramic.2009.10.007. (Cited on page 62.)

[196] B. J. McMorran, A. Agrawal, I. M. Anderson, A. A. Herzing, H. J. Lezec, J. J. McClelland, J. Unguris, Electron vortex beams with high quanta of orbital angular momentum, Science 331 (6014) (2011) 192–195. doi:10.1126/science.1198804. (Cited on page 62.)

[197] E. Mafakheri, A. H. Tavabi, P.-H. Lu, R. Balboni, F. Venturi, C. Menozzi, G. C. Gazzadi, S. Frabboni, A. Sit, R. E. Dunin-Borkowski, E. Karimi, V. Grillo, Realization of electron vortices with large orbital angular momentum using miniature holograms fabricated by electron beam lithography, Applied Physics Letters 110 (9) (2017) 093113. doi:10.1063/1.4977879. (Cited on page 62.)

[198] G. Pozzi, P.-H. Lu, A. H. Tavabi, M. Duchamp, R. E. Dunin-Borkowski, Generation of electron vortex beams using line charges via the electrostatic Aharonov-Bohm effect, Ultramicroscopy 181 (2017) 191–196. doi:10.1016/j.ultramic.2017.06.001. (Cited on page 64.)

[199] J. Verbeeck, H. Tian, G. Van Tendeloo, How to manipulate nanoparticles with an electron beam?, Advanced Materials 25 (8) (2013) 1114–1117. doi:https://doi.org/10.1002/adma.201204206. (Cited on pages 66 and 94.)

[200] C. Hébert, P. Schattschneider, A proposal for dichroic experiments in the electron microscope, Ultramicroscopy 96 (3-4) (2003) 463–468. doi:10.1016/s0304-3991(03)00108-6. (Cited on page 66.)

[201] P. Schattschneider, S. Rubino, C. Hébert, J. Rusz, J. Kuneš, P. Novák, E. Carlino, M. Fabrizioli, G. Panaccione, G. Rossi, Detection of magnetic circular dichroism using a transmission electron microscope, Nature 441 (7092) (2006) 486–488. doi:10.1038/nature04778. (Cited on page 66.)

[202] A. Edström, A. Lubk, J. Rusz, Elastic scattering of electron vortex beams in magnetic matter, Phys. Rev. Lett. 116 (2016) 127203. doi:10.1103/PhysRevLett.116.127203. (Cited on pages 66 and 94.)

[203] V. P. Oleshko, J. M. Howe, Are electron tweezers possible?, Ultramicroscopy 111 (11) (2011) 1599–1606. doi:https://doi.org/10.1016/j.ultramic.2011.08.015. (Cited on pages 66 and 94.)

[204] D.-X. Chen, L. Pascual, F. J. Castaño, A. Hernando, M. Vazquez, Anomalous asymmetric magnetoinductance in amorphous $Co_{68.2}Fe_{4.3}Si_{12.5}B_{15}$ wire with shifted hysteresis loop, Journal of Physics D: Applied Physics 33 (2) (1999) 111–114. doi:10.1088/0022-3727/33/2/303. (Cited on page 72.)

[205] Y.-F. Li, M. Vázquez, D.-X. Chen, Asymmetric axial-field-dependent circular susceptibility in annealed FeCrSiB amorphous wire, Journal of Physics D: Applied Physics 37 (3) (2004) 389–391. doi:10.1088/0022-3727/37/3/013. (Cited on page 72.)

[206] R. Baartman, Optimal 3D quadrupole shapes, in: Proceedings of PAC2013, Pasadena, CA USA, no. 05 Beam Dynamics and Electromagnetic Fields in D01 - Beam Optics - Lattices, Correction Schemes, Transport, Spin Dynamics, 2013, pp. 773 – 777. (Cited on page 76.)

[207] V. K. Arkadyev, Absorption of electric waves in parallel wires, Journal of the Russian Physical and Chemical Society. Physics. 44 (1912) 165–200. (Cited on page 84.)

[208] J. H. E. Griffiths, Anomalous high-frequency resistance of ferromagnetic metals, Nature 158 (4019) (1946) 670–671. doi:10.1038/158670a0. (Cited on page 84.)

[209] C. Kittel, Interpretation of anomalous larmor frequencies in ferromagnetic resonance experiment, Physical Review 71 (4) (1947) 270–271. doi:10.1103/physrev.71.270.2. (Cited on page 84.)

[210] C. Kittel, On the theory of ferromagnetic resonance absorption, Physical Review 73 (2) (1948) 155–161. doi:10.1103/physrev.73.155. (Cited on page 84.)

[211] M. Hayashi, L. Thomas, R. Moriya, C. Rettner, S. S. P. Parkin, Current-controlled magnetic domain-wall nanowire shift register, Science 320 (5873) (2008) 209–211. doi:10.1126/science.1154587. (Cited on pages 84 and 96.)

[212] S. Emori, U. Bauer, S.-M. Ahn, E. Martinez, G. S. D. Beach, Current-driven dynamics of chiral ferromagnetic domain walls, Nature Materials 12 (7) (2013) 611–616. doi:10.1038/nmat3675. (Cited on page 84.)

[213] T. Sannomiya, Y. Arai, K. Nagayama, Y. Nagatani, Transmission electron microscope using a linear accelerator, Physical Review Letters 123 (15) (2019) 150801. doi:10.1103/physrevlett.123.150801. (Cited on page 85.)

[214] K. Harada, J. Endo, N. Osakabe, A. Tonomura, Direction-free magnetic field application system, e-Journal of Surface Science and Nanotechnology 6 (2008) 29–34. doi:10.1380/ejssnt.2008.29. (Cited on page 85.)

[215] A. Broers, Fabrication limits of electron beam lithography and of UV, X-ray and ion-beam lithographies, Philosophical Transactions of the Royal Society of London. Series A: Physical and Engineering Sciences 353 (1703) (1995) 291–311. doi:10.1098/rsta.1995.0101. (Cited on page 85.)

[216] F. Gao, L. Han, Implementing the Nelder-Mead simplex algorithm with adaptive parameters, Computational Optimization and Applications 51 (1) (2010) 259–277. doi:10.1007/s10589-010-9329-3. (Cited on page 90.)

[217] S. V. Yalunin, A. Feist, C. Ropers, Tailored high-contrast attosecond electron pulses for coherent excitation and scattering, Phys. Rev. Research 3 (2021) L032036. doi:10.1103/PhysRevResearch.3.L032036. (Cited on page 95.)

[218] R. Tomasello, E. Martinez, R. Zivieri, L. Torres, M. Carpentieri, G. Finocchio, A strategy for the design of skyrmion racetrack memories, Scientific Reports 4 (1) (oct 2014). doi:10.1038/srep06784. (Cited on page 96.)

[219] D. Liang, J. P. DeGrave, M. J. Stolt, Y. Tokura, S. Jin, Current-driven dynamics of skyrmions stabilized in MnSi nanowires revealed by topological Hall effect, Nature Communications 6 (1) (sep 2015). doi:10.1038/ncomms9217. (Cited on page 96.)

[220] S. Woo, K. Litzius, B. Krüger, M.-Y. Im, L. Caretta, K. Richter, M. Mann, A. Krone, R. M. Reeve, M. Weigand, P. Agrawal, I. Lemesh, M.-A. Mawass, P. Fischer, M. Kläui, G. S. D. Beach, Observation of room-temperature magnetic skyrmions and their current-driven dynamics in ultrathin metallic ferromagnets, Nature Materials 15 (5) (2016) 501–506. doi:10.1038/nmat4593. (Cited on page 96.)

[221] K. Litzius, I. Lemesh, B. Krüger, P. Bassirian, L. Caretta, K. Richter, F. Büttner, K. Sato, O. A. Tretiakov, J. Förster, R. M. Reeve, M. Weigand, I. Bykova, H. Stoll, G. Schütz, G. S. D. Beach, M. Kläui, Skyrmion Hall effect revealed by direct time-resolved X-ray microscopy, Nature Physics 13 (2) (2016) 170–175. doi:10.1038/nphys4000. (Cited on page 96.)

[222] S. S. P. Parkin, M. Hayashi, L. Thomas, Magnetic domain-wall racetrack memory, Science 320 (5873) (2008) 190–194. doi:10.1126/science.1145799. (Cited on page 96.)

[223] S. Parkin, S.-H. Yang, Memory on the racetrack, Nature Nanotechnology 10 (3) (2015) 195–198. doi:10.1038/nnano.2015.41. (Cited on page 96.)

[224] M. Arita, R. Tokuda, K. Hamada, Y. Takahashi, Development of TEM holder generating in-plane magnetic field used for in-situ TEM observation, Materials Transactions 55 (3) (2014) 403–409. doi:https://doi.org/10.2320/matertrans.MD201310. (Cited on page 96.)

[225] Z. Huang, K.-J. Kim, Review of X-ray free-electron laser theory, Physical Review Accelerators and Beams 10 (3) (2007) 034801. doi:10.1103/physrevstab.10.034801. (Cited on page 97.)

[226] G. Petrov, J. Davis, W. Schumaker, M. Vargas, V. Chvykov, B. Hou, A. Maksimchuk, V. Yanovsky, A. G. R. Thomas, K. Krushelnick, A. Garraud, D. P. Arnold, B. A. Peterson, M. G. Allen, Development of mini-undulators for a table-top free-electron laser, Laser and Particle Beams 36 (3) (2018) 396–404. doi:10.1017/s0263034618000423. (Cited on page 97.)

[227] B. Peterson, O. Oniku, W. Patterson, D. L. Roy, A. Garraud, F. Herrault, N. Dempsey, D. Arnold, M. Allen, Technology development for short-period magnetic undulators, Physics Procedia 52 (2014) 36–45. doi:10.1016/j.phpro.2014.06.007. (Cited on page 97.)

[228] M. Fuchs, R. Weingartner, A. Popp, Z. Major, S. Becker, J. Osterhoff, T. Seggebrock, R. Hörlein, G. D. Tsakiris, U. Schramm, T. P. Rowlands-Rees, S. M. Hooker, D. Habs, F. Krausz, S. Karsch, F. Grüner, First milestone on the path toward a table-top free-electron laser (FEL), AIP Conference Proceedings 1228 (1) (2010) 295–299. doi:10.1063/1.3426066. (Cited on page 97.)

[229] A. Dymnikov, T. Fishkova, S. Yavor, Spherical aberration of stigmatic doublets consisting of short quadrupole lenses, Radio Engineering and Electronic Physics - USSR 12 (4) (1967) 613. (Cited on page 97.)

[230] R. Parker, K. Jensen, R. Abrams, Field emitter array development for high frequency applications, in: 10th International Conference on Vacuum Microelectronics, 1997, pp. 92–97. doi:10.1109/IVMC.1997.627395. (Cited on page 99.)

[231] C. A. Spindt, A thin-film field-emission cathode, Journal of Applied Physics 39 (7) (1968) 3504–3505. doi:10.1063/1.1656810. (Cited on page 99.)

Danksagung

Zum Abschluss dieser Arbeit möchte ich mich gerne bei einigen Menschen bedanken, ohne die mein Promotionsprojekt bei Weitem nicht so erfolgreich oder schlicht nicht möglich gewesen wäre und die mir die Fertigstellung der Dissertation in der pandemischen Ausnahmesituation erleichtert haben. Zuallererst möchte ich Axel für die hervorragende Betreuung, die vielen Erklärungen und Hilfestellungen und die konstruktive Kritik meinen Dank aussprechen. Nach Gesprächen mit ihm hatte ich immer das gute Gefühl, dass alles halbwegs nach Plan verläuft und falls dies einmal nicht der Fall war, hatte er immer zeitnah einen Plan B parat. Axel hat einen nicht unerheblichen Teil dazu beigetragen, dass ich mich in der Arbeitsgruppe und beim Anfertigen dieser Arbeit stets wohlgefühlt habe. Des Weiteren bedanke ich mich bei Jonas und Johannes dafür, dass sie mir durch Diskussionen wie auch mit Rat und Tat in Bezug auf wissenschaftliche und technische Fragestellungen zur Seite standen. Zusätzlich hat Jonas mich bei der numerischen Auswertung der Ergebnisse unterstützt, indem er mir seine DPC-Skripte zur Verfügung gestellt hat. Weiterhin möchte ich Daniel dafür danken, dass er mir bei vielen praktischen Problemen am Mikroskop geholfen hat. Mein Dank gilt außerdem den noch nicht genannten Mitgliedern der Arbeitsgruppe "Advanced Methods of Electron Microscopy" Arsha, Franziska, Gesine, Pavel, Sebastian und Subakti, die immer hilfsbereit waren und mir den Arbeitsalltag verschönert haben. Ferner möchte ich mich bei unseren Kollaborationspartnern vom Institut für integrative Nanowissenschaften bedanken, die unter der Leitung von Oliver G. Schmidt das Polymer-basierte Selbstassemblierungsverfahren für die Mikrospulen, die in meinem Promotionsprojekt eingesetzt wurden, entwickelt haben. Maßgeblich für den Erfolg des Projekts waren Renato Huber sowie Dmitriy und Daniil Karnaushenko. Ihnen und allen anderen am Projekt Mitwirkenden gilt mein Dank für das kollegiale Miteinander und die Einführung in die spannende Welt der Mikro- und Nanofabrikation. Außerdem möchte ich Eric Eisner, Piotr Lepucki, Alaleh Mirhajivarzaneh, Christian Becker und Tong Kang danken, die ebenfalls am Projekt beteiligt waren. Im Rahmen der Arbeit konnte ich außerdem einen Einblick in viele verschiedene Analyse- und Fabrikationsmethoden gewinnen. Dafür wurde ich von verschiedenen Kolleg:innen in die jeweiligen Geräte eingearbeitet, auch ihnen gilt mein Dank: Thomas Wiek (FIB), Sabine Neitsch (VSM) und Volker Neu (PPMS). Außerdem möchte ich Stefan Baunack, Almut Pöhl, Dina Biberstein, Thomas Wiek und Tina Walter dafür danken, dass sie in der FIB Proben für mich präpariert und ihr FIB-Wissen mit mir geteilt haben, sodass ich im weiteren Verlauf die Proben selbst präparieren konnte. Vivienne Engemaier danke ich für die Zurverfügungstellung der zunächst verwendeten GaAs-Mikrospulen, die sich leider nicht als geeignet für unsere Anwendung erwiesen haben. Außerdem spreche ich meinen Dank dem gesamten Reinraumpersonal aus. Hier möchte ich vor allem Liesa Raith und Sandra Nestler für diverse Einweisungen danken. Ulrike Nitsche möchte ich für die Hilfe bei der Einrichtung der magnetischen FEM-Simulationen auf dem Server-Cluster danken. Ralf Voigtländer, Falk Sander, Steffen Grundkowski und Alexander Müller-Knappe spreche ich für die Hilfe bei der Planung und der Fertigung des Aperturhalters, der für die Hochfrequenzmessungen benutzt wurde, meinen Dank aus. Ich danke weiterhin Frauke Thunig, Marco Naumann und Roland Hübel

für die praktische Unterstützung und die Bereitstellung der vielen Kleinteile und Werkzeuge. Außerdem möchte ich Herrn Prof. Büchner für die Möglichkeit, diese Arbeit in dem von ihm geleiteten Institut anzufertigen und für die Übernahme des Erstgutachtens danken. Abschließend danke ich Herrn Prof. Johan Verbeek für seine Bereitschaft, das Zweitgutachten zu übernehmen.

Aus meinem freundschaftlichen Umfeld danke ich zuerst Lukas, Louis, Martin, Max, Moritz und Robert als zeitweilige und dauerhafte Teilnehmer unseres lunch tables. Die gemeinsamen Mittagessen, after work sessions und anderen Aktivitäten waren mir stets ein großes Vergnügen. Außerdem danke ich allen permanenten und zeitweisen Bewohner:innen der DammWeG, Mönchi 11 und R21.3 für die tolle Zeit während der Promotion, die vielfältigen Freizeitaktivitäten und das schöne WG-Leben. Besonders und von ganzem Herzen möchte ich mich bei „meiner" Franzi bedanken, die mich in allen Lebenslagen während der Promotion unterstützt, mir Rückhalt geboten und mir viele schöne gemeinsame Stunden in der ganzen Zeit beschert hat. Außerdem möchte ich Martha meinen Dank aussprechen, die mir mit ihrem herzlichen Wesen ein zweites Zuhause gegeben hat. Zum Schluss möchte ich meinen Eltern und Großeltern, die auf direktem sowie indirektem Wege die Begeisterung für die Physik in mir geweckt und mich für die gesamte Dauer meines Studiums unterstützt haben, herzlichst danken.

Erklärung des Promovierenden zum Antrag auf Eröffnung des Promotionsverfahrens

1. Die folgende Promotionsordnung in ihrer gültigen Fassung erkenne ich an:

   Bereich Mathematik und Naturwissenschaften - Promotionsordnung vom 23.02.2011

2. Die Promotion wurde an folgendem Institut/an folgender Professur durchgeführt:

   Leibniz-Institut für Festkörper- und Werkstoffforschung Dresden

3. Folgende Personen haben die Promotion wissenschaftlich betreut und/oder mich bei der Auswahl und Auswertung des Materials sowie bei der Herstellung des Manuskripts unterstützt:

   Dr. Axel Lubk

   Dr. Daniil Karnaushenko

4. Ich bestätige, dass für meine Person bisher keine früheren, erfolglosen Promotionsverfahren stattgefunden haben. Andernfalls habe ich diesem Antrag eine Erklärung bzw. Nachweise beigelegt, in dem ersichtlich ist, wo, wann, mit welchem Thema und mit welchem Bescheid diese Promotionsversuche stattgefunden haben

5. Ich versichere weiterhin, dass

(a) ich die vorliegende Arbeit mit dem Titel „Miniaturized Electron Optics based on Self-Assembled Micro Coils" ohne unzulässige Hilfe Dritter und ohne Benutzung anderer als der angegebenen Hilfsmittel selbst angefertigt habe. Hilfe Dritter wurde nur in wissenschaftlich vertretbarem und prüfungsrechtlich zulässigem Ausmaß in Anspruch genommen. Es sind keine unzulässigen geldwerten Leistungen, weder unmittelbar noch mittelbar, im Zusammenhang mit dem Inhalt der vorliegenden Dissertation an Dritte erfolgt.

(b) die aus fremden Quellen direkt oder indirekt übernommenen Gedanken als solche kenntlich gemacht sind.

(c) ich die vorliegende Arbeit bisher weder im Inland noch im Ausland in gleicher oder ähnlicher Form einer anderen Prüfungsbehörde zum Zwecke einer Promotion oder eines anderen Prüfungsverfahrens vorgelegt habe.

6. Mir ist bekannt, dass die Nichteinhaltung dieser Erklärung oder unrichtige Angaben zum Verfahrensabbruch oder zum nachträglichen Entzug des Doktortitels führen können.

Ort, Datum

Unterschrift Antragsteller:in